DESIGN OF BIOSENSORS AND TARGETED NANOTHERANOSTICS FOR NEURODEGENERATIVE DISEASE

RESMI A.N.

PhD THESIS

2024

SREE CHITRA TIRUNAL INSTITUTE FOR MEDICAL SCIENCES AND TECHNOLOGY, TRIVANDRUM

An Institution of National Importance established by an Act of the Indian Parliament
(Act No.52 of 1980)
Department of Science and Technology, Govt. of India
www.sctimst.ac.in

DESIGN OF BIOSENSORS AND TARGETED NANOTHERANOSTICS FOR NEURODEGENERATIVE DISEASE

A THESIS SUBMITTED BY

RESMI A.N.

TO

SREE CHITRA TIRUNAL INSTITUTE FOR MEDICAL SCIENCES AND TECHNOLOGY, TRIVANDRUM.

IN PARTIAL FULFILMENT OF THE REQUIREMENTS

FOR THE AWARD OF

DOCTOR OF PHILOSOPHY

2024

DECLARATION BY THE STUDENT

CERTIFICATE

I, **RESMI A.N.** hereby certify that I had personally carried out the work depicted in the thesis titled, **"DESIGN OF BIOSENSORS AND TARGETED NANOTHERANOSTICS FOR NEURODEGENERATIVE DISEASE"**. No part of this thesis has been submitted for the award of any other degree or diploma prior to this date.

Signature

RESMI A.N.

Date

CERTIFICATE BY THE RESEARCH GUIDE
(*in institute letterhead)

Name of the Guide: Dr R.S. Jayasree

Division: Biophotonics and Imaging

This is to certify that **RESMI A.N.**, Division of Biophotonics and Imaging of this institute has fulfilled the requirements prescribed for the Ph.D. degree of the Sree Chitra Tirunal Institute for Medical Sciences and Technology, Trivandrum.

The thesis entitled, "**DESIGN OF BIOSENSORS AND TARGETED NANOTHERANOSTICS FOR NEURODEGENERATIVE DISEASE**" was carried out under my direct supervision. No part of the thesis was submitted for the award of any degree or diploma prior to this date.

Clearance was obtained from the Institutional Ethics Committee for carrying out the study. (Order no: SCT/IEC/IEC-1669/DECEMBER-2020).

Clearance was obtained from the Institutional Animal Ethics for carrying out the study. (IAEC approval No-SCT/IAEC399/MARCH/2021/109).

Signature

Name of the Guide

Date

CERTIFICATE BY THE RESEARCH CO-GUIDE
(*in institute letterhead)

Name of the Guide: Dr R.S. Jayasree

Division: Biophotonics and Imaging

This is to certify that **RESMI A.N**., Division of Biophotonics and Imaging of this institute has fulfilled the requirements prescribed for the Ph.D. degree of the Sree Chitra Tirunal Institute for Medical Sciences and Technology, Trivandrum.

The work under the thesis entitled, "**DESIGN OF BIOSENSORS AND TARGETED NANOTHERANOSTICS FOR NEURODEGENERATIVE DISEASE"** was carried out under my direct supervision. No part of the thesis was submitted for the award of any degree or diploma prior to this date.

Clearance was obtained from the Institutional Ethics Committee for carrying out the study. (Order no: SCT/IEC/IEC-1669/DECEMBER-2020).

Clearance was obtained from the Institutional Animal Ethics for carrying out the study. (IAEC approval No-SCT/IAEC399/MARCH/2021/109).

Signature

Name of the Co-guide

Date

APPROVAL OF THE THESIS

(in institute letterhead)

The thesis entitled

DESIGN OF BIOSENSORS AND TARGETED NANOTHERANOSTICS FOR NEURODEGENERATIVE DISEASE

Submitted by

RESMI A.N.

for the degree of

Doctor of Philosophy

of

SREE CHITRA TIRUNAL INSTITUTE FOR MEDICAL SCIENCES AND TECHNOLOGY, TRIVANDRUM

is evaluated and approved by

…… ……

(Name & Signature of the Guide) (Name & Signature of thesis examiner)

ACKNOWLEDGEMENTS

The journey of pursuing a PhD has been filled with the support of many individuals, without whom I wouldn't be where I am today. I am deeply grateful to everyone who has shaped and supported me throughout this process, enabling the successful completion of my research. First and foremost, I owe immense gratitude to my supervisor, Dr. R.S. Jayasree, Scientist G, Division of Biophotonics and Imaging, for her constant support and guidance throughout my PhD. Her encouragement and assistance during challenging times were invaluable. I sincerely thank her for all the timely help and healthy discussions that paved the way for completing this thesis.

I would like to express my heartfelt gratitude to my doctoral advisory committee (DAC) members: Dr. Rekha M.R., Dr. Anoop Kumar Thekkuveetil, and Dr. Jinesh K.B., for their constructive criticism, invaluable feedback, and insightful suggestions. I am deeply thankful to Dr. Jinesh K.B. for his constant motivation and mental support throughout my research journey. I am also grateful to the lab memebers at Indian Institute of Space Science and Technology (IIST).

I owe my sincere gratitude to The Director, SCTIMST and Head BMT Wing for providing all the facilities during the course of my PhD work. I extend my thanks to Dean, Associate Dean (PhD affairs), Registrar, Deputy Registrar and all members of academic division and Director's office for their support and help.

I would like to extend my heartfelt thanks to all the staffs of the BMT Wing and Hospital wing, who, whether directly or indirectly, contributed to the success of my PhD program.

I would like to express my deepest gratitude to Dr. Rekha C. R., Dr. Anna Thomas, and Dr. Sheena for their invaluable guidance and teachings. I especially want to acknowledge Mr. Willi Paul for his support on the Raman spectral studies. I thank Dr. Kamalesh K. Gulia, for supporting the animal model development for Alzheimer's disease. I am also sincerely grateful to Dr. Sachin J Shenoy and his team for their invaluable support in the animal experiments. I thank Jijo P.T. for his support in developing the prototype for the electronic sensor.

I am also incredibly thankful to all my lab members Dr. Sivaselvam, Dhushyandhun, Anjana., Rinta, Sarath, Dhujana, Anila, Bilal, Neelakandan, and Arun—who have shared this journey with me. The wonderful times we spent together will always be cherished. I extend my heartfelt thanks to all my friends, especially Dr. Shaiju S. Nazeer and Pratheesh K.V. for their unwavering support.

I cannot fully express my gratitude to my husband, Mr. Vimal Krishnan, and my daughter, Ammu Krishnan, with words alone. Their unwavering love and support have been my constant source of strength. I am forever grateful for both of you. This achievement is yours as much as it is mine.

Finally, I want to extend my heartfelt thanks to my parents, father-in-law, mother-in-law, brothers, and sisters. Without their affection, love, and parental support, I wouldn't have reached here. A special thanks to my sister Simi for her boundless love and encouragement. Having a supportive family as a strong foundation has truly made it possible to overcome many challenges.

TABLE OF CONTENTS

LIST OF FIGURES

LIST OF TABLES

LIST OF ABBREVIATIONS

S No	Abbreviation	Full Form
1	NPs	Nanoparticles
	NCs	nanoclusters
	SERS	Surface-Enhanced Raman Scattering
	AuNPs	Gold nanoparticles
	AuNCs	Gold nanoclusters
	SPR	Surface Plasmon Resonance
	NIR	Near Infrared
	ATR	Attenuated Total Reflection
	LSPR	Localized Surface Plasmon Resonance
	ANN	Artificial neural networks
	PDT	Photodynamic therapy
	ROS	Reactive Oxygen Species
	AD	Alzheimer's disease
	MCI	Mild Cognitive Impairment

	APP	Amyloid β-precursor protein
	Aβ	Amyloid β
	p-Tau	Phosphorylated tau
	t-Tau	Total tau
	APOE4	Apolipoprotein E4
	NFT	Neurofibrillary tangles
	BBB	Blood-Brain Barrier
	CSF	Cerebrospinal fluid
	NFT	Neurofibrillary tangles
	PET	Positron Emission Tomography
	MRI	Magnetic Resonance Imaging
	ELISA	Enzyme-linked immunosorbent assay
	NMs	Nanomaterials
	CV	cyclic voltammetry
	DPV	Differential pulse voltammetry
	LSV	Linear sweep voltammetry
	EIS	Electrochemical impedance spectroscopy
	PBS	Phosphate-buffered saline

	L-dopa	Levodopa
	LAT1	Large amino acid transporter 1
	$HAuCl_4$	Gold(III) chloride trihydrate
	$AgNO_3$	Silver nitrate
	APTES	3-aminopropyl triethoxysilane
	BSA	Bovine serum albumin
	GA	Glutaraldehyde
	Cs-AuNPs	Chitosan-coated gold Nanoparticles
	Al	Aluminum
	FTIR	Fourier-transform infrared
	ICP-MS	Inductively Coupled Plasma Mass Spectrometry
	TEM	Transmission electron microscopy
	WCA	Water Contact Angle
	SEM	Scanning Electron Microscopy
	MLP	Multi-Layer Perceptron
	SVM	Support Vector Machine
	RBF	Radial Basis Function
	H_2SO_4	Sulphuric acid

	H_2O_2	Hydrogen peroxide
	HOPG	Highly Oriented Pyrolytic Graphite
	STM	Scanning Tunneling Microscopy
	STM	Scanning Tunneling Spectroscopy
	LDOS	Local Density of States
	EDC	1-Ethyl-3-(3-dimethylaminopropyl)
	NHS	N-Hydroxysuccinimide
	DPBF	Diphenylisobenzofuran
	bEnd.3	brain endothelial cells
	FBS	Fetal Bovine Serum
	Cy-AuNCs	Cysteine gold nanoclusters
	AuCs-LD	Levodopa-conjugated Cysteine gold nanoclusters
	MALDI	Matrix Assisted Laser Deposition Mass Spectroscopy
	TEER	Trans epithelial/trans endothelial electrical resistance
	ThT	Thioflavin T
	N2A	Neuro-2a

	STZ	Streptozotocin
	ICV	Intracerebroventricular
	ThS	Thioflavin S
	H & E	Hematoxylin and eosin
	IHC	Immunohistochemistry (IHC)
	IF	Immunofluorescence

SYNOPSIS

The advancements in material science and nanotechnology have significantly influenced the development of nanosystems characterized by their unique nanostructures and compositions with distinct chemical and physical properties. Over the past few decades, substantial progress in the design and fabrication of these nanosystems has propelled their application, particularly in the biological and biomedical fields. Nanomaterials exhibit unique properties such as size-dependent reactivity, distinctive optical and magnetic characteristics, and a high surface-to-volume ratio, making them exceptionally valuable in various domains, especially biomedicine, where they play a pivotal role in disease diagnosis and treatment. Nanotechnology opens a new approach in the field of molecular detection, drug delivery and monitoring for several ever-challenging human diseases including neurodegenerative disorders. Alzheimer's disease (AD) is the most prevalent neurodegenerative condition, accounting for approximately 70% of dementia cases. With the aging population on the rise, AD is expected to become a significant societal and health challenge. Currently, around 50 million people worldwide are affected by AD, and this number is projected to triple by 2050. AD progressively impairs cognitive abilities and causes memory loss. Several drugs have been approved for the therapeutic management of mild and moderate AD. These drugs are neurotransmitter regulators and can only temporarily enhance the patient’s status. There is currently no drug that can stop or reverse the pathological progression of

this disease. The pathogenesis of AD is assumed to originate as a result of the conversion of Amyloid beta (Aβ) from its healthy monomeric forms to insoluble precipitates, which combine to form fibrils and plaques. Since there is no effective cure for AD, early diagnosis and management are crucial. At present, the methods used to diagnose AD are only useful when the disease has advanced significantly. Therefore, there is an urgent need to develop accurate and sensitive diagnostic techniques for early detection. Moreover, tools or techniques with higher efficacy for the management of the disease need to be developed. Another major limiting factor in the management of this disease as in the case of any other brain related disorders is the presence of a polarized layer of endothelial cells that comprise the blood-brain barrier (BBB) which prevents the passage of almost 98% of all potential neurotherapeutics to the brain. Therefore, the design of highly potent therapeutic agents that can cross the BBB is a challenging field of research that will facilitate better management of AD. The fundamental requirement for accomplishing this is the development of a biocompatible nanosystem capable enough to cross the blood-brain barrier and disintegrate amyloid fibrils.

With these backgrounds and the gap areas discussed as above, we hypothesize that nanoformulations with unique properties could be designed for the development of nanosensors for the biomarkers for AD at an early stage of mild cognitive impairment and the same could also be designed to cross BBB to target and inhibit/disintegrate the amyloid fibrils to combat the main reason identified for the cause of AD.

Thus the main objectives of the thesis are: -

i. Design and development of biosensors for the detection of Mild Cognitive Impairment

ii. Development of nanocarriers to cross the blood-brain barrier.

iii. Brain targeting for imaging and therapy of neurodegenerative disease.

In this regard, gold nanoparticle-based optical and electronic biosensors were developed for the detection of AD/ Mild cognitive impairment(MCI) biomarkers. The efficacy of these sensors was evaluated in clinical samples. For the therapeutic management of AD, bi-functional cysteine gold nanoclusters were developed, and its efficacy was evaluated *in vitro* and *in vivo* models.

The thesis has been organized into five chapters: Introduction, Literature Review, Materials & Methods, Results & Discussion and Conclusion.

Chapter 1 provides a general **introduction** to the application of nanomaterials in the biomedical field, specifically highlighting the nanoparticles used in this study, namely gold nanoparticles and gold nanoclusters, as well as an overview of neurodegenerative diseases with an emphasis on Alzheimer's disease.

Chapter 2 summarizes the **literature review** on various nanotechnology-based techniques for bio-sensing and therapy for Alzheimer’s disease, and nanotechnology-based bio-imaging.

Chapter 3 details the **materials and methods** used for the development of optical and electronic biosensors and the synthesis of cysteine gold nanoclusters. This chapter also details the various procedures used to evaluate the developed materials.

Chapter 4 describes the **results and discussion** which is subdivided into four sections:

The first section deals with the development of the optical biosensor. The optical biosensor is designed for the precise and ultrasensitive detection of AD biomarkers from the blood, wherein the concentration of the biomarkers is very low compared to that of cerebrospinal fluid (CSF). All the major markers of AD including $A\beta_{40}$, $A\beta_{42}$, p-Tau, and t-Tau are studied using surface-enhanced Raman spectroscopy (SERS). This sensor was designed based on spiky star-shaped chitosan-coated gold nanoparticles conjugated with antibodies specific to each biomarker, which are coated on an aluminium substrate. Aluminium was chosen as the base material due to its low fluorescence, cost-effectiveness, and ready availability. The spiky star-shaped gold nanoparticles facilitated the plasmon coupling effect, significantly amplifying the Raman signal. The results obtained demonstrate the high sensitivity of this approach in detecting Aβ and tau proteins across a concentration of micromolar (μM) to attomolar (aM) range. To evaluate the potential of this sensor in clinical applications, it was used to identify mild cognitive impairment (MCI), a potential precursor to AD, from AD patients, from their blood samples. This objective was also supported by employing a range of machine-learning algorithms on the SERS data. These algorithms can identify patterns indicative of specific diseases or predict the likelihood of disease progression, thereby aiding clinicians in making decisions about patient care. This approach demonstrates the potential for developing a rapid, reliable, and cost-effective blood plasma test, which could serve as a valuable tool for early AD detection.

The second section deals with the development of an electronic biosensor. This system utilizes antibody-conjugated gold nanoparticles decorated on a specifically designed and developed interdigitated gold electrode and monitors change in current resulting from antigen-antibody interactions when the AD biomarkers ($A\beta_{40}$, $A\beta_{42}$, p-Tau and t-Tau) are introduced. The device features a base charge transport layer made of gold nanoparticles, which plays a crucial role in its operation. The interaction between charged species, such as antigens and antibodies, affects the overall charge density, making it possible to observe changes in the device's current as a straightforward method to record these interactions. At room temperature, the sensor monitors the change in current in response to the various AD biomarker concentrations in the range from micromolar (μM) to femtomolar (fM). Initially, the conductivity properties of Aβ and tau proteins were verified using scanning tunneling microscopy (STM) and scanning tunneling spectroscopy (STS). When tested in clinical samples, the sensor was able to detect these interactions and the corresponding changes in current highlighting the sensor's potential for use in early and accurate AD diagnostics. A technology lead based on the concept of electronic sensor has also been arrived.

The third section focuses on the development of a carrier which can potentially cross BBB with real-time imaging capability, and contribute towards the effective management of AD. While various studies report the use of nanosystems for the management of AD, no system has been reported for both imaging and therapeutic applications. Herein bifunctional cysteine gold nanoclusters (Cy-AuNCs) were synthesized and tested for its potential to cross BBB with imaging possibilities and also studied the interaction of this unique nanomaterial with the amyloid fibrils,

in vivo. The nanocluster possessed inherent fluorescence with a strong fluorescence emission at 610 nm and a shoulder peak at 665 nm to utilize them for imaging application. It showed self-assembled structure with an average particle size of the nanocluster of 3 nm. These clusters were then functionalized with Levodopa (AuCs-LD), enabling the cluster to cross the BBB, as demonstrated in *in vitro* and *in vivo* experiments. To explore the molecular interactions between Aβ and the nanocluster, a molecular docking study was conducted, wherein it showed that cysteine was able to bind to the Aβ fibrils through thiophilic interactions. In *in vitro* studies, the nanoclusters were able to inhibit/ disintegrate the Aβ plaques.

The fourth section investigates the therapeutic potential of gold nanocluster in AD animal model. For this, AD animal models were developed in mouse using intra-cerebroventricular (ICV) injection of streptozotocin (STZ) and treated with the cysteine gold cluster. The study evaluates the efficacy of the nanoclusters in inhibiting and disintegrating Aβ plaques as observed through various behavioural tests (Y Maze and Open field test) and histological evaluations (H&E staining, Immunohistochemistry). In the behavioural tests, the treated animals showed improved behaviour compared to the animals without treatment. In the histological evaluation, animals in the treatment group showed less lesions, reduced plaques and lowered expression of biomarkers when compared to the animals without treatment. This confirms the therapeutic potential of the nanocluster.

Chapter 5 summarizes the findings of the study, presents **conclusions**, and discusses future research directions and potential applications. A highly sensitive SERS biosensor, capable of detecting attomolar concentrations, has been developed for the diagnosis of AD, using AD biomarkers ($A\beta_{40}$, $A\beta_{42}$, p-Tau, and t-Tau). This

biosensor is aided by a machine learning algorithm, which allows for more accurate and rapid analysis of results. In parallel, a simple and portable electronic ultrasensitive biosensor has been fabricated for detecting the same biomarkers. In addition to diagnosis, nanosystems were developed for the management of AD. In this regard, cysteine gold nanoclusters exhibit excellent disintegration properties and was able to cross the BBB *in vitro*. Functionalization with L-Dopa further enabled these nanoclusters (AuCs-LD) to successfully target the brain and cross the BBB *in vivo.* In an STZ-induced AD model, the therapeutic efficacy of AuCs-LD has been demonstrated, as observed through both behavioral assessments and histological evaluations. Moreover, the intrinsic fluorescence of the gold nanocluster facilitated image-guided therapy. However, further advancements are required to fully realize these techniques. These include developing a fully functioning prototype for both the optical and electronic biosensors. The nanoclusters need to be evaluated more extensively in pre-clinical models before confirming its use for clinical trials.

CHAPTER 1

INTRODUCTION

The field of science is currently undergoing a transformative era, driven by the rapid advancements in the growing field of nanoscience and its practical applications, nanotechnology. Nanoscience investigates the unique characteristics that arise from manipulating matter at the nanoscale. At this scale, the laws of physics and chemistry deviate from our macroscopic experience, giving rise to novel phenomena with immense potential for technological advancements. Nanotechnology acts as the bridge, translating the fundamental knowledge from nanoscience into tangible applications. By precisely designing, synthesizing, and manipulating materials at this scale, scientists and engineers are pioneering the creation of revolutionary structures, devices, and systems with superior properties.

The sizes of objects can vary greatly depending on their scale, ranging from macroscale to nanoscale (Figure 1). Their small size gives rise to distinctive magnetic, electronic, optical, and catalytic behaviors that differ from their bulk counterparts (Joudeh and Linke, 2022). These unique properties, combined with the ability to precisely control their size and shape using various synthesis methods, make them versatile building blocks for a wide range of applications (Baig *et al.*, 2021).

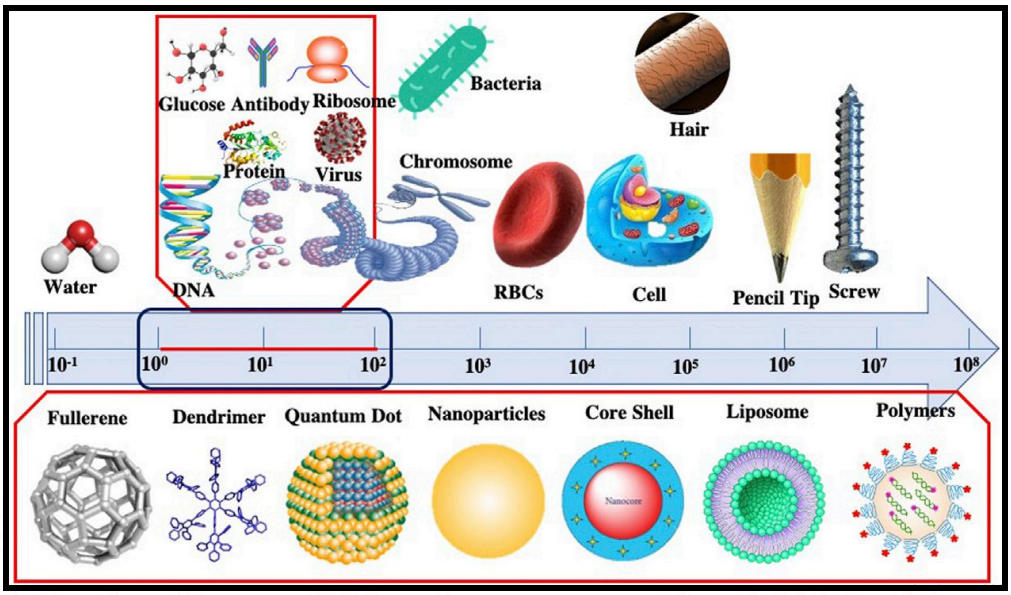

Figure 1. A comparative size scale ranging from macroscale to nanoscale, illustrated by various objects. The figure reproduced from (Shukla *et al*., 2021).

The concepts behind the rapidly expanding field of nanotechnology were inspired by Nobel Laureate Richard Feynman's 1959 lecture, "There is plenty of room at the bottom." He envisioned a future where we could manipulate matter at the atomic level, paving the way for today's exciting field. The ability to tailor properties at the atomic level opens doors for many applications in fields like health care, environmental protection, food, cosmetics, engineering, optics, biomedical sciences, chemical industries, electronics, space industries, drug delivery, and various advanced technologies. Their properties surpass many of today's scientific challenges, transcending the limitations of conventional methods. This versatility has led to their evaluation and application across numerous fields (Granqvist and Laurila, 2011).

In biomedical sciences, nanomaterials have brought significant advancements in both diagnostics and therapeutics. They enable precise targeting and controlled release of drugs/pharmaceuticals, improving treatment efficacy while minimizing

side effects, enhancing imaging techniques, facilitating early disease detection and monitoring (Malik, Muhammad and Waheed, 2023). The integration of nanotechnology with biomedicine holds the promise of highly personalized and effective healthcare solutions.

1.1. Biomedical Applications of Nanoparticles

Based on the nano concept, nanomedicine, a specialized field, focuses on utilizing nanoparticles to diagnose, treat and monitor biological systems. Given their small size, comparable to or smaller than essential biological entities such as genes (2 nm wide and 10–100 nm long), proteins (5–50 nm), viruses (20–450 nm), and cells (10–100 μm), nanoscale materials show immense potential in biomedicine (Krishnan, 2010). These particles can access previously inaccessible biological regions and interact at the molecular level, enabling efficient delivery of therapeutic agents. Numerous nanomaterial-based imaging and diagnostic devices, as well as drug delivery systems, are currently in various stages of preclinical, clinical, or commercial development, with their numbers rapidly increasing each year.

In recent years, metal nanoparticles and nanoclusters (NCs) have become a focal point of research due to their distinctive size-dependent properties. These nanomaterials exhibit unique optical, electrochemical, and catalytic behaviors, which make them highly suitable for a diverse array of applications. Metal NCs, which are sub-nanometer particles, act as intermediaries between molecular and nanoparticle systems, comprising a few to hundreds of metal atoms surrounded by a protective ligand shell. Despite their tiny size, NCs possess optical, electrical, physical, and chemical properties that are distinctly different from those of metal nanoparticles (Deepak, 2017; Sousa, Schuck and Hassan, 2021).

Gold, in particular, has garnered special interest within these metal nanosystems due to its remarkable optical characteristics, low toxicity, superior biocompatibility, high stability under ambient conditions, and ease of functionalization with biologically relevant molecules. Both gold nanoparticles and gold nanoclusters have shown significant potential in fields such as catalysis, sensing, surface-enhanced Raman scattering (SERS), and fluorescence imaging (Kohout, Santi and Polito, 2018; Dan *et al.*, 2022). Consequently, our research focuses on gold-based nanosystems. This thesis explores the preparation, characterization, and design of gold-based nanoparticles and nanoclusters for various biomedical applications, including sensing, imaging and therapy.

1.1.1 Gold Nanoparticles (AuNPs)

AuNPs have exceptional optoelectronic properties, low toxicity, and excellent biocompatibility. Unlike bulk gold, AuNPs possess unique characteristics such as surface plasmon resonance (SPR), size-dependent electronic properties, and photothermal effects, which are crucial in nanoscience and nanotechnology. AuNPs are available in various sizes (ranging from 1 nm to 8 μm) and shapes (including nanospheres, nanorods, nanoshells, etc) (Khan *et al.*, 2014).

Surface plasmon resonance is a phenomenon that occurs when light interacts with the free electrons on the surface of a metal, such as gold, at the nanoscale. When light hits the AuNPs, it can cause the conduction electrons on the nanoparticle's surface to oscillate collectively. This oscillation leads to a strong absorption and scattering of light, which is the basis for SPR. AuNPs are especially important in SPR because their size and shape can be tuned to resonate with specific wavelengths

of light. SPR is highly sensitive to changes in the local environment around the nanoparticles, which makes AuNPs useful in detecting molecules, measuring distances at the nanoscale, and even in medical diagnostics (Garcia, 2011).

The intensity and wavelength of the SPR band are influenced by factors such as particle shape, size, structure, composition, and the dielectric constant of the surrounding medium, which affect the electron charge density on the particle surface. AuNPs smaller than 10 nm have a more damped SPR band due to higher electron collision rates at their surfaces compared to larger particles. Increasing particle size enhances the intensity of the SPR wavelength. The growing use of AuNPs in biosensors and photothermal therapy can be attributed to their unique optical properties (J. Liu *et al.,* 2018).

Surface modification of AuNPs is essential for improving their functionality, stability, and compatibility within biological systems. AuNPs can be conjugated with a variety of biological molecules or chemical groups, making them ideal for diagnostic, therapeutic, and drug delivery applications. One common method for functionalizing AuNP surfaces involves forming self-assembled monolayers with compounds like amides, thiols, and carboxylic acids. Functionalizing AuNPs with amino acids can significantly enhance the efficiency and specificity of nanoparticle-based delivery systems, leading to improved efficacy without toxicity effects (Tiwari *et al.*, 2011; Mahato *et al.*, 2019).

1.1.2 Gold nanocluster (AuNCs)

When the size of metal nanoparticles is further reduced to form NCs, i.e. reduced to the size comparable to the Fermi wavelength of electrons, the properties of nanoparticles vanish and the NCs exhibit molecule-like properties. Gold

nanoclusters (AuNCs) are significantly smaller than AuNPs, with typical sizes ranging from 1 to 2 nanometers and consisting of a few to a hundred gold atoms. This tiny size causes a phenomenon called quantum confinement, which limits electron movement within the AuNCs, similar to how electrons are confined in atoms. Because of this quantum confinement, AuNCs exhibit discrete energy levels, unlike the continuous energy bands found in bulk gold (Figure 2). This characteristic allows AuNCs to absorb light at specific wavelengths and emit light at different wavelengths as electrons return to their original state, a process known as photoluminescence, with the fluorescence ranging from Visible to near Infrared region (NIR). By adjusting the size and structure of AuNCs, researchers can manipulate the energy levels and thus the color of the emitted light. This tunable luminescence is particularly useful in bioimaging applications, where different colors can be used to target and visualize biological processes (Lin *et al.*, 2009; Mussa Farkhani *et al.*, 2024).

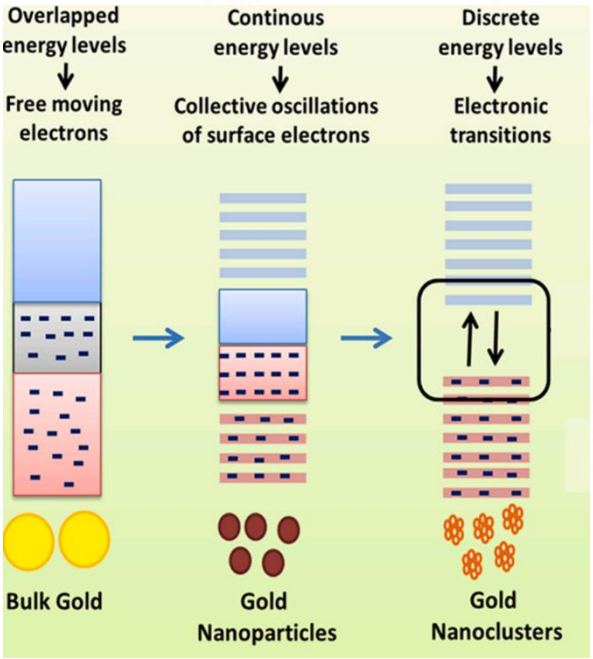

Figure 2. Electronic structures of bulk gold, gold nanoparticles, and gold nanoclusters. The figure reproduced from (Sonia *et al.*, 2021).

1.2. AuNPs and AuNCs in Biomedical Application

AuNPs and AuNCs have been widely studied for their roles in biosensing, bioimaging, and various therapeutic applications (Figure 3). Over time, AuNPs have been pivotal in numerous medical applications due to their properties such as shape, size, surface coating, functionalization, and interactions. The utilization of AuNPs and AuNCs in nanotechnology shows great promise for disease diagnosis through sensing, imaging and treatment.

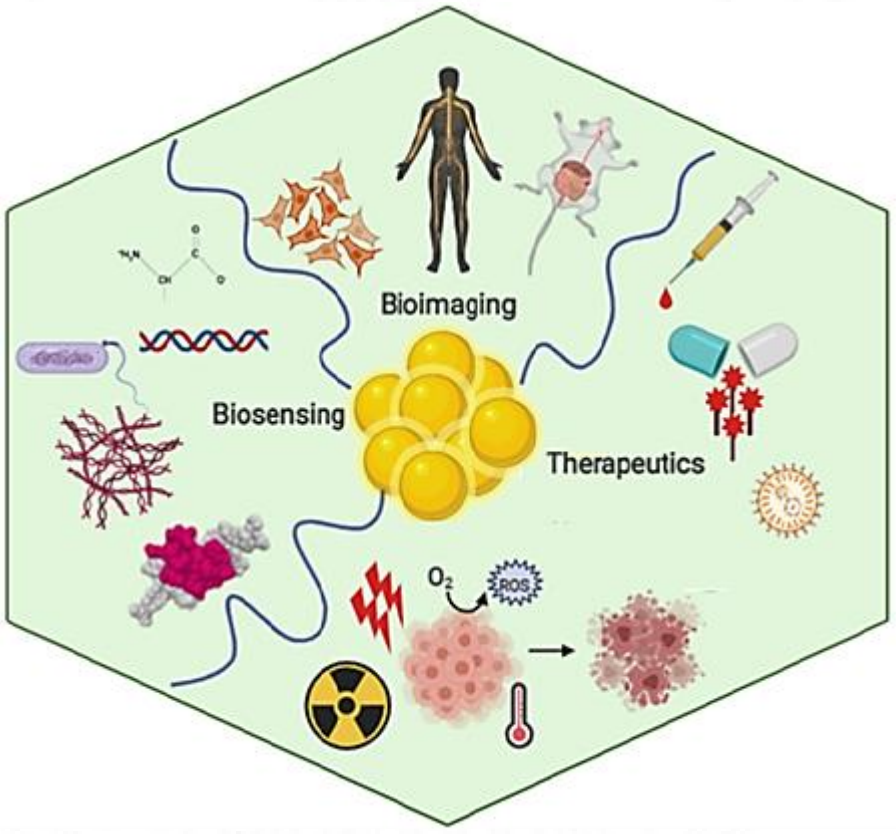

Figure 3. Application of AuNPs and AuNCs in the biomedical field. The figure reproduced from (Sood and Shanavas, 2022).

1.2.1. Sensing & Bio-sensing

Sensing technologies are crucial for developing rapid, sensitive, and specific diagnostic tools across various fields. A sensor is broadly defined as a device that detects and measures a physical property or changes in the environment and converts this information into a signal that can be read or interpreted by an observer or an instrument. Biosensing stands at the intersection of biology, engineering, and technology, striving to create innovative tools for precisely and sensitively detecting biological substances (Bhalla *et al.*, 2016). The diagrammatic representation of biosensors is shown in Figure 4.

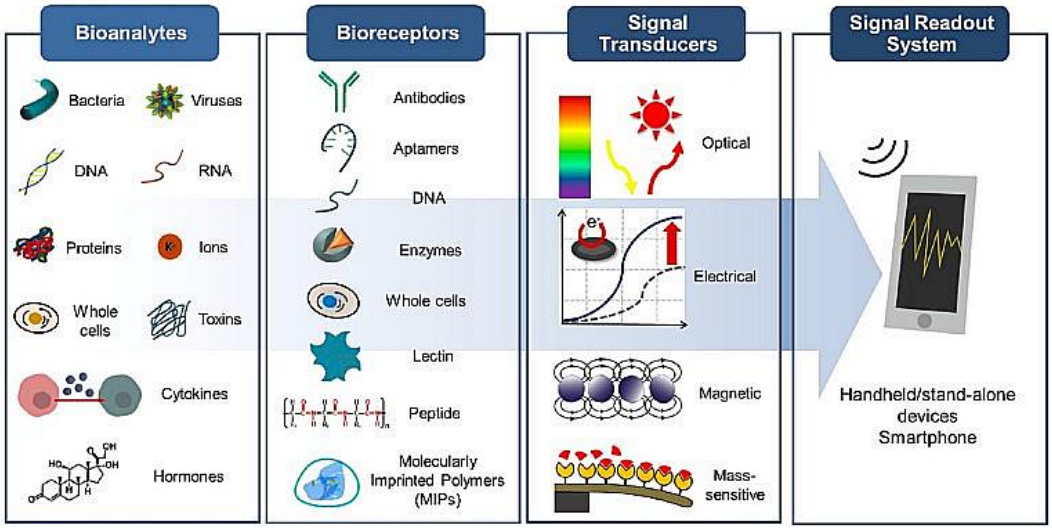

Figure 4. Schematic overview of a biosensor system. The figure reproduced from (Li *et al.*, 2021).

A standard biosensor typically includes the following components:

Sample and Bio-analytes: This refers to the material or specimen that contains the analyte of interest, which the biosensor is designed to detect or measure. The type of sample can vary greatly depending on the application, such as bodily fluids like blood, urine, or saliva in medical diagnostics, or environmental samples like water or soil. Bioanalyte is the specific substance that the sensor or assay is designed to detect

and measure. For example, glucose in blood is a common bioanalyte measured by glucose sensors, and specific DNA sequences may be bioanalytes in genetic tests.

Recognition Element (Bio-receptor): This component is a biomolecule that specifically binds to the target analyte, enabling its detection. Common bio-receptors include enzymes, antibodies, aptamers, or nucleic acids, selected for their high specificity and affinity for the analyte. The interaction between the recognition element and the analyte forms the basis for the biosensor's selectivity.

Transducer: The transducer converts the biochemical or biophysical signal generated by the binding event between the recognition element and the analyte into a measurable output signal. The methods of transduction can vary widely, including electrochemical, optical, piezoelectric, or thermal techniques. The choice of transducer depends on factors such as the type of analyte, required sensitivity, and the intended detection platform.

Signal Processing: After the transducer produces a signal proportional to the analyte concentration, signal processing techniques are used to enhance the accuracy, reliability, and interpretability of the measurement. This may involve amplification, filtering, noise reduction, calibration, and data analysis algorithms to extract meaningful information from the raw sensor output.

These components work together to enable the detection, quantification, and analysis of target analytes in complex samples. Biosensors are widely used in healthcare for their ability to provide rapid, sensitive, and selective detection capabilities for a broad range of analytes.

1.2.1.1 Characteristics of Biosensors

It is essential to meet specific static and dynamic requirements to create a highly efficient and robust bio-sensing system. These factors are crucial for enhancing the performance of biosensors for commercial use.

Selectivity: It is the capability to identify and measure the target analyte accurately, without being affected by other substances present in the sample.

Sensitivity: It indicates its capacity to identify and measure extremely low levels of a target substance. It is fundamentally an assessment of how well the biosensor reacts to variations in analyte concentration.

Linearity: It means the sensor can generate a response that is directly proportional to the concentration of the substance being analyzed. A higher degree of linearity, indicated by a straight line, enhances the precision in detecting various substrate concentrations.

Response Time: It refers to how quickly the biosensor can identify and react to a target substance. It indicates the duration required for the sensor to deliver a stable output signal following a shift in analyte concentration.

Reproducibility: It reflects the sensor's capacity to provide consistent results when the same sample is measured multiple times.

Stability: It evaluates the sensor's resistance to environmental changes both inside and outside the bio-sensing device. Stability is influenced by factors such as the bioreceptor's affinity and the bioreceptor's degradation over time.

1.2.1.2 Types of Biosensors

As the demand for devices with higher sensitivity, selectivity, rapid response time, and low-cost increases, sensors that operate at the nanometer scale, often exploiting

the unique properties of nanomaterials have become prevalent in biosensor research. AuNPs, due to their excellent stability, biocompatibility, high surface energy, optical and electrical properties and significant signal amplification potential are most widely used for biosensor applications. In various sensing techniques, these nanoparticles can detect multiple molecules, such as nucleotides, proteins, saccharides, toxins, and analytes like anions and metal ions. Depending on the mechanism of transduction, biosensors that incorporate AuNPs can be classified into:

i) Optical biosensors

Optical biosensors utilize the interaction between light and biomolecules to identify analytes. By leveraging various optical phenomena such as fluorescence, SPR, and absorbance changes, optical biosensors can rapidly and accurately identify specific biomolecules. This process minimizes the need for extensive sample preparation and complex labeling techniques. Furthermore, the small size of optical biosensors makes them ideal for portable and point-of-care applications, enhancing their practicality and cost-efficiency across a wide range of uses, from medical diagnostics to environmental monitoring (Damborský, Švitel and Katrlík, 2016). These biosensors leverage the unique optical characteristics of nanomaterials (eg: AuNPs) having optical properties for their detection capabilities.

a) Surface plasmon resonance (SPR) based sensing

SPR occurs when a photon of incoming light strikes a metal surface at a specific angle of incidence, and a portion of its energy couples with the electrons in the metal surface layer. This interaction leads to the excitation of these electrons, causing them to collectively oscillate, forming what are known as plasmons. SPR-based sensing is a sophisticated technology that can detect the interaction between a

ligand and a target biomolecule in real-time and it is widely used in medicine and research for sensing applications. In the design of a commercial SPR biosensor, incident light is typically utilized through the implementation of a high-reflective index glass prism in the Kretschmann geometry of the attenuated total reflection (ATR) technique. This setup allows for the efficient coupling of light with the metal surface, enhancing the sensitivity and performance of the SPR system for detecting molecular interactions (Figure 5). The gold layer enhances the SPR signal, which facilitates the detection of interactions between the target analyte and the biomolecule on the sensor surface. This enhancement is advantageous for real-time observation of molecular interactions (Li, Cushing and Wu, 2015).

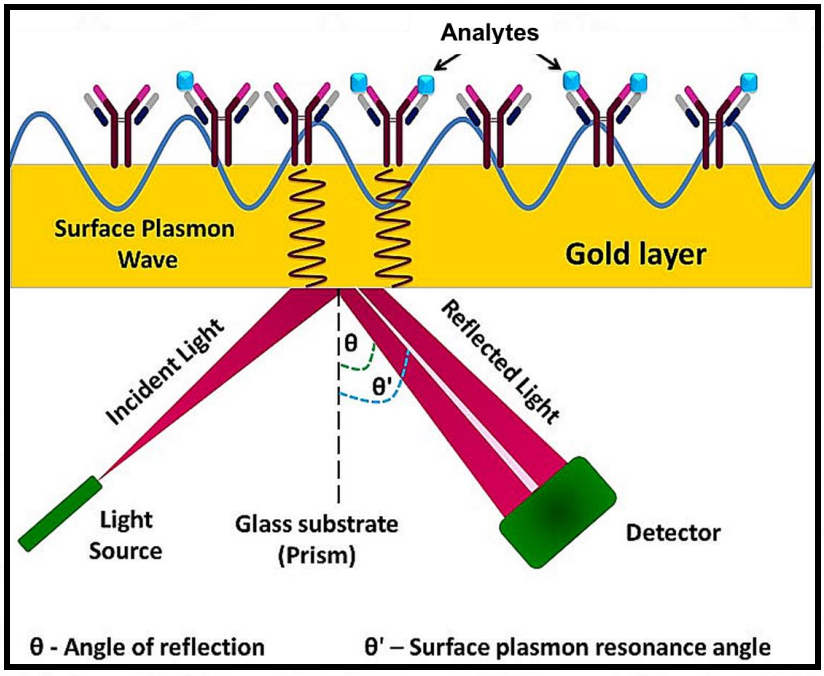

Figure 5. Schematic representation of a Surface Plasmon Resonance (SPR) biosensor. The figure reproduced from (Ragavan, Rastogi and Thakur, 2013).

a-i) Localized surface plasmon resonance (LSPR) based sensing

LSPR-based sensing operates similar to SPR-based sensing but with some key differences. Instead of measuring changes in the surface plasmon resonance of a metal film, LSPR measures the resonance of metal nanoparticles. A shift in the LSPR peak occurs after specific interactions between biomarkers and recognition elements. In LSPR, the plasmonic materials are typically nanoparticles with dimensions smaller than the wavelength of light. This size constraint results in confined electron oscillations within the nanoparticle, leading to the generation of localized surface plasmons. These localized plasmons are induced in the metal nanoparticles when they interact with photons of a certain wavelength, regardless of the incidence angle of the light (Figure 6). One significant advantage of LSPR-based technology is the ease with which the form and size of the metal nanoparticles can be controlled. This control allows for precise tuning of the localized plasmon oscillations, enhancing the sensitivity and specificity of the sensing platform. Moreover, LSPR-based systems assess variations in the extinction wavelength caused by biomarker binding to the relevant bio-receptors, providing a means to detect and quantify molecular interactions in real-time (Willets and Van Duyne, 2007b; Hong *et al.*, 2012; Fu *et al.*, 2023).

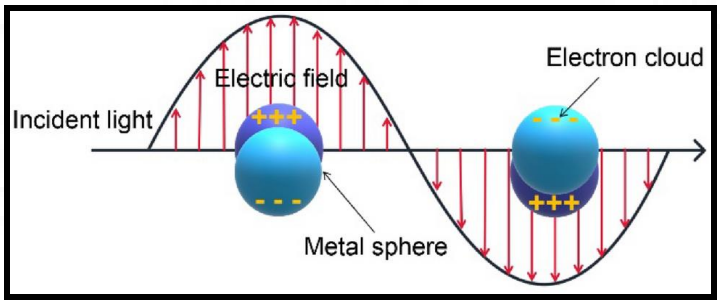

Figure 6. Localized Surface Plasmon Resonance (LSPR) in a metal nanoparticle. The figure reproduced from (Ta *et al.*, 2024).

b) Raman spectroscopy

Raman spectroscopy is a powerful technique used for non-invasive identification of molecular structures, providing a unique fingerprint of the molecule being analyzed. It relies on the phenomenon of inelastic scattering of light, known as Raman scattering. In Raman scattering, when photons interact with molecules in solids, liquids, or gases, most of them scatter at energies similar to the incident photons, known as Rayleigh or elastic scattering. However, a small fraction changes frequency compared to the incident photon, resulting in Raman scattering (Figure 7a). This phenomenon, named after Sir C.V. Raman, who won the Nobel Prize in Physics in 1930 for its discovery, provides valuable information about the vibrational and rotational modes of molecules (Jones *et al.*, 2019).

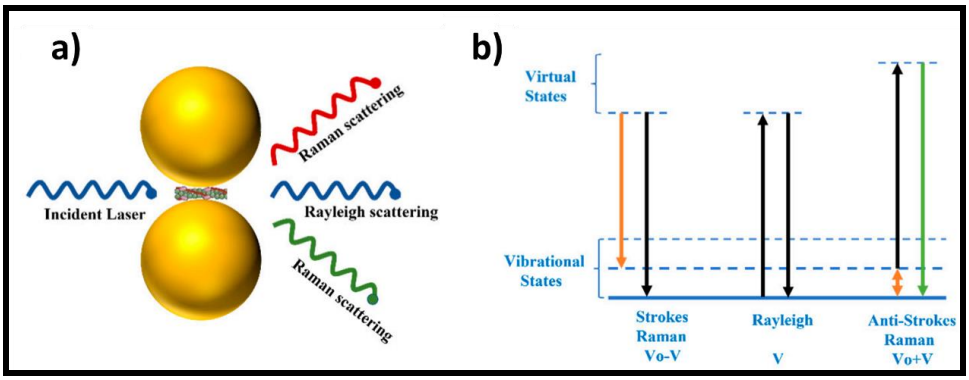

Figure 7. Raman Scattering Process. a) Schematic representation of Raman scattering by a metal nanoparticle**.** b) Energy level diagram illustrating the Raman scattering process. The figure reproduced from (Gao *et al.*, 2023).

The Raman effect causes a shift in the energy of scattered photons when a molecule relaxes to an energy level different from its incident radiation. If the resulting state has higher energy than the initial state, the scattered photons exhibit a lower energy, known as a Stokes shift. Conversely, if the subsequent state possesses lower energy, the scattered photons will display higher energy, termed an anti-Stokes

shift (Figure 7b). Raman spectroscopy enables the collection of a molecule's vibrational signature, offering insights into its structure and interactions with other molecules. Changes in molecular polarizability can be observed through Raman spectroscopy.

A typical Raman spectroscopy setup includes a light source, often a laser with specific wavelengths like 532/633/785 nm, a filter to eliminate Rayleigh scattering, and a spectrograph-based CCD detector. This technique offers numerous advantages, including the use of less harmful Near Infrared (NIR) radiation, high spatial resolution, minimal sample preparation, resistance to water band interference, and suitability for *in vivo*/in situ measurements. However, since the Raman scattering is a low-probability event, with only about one in 10^6 to 10^8 photons being inelastically scattered, resulting in weak Raman signals, signal enhancement techniques likes Surface-Enhanced Raman Scattering (SERS) and Surface-Enhanced Resonance Raman Scattering (SERRS) etc. are often employed especially in biological sensing (Jones *et al.*, 2019; Gao *et al.*, 2023).

b-i) Surface Enhanced Raman Scattering (SERS) and role of metal nanoparticles

In 1974, Fleischmann and his team observed a unique phenomenon for the first time, the Raman signal intensity of pyridine increased when pyridine was applied to rough silver electrodes. Further research revealed that this Raman signal enhancement also occurred when the Raman spectrum of a molecule was recorded on a roughened metal surface. This led to the development of the concept of SERS (Pilot *et al.*, 2019).

The theoretical explanation for SERS enhancement is based on either electromagnetic enhancement or chemical enhancement or both. Electromagnetic enhancement, considered as the main factor, depends mostly on LSPR. This theory suggests that incident light induces collective oscillations of free electrons on the surface of plasmonic nanoparticles, thereby enhancing the electromagnetic field intensity around the metallic nanostructure and increasing the Raman signal. The enhancement due to LSPR is approximately proportional to the fourth power of that produced by the metal structure itself (Figure 8a).

Another cause of SERS enhancement is chemical enhancement (Figure 8b), which occurs due to electron transfer between modified molecules and nanoparticles. For chemical enhancement to take place, the electron transfer distance between the modified molecules and nanoparticles must be less than 10 nm. Consequently, chemical enhancement typically increases the signal by only two to three orders of magnitude compared to traditional Raman. This shows that chemical enhancement contributes significantly less to the total SERS enhancement than electromagnetic enhancement (Tim, Błaszkiewicz and Kotkowiak, 2021; H. Liu *et al.*, 2022).

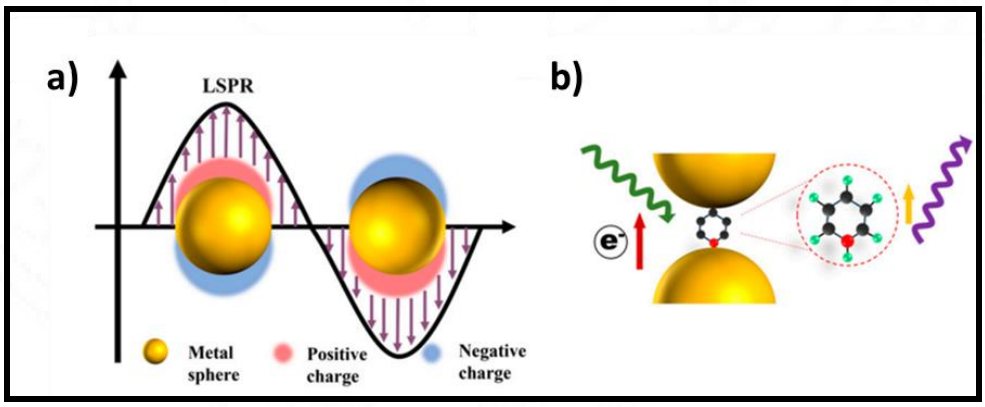

Figure 8. a) Electromagnetic enhancement in SERS: Localized Surface Plasmon Resonance (LSPR) induced charge distribution on metal nanospheres. b) Chemical

enhancement in SERS: Charge transfer between a metal nanoparticle and analyte molecule. The figure reproduced from (Gao et al., 2023).

The optical characteristics of metal nanostructures are determined by their dimensions and geometry, which also govern the enhancement of local electromagnetic fields. By manipulating the size and shape of AuNPs, various optical properties can be tailored, including absorption and scattering coefficients, SERS, fluorescence, and more. Researchers have developed numerous types of Au nanostructures, like nanospheres, nanorods, nanoshells, nanoprisms, nanopyramids, nano bipyramids, nanocages, nano rings, nanodisks, nanostars, nano rice, nano bowls, nano crescents etc, each exhibiting distinct optical behaviors (Figure 9).

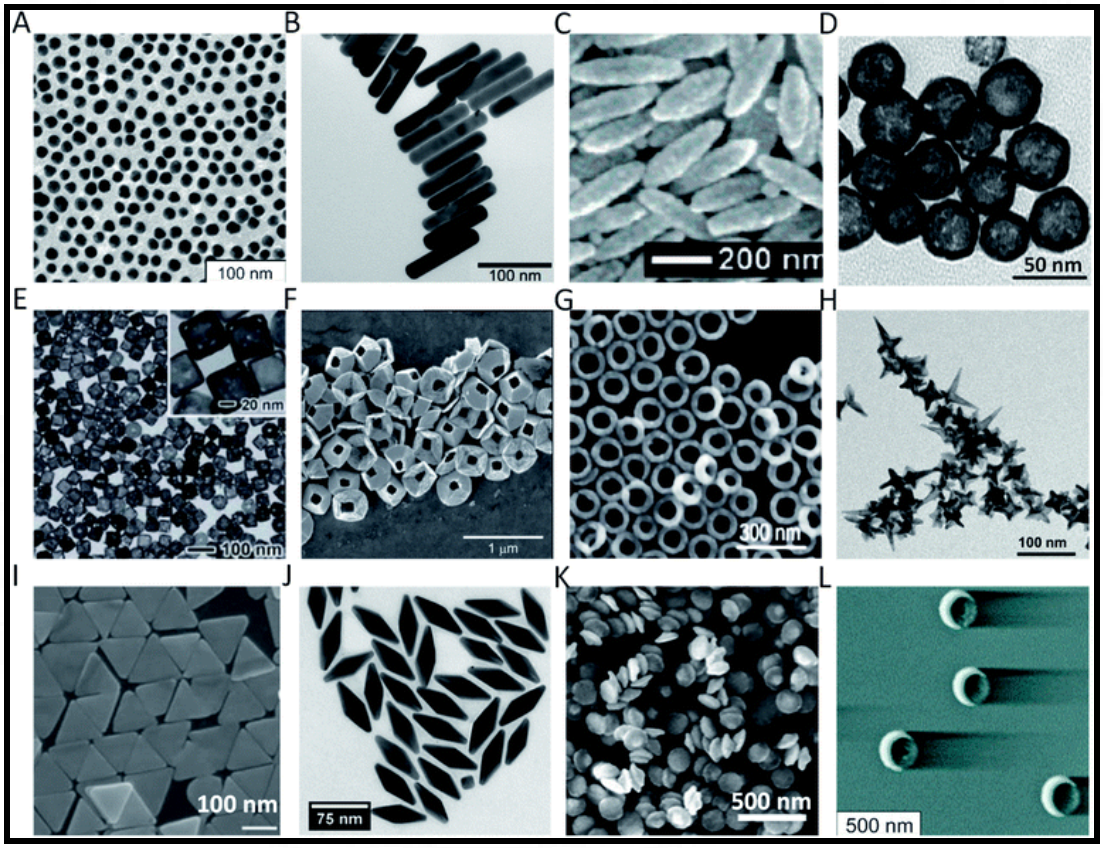

Figure 9. Au nanostructures of different shapes and sizes (A)AuNS (B) AuNR (C) Au nano rice (D) AuNSh (E) AuNC (F)AuNPy(G) AuNRg (H) AuNSt (I) AuNPr (J) AuNBP (K) AuND and (L) AuNCr. The figure reproduced from (Si *et al.*, 2021).

For instance, the sharp tips of star-shaped nanoparticles typically exhibit greater local field enhancements compared to their blunt faces, a phenomenon known as the "lightning rod effect," occurring at regions with high curvature on the nanoparticle tips (Meng *et al.*, 2020). Moreover, aggregated plasmonic nanoparticles can further amplify this local field. When these nanoparticles are closely positioned, closer than their dimensions, they exhibit coupled LSPR. These coupled resonances are shifted spectrally from their resonances, forming 'hotspots' with highly intensified electromagnetic fields. The intensity of Raman scattering from molecules can be greatly enhanced by the local electromagnetic field, leading to an amplification that is approximately 10^6 to 10^8 times stronger than the conventional Raman signal (Pilot *et al.*, 2019). Various morphologies of AuNPs such as star-shaped (AuNSt), pyramidal (AuNPy), and nanourchins (AuNCr) can create such Raman hotspots. Placing molecules within these hotspots greatly enhances their Raman signal intensity (Figure 10). Incident light interacts with AuNPs leading to LSPR, enhancing the electromagnetic field (red lines) around the AuNPs. An analyte molecule (green star) adsorbed on the AuNP experiences both electromagnetic (1, 2) and chemical (3) enhancement of Raman scattering, resulting in an amplified Raman signal. The Raman spectrum shows the characteristic peaks of the analyte with significantly enhanced intensity compared to normal Raman (black line).

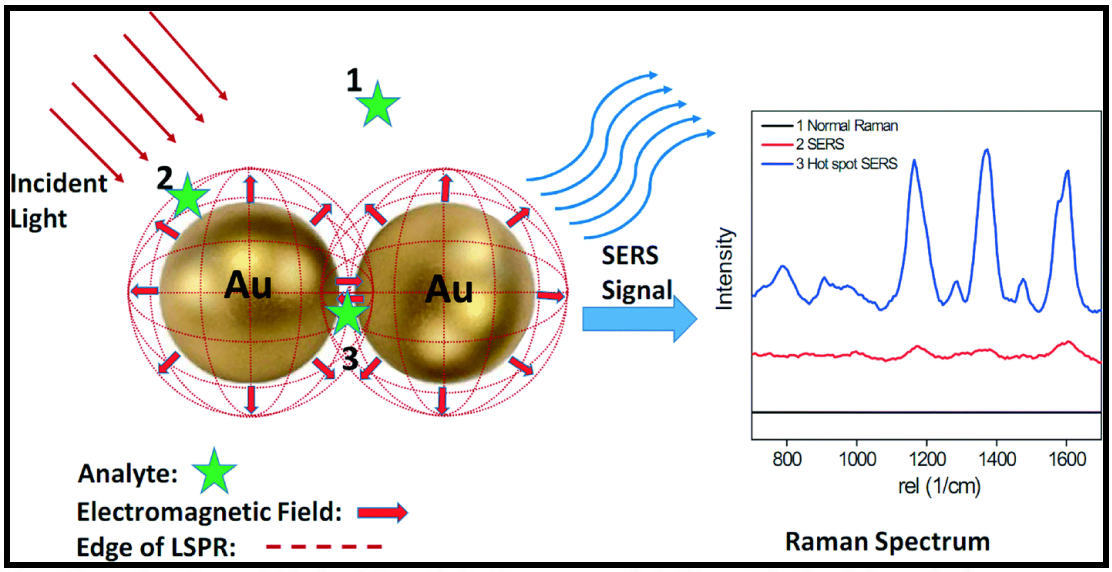

Figure 10. Schematic representation of SERS hotspot creation by plasmonic nanoparticles in the presence of analyte molecules, along with the associated Raman spectra. The figure reproduced from (Wei, Hossein Abtahi and Vikesland, 2015).

c) Colorimetric Biosensors

Colorimetric biosensors are widely used in various fields for the detection of biological analytes due to their simplicity, cost-effectiveness, and ease of use. These sensors typically rely on a color change as the readout signal, which can be easily observed with the naked eye or measured using simple optical instruments. AuNPs are known for their pronounced color changes in response to environmental variations, which affect their optical absorption characteristics due to LSPR. The presence of a target analyte can cause AuNPs to cluster together through various interactions (such as electrostatic forces, hydrophobic effects, or specific binding). This clustering changes the distance between the particles, which alters the LSPR and typically shifts the color from red to blue or purple. These colorimetric changes can be easily detected either visually or through spectrophotometric measurement (Chang *et al.*, 2019). For example, hybridization of single-stranded DNA with its

complementary target DNA in the presence of an electrolyte will alter the color of gold AuNPs (Figure 11) (Ahmadi *et al.*, 2018).

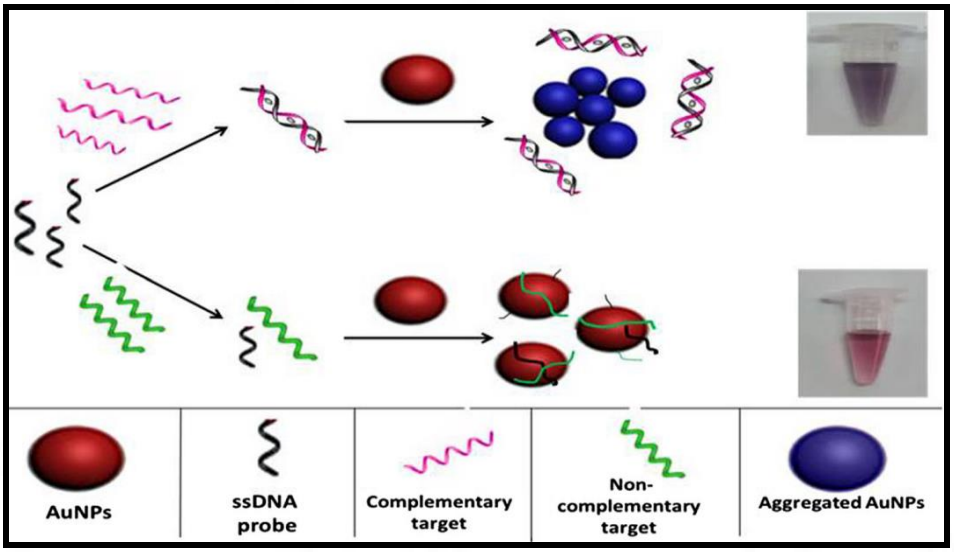

Figure 11. Colorimetric detection of target DNA using AuNPs. The figure reproduced from (Ahmadi *et al.*, 2018).

ii) Electrochemical/Electronic biosensors:

Electrochemical/electronic biosensors serve as analytical devices that convert biochemical events, such as enzyme-substrate reactions and antigen-antibody interactions, into electrical signals like current, voltage, or impedance (Figure 12). Electrochemical/Electronic biosensors play a crucial role in various fields due to their ability to convert biological interactions into measurable electrical signals. Recent advancements in nanotechnology have significantly enhanced the performance of these biosensors, particularly through the integration of functional nanomaterials. Metallic nanoparticles, in particular, serve as exceptional platforms for biosensors, amplifying signal detection through their large surface area and efficient electron transfer properties. AuNPs are particularly effective in constructing highly sensitive electrochemical biosensors due to their unique properties, such as

facilitating biomolecule immobilization and electron transfer at the electrode interface. Integration of AuNPs with other materials like silicon dioxide and carbon nanospheres in hybrid electrodes has been explored to boost analytical performance, leveraging enhanced catalytic activity and conductivity to achieve greater biosensor sensitivity (Cho, Kim and Park, 2020).

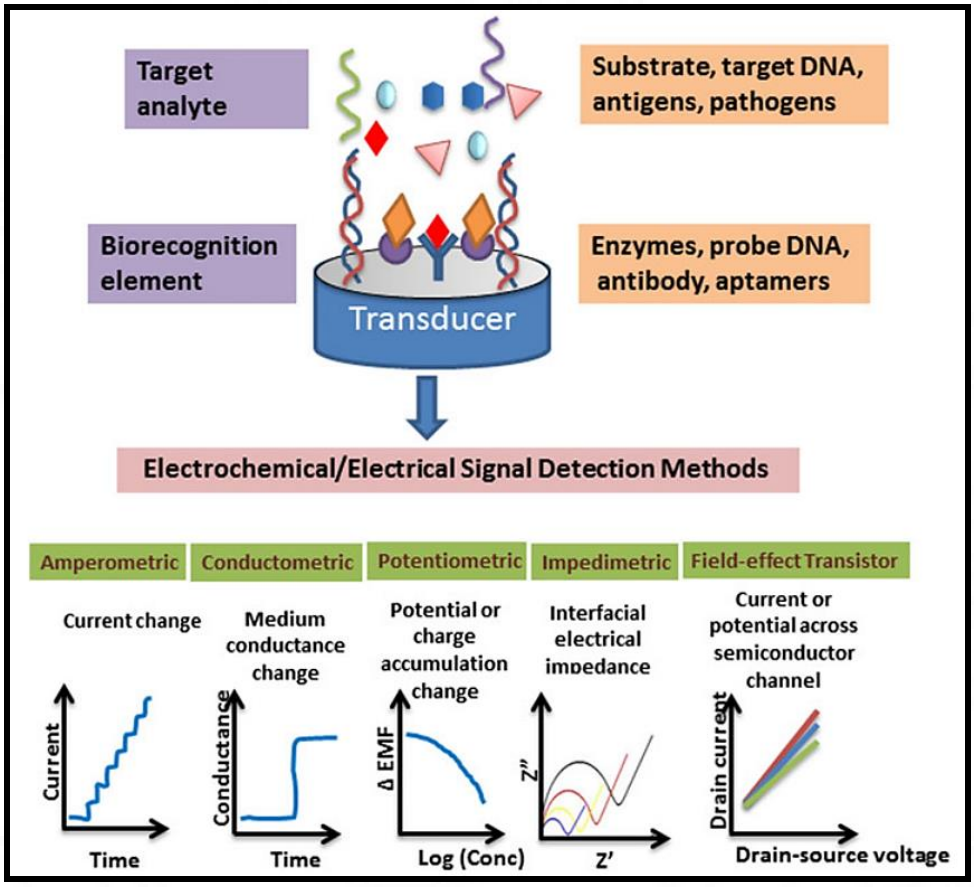

Figure 12. Schematic representation of electrochemical/ electronic biosensor detection methods. The figure reproduced from (Terse-Thakoor, Badhulika and Mulchandani, 2017)

a) Voltammetric /amperometric electrochemical biosensor

Specific binding events between the analytes and recognition elements are tracked in voltammetric/amperometric analysis by monitoring changes in transducer currents at a defined bias potential. These platforms are commonly configured with

three electrodes: a counter electrode (e.g., graphite, Pt wire), a reference electrode (e.g., Ag/AgCl, Ag wire), and a working electrode. Because of their high conductivity, carbon-based materials (e.g., carbon fiber, graphene, and glassy carbon), gold nanoparticles (e.g., nanoparticle, wire, and thin film), and commercial screen-printed electrodes are often used as working electrodes in voltammetric and amperometric platforms (Figure 13). The application of AuNPs enhance electrochemical signals by expanding the surface area and enhancing electron transfer efficiency. These sensor devices measure the current response relative to the applied voltage, which helps to determine the concentration of specific analytes.

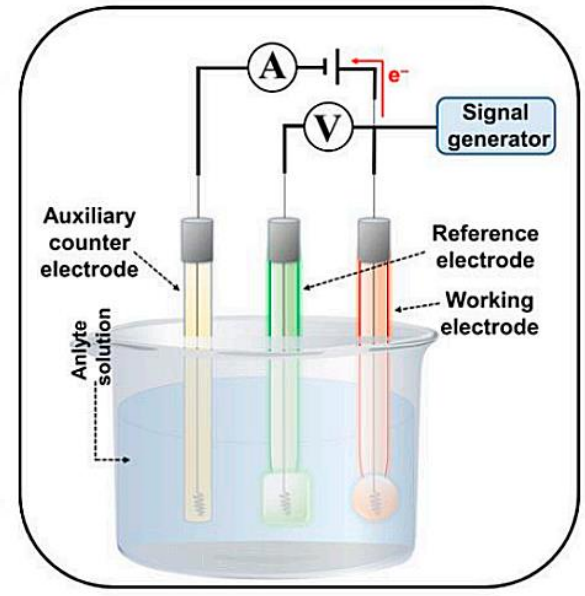

Figure 13. Schematic diagram of voltammetric /amperometric biosensor. The figure reproduced from (Curulli, 2021).

b) Impedometric electrochemical biosensor

The Impedometric sensing substrate examines the transducers' resistive and capacitive changes in response to interactions between the analyte and bio-receptor. A sinusoidal potential with a small amplitude (<10 mV) is given to the probe layer

for impedance measurement, and the ensuing in-phase and out-of-phase currents identify the resistive and capacitive components of impedances, respectively (Daniels and Pourmand, 2007). In general, the applied voltage in the Impedometric assay is substantially lower than in the voltammetric and amperometric platforms, which provides advantages in preventing noise. The resultant impedance values are typically fitted to Randles equivalent circuit, resulting in a Nyquist plot. The diameter of the Nyquist curve's semi-circular zone correlates to the charge-transfer resistance (R_{ct}) at the transducer's surface, whereas the linear region is defined by the diffusion rate of redox species (Figure 14).

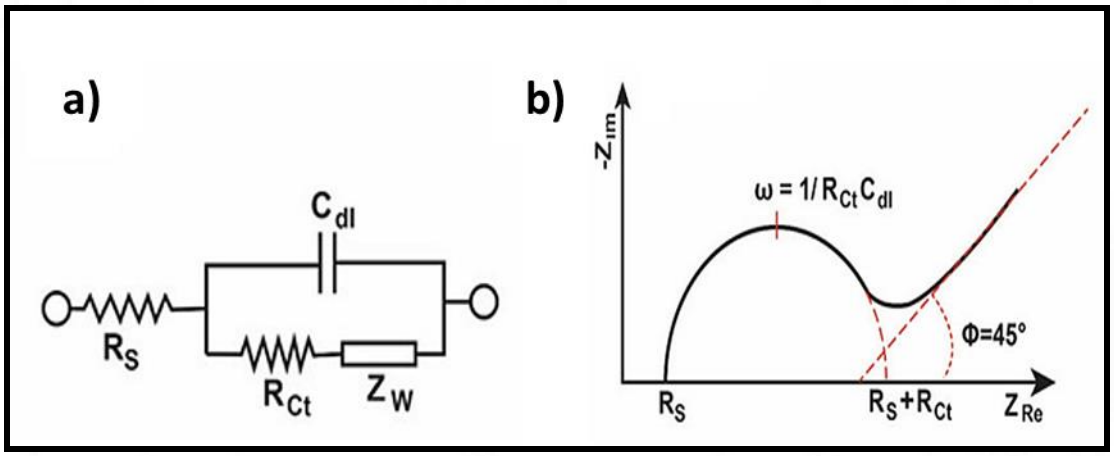

Figure 14. Electrochemical impedance spectroscopy (EIS) model. (a) Randles equivalent circuit representing an electrochemical system (b) Nyquist plot showing the relationship between the real (Z_{Re}) and imaginary ($-Z_{im}$) components of impedance. The figure reproduced from (Khan and Song, 2020).

c) Conductometric Biosensors

Numerous biological processes involve changes in the concentrations of ionic species. Biosensors take advantage of these fluctuations in electrical conductivity, using interdigitated electrodes exposed to an alternating field to measure conductivity variations. These electrodes, featuring interlocking fingers, are designed

to maximize the track length within a compact sensing area. These biosensors provide several benefits: they do not require a reference electrode; they function at low-amplitude alternating voltage, preventing Faraday processes on electrodes; they are not affected by light; and they can be easily miniaturized and integrated using inexpensive thin-film standard technology (Dzyadevych and Jaffrezic-Renault, 2014). These sensors detect changes in electrical resistance or conductance due to the binding of analytes (Figure 15). For instance, a biosensor where the binding of an analyte induces a conformational change in the bio-recognition element, thereby altering the conductive pathway and, consequently, the resistance. When AuNPs are immobilized onto electrode surfaces, the target analyte interacts with the biomolecules linked to these AuNPs alters the electrode's conductivity, and this variation is measured to assess the analyte's concentration.

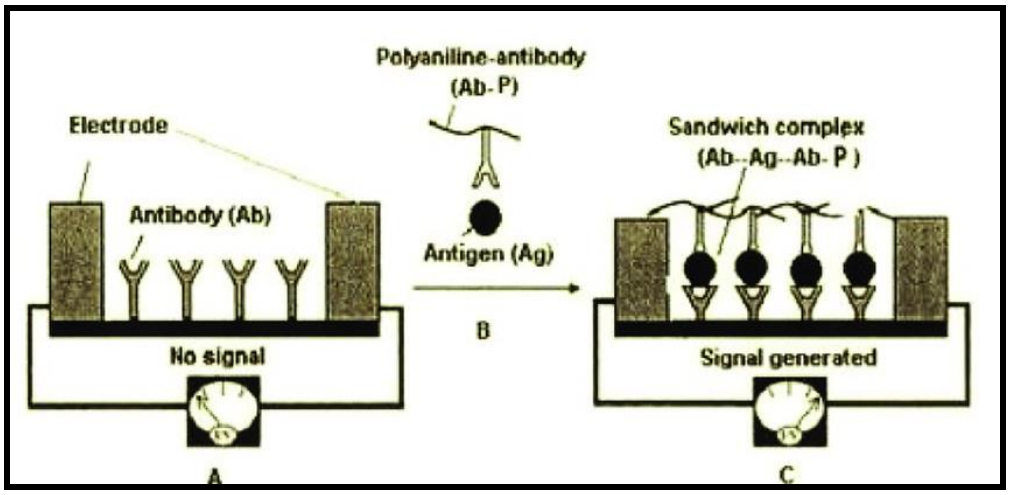

Figure 15. Schematic representation of a conductometric immunosensor. A) A bare electrode is coated with a layer of antibodies (Ab). B) Upon exposure to the target antigen.C) The formation of the sandwich complex leads to an increase in conductivity, generating a detectable signal. The figure reproduced from (Muhammad-Tahir and Alocilja, 2003).

1.2.1.3 Artificial neural networks (ANNs) in bio-sensing

ANNs are highly promising in bio-sensing applications because they can analyze complex data patterns and improve detection accuracy. In the realm of bio-sensing, ANNs are used to interpret signals from various sensors, allowing for the precise identification and measurement of biomolecules. By training on extensive datasets, ANNs enhance the sensitivity and specificity of biosensors, making them more effective for diagnosing conditions like Alzheimer's disease. Their ability to process and analyze large volumes of data in real-time supports the creation of responsive and adaptable biosensing systems. Furthermore, ANNs enable the integration of multiple sensor outputs, thereby boosting the overall performance and reliability of systems that detect biomarkers and other biological entities (Wasilewski, Kamysz and Gębicki, 2024). Figure 16, illustrates a basic artificial neural network with three layers: an input layer, a hidden layer, and an output layer. The input layer receives sensed features (X) and processes them through interconnected nodes (neurons) in the hidden layer. The hidden layer transforms the input data and passes the information to the output layer, which generates the final output (Z).

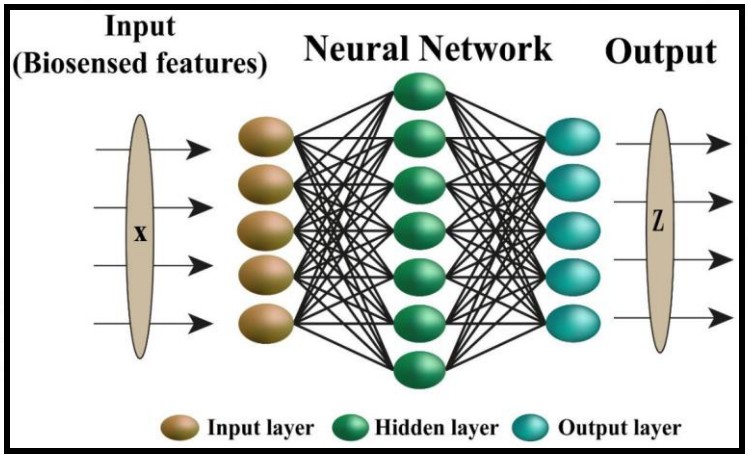

Figure 16. Schematic representation of an ANN for biosensor data processing. The figure reproduced from (Arano-Martinez *et al.*, 2022).

Moreover, ANNs facilitate the integration of outputs from multiple sensors, boosting the overall performance and reliability of bio-sensing systems. This integration is vital for the accurate detection of biomarkers and other biological entities. Utilizing ANNs in bio-sensing not only enhances the efficiency and accuracy of these systems but also paves the way for advanced diagnostic and monitoring capabilities in healthcare. By capitalizing on the strengths of various classifiers, ANNs enable the creation of sophisticated biosensors that adapt to changing conditions, providing precise, real-time monitoring of biological systems, and thereby significantly advancing early diagnosis and effective disease management (Schackart and Yoon, 2021).

1.2.2 Bio-imaging

Bio-imaging involves visualizing and analyzing the structures, processes, and interactions within living organisms or biological samples. This field includes various techniques and methods designed to produce images that offer insights into different aspects of biological systems. Essential bio-imaging methods include visible light fluorescence (FL) imaging, near-infrared fluorescence (NIR-FL) imaging, two-photon near-infrared fluorescence (TP-NIR-FL) imaging, computed tomography (CT) imaging, positron emission tomography (PET) imaging, magnetic resonance imaging (MRI), and photoacoustic (PA) imaging (Figure 17). These techniques are critical in biological research and medical diagnostics, helping to understand tissue structures and elucidate physiological functions. Advances in optical technology, particularly the advent of digital imaging and computer vision, the development of contrast agents for multiple imaging modalities, and the integration of different imaging techniques, have significantly enhanced the

efficiency and precision of medical diagnostics (Si *et al.*, 2021) (Yadav and Mandal, 2023).

AuNCs are gaining attention as a valuable material for bioimaging due to their tunable photoluminescence, significant Stokes shift, resistance to photobleaching, and high biocompatibility. In the past decade, considerable research has been dedicated to enhancing AuNCs to improve imaging contrast and develop multimodal imaging techniques. Various factors, such as the size of the gold nucleus, the type of surface ligands, and the surrounding environment, can affect the fluorescence of AuNCs (Zhang *et al.*, 2022). Their superior photostability and biocompatibility make AuNCs highly suitable for biomedical imaging applications.

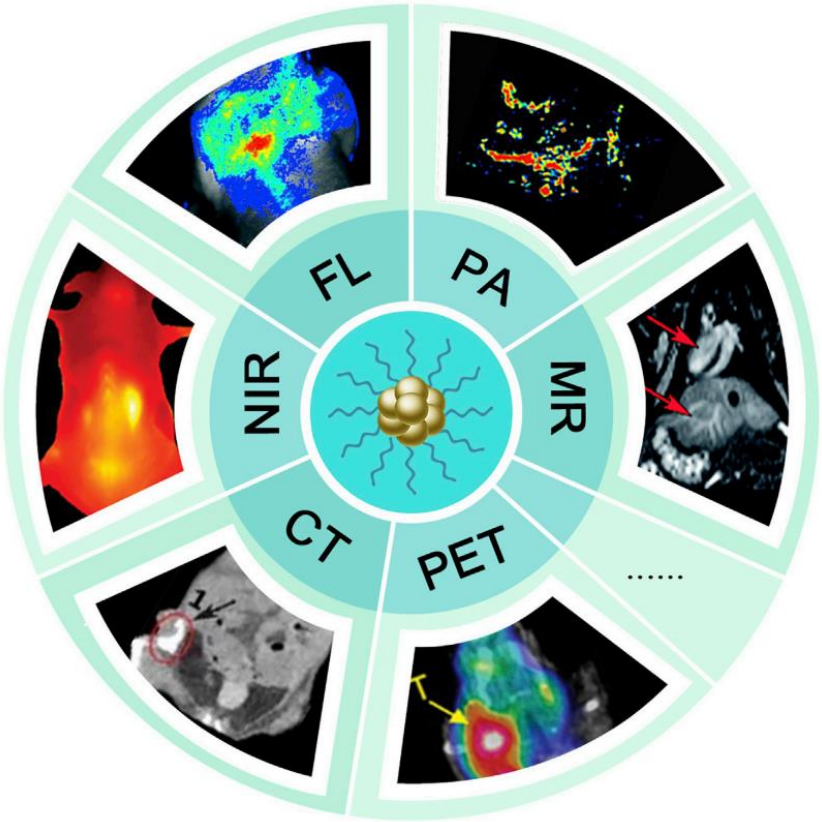

Figure 17. Multimodal imaging capabilities of AuNCs. The figure reproduced from (Zhang *et al.*, 2022).

1.2.2.1 Fluorescence property of AuNCs

Fluorescence is an important and unique property exhibited by AuNCs compared to its bigger counter parts, which is useful for imaging applications (Purohit and Singh, 2018). Larger AuNPs exhibit a distinct ultraviolet (UV)-visible absorption peak at 520 nm, indicating surface plasmon resonance. However, as the size of AuNPs decreases to below 3 nm, this absorption peak at 520 nm diminishes. Instead, these smaller AuNPs, called as AuNCs display molecule-like properties, with absorption peaks corresponding to electron transitions between quantized energy levels. When light interacts with AuNCs, it excites electrons, causing them to leap between discrete energy levels and resulting in bright photoluminescence (Huang, Fuksman and Zheng, 2018) .

The basic mechanism of fluorescence in AuNCs is illustrated in figure 18a. The process starts with the absorption of a photon ($h\nu_{ex}$), which excites the molecule from its ground state to a higher electronic singlet state (S_1). This transition occurs almost instantaneously, within femtoseconds (10^{-15} s), demonstrating the rapid interaction between light and the material. Following this, the excited molecule undergoes vibrational relaxation, releasing excess energy through vibrations to reach a lower-energy excited state (S_1). This phase happens over picoseconds (10^{-12} s), offering a glimpse into the molecular dynamics post-excitation. Finally, the molecule returns to its ground state by emitting a photon of longer wavelength ($h\nu_{em}$), a process that occurs over nanoseconds (10^{-9} s), allowing for the detection of fluorescence. These sequential processes, from excitation to emission, occur within

nanoseconds, underscoring the transient nature of fluorescence. Despite its brief duration, fluorescence is a powerful technique for understanding molecular interactions and dynamics, especially in fluorescence microscopy (Ishikawa-Ankerhold, Ankerhold and Drummen, 2012). Its high sensitivity, spatial resolution, and specificity are invaluable for exploring the complexities of biological systems at the cellular level (Figure 18b).

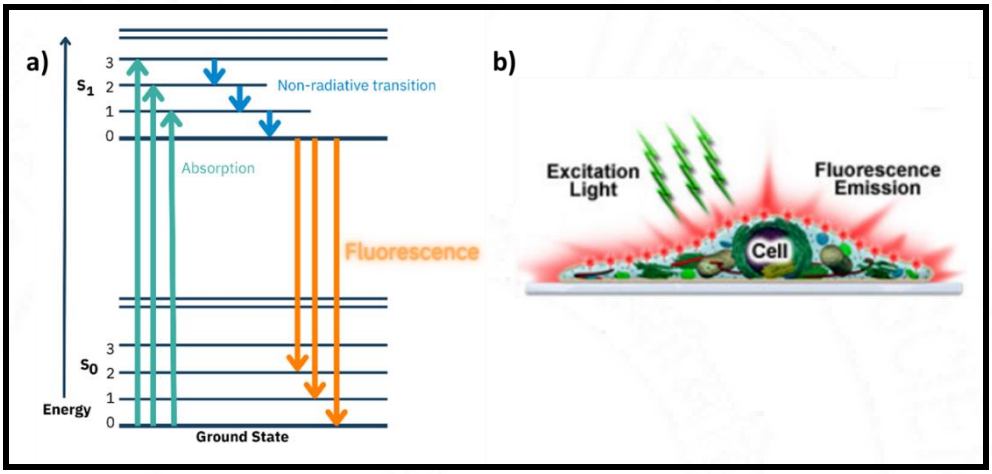

Figure 18. Fluorescence Process. a) Jablonski diagram illustrating energy levels of a molecule. The figure reproduced from (Lighting up! Fluorescence, Chemiluminescence and Bioluminescence- what's the difference | Blog | Biosynth). (b) Schematic representation of fluorescence in a cell. Excitation light is absorbed by the cell, leading to fluorescence emission. The figure reproduced from (ZEISS Microscopy Online Campus | Microscopy Basics | Fluorescence Microscopy).

AuNCs typically have cores made of varying numbers of gold atoms, which provide strong fluorescence intensity and high X-ray attenuation, making them suitable for both fluorescence and CT imaging. They can also be combined with contrast agents for additional imaging methods, such as radionuclides (e.g., ^{64}Cu, ^{68}Ga, ^{124}I) for PET imaging or gadolinium chelates for MRI contrast. Consequently, AuNCs are anticipated to serve as excellent probes for multimodal imaging (Figure 19). To improve their solubility and biocompatibility, these cores are coated with

polymers, proteins, or other compounds. Additionally, the coating can carry drugs or targeting molecules like antibodies, peptides, nucleic acids, proteins, or aptamers for combined diagnostic and therapeutic purposes (Zhang *et al.*, 2022).

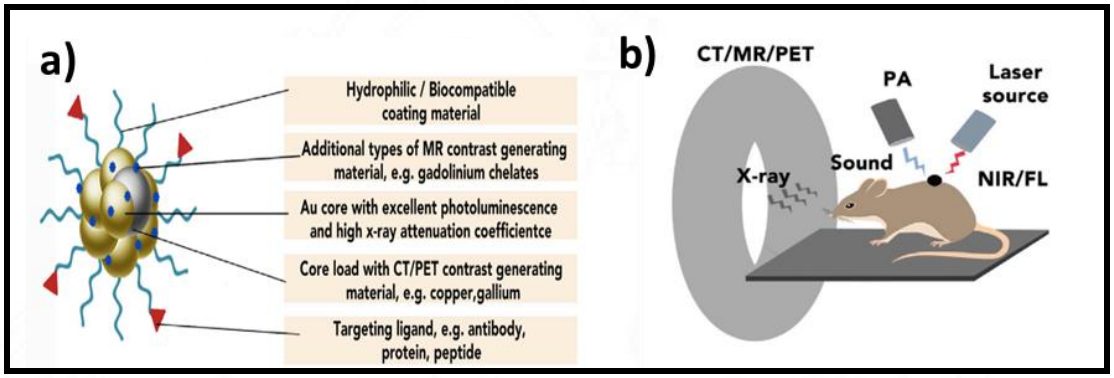

Figure 19. a) Schematic representation of multifunctional AuNCs and b) their application in multimodal imaging. The figure reproduced from (Zhang *et al.*, 2022).

1.2.3 Therapeutic approaches

Nanomaterials have revolutionized therapeutic applications, offering innovative solutions for enhancing the efficacy and safety of various treatments. These materials, due to their unique physicochemical properties, enable precision in targeting, delivery, and treatment that was previously unattainable with conventional methods.

1.2.3.1 Drug Delivery

The field of drug delivery systems (DDS) focuses on the targeted delivery of various drugs to specific cells. The primary objective of a targeted DDS is to increase the drug concentration in the intended tissues while reducing its concentration in non-targeted tissues. Nanoparticles like AuNPs and AuNCs based DDS can be engineered through surface modification with ligands, antibodies, or other molecules that recognize and bind to specific cellular markers or receptors on target cells to

achieve precision targeting AuNPs can transport drugs to their targets and control their release in response to external or internal stimuli. There are two methods for targeting therapeutic agents to specific cells or tissues using AuNPs (Huang *et al.*, 2023). In passive targeting, particularly in cancer, nanoparticles or drugs accumulate at a specific site (tumour) leveraging the enhanced permeability and retention (EPR) effect. In active targeting, the surface of the nanoparticles or drugs is modified with a specific active molecule that can recognize and bind to receptors at the target site (Chehelgerdi *et al.*, 2023). Conjugates of AuNPs with drug molecules have shown promising results in treating intracellular diseases. Consequently, incorporating AuNPs in antibiotic treatments can significantly enhance drug delivery efficiency to target cells. Nanomaterials can also be designed to release therapeutic agents in a controlled manner over time or in response to specific stimuli (e.g., pH, temperature, or light). This controlled release minimizes the need for frequent dosing and ensures that drugs are delivered at the optimal therapeutic concentration, reducing the risk of side effects (Kong *et al.*, 2017).

1.2.3.2 Photodynamic and photothermal therapy

Photodynamic therapy (PDT) and photothermal therapy (PTT) are cancer therapeutic methods where the contribution of light and photosensitizers are made use off (Figure 20). Due to their strong plasmonic properties, AuNPs are highly effective in converting light into heat, making them ideal for use in photothermal therapy to selectively destroy cancer cells (Overchuk *et al.*, 2023). PDT is a non-invasive treatment that involves a reaction between photosensitizers (PS) and oxygen-containing substrates (such as oxygen and water) when exposed to light of specific wavelengths. This interaction generates singlet oxygen ($^1O_2$) or other

reactive oxygen species (ROS), including peroxides and hydroxyl radicals, which can interact with biological molecules to effectively destroy the target thereby achieving therapeutic outcomes. Its targeted approach, safety, low toxicity, and minimal side effects have made PDT an increasingly important method in clinical treatments (Correia *et al.*, 2021). AuNCs are promising photosensitizer candidates for PDT because of their long triplet state lifetime, low dark toxicity, and rapid clearance to prevent systemic toxicity. Their fluorescence lifetime in the range of microseconds is due to electron transfer to the ligand during reduction, and this extended triplet-state lifetime is advantageous for energy transfer to molecular oxygen under light irradiation, producing high levels of ROS. Several studies have indicated that AuNCs can generate ROS and function as effective photosensitizing agents (Poderys *et al.*, 2020).

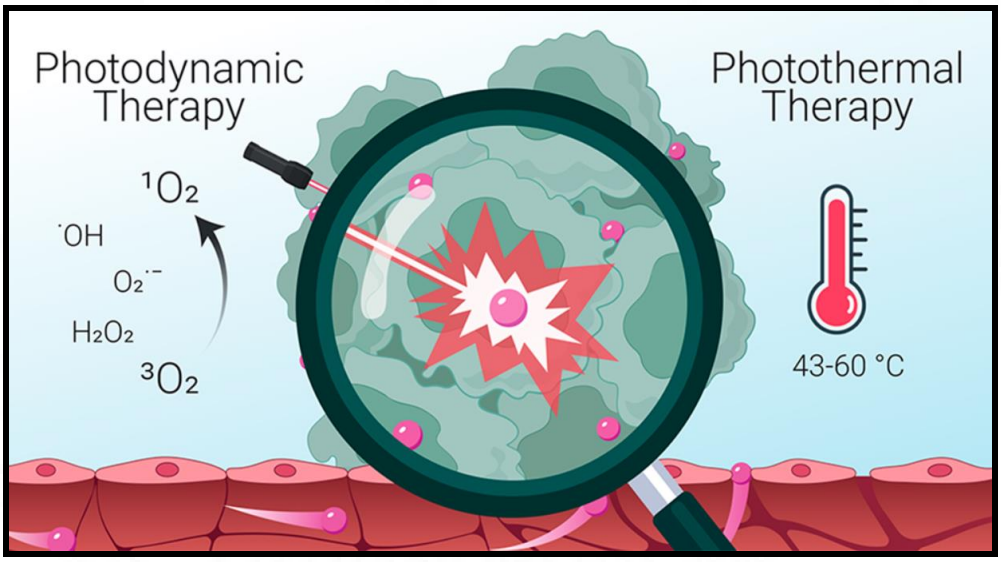

Figure 20. Schematic representation of PDT and PTT. The figure is reproduced from (Overchuk *et al.*, 2023).

AuNPs have been employed in PTT due to their significant properties, such as SPR absorption and efficient fluorescence quenching. When exposed to NIR light, these nanoparticles absorb the light and convert it into heat, raising the temperature of the surrounding tissue to induce cell death. Additionally, their affinity for binding with amines, disulfides, and thiols enhances their ability to penetrate intracellularly (Riley and Day, 2017).

Therefore, it is clear that AuNPs and AuNCs represent cutting-edge technologies that play a crucial role in diagnosing and treating various diseases. This thesis seeks to explore the functions and essential contributions of gold-based nanotechnology in tackling neurodegenerative diseases, particularly focusing on AD. A nanotechnological approach to tackle the major challenge of the blood-brain barrier (BBB) in effectively managing AD is also explored.

1.3 Basic Concept of Neurodegenerative Diseases

Neurodegenerative diseases are a group of disorders characterized by the progressive disorder of the nervous system's structure and function, particularly affecting neurons in the brain and spinal cord. These conditions typically lead to a gradual decline in cognitive, motor, and sensory abilities. Common examples of neurodegenerative diseases include Alzheimer's disease, Parkinson's disease, Huntington's disease, and Amyotrophic Lateral Sclerosis (ALS) (Gao and Hong, 2008). Among them, Alzheimer’s disease (AD) is one of the most progressive complex neurodegenerative disorders affecting millions of individuals worldwide. The World Health Organization (WHO) reports that AD is the most common form of dementia which may contribute to 60-70% of cases and is most often characterized by memory deficit and cognitive decline (*Dementia*, no date). At present more than

55 million people have been diagnosed with AD globally and this figure is expected to be more than 130 million by 2050 (Figure 21).

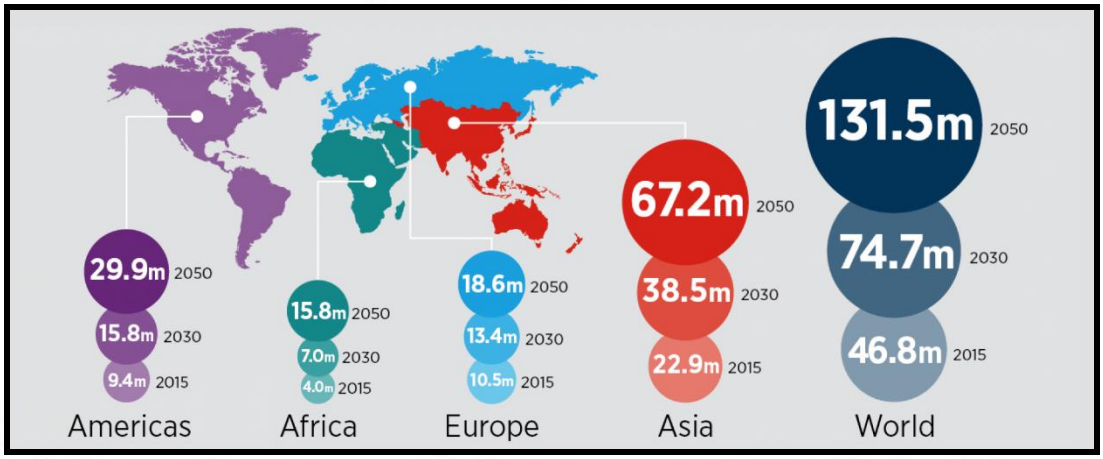

Figure 21. Projected number of people living with dementia worldwide by region, 2015-2050. The figure reproduced from (Martin Prince *et al.*, 2015).

In 2019, India had approximately 3.69 million active cases of AD and other forms of dementia. The prevalence of AD varies significantly across different states, with Kerala, Goa, Andhra Pradesh, Tamil Nadu, and Himachal Pradesh being the top five contributors to the nation's total caseload (Figure 22). This highlights the concern that AD is one of the most persistent global health crises today.

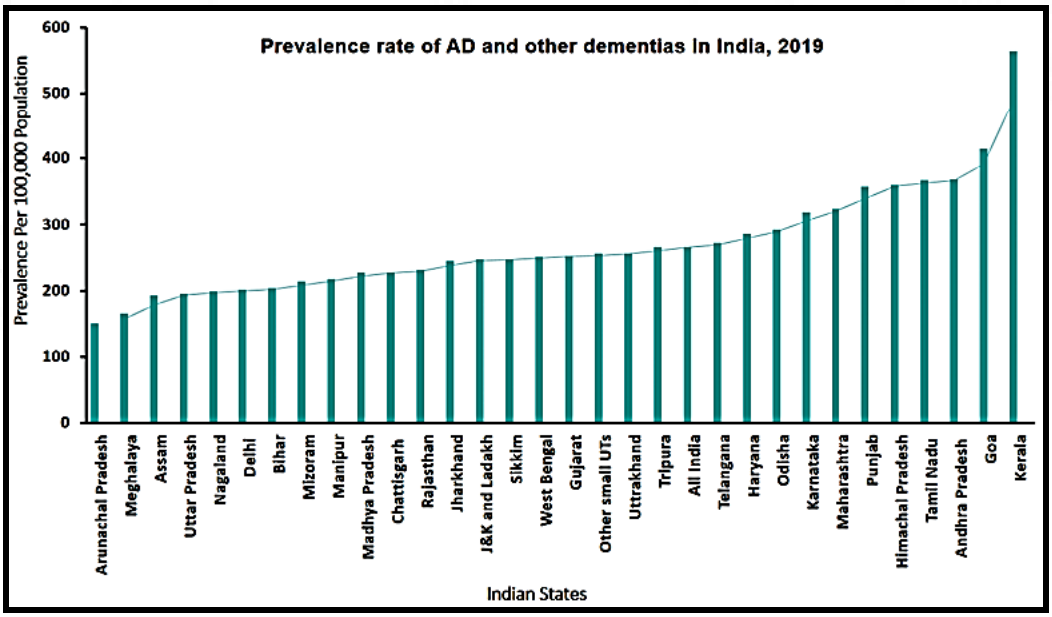

Figure 22. The prevalence of AD and other dementia cases in the different Indian states in the year 2019.The figure reproduced from (https://niscpr.res.in/includes/images/bulletin/bulletin-2023-03-15).

1.3.1 Alzheimer's Disease (AD)

AD is a progressive brain disorder that impairs cognitive function, resulting in memory loss, diminished mental abilities, and behavioural changes. It is the most prevalent type of dementia, especially among older individuals. Moreover, there is an intermediary state between the cognition of normal aging and mild dementia, known as mild cognitive impairment (MCI). MCI is often an originator of AD and a small group of people; typically, 12 to 18% of people aged 60 years or above with MCI can progress to AD (*Mild Cognitive Impairment (MCI) | Symptoms & Treatments | alz.org*). Furthermore, estimates indicate that the annual prevalence of AD augments significantly with age and it has huge personal and financial impacts on society. Consequently, monitoring diagnostic biomarkers is crucial for timely treatment decisions and effective decision-making in the early stages of AD.

1.3.1.1 Biomarkers for AD

A biomarker is an indication of normal biological processes, abnormal activities, or pharmacological treatment responses. In the case of AD, identifying pathogenic processes based only on clinical phenotype is challenging because the disease progresses slowly and the initial symptom viz cognitive impairment, does not appear for decades. During this phase, diagnostic biomarkers can play a significant role in deciding treatment and decision-making MCI. The AD biomarkers include amyloid β (Aβ) plaque accumulation and tau (phosphorylated tau and truncated tau (total tau)), a significant component of neurofibrillary tangles (Janeiro *et al.*, 2021).

Amyloid β (Aβ) plaque

The presence of sticky Aβ plaques that form around neurons is one of the main characteristics of AD. Amyloid plaques are generated in the brain by amyloid β-precursor protein (APP), a membrane protein involved in synapse development and signaling. β-secretase (BACE 1) and γ-secretase cleave APP into varying lengths of hydrophobic Aβ peptides. These peptides are normally cleared into the CSF or transferred into the bloodstream across the blood-brain barrier in normal brain function. Overproduction or reduced clearance of amyloid peptides, on the other hand, results in the development of amyloid plaques, which are a hallmark of AD (Figure 23). The main components of the accumulated Aβ plaques are $A\beta_{40}$ and $A\beta_{42}$, which contain 40 and 42 amino acid residues, respectively. $A\beta_{42}$ is more hydrophobic than $A\beta_{40}$. An increase in $A\beta_{42}$ level causes the formation of Aβ fibrils, and the accumulated Aβ fibrils form a senile plaque, lowering $A\beta_{42}$ levels in both CSF and blood thereby inducing neurotoxicity and tau pathology induction (Figure 23). Aβ plaques can interfere with neuron communication (synaptic transmission), weakening neural networks and leading to cognitive decline, neuronal cell death, and neurodegeneration (Saido and Iwata, 2006; MP and H, 2010; Sadigh-Eteghad *et al.*, 2015).

Tau protein

The development of intracellular neurofibrillary tangles composed of hyperphosphorylated tau protein is the second characteristic of AD. Tau is responsible for sustaining the microtubular skeleton of axons, which allows nutrients to flow via synapses. Oligomeric Aβ binds to tau protein, causing fast dissociation of tau from microtubules and collapse of the axonal structure, resulting in the dysfunction of synapses and, eventually, the death of neurons. Furthermore, $A\beta_{42}$ and

Apolipoprotein E4 (ApoE4) activate glycogen synthase kinase-3b (GSK3b) and other kinases that are important for tau hyperphosphorylation, which leads to tau separation from microtubules. The inability of tau to maintain axon structure by supporting microtubules leads to damaged synapses which eventually cause neuron death (Panza *et al.*, 2016) (Iqbal *et al.*, 2010).

Studies have clearly shown that AD is associated with lower CSF levels of $A\beta_{42}$ and higher CSF levels of total tau (t-tau) and phosphorylated (p-tau), and thereby can distinguish patients with AD versus controls, also in the early stages. In addition, the evaluation of the ratio $A\beta_{42}/A\beta_{40}$ has proven to increase diagnostic accuracy (Baldeiras *et al.*, 2018). Accessing CSF involves procedures that are not welcomed by many patients as a screening or diagnostic method due to the complications involved. Therefore, the focus on the development of blood-based AD biomarkers has been an interest to researchers (Barthélemy *et al.*, 2024).

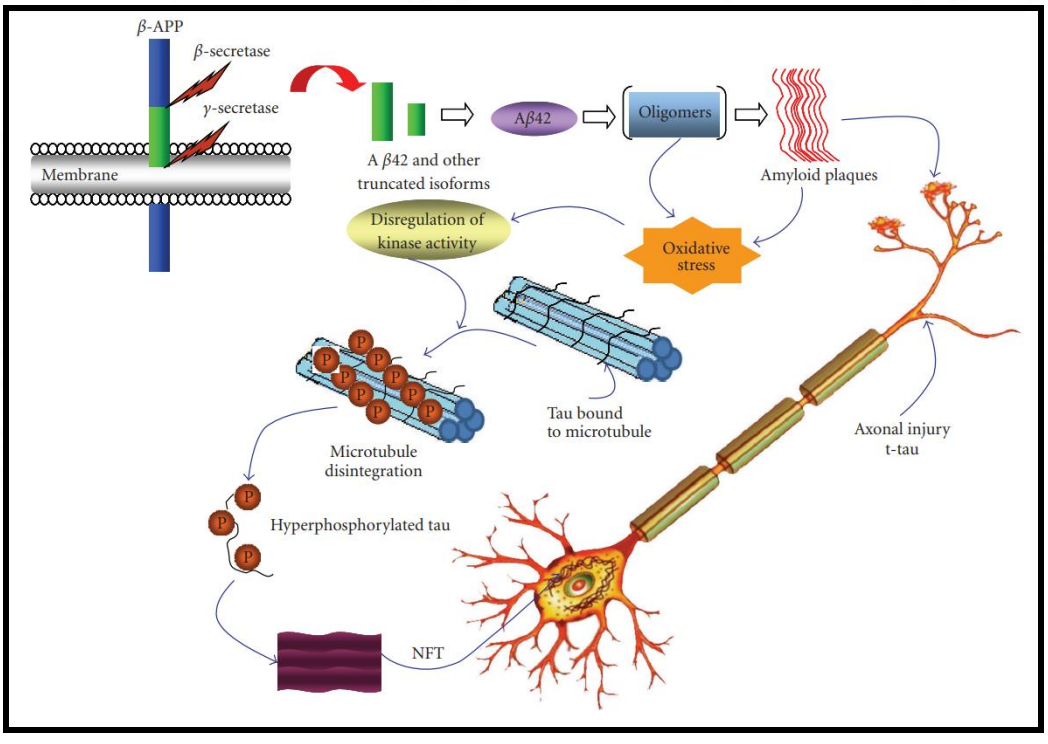

Figure 23. Pathological Cascades in AD and potential biomarkers. The figure reproduced from (Maji *et al.*, 2010).

The pathological mechanism of AD is diverse and complex, making it challenging to attain early detection and intervention.

1.4 Blood-brain barrier and Nanotechnology

The blood-brain barrier (BBB) is a highly selective semi-permeable membrane created by endothelial cells lining the brain's blood vessels. It controls the movement of substances from the blood into the brain, permitting essential nutrients to enter while preventing harmful substances and pathogens. This barrier ensures a stable environment in the brain, which is essential for proper neuronal function. However, this selective barrier also poses a significant challenge for delivering therapeutics to the brain, as it restricts the entry of many drugs and nanoparticles (Teleanu *et al.*, 2018; Hersh, Alomari and Tyler, 2022).

The BBB is structurally composed of endothelial cells, the vascular basement membrane, pericytes, and astrocyte end feet (Figure 24). The endothelial cells have tight junctions that lack fenestration and pinocytic activity, preventing most molecules and ions from paracellular transport. Pericytes, located on the abluminal side of endothelial cells and wrapped by astrocyte end feet, regulate cerebral blood flow by controlling capillary vascular tone. They are crucial for BBB formation and for reducing transcytosis activity as endothelial cells mature. Astrocytes maintain BBB integrity by releasing neurotrophic factors and regulating permeability through the secretion of vasoconstrictor or vasodilator mediators. Thus, pericytes and astrocytes significantly influence transportation across the BBB (Lombardo *et al.*, 2020).

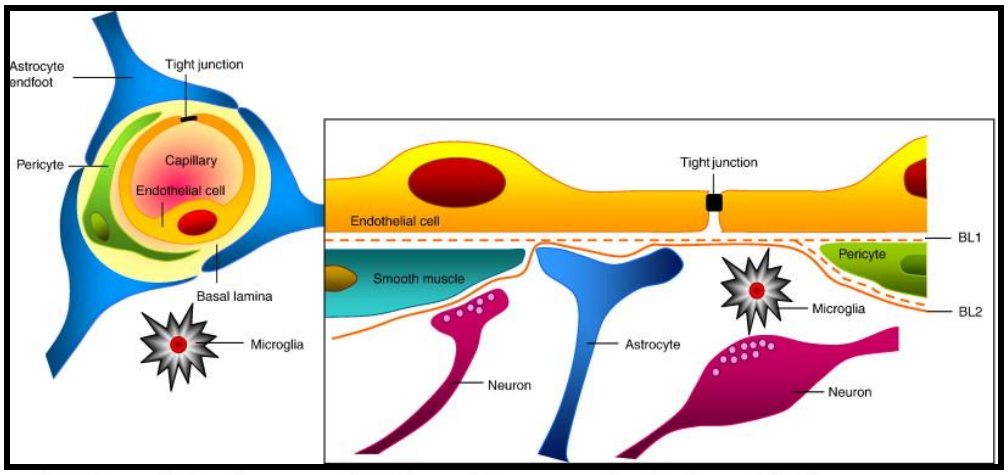

Figure 24. The structural components of the BBB. The figure reproduced from (Martinelli *et al.*, 2020).

Various strategies have been developed to enhance the transport of nanoparticles across the BBB, including surface modification with targeting ligands, such as antibodies or peptides, that can interact with receptors expressed on the endothelial cells of the BBB. Additionally, the use of nanocarriers, such as liposomes, polymeric nanoparticles, or dendrimers and AuNps can encapsulate drugs and protect them from degradation, while also facilitating their transport across the BBB. Due to the small size, AuNCs are more readily taken up by cells through various endocytic pathways, enhancing their potential to cross the BBB (Teixeira *et al.*, 2023).

Moreover, the application of external stimuli, such as ultrasound or magnetic fields, can further enhance the permeability of the BBB to nanoparticles, enabling targeted drug delivery to specific regions of the brain. Overall, nanotechnology holds great promise for improving drug delivery to the brain by overcoming the challenges posed by the blood-brain barrier. Continued research in this area is expected to lead to the development of novel nanomedicines for the treatment of various neurological disorders.

1.5 Current Diagnosis tools and Therapeutic approaches for AD

The current clinical diagnosis of AD is based on the clinical evaluation of the patient's cognitive and behavioural states, both of which can only be confirmed at advanced stages of neurodegeneration. The key neuropathological properties of AD are the death of neurons and synaptic damage in brain regions such as the hippocampus, cortex, and ventral striatum. This disease causes brain atrophy thereby developing cognitive symptoms of AD. Radiological studies of AD-affected brains demonstrate brain atrophy with narrowed gyri, enlarged ventricles, and sulci. Nonetheless, post-mortem AD brain histological analysis is likely to show extracellular Aβ plaques, intracellular neurofibrillary tangles (NFTs), and vascular amyloid deposits. There are many clinical techniques available for the demonstration of the accumulation of these proteins in the brain and diagnosis of AD viz., PET, mass spectrometry, MRI, and enzyme-linked immunosorbent assay (ELISA). Imaging technologies have allowed researchers to get a better understanding of the complex, interconnected pathophysiological pathways that underpin AD. Furthermore, the local impact of neurodegeneration can be characterized in great detail, defects in brain glucose metabolism, regional tissue atrophy, and brain network disruption can all be assessed using PET, structural, and functional magnetic resonance imaging (fMRI). As a result, collecting data from imaging, the spatiotemporal dynamics of AD pathophysiology could provide more insights into the biology and evaluation of the disease's progression in specific individuals (Johnson *et al.*, 2012)(van Oostveen and de Lange, 2021).

Detecting AD biomarkers (particularly Aβ and tau/p-tau) in body fluids such as blood, cerebrospinal fluid (CSF), saliva, and others has been noted in several research articles. In clinical practice, it has been shown that CSF or blood samples taken from AD patients have a greater amount of tau protein and a lower content of the $A\beta_{42}/A\beta_{40}$ ratio than normal age-matched controls. However, several obstacles have limited their application in the clinical diagnosis of AD. For example, the limited sensitivity of ELISA makes precise detection of AD biomarkers in minimally invasive bodily fluids (such as plasma and serum) difficult. t-tau and p-tau protein levels in blood plasma are more than 10 times lower than those in CSF, which is below the detection limits of common ELISA kits. Therefore, accurately diagnosing AD biomarkers from blood is challenging, particularly during its early stages. Nanoparticles, with their superior physicochemical and electronic characteristics, can be employed in the development highly sensitive biosensors to overcome this challenge (Yang *et al.*, 2018; Kim, Lee and Park, 2020).

Currently, there is no cure for AD, and available treatments aim to manage symptoms and slow down disease progression. Drugs like donepezil, rivastigmine, and galantamine are commonly prescribed to improve cognitive function and manage symptoms of AD by increasing levels of acetylcholine in the brain. Memantine is an NMDA receptor antagonist that helps regulate glutamate activity in the brain, reducing symptoms of confusion and agitation. Also, the treatments may include medications to improve cognitive function and manage behavioural symptoms, as well as lifestyle interventions such as exercise and cognitive stimulation.

1.6 Gold-based nanomaterials for AD diagnosis and therapy

AuNPs have become a cornerstone in the field of bio-sensing due to its distinctive characteristics to amplify the accuracy and sensitivity of biomolecular detection. These biosensors are specifically engineered to identify disease-related biomarkers such as those associated with AD in bodily fluids including blood, CSF, or saliva. Functionalized AuNPs are customized to selectively attach to target biomolecules using mechanisms such as antibody-antigen interactions or receptor-ligand binding. Upon binding, AuNPs induce detectable changes in signals through optical, electrochemical, or other sensing approaches, enabling precise quantification of biomarker concentrations. Their rapid response, high sensitivity, and potential for label-free operation make them promising tools for advancing personalized medicine and enhancing patient outcomes.

Compared to traditional AD treatments, nanocarriers or nano-formulations offer multiple benefits, including avoiding hepatic metabolism, reducing dosage, enhancing drug stability and bioavailability, and ensuring targeted delivery to the site of action(Mir Najib Ullah *et al.*, 2023). The aggregation of Aβ peptides into insoluble amyloid fibrils is recognized as a significant pathological feature of AD. Inhibiting Aβ aggregation could offer therapeutic benefits for AD, and extensive research has explored the inhibitory effects of nanoparticles. Specially designed functional nanoparticles can effectively prevent protein aggregation. Among the various nanoparticles, small AuNPs can inhibit Aβ aggregation and fibrillation by slowing down the nucleation process and it could prevent β-sheet formation (Gao *et*

al., 2017a). Thus, the materials like AuNCs can be considered as drug candidates for the treatment of AD.

Recent research indicates that the size of AuNCs plays a crucial role in their ability to inhibit Aβ fibrillation. Smaller AuNCs, typically consisting of fewer atoms, demonstrate more pronounced inhibitory effects compared to larger ones. This size-dependent inhibition is attributed to the unique surface properties and electronic structure of AuNCs, which influence their interactions with Aβ peptides. Aβ fibrillation is a multistep process involving the aggregation of monomeric Aβ peptides into toxic oligomers and eventually into insoluble fibrils. AuNCs have been shown to interfere with this process by preventing the formation of intermediate oligomeric species. By binding to Aβ peptides, AuNCs inhibit their self-assembly into oligomers, thereby impeding the progression toward fibril formation (Gao *et al.*, 2017a). AuNCs exhibit excellent biocompatibility and stability, making them suitable candidates for biomedical applications.

Given the diverse applications of AuNPs, it is proposed that gold nanosystems can be tailored to address the demands of diagnostics and therapies. Among the uncountable uses of nanoparticles, their optical and electrical properties hold particular significance in biosensing, with their optical attributes offering potential in imaging and therapy for neurodegenerative diseases. Thus, the central aim of this thesis is to develop gold nanosystems for biomedical sensing, imaging, and therapy of AD.

1.7 Hypothesis

Nanotechnology and nanosensors open up new perspectives for the development of ultra-sensitive and specific biosensors for the detection of AD biomarkers and target interactions with amyloid-beta aggregates. As CSF biomarkers is limited because of the complexity involved in accessing CSF samples, nanosensors with ultra sensitivity to detect blood-based markers will be beneficial. With these backgrounds and the gap areas discussed above, it is hypothesized that nanoformulations with unique properties could be designed for the development of nanosensors for the early and less invasive detection of biomarkers for AD and the same could also be designed to cross BBB to target and inhibit/disintegrate the amyloid fibrils as a therapeutic approach to AD.

Accordingly, the objectives of the thesis are outlined as follows:

1.8 Objectives

Objective 1: Design and development of biosensors for the detection of Mild Cognitive Impairment (MCI)

Objective 2: Development of nanocarriers to cross the blood-brain barrier

Objective 3: Brain targeting for imaging and therapy of neurodegenerative disease.

CHAPTER 2

LITERATURE REVIEW

In recent years, the prevalence of AD has been increasing, greatly impacting the quality of life and placing a substantial burden on society. Although numerous researchers have identified the causes, signs, and symptoms of AD, it remains an incurable disease with current treatments (Skaria, 2022). For early diagnosis of AD, neuroimaging and laboratory tests using CSF samples are the most commonly used methods. However, these traditional methods often involve lengthy procedures and may produce fewer sensitive results, leading to potential false-positive diagnoses. Additionally, acquiring CSF for diagnostic purposes is invasive and often causes discomfort for patients (Bouwman *et al.*, 2022). As a result, scientists are increasingly looking to develop blood-based biomarkers for AD. However, a major challenge is that the concentration of these proteins in plasma or serum is approximately ten times lower than in CSF. This scarcity demands the development of highly sensitive and selective detection techniques. Consequently, there is a critical need to create more effective detection methods that can provide accurate information on the occurrence and progression of the disease quickly and cost-effectively. In addition, treating AD faces drug delivery challenges due to the presence of BBB. The ability of nanomaterials (NMs) to cross the BBB and the amount of drug they deliver are crucial factors. This chapter reviews the role of NMs in detecting AD biomarkers and outlines the advancements in using these nanomaterials for treating AD. Nanotechnologies demonstrate significant potential,

and the development of new nanoparticles with high efficacy and biocompatibility is expected to enhance theranostics for AD.

2.1 Biosensors for AD Biomarker Detection

Early detection of AD is critical due to the lack of potent therapeutic approaches in its later stages. Progress in the development of *in vivo* biomarkers has shifted AD detection from the dementia stage to the prodromal phase, with several methods currently undergoing preclinical evaluation. Biomarkers used in CSF tests and PET imaging are valuable for detecting AD, despite being complex and expensive. Blood screening presents more clinical opportunities compared to these invasive and complicated procedures, although it remains primarily in the research phase. To create more clinically applicable detection platforms, researchers have developed various nanoparticle-based optical and electrochemical/electronic biosensors. Optical and electrochemical/electronic biosensors are favoured in AD detection due to their high sensitivity, specificity, and practical advantages. Optical biosensors offer real-time, label-free detection using techniques like fluorescence and surface plasmon resonance, making them ideal for detailed biomarker studies (Vigneshvar *et al.*, 2016). Electrochemical/electronic biosensors, on the other hand, provide rapid, cost-effective, and portable detection, often allowing for multi-analyte measurements (Zhang *et al.*, 2023). While other biosensors, such as piezoelectric, thermometric, and microwave sensors, also have potential, they are less commonly used due to their specific challenges or less established technology. The choice of biosensor depends on factors such as the required sensitivity, the nature of the biomarker, and practical considerations like cost and ease of integration. The origin

of the pathophysiology of AD is also provided for easy understanding, for the readers.

As the demand for devices with higher sensitivity, selectivity, rapid response time, and low-cost increases, various nanomaterials have become prevalent in biosensor research. These include AuNPs, graphene, carbon nanotubes, and photonic crystals etc. Their benefits such as excellent stability, biocompatibility, high surface energy, and significant signal amplification make them ideal for biosensor applications.

With the rising need for early detection of AD, continuous efforts are being made to develop sensor systems targeting AD biomarkers with clinically acceptable sensitivities. Recognition probes have been designed to selectively detect specific AD biomarkers, leading to the development of optical and electrochemical/electronic sensing systems with sophisticated signalling processes. In these analytical platforms, the interaction between AD biomarkers and their corresponding bio-receptors is typically converted into optical signals (e.g., absorption, emission, and Raman scattering) or electrical signals (e.g., current, resistance, and impedance) (Figure 25).

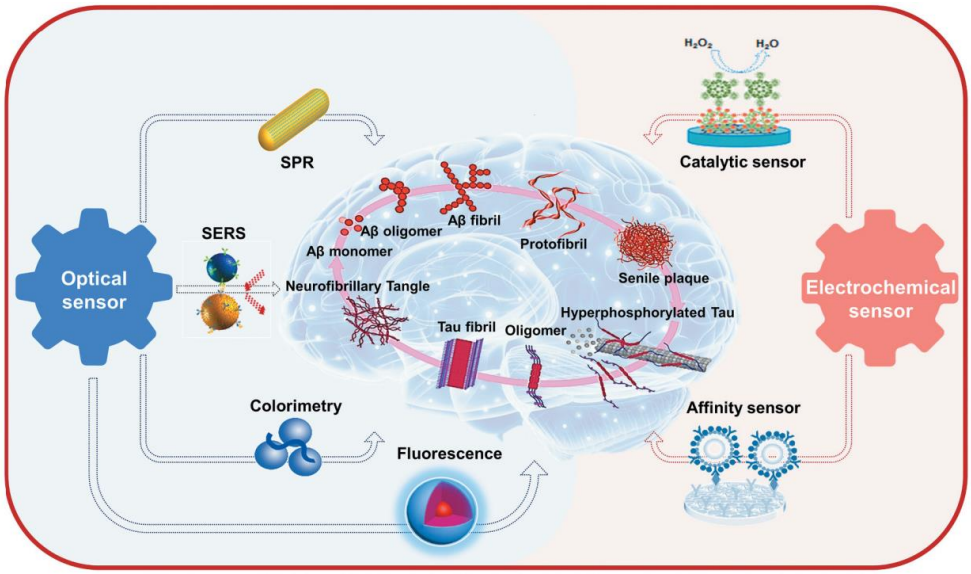

Figure 25. Schematic diagram of optical and electrochemical biosensors for ultrasensitive biomarker detection in the early diagnosis of AD. The figure reproduced from (Phan *et al.*, 2021).

2.1.1 Optical Nano-Biosensors

Optical biosensors utilize the interaction between light and biomolecules to identify biomarkers. Typically, an optical biosensor consists of a biorecognition element integrated with an optical transducer system, which generates a signal proportional to the analyte concentration. The integration of NMs with biosensors holds significant promise for the simultaneous detection of multiple AD biomarkers at an early stage. This integration can greatly enhance sensitivity and specificity while reducing screening time. One of the primary benefits of using NMs is their ability to show different optical properties such as emission wavelength, intensity, polarization, and emission kinetics, which can be exploited in optical sensor systems. Because of these advantages, numerous optical biosensors have been developed to measure AD biomarkers for early diagnosis (Kumar *et al.*, 2023; Zu *et al.*, 2024). This section describes recent progress in the introduction of optical biosensors

targeting AD biomarkers in human blood samples. These include Surface plasmon resonance (SPR), surface-enhanced Raman scattering (SERS) detectors, localized surface plasmon resonance (LSPR) detectors, colorimetric biosensors and fluorescent biosensors,

2.1.1.1 Surface plasmon resonance (SPR)

Changes in the refractive index of the medium are induced by a highly sensitive surface plasmon excited at the metal-dielectric interface. Kim *et al.* developed a combination of DNA aptamer and antibody sandwich assays, which was utilized on a multichannel SPR platform to detect human tau-381 in undiluted plasma at concentrations as low as 10 fM (Kim, Wark and Lee, 2016) (Figure 26). Initially, a mixed monolayer of 11-mercaptoundecanoic acid (MUA) and 11-mercaptoundecanol (MUD) was applied to the SPR gold chip. Using EDC/NHS linking chemistry, the tau-specific DNA aptamer and control sequences were covalently attached to the MUA. This covalent attachment of the DNA aptamer minimizes non-specific interactions while maintaining the analytical effectiveness of the proposed surface sandwich assay. Compared to ELISA measurements for tau analysis in plasma, the SPR-based sandwich assay demonstrated higher sensitivity.

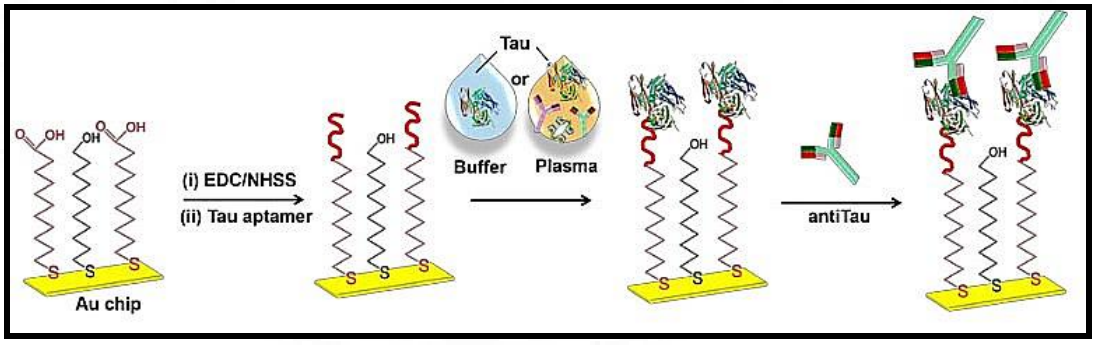

Figure 26. Schematic diagram of the tau detection. tau-381 measurements were performed in the binding affinity of the DNA aptamer followed by subsequent binding of anti-tau. The figure reproduced from (Kim, Wark and Lee, 2016).

The SPR fiber sensor-based immunoassay was developed to identify tau proteins, including both total tau and phosphorylated tau, in human serum (Vu Nu *et al.*, 2018). This study utilized serum from 40 subjects, divided into two groups: AD patients and control subjects, based on several neuropsychological assessments. The detection limits for total tau and phosphorylated tau proteins were 2.4 pg/mL and 1.6 pg/mL, respectively. Notably, the average concentration of total tau proteins in the AD group was found to be six times higher than in the control group, while the concentration of phosphorylated tau proteins was three times higher in the AD group compared to the control group.

Shashank and colleagues designed a label-free real-time SPR technology utilizing specific antibodies to monitor tau and p-tau181 levels in the serum of patients with AD and mild cognitive impairment (MCI) (Shekhar *et al.*, 2016). The primary objective was to explore these levels in search of a more accessible method for developing protein-based markers. In AD patients, serum concentrations of tau (47.49 ± 9.00 ng/L) and p-tau181 (0.16 ± 0.04 ng/L) were notably higher compared to those with MCI (tau: 39.26 ± 7.02 ng/L, p-tau181: 0.13 ± 0.02 ng/L) and elderly controls (tau: 34.92 ± 6.58 ng/L, p-tau181: 0.12 ± 0.01 ng/L). Importantly, a significant positive correlation between tau and p-tau181 levels across AD, MCI, and control groups suggests that increases in tau are mirrored by corresponding increases in p-tau181 in serum.

2.1.1.2 Localized surface plasmon resonance (LSPR)

The sensing mechanism in LSPR-based sensing resembles SPR-based platforms but with a focus on measuring changes in metal nanoparticles rather than metal films following specific interactions between AD biomarkers and recognition elements (Willets and Van Duyne, 2007). Plasmonic materials used in LSPR are typically smaller than the wavelength of light, limiting electron oscillations within the nanoparticles.

A nanoplasmonic biosensor utilizing LSPR was developed for highly sensitive detection of tau protein in human plasma without dilution (Kim *et al.*, 2019) (Figure 27). Addressing the challenges of AD diagnostics using blood samples, guanidine hydrochloride was employed as a chaotropic agent. This chemical disrupts water molecule networks and reduces hydrophobic interactions among proteins, thereby significantly enhancing the detection capabilities for tau protein targets. This innovative combination of an LSPR biosensor with a chaotropic agent represents a novel approach to identifying tau protein in blood samples. The gold nanorod platform achieved a limit of detection in the 153.17−179.85 fM range. Such nanoplasmonic biosensors could standardize biomarker assays for AD diagnosis and establish blood-based diagnostics for other tau-related disorders.

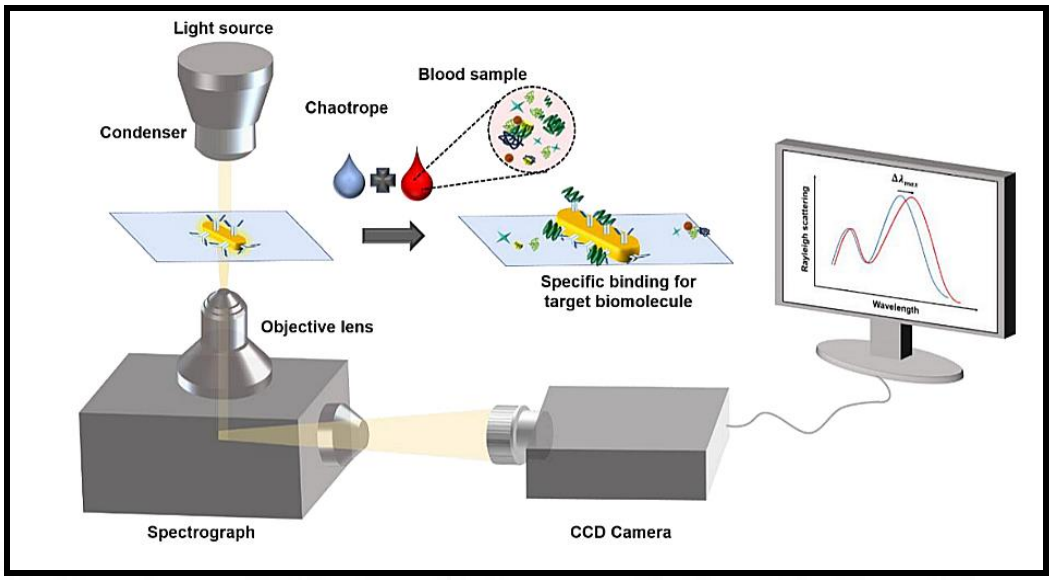

Figure 27. Diagram illustrating a nano-plasmonic biosensor device designed for the precise detection of AD through hemodiagnosis. The figure reproduced from (Kim *et al.*, 2019).

2.1.1.3 Surface-enhanced Raman spectroscopy (SERS)

SERS biosensors detect AD biomarkers with exceptional precision using enhanced Raman scattering. These sensors employ metal nanoparticles to amplify the Raman signals of extremely low levels of AD-related molecules. Commonly, SERS substrates use gold or silver nanoparticles to intensify the Raman signals through the powerful electromagnetic field generated around their surfaces (Elsheikh *et al.*, 2024).

Yu *et al.* developed a sensitive SERS-based technique to identify serum biomarkers ($A\beta_{42}$ and P-tau-181) for the early detection of AD (Yu *et al.*, 2021). A sandwich immunoassay was created in this work, which uses tannin-capped silver nanoparticles and magnetic graphene oxide (Fe_3O_4@GOs) (Figure 28). Here tannin-protected Ag nanoparticles were chosen as a SERS detection probe and the sandwich assay was used to capture the target proteins. Both protein standards and real serum samples were used in this SERS-based immunoassay. The findings showed that this

technique could identify $A\beta_{42}$ and p-tau-181 in human serum samples with high accuracy and sensitivity.

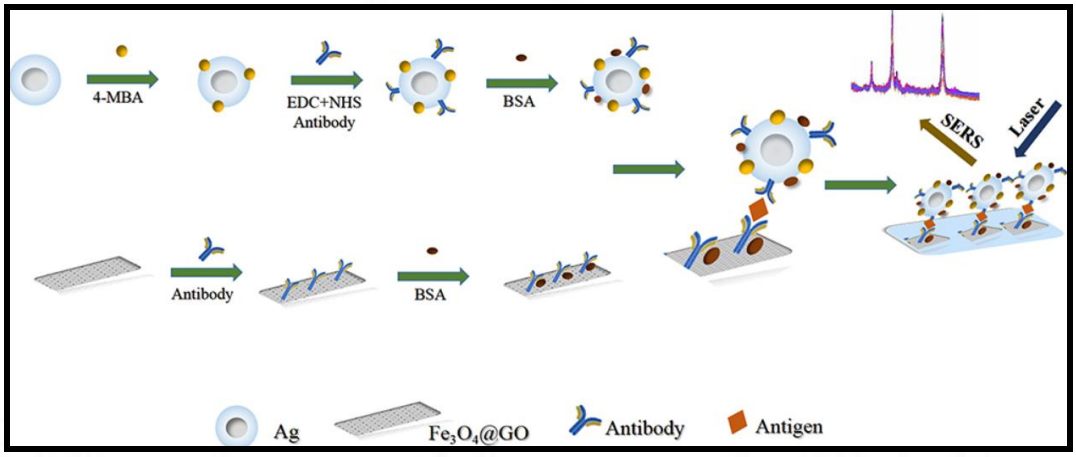

Figure 28. Schematic representation of the SERS-based immunoassay for identifying biomarkers associated with AD. The figure reproduced from (Yu *et al.*, 2021).

Jin-Kyoung Yang *et al*. reported that silver nanogap shells (AgNGSs) function as SERS colloidal nanoprobes, enabling sensitive, selective, and multiplexed detection of $A\beta_{40}$ and $A\beta_{42}$ in blood (Yang *et al.*, 2019) (Figure 29) These AgNGSs, embedded with Raman label chemicals, produce distinct SERS signals with a significant intensity enhancement, reaching up to 10^7, and demonstrate long-term stability. Detection is achievable at concentrations as low as 0.25 pg/mL. Moreover, the AgNGS nanoprobe-based sandwich assay offers a detection dynamic range that is two orders of magnitude broader than that of conventional enzyme-linked immunosorbent assays.

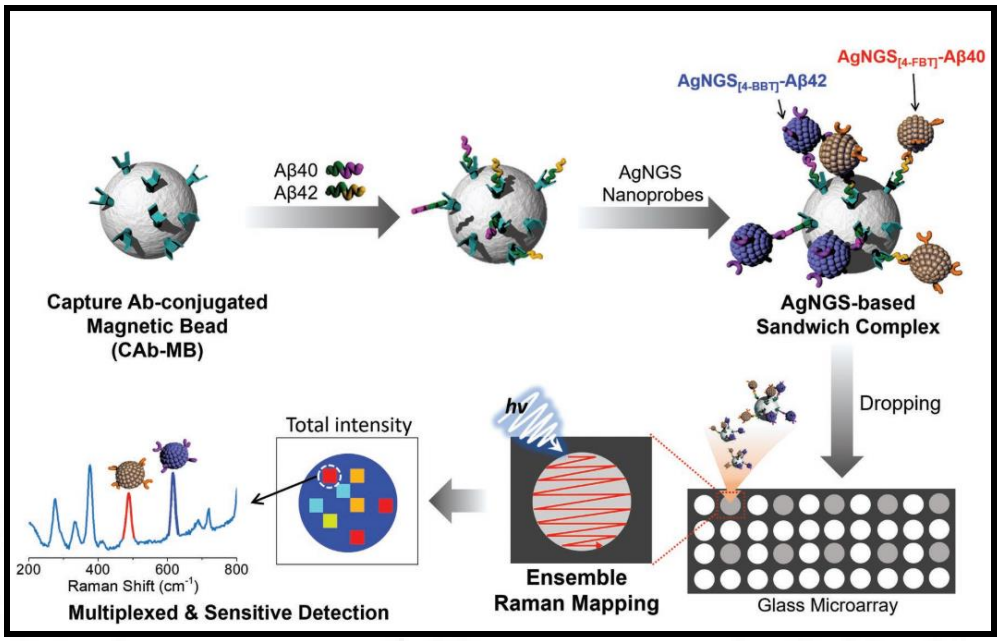

Figure 29. Schematics of SERS biosensors utilizing AgNGS nanoprobes for the detection of $A\beta_{40}$ and $A\beta_{42}$. The figure reproduced from (Yang *et al.*, 2019).

An innovative lateral flow assay (LFA) using Surface-Enhanced Raman Scattering nanotags (SERS-LFA), shown in Figure 30, enables the simultaneous quantification of several AD biomarkers (Zhan *et al.*, 2022). These biomarkers include $A\beta_{42}$, $A\beta_{40}$, tau proteins, and neurofilament light chain. Remarkably, the method achieves low detection limits: 138.1 fg/mL for $A\beta_{42}$, 191.2 fg/mL for $A\beta_{40}$, 257.1 fg/mL for tau proteins, and 309.1 fg/mL for neurofilament light chain. Compared to existing detection technologies, SERS-LFA offers notable advantages such as enhanced specificity and sensitivity, cost-effectiveness, multiplex target detection capability, and rapid assay outcomes.

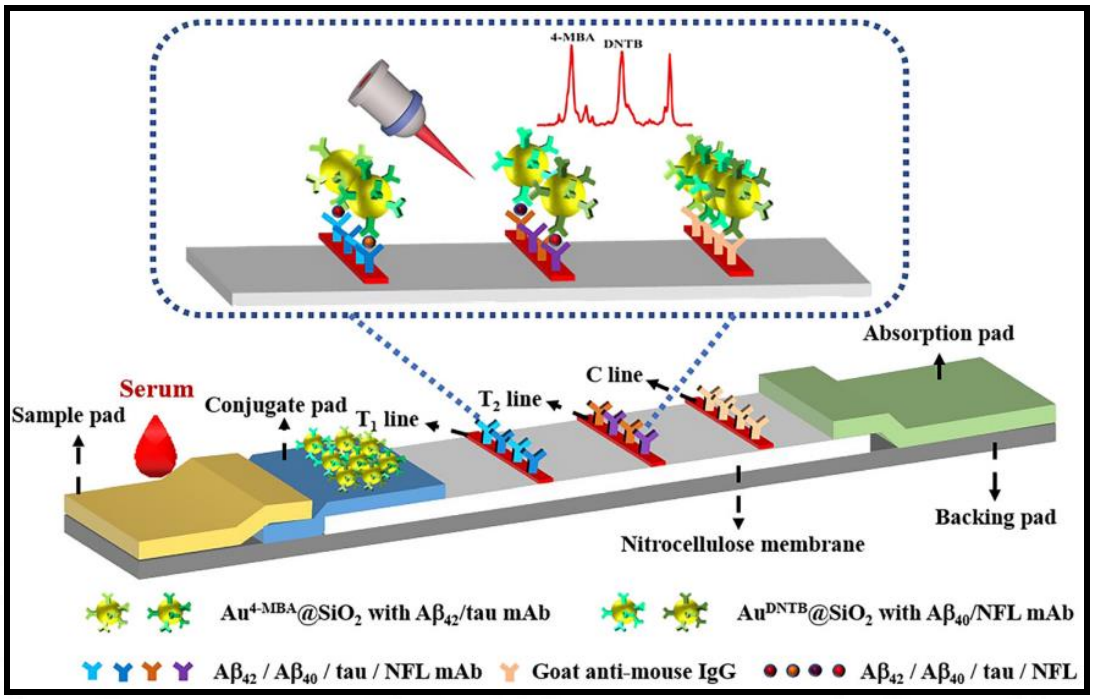

Figure 30. Schematic representation of detecting various AD biomarkers ($A\beta_{42}$, $A\beta_{40}$, tau proteins, and neurofilament light chain) using SERS-LFA. The figure reproduced from (Zhan *et al.*, 2022).

2.1.1.4 Colorimetric biosensors

Colorimetric biosensors are particularly used for point-of-care applications because they allow for the detection of analytes through visible color changes, which can be seen with the naked eye or measured using simple portable optical detectors. Gold nanostructures, which can be easily functionalized, exhibit varying colors based on their size, shape, and aggregation state. This makes them an ideal platform for developing colorimetric biosensors.

Figure 31 illustrates colorimetric biosensors, showing a technique for detecting $A\beta_{1\text{-}40}$ using AuNPs-Aβ-Ni-horseradish peroxidase (HRP). In this method, $A\beta_{40}$ sequentially attaches to AuNPs and metal ions (Cu^{+} and Ni^{+}), causing specific aggregation of AuNPs. This interaction produces measurable colorimetric signals. The assay showed good linearity in the range of 0 nM to 10 nM, with detection limits

of 0.22 nM in standard samples and 0.23 nM in human serum samples (Khan and Park, 2022).

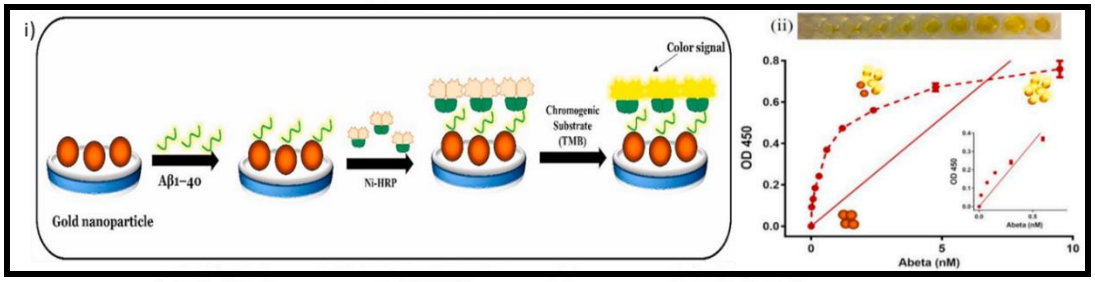

Figure 31. Diagram illustrating a colorimetric biosensor designed for the detection of $A\beta_{1\text{-}40}$ using AuNPs, Aβ, nickel (Ni), and horseradish peroxidase (HRP). ii) detection of $A\beta_{1\text{-}40}$ in human serum samples with inset showing fitted curve. The figure reproduced from (Khan and Park, 2022).

2.1.1.5 Fluorescent biosensors

Fluorescence-based biosensors are highly favored among optical biosensors due to their remarkable sensitivity in detecting fluorescence. These devices utilize the fluorescent properties of fluorophores or fluorescently labelled molecules, which absorb electromagnetic radiation and then emit fluorescence, to assess the concentration (through intensity correlation), distribution (through imaging), and behavior of biomolecules (through lifetime measurement) (Strianese *et al.*, 2012).

A sandwich fluorescence immunoassay designed to detect tau protein is shown in figure 32, utilizing a combination of tyrosinase (TYR)-induced tau aptamer, tau protein, and tau antibody (anti-tau). For the fluorophore, dopamine (DA)-functionalized CuInS2/ZnS quantum dots were used (Chen *et al.*, 2019). The assay demonstrated a strong linear correlation between fluorescence intensity and the logarithm of tau protein concentrations, spanning from 10 pM to 200 nM. The limit of detection (LOD) was determined to be 9.3 pM by inserting the mean fluorescence intensity of the blank sample into the standard curve equation.

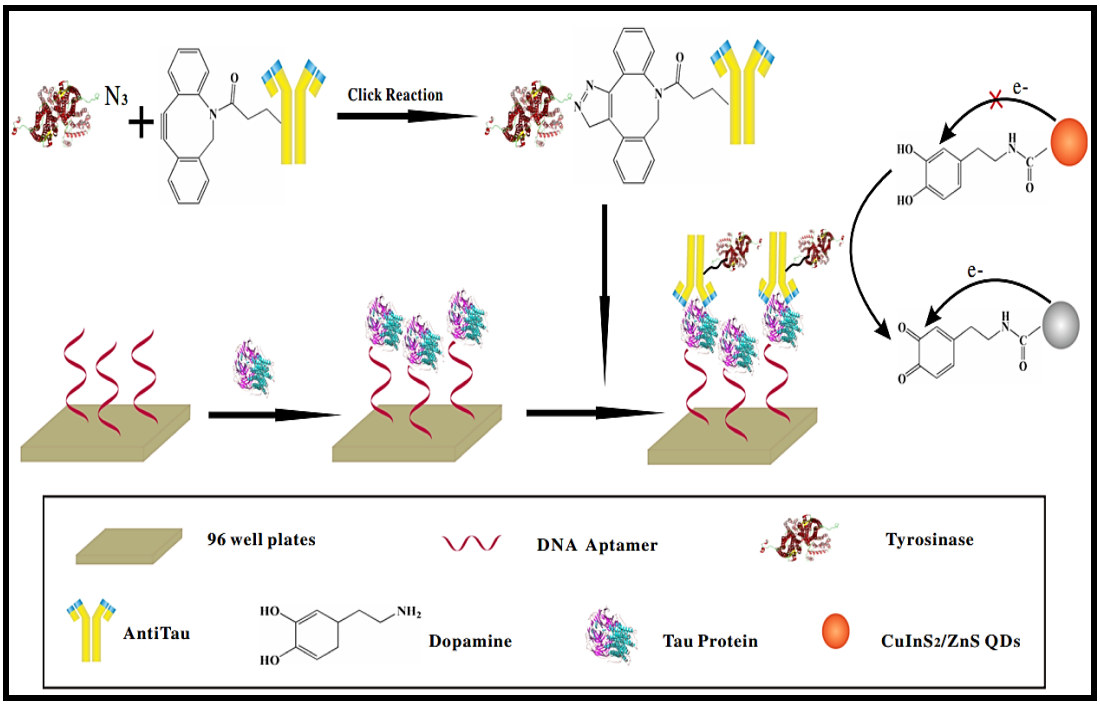

Figure 32. A fluorescence immunoassay utilizing a redox-mediated sandwich approach for the detection of tau protein. The figure reproduced from (Chen *et al.*, 2019).

Lanthanide-functionalized Metal-Organic Coordination Polymers (LMOCPs) have been utilized as sensor materials for the detection of $A\beta_{40}$ monomers (B. Liu *et al.*, 2018). The research revealed that $A\beta_{40}$ significantly enhances the emission in Cu-BTC/Tb, likely due to $A\beta_{40}$'s strong binding to Cu^{2+}, which diminishes the quenching effect and leads to increased fluorescence. The LMOCP sensor demonstrated a high level of sensitivity, with a detection threshold as low as 0.3 nM for $A\beta_{40}$. Moreover, Cu-BTC/Tb proved effective for time-gated detection of $A\beta_{40}$ in human plasma.

This section provided an overview of the most recent nanomaterial-based optical biosensors used for detecting AD biomarkers in blood, which are vital for early diagnosis of the disease. Subsequently, we discuss nanoparticle-based electrochemical biosensors utilized for identifying blood-based biomarkers of AD.

2.1.2 Nanoparticle-Based Electrochemical/electronic Biosensors

Electrochemical platforms are highly advantageous for detecting Aβ and Tau due to their easy manufacturing, affordability, portability, and high sensitivity. To enhance signal transduction efficiency, various chemical modification techniques are applied to the electrode, including the addition of functional nanomaterials or the introduction of different types of nanoparticles. Proper immobilization techniques, using suitable functional materials for the electrode, can lead to high-performance and cost-effective detection systems. These modifications have led to the development of various nanostructured biosensors that enable the early diagnosis of AD by quantifying low-concentration biomarkers. This section describes recent progress in the creation of electrical detection systems targeting AD biomarkers in human blood samples. These systems are categorized based on the type of electrical signals they utilize: voltammetric/amperometric, Impedometric, and conductometric (DR *et al.*, 2001; Grieshaber *et al.*, 2008).

2.1.2.1 Voltammetric/Amperometric biosensors

Voltammetry is the main electrochemical method used in biosensors, recognized for its extensive dynamic range and exceptionally low detection limit. This technique has been applied in electrochemical biosensors to detect AD biomarkers, utilizing methods such as cyclic voltammetry (CV), differential pulse voltammetry (DPV), and linear sweep voltammetry (LSV).

A single-use *in vitro* biosensor was developed to detect t-tau in phosphate-buffered saline (PBS) and undiluted human serum, with a detection range from 1000 pg/mL to 100,000 pg/mL using differential pulse voltammetry (DPV) for measurement (Dai, Molazemhosseini and Liu, 2017). The bio-recognition

mechanism is based on the interaction between antibodies and antigens, enhanced by the presence of a $[Fe\ (CN)_6]^{3-/4-}$ redox probe. Figure 33 shows the structure and dimensions of this gold thin film-based t-tau biosensor system, which includes three electrodes, reference, working, and counter electrode on a polyethylene terephthalate sheet. Each biosensor measures 33.0 × 8.0 mm² in total, with a working electrode area of 1.54 mm² and a liquid test sample volume of 10-25 µL. DPV assays were performed to measure various t-tau protein concentrations in undiluted human serum.

The results suggest that this biosensor is effective for *in vitro* detection of t-tau in blood serum, offering the potential for diagnosing neurodegenerative diseases such as AD, traumatic brain injury (TBI), and other dementia-related conditions.

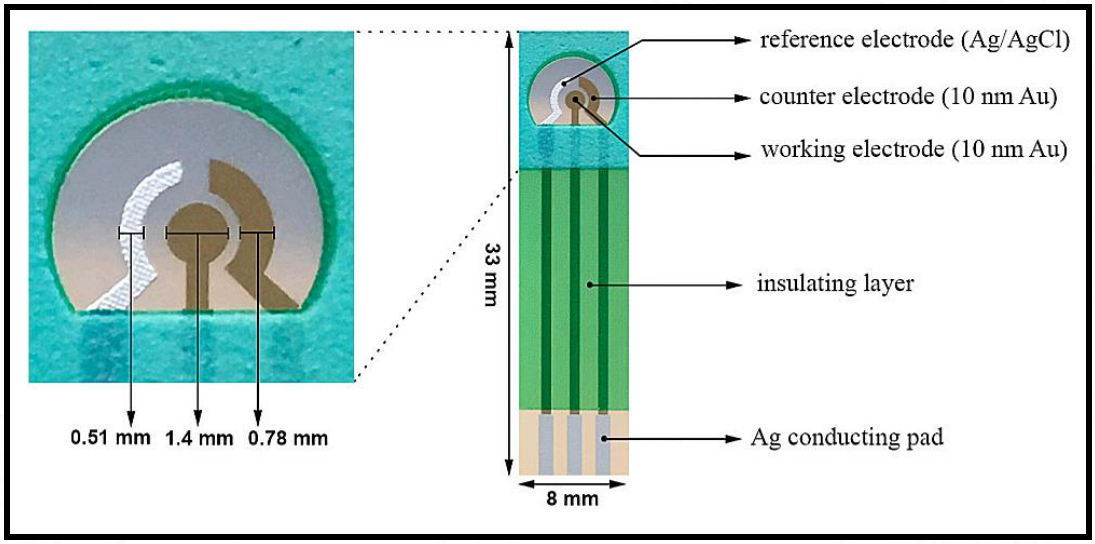

Figure 33. Development of a gold thin film t-tau biosensor prototype. The figure reproduced from (Dai, Molazemhosseini and Liu, 2017).

A voltammetric biosensor was developed by integrating a dual layer of graphene with electrochemically reduced graphene oxide (Sethi *et al.*, 2020). The biosensor's effectiveness was evaluated through DPV. This setup exhibited swift and significantly enhanced sensitivity in detecting $A\beta_{40}$ in human and mice plasma samples spiked with

the compound. It achieved a low detection limit of 2.398 pM, detectable following a 60-min incubation period with the sensor (Figure 34).

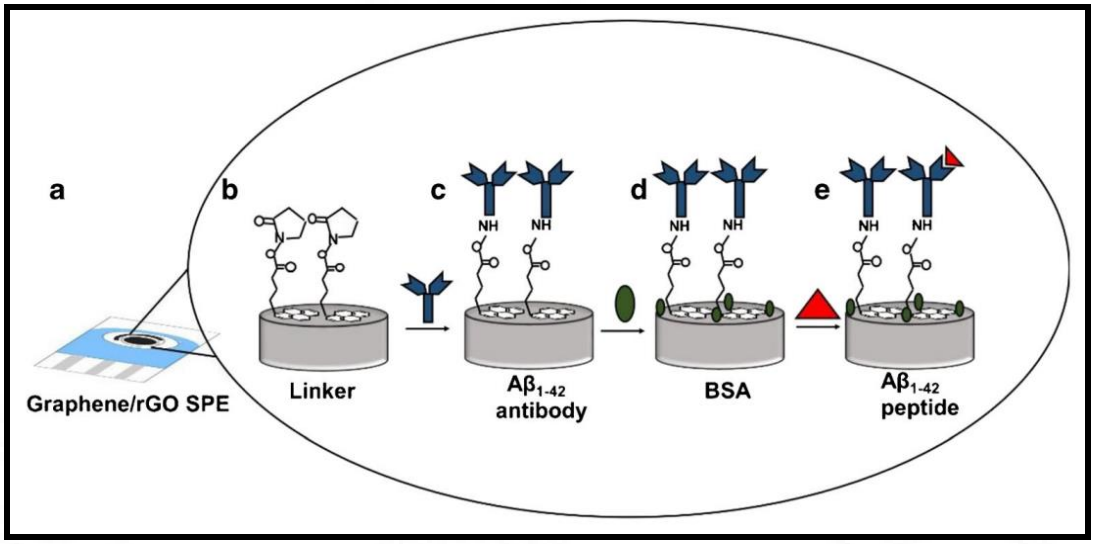

Figure 34. Schematic representation of the electrochemical setup for detecting $A\beta_{1-42}$: a specialized graphene/ rGO screen-printed electrode (SPE) enhanced with a linker (b), antibody (c), BSA (d), and $A\beta 1_{-42}$ peptides (e). The figure reproduced from (Sethi *et al.*, 2020).

2.1.2.2 Impedometric biosensors

The Impedometric sensing substrate evaluates the changes in resistance and capacitance of transducers in response to specific interactions between AD biomarkers and bio-receptors. Generally, the voltage applied in the Impedometric assay is significantly lower than that used in voltammetric and amperometric methods, which helps minimize unwanted disturbances. The obtained impedance values are usually modelled using a Randles equivalent circuit, resulting in a Nyquist plot.

Wang and colleagues have created a four-electrode electrochemical biosensor designed to detect tau protein (Wang *et al.*, 2017). This biosensor utilizes a stable antibody-antigen complex formed on a gold electrode. Figure 35a shows gold microband electrodes fabricated on a p-doped silicon substrate. In their research, they

used electrochemical impedance spectroscopy (EIS) in a tetrapolar configuration to identify various layers of material binding to the electrode surface by measuring impedance changes. The method showed a linear response with increasing tau concentrations, with a detection limit for the full-length 2N4R tau protein at 0.03 pM. As tau concentration increased, interfacial charge-transfer resistance (R_{ct}) values were obtained by fitting semi-circle spectra to the Randles equivalent circuit model. Western blotting confirmed the selectivity and specificity of the tau antibody. By utilizing protein G and different antibodies, a multiplex system for detecting multiple AD biomarkers could be developed. Figure 35b details the electrochemical analysis of tau protein binding to the immobilized tau-Au interface. The standard microelectrode setup includes four gold-plated pins connected to an impedance analyzer's BNC socket, with the working electrode (WE) linked to the signal generator output, and the second and third electrodes serving as reference electrodes (RE) connected to the V1 HI and V1 LO BNCs, respectively. The fourth electrode, the counter electrode (CE), was connected to the instrument's input BNC socket. The cross-linker DTSSP was attached to the microband electrodes through dissociative chemisorption, forming a self-assembled monolayer (SAM). Protein G and antibodies were then applied over the SAM and incubated in PBS for 45 min, with intermittent washing. DTSSP binds protein G through the interaction between the sulpho-NHS ester and amino groups. Throughout the experiments, the optimal concentration of anti-tau antibodies was determined to be 125 μg/mL. Finally, the biosensor's capability to detect tau in human serum was assessed, confirming a detection limit of 0.03 pM, which is significant for AD diagnosis.

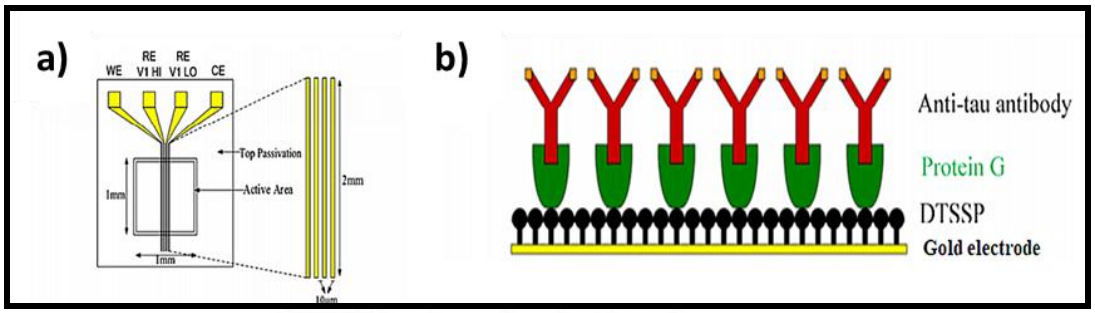

Figure 35. a) Gold microband electrodes created on a P-doped silicon substrate. b) Schematic representation of the biosensor, showing from bottom to top: gold microband electrode, a self-assembled monolayer, a protein G layer, and antibodies. The figure reproduced from (Wang *et al.*, 2017).

2.1.2.3 Conductometric biosensors

In conductometric sensing systems, targeted AD biomarkers are identified through the observation of variations in the transducer's electrical conductance. Recent advancements in nanoparticle-based field-effect transistor (FET) networks highlight the potential and promise of next-generation biosensing technologies that are label-free, highly sensitive, and highly integrated.

Jeseung and colleagues developed a biosensor using a carbon nanotube (CNT) film-based metal-semiconductor field-effect transistor (MESFET) with immobilized probe antibodies to detect Aβ in human serum (Oh *et al.*, 2013). They successfully measured Aβ in human serum at a concentration as low as 1 pg/mL. The plot of conductance changes versus concentration on a semi-logarithmic scale demonstrated a linear relationship in the range of 10^{-12} to 10^{-9} g/mL. Figure 36 illustrates the CNT film-based biosensor with a metal-semiconductor field-effect transistor structure (CNT-MESFET).

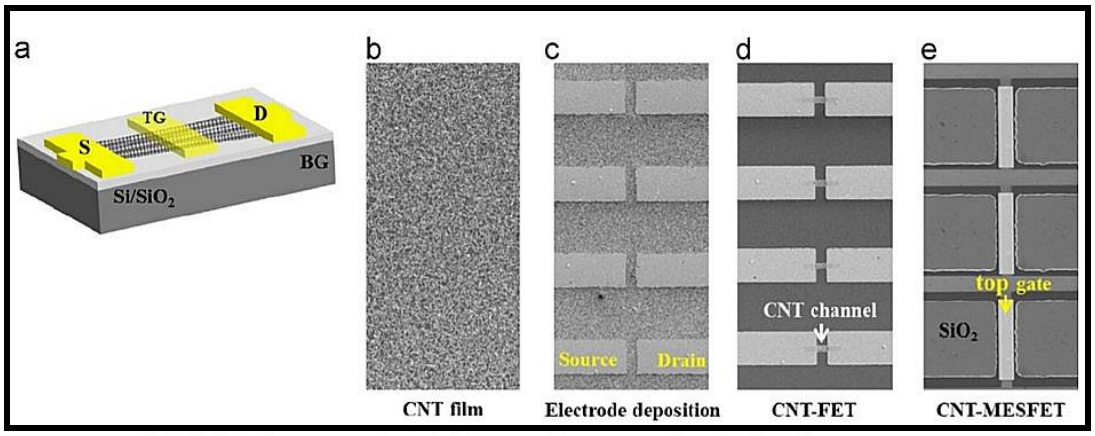

Figure 36. (a) A schematic representation of the CNT-MESFET platform, and (b-e) various stages involved in the fabrication process of the CNT-MESFET device. The figure reproduced from (Oh *et al.*, 2013).

To evaluate the CNT-MESFET biosensor, anti-HRP antibodies were anchored onto the Au top gate surface using either protein G (referred to as MESFET-G) or Escherichia coli outer membrane (OM) presenting Z-domains of protein A (referred to as MESFET-Z), along with pyrene butyric acid N-hydroxysuccinimide ester (FET-C) (Figure 37). This study concluded that MESFET-Z demonstrated superior sensitivity compared to MESFET-G, highlighting its potential for real-time Aβ detection in blood samples.

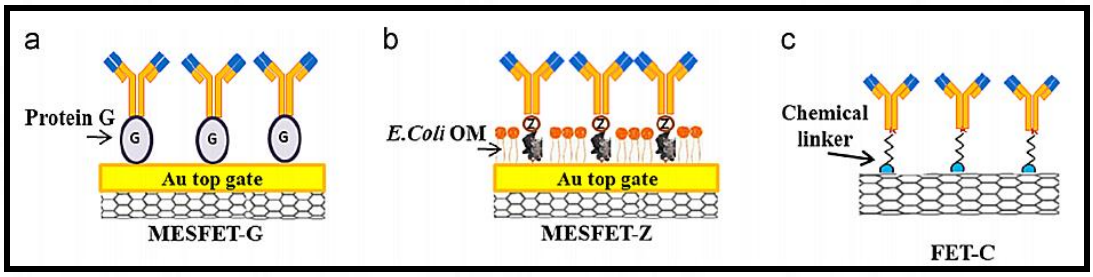

Figure 37. Illustrates of three types of field-effect transistors: (a) MESFET-G, (b) MESFET-Z, and (c) FET-C. Each structure was sequentially constructed layer by layer. The figure reproduced from (Oh *et al.*, 2013).

Negahdary and colleagues developed a highly sensitive electrochemical aptamer sensor technique for quantifying Aβ (M and H, 2019). In their approach, they immobilized a specific RNA aptamer on a gold nanostructure resembling fern leaves. The binding events were detected using a ferro/ferricyanide redox marker specific to the RNA aptamer. Their aptasensor demonstrated the capability to detect Aβ within a linear range of 0.002–1.28 ng/mL, with an impressive detection limit of 0.4 pg/mL (88.6 amol/L). To validate its applicability, the aptasensor was successfully tested with human blood serum and artificial cerebrospinal fluid containing Aβ.

A novel and highly sensitive method has been developed for detecting multiple core biomarkers of AD in human plasma using CNTs arranged in a tightly packed, unidirectional manner (Kim *et al.*, 2020). In this approach, thin films were fabricated via the Langmuir–Blodgett (LB) process, as illustrated in Figure 38. The LB process facilitated the creation of CNT films characterized by dense packing and aligned structures, although some minor loop formations were noted after a single LB cycle. The sensor array achieved exceptional density and precise alignment, enabling the accurate detection of target analytes at extremely low concentrations. Specifically, this multiplexed sensor array successfully identified four key AD biomarkers in blood plasma with high sensitivity. Moreover, the CNT sensor array demonstrated improved diagnostic accuracy by evaluating composite biomarkers ($A\beta_{42}/A\beta_{40}$, t-tau/$A\beta_{42}$, and p-tau181/$A\beta_{42}$), achieving an average sensitivity and selectivity of 90%. These results suggest that integrating compact sensor and readout electronics could pave the way for a portable device capable of distinguishing Alzheimer's patients from healthy individuals.

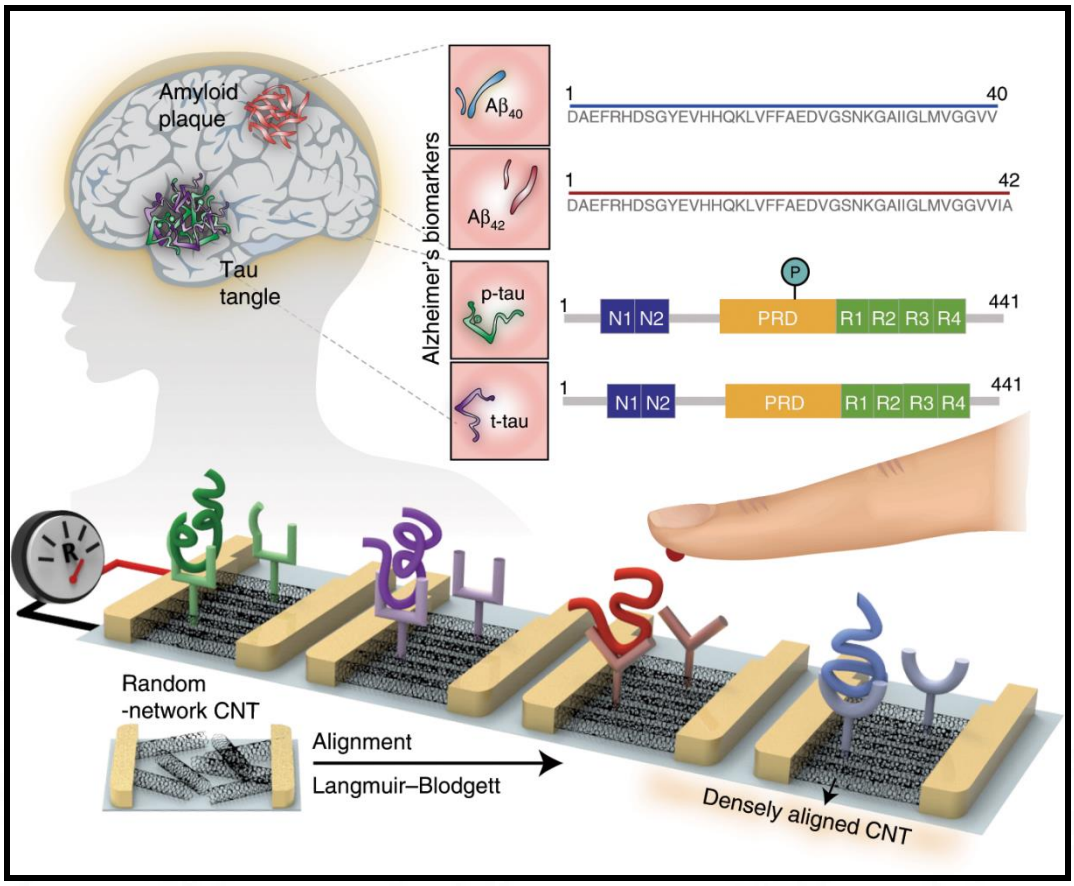

Figure 38. Schematic representation of the closely arranged array of CNT sensor. The figure reproduced from (Kim *et al.*, 2020).

In this section, we explained an overview of how Aβ and Tau pathological pathways interact, emphasizing their role as validated biomarkers crucial for early AD diagnosis. Recent advancements in nanomaterial-based optical and electrochemical/electronic biosensors are highlighted for their effectiveness in detecting these biomarkers. These innovative biosensors, integrating nanostructures, present significant advantages over traditional methods in enabling early AD diagnosis in blood samples. They are on track to become standard in clinical practice, offering broad applicability and potentially reducing the economic and social impacts of AD by improving disease management.

2.2 Artificial neural networks (ANNs) for AD detection

ANNs are becoming a powerful tool for detecting AD because of their ability to analyze complex data and identify subtle disease patterns. By processing extensive datasets that include biological signals and imaging data, ANNs improve the accuracy of early diagnosis. These networks are trained to recognize specific biomarkers associated with AD, such as amyloid plaques and tau tangles, which allows for more precise identification and measurement. Additionally, the adaptability and real-time processing capabilities of ANNs enable the integration of data from multiple sources, enhancing the reliability of detection systems. As a result, ANNs have significant potential to advance the early diagnosis and treatment of AD.

In recent years, ANN have become more commonly used in Raman spectral analysis for diagnosing diseases such as AD. Various machine learning models have enabled high diagnostic accuracy. Beyond achieving exceptional classification performance, machine learning can also elucidate correlations between Raman modes and diseases through important spectral feature mapping (Qi *et al.*, 2023). SERS has emerged as a highly attractive bioassay platform for bioanalytical sensing, offering low detection limits and high specificity. ANNs have been employed to analyze SERS spectral signatures for AD detection and differentiation. Ryzhikova *et al*. analyzed blood serum samples from patients with AD using SERS combined with multivariate statistical techniques (Ryzhikova *et al.*, 2019). These spectra were compared with those obtained from healthy control (HC) subjects to establish a diagnostic tool for detecting AD. Additionally, the serum spectra of AD patients were compared with those of individuals suffering from other forms of

neurodegenerative dementia (OD). The SERS technique employed colloidal silver nanoparticles (AgNPs) as the active substrates. Through classification experiments utilizing ANNs, the diagnostic sensitivity reached approximately 96% for distinguishing AD samples from HC samples in a binary model and 98% for distinguishing AD, HC, and OD samples in a tertiary model. These findings underscore the potential of SERS-based serum analysis as a promising avenue for developing a novel clinical assay capable of effectively and accurately diagnosing AD.

Ziyang *et al.* recently developed a platform for rapid screening of AD biomarkers (Wang *et al.*, 2022). This innovative approach combines graphene-assisted Raman spectroscopy with machine learning for interpreting AD-related changes in transgenic animal brains. The method involved acquiring Raman spectra from brain slices of AD and non-AD mice, utilizing machine learning algorithms to distinguish between the two. By using monolayer graphene in these brain slices, the classification accuracy improved significantly from 77% to 98% in machine learning models. Additionally, employing a linear support vector machine (SVM) allowed the team to create a spectral feature importance map, highlighting crucial Raman wavenumbers essential in AD classification (Figure 39). This map identified key AD biomarkers such as Aβ and tau proteins, along with potential markers like triolein, phosphatidylcholine, and actin, which are consistent with current biochemical research findings.

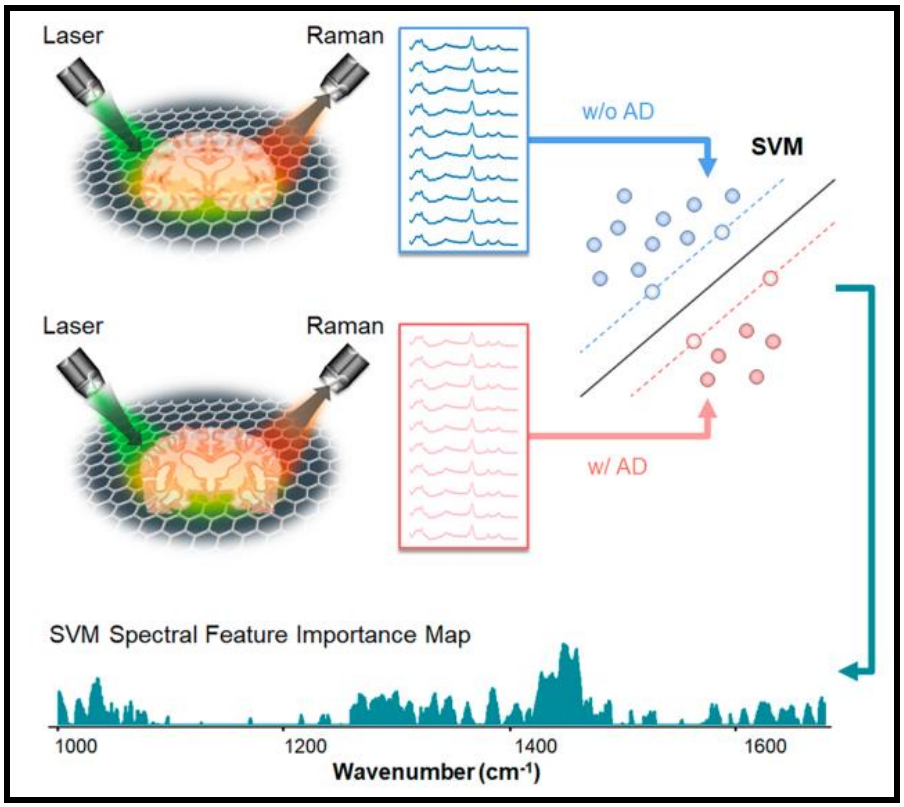

Figure 39. Schematic representation of the machine learning classifier utilized in the linear SVM model, designed to distinguish between AD and non-AD Raman spectra. The figure reproduced from (Wang *et al.*, 2022).

2.3 Nanotechnology-Based Treatment of AD

Recently, significant efforts have been dedicated to developing effective techniques to inhibit Aβ deposition and Tau phosphorylation as a treatment method for AD. However, more than 100 different medications for AD have failed in phase II and III clinical trials (Tolar, Abushakra and Sabbagh, 2020). To date, only one medication, Aduhelm™ (aducanumab, an Aβ-directed antibody), has received approval from the U.S. Food and Drug Administration (FDA) for AD treatment (Khanna *et al.*, 2024). While Aduhelm™ has been shown to reduce Aβ plaques in the brain, its therapeutic benefits remain unclear, as phase III trials did not provide statistically significant evidence that reducing Aβ plaques slows cognitive and

functional decline (Sevigny *et al.*, 2016). In light of these drawbacks, there is an urgent need for alternative treatment approaches. Ongoing research into small organic molecules, nanoparticles, peptide inhibitors, and Aβ-specific antibodies continues to drive drug development for this devastating disease.

Nanotechnology presents promising new methods for addressing AD. One notable application is the use of NMs as medications that can directly influence disease-related physiological processes, to improve treatment results. Despite significant progress, there are still challenges, including the toxicity of NMs, difficulties in crossing the BBB and ensuring sufficient drug bioavailability. Moreover, certain NMs can act as drug carriers that specifically target receptors or transporters associated with the BBB, thereby increasing selectivity and permeability in the central nervous system.

In AD research, various hypotheses have emerged to explain its pathogenesis. One prominent theory is the Aβ cascade hypothesis, which suggests that changes in amyloid precursor protein (APP) processing by α-secretase, β-secretase (BACE1), and γ-secretase enzymes lead to the production of Aβ peptides. Following cleavage by BACE1, the C99 fragment binds to cell membranes, where γ-secretase further processes it to release $A\beta_{42}$ and other shorter peptides into the interstitial fluid. These peptides can aggregate into toxic oligomers, fibrils, and plaques, contributing to neurodegeneration and cognitive decline (Wang *et al.*, 2021)(Montesinos *et al.*, 2020)(Panza *et al.*, 2019). Consequently, one therapeutic strategy involves inhibiting the growth of these Aβ fibrils. Various methods have been developed to hinder amyloid fibrillization, including the use of small molecules, functional polymers, and nanoparticles. Among these, nanoparticle-based approaches are the most effective,

with their ability to either stimulate, inhibit, or delay fibrillization kinetics depending on their surface chemical groups (Chakraborty *et al.*, 2023). In particular, AuNPs and AuNCs are notable for their capacity to inhibit and redirect Aβ fibrillization due to their unique properties and versatile surface functionalities(Wang *et al.*, 2019).

2.3.1 AuNPs mediated inhibition of Aβ fibrillization

In recent studies, it has been shown that AuNPs slow down the nucleation process, effectively preventing Aβ aggregation and fibrillization. Palmal and colleagues reported that AuNPs functionalized with curcumin (Au-curcumin), with a hydrodynamic diameter of 10-25 nm, inhibit amyloid fibrillization and dissolve existing amyloid fibrils (Palmal *et al.*, 2014). Curcumin inhibits protein self-assembly by binding to oligomers and fibrils through aromatic π-stacking interactions, without binding to the native protein. The curcumin moiety on Au-curcumin binds to the oligomers/fibrils, interfering with the elongation phase of fibrillization. The enhanced inhibitory effect of Au-curcumin compared to free curcumin is attributed to its water solubility and the multiple curcumin moieties on the AuNPs, which enable multivalent interactions. As a result, Au-curcumin effectively reduces amyloid-induced neurotoxicity (Figure 40).

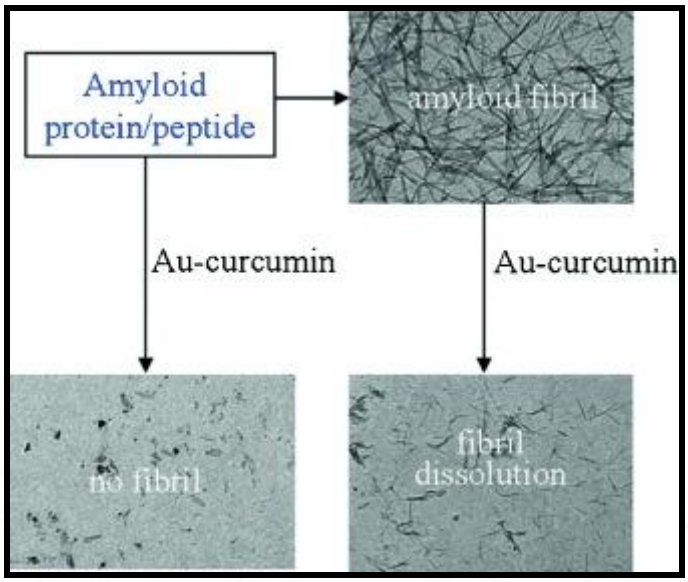

Figure 40. disintegration/dissolution of long Aβfibrils after incubation with Au-curcumin. The figure reproduced from (Palmal *et al.*, 2014).

In another study, Yi-Hung Liao *et al.* reported, that AuNPs exhibited a negative surface potential function as nano-chaperones, restraining and altering Aβ fibrillization, potentially aiding in AD therapies (Liao *et al.*, 2012). The AuNPs utilized were 30 nm in size, with amine-conjugated and carboxyl-conjugated variants having zeta potentials of +7 mV and -39 mV, respectively. The use of negatively charged metallic AuNPs predominantly influenced the elongation phase rather than the nucleation phase of Aβ fibrillization. Hence, the negative zeta potential appears crucial in inhibiting fibril formation.

Delcea *et al.* showed that AuNPs coated with dextrin (Dex) and chitosan (Cht) exhibit significant inhibition of fibril formation (Meesaragandla *et al.*, 2020). This highlights the critical influence of ligand structure and surface functional groups on the inhibitory effectiveness of AuNPs. The surface of fibrils is particularly heterogeneous, with a balanced distribution of carboxyl, amino, and amino groups. The functional groups and structural characteristics of biopolymers such as Dex-40,

Dex-10, Dxt, and Cht contribute to the inhibition of amyloid fibril formation. Dex-40 and Dex-10 molecules are characterized by abundant -OH groups and a branched structure, while Dxt and Cht molecules are linear and possess both -OH and -NH_2 groups. During the nucleation phase, both Dxt and Cht-AuNPs strongly interact with insulin monomers through their respective -OH and -NH_2 groups, effectively hindering oligomer formation and protofibril elongation. This interaction results in the formation of thinner and shorter fibrils (Figure 41).

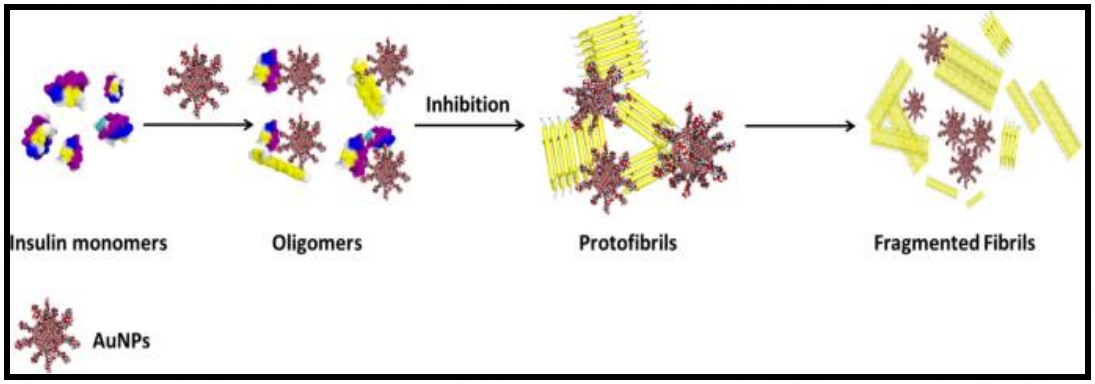

Figure 41. Schematic representation of inhibition of amyloid fibrils in the presence of biopolymer-coated AuNPs. The figure reproduced from (Meesaragandla *et al.*, 2020).

Javed *et al.* explored the chaperone-like activity of β-casein (βCas) combined with αs1-casein and found a dual strategy to inhibit amyloid-beta toxicity in zebrafish using βCas-AuNPs (Javed *et al.*, 2019) . The dynamic equilibrium between Aβ peptides in the brain and the peripheral system results in a simultaneous reduction of Aβ levels in both areas, which can lead to side effects or reduced efficiency.

Sanati *et al.* demonstrated that AuNPs might help improve memory loss and neural damage in an animal model of AD(Sanati *et al.*, 2019). The beneficial behavioural effects of AuNPs are likely attributed to their influence on the kinetics of

Aβ peptide fibrillization, thereby reducing the harmful impact of fibrils on p-CREB, BDNF, STIM1, and STIM2..

Hou *et al.* developed 3.3 nm L- and D-glutathione-stabilized AuNPs, which were capable of inhibiting the aggregation of Aβ and crossing the BBB after intravenous injection without significant toxicity (Hou *et al.*, 2020). The introduction of chiral glutathione ligands is anticipated to grant AuNPs exceptional chiral recognition of Aβ and enantioselective inhibition of Aβ fibrillization. Moreover, AuNPs serving as carriers offer a unique opportunity to optimize BBB permeability and *in vivo* efficacy by modifying their size or shape.

2.3.2 AuNCs mediated inhibition of Aβ fibrillization

AuNCs have unique structural advantages, such as excellent stability, surface modification diversity, fluorescence property, and the characteristic for crossing the BBB, that have attracted much attention in the management of AD.

Hao *et al*. investigated the application of AuNCs functionalized with the hexapeptide CLVFFA to prevent the aggregation of Aβ peptides, the extension of fibrils, and the disaggregation of mature fibrils (Hao *et al.*, 2019).The hexapeptide CLVFFA was specifically designed based on the central hydrophobic fragment LVFFA of Aβ, with the cysteine (C) residue enabling attachment to AuNCs via gold-sulfur (Au-S) bonds. To enhance its inhibitory properties, CLVFFA was conjugated with AuNCs, creating a nanoscale inhibitor, AuNCs-CLVFFA, anticipated to exert synergistic effects on Aβ fibrillogenesis. Unlike the limited inhibition capacity of free CLVFFA, AuNCs-CLVFFA effectively inhibits Aβ fibrillogenesis, the elongation of fibrils, and the disaggregation of mature fibrils. The dual-inhibitory mechanism of AuNCs-CLVFFA involves the combined action of CLVFFA and AuNCs. CLVFFA likely interacts

with homologous sequences of Aβ, while AuNCs enhance peptide stability and biocompatibility. Ultimately, AuNCs-CLVFFA prevents the conformational change of Aβ40 from random coils to β-sheet structures. This AuNCs-peptide composite shows potential for use in AD therapy.

Guanbin and colleagues investigated how the size of AuNPs and AuNCs affects Aβ fibrillization(Gao *et al.*, 2017b) . They discovered that nanoparticles with diameters of 36 and 18 nm accelerated Aβ fibrillization, whereas smaller AuNPs with a diameter of 1.9 nm significantly delayed or completely inhibited this process. These findings revealed that larger AuNPs can accelerate Aβ fibrillization, whereas smaller AuNPs exhibit significant inhibition of this process. Specifically, AuNPs with a flat surface and modified with glutathione (GSH) were observed to enhance the nucleation and growth rates of Aβ fibrils by enriching monomers on their surfaces. For smaller AuNPs, the curvature of their surfaces influences the spatial arrangement of GSH motifs. This spatial arrangement may render them incompatible with the fibrillization pathway of Aβ, thereby suppressing the fibrillization kinetics near the AuNPs. The inhibitory effect is further pronounced in gold nanocrystals due to their tiny size, which disrupts the aggregation and nucleation processes of Aβ, possibly by interfering with the β-hairpin structure of the peptide (Figure 42). These insights underscore the size-dependent effects of AuNPs and gold nanocrystals on Aβ fibrillization, highlighting their potential in modulating amyloid aggregation pathways for therapeutic in AD.

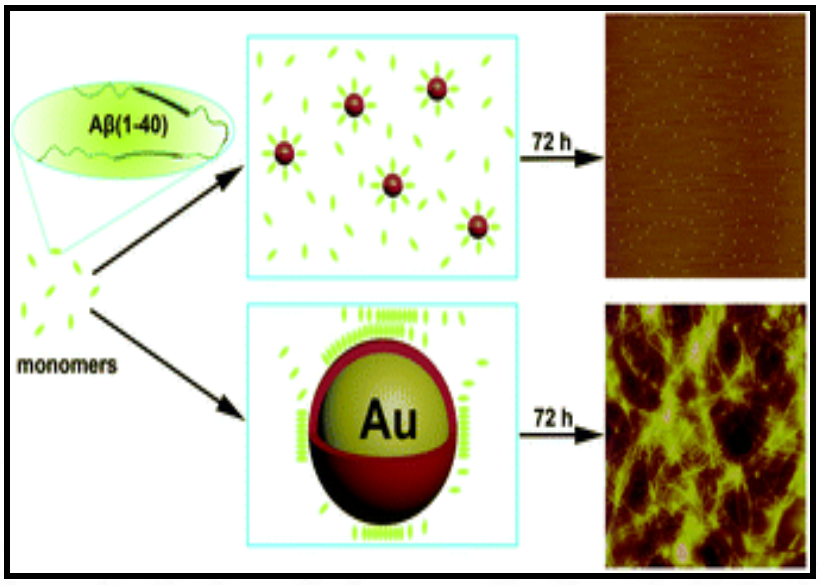

Figure 42. The impact of AuNPs size on their interactions with Aβ interfaces. The figure reproduced from (Gao *et al.*, 2017b)

2.3.3 Inhibition of Aβ fibrillization through thiophilic interaction

The Aβ peptide is produced through the proteolysis of APP and ranges from 39 to 43 residues in length, with $A\beta_{1\text{-}42}$ being the most common form in AD patients' brains. This peptide is prone to aggregation, particularly due to its LVFFA and GxxxG motifs (Kumar and Sim, 2014). Recently, numerous compounds have been created to inhibit or dissolve Aβ aggregates. These include peptidic β-sheet breakers, biocompatible nanogels, molecular tweezers, indole derivatives, catechol derivatives, piceid, and polymers. Among these, polyphenols are the most frequently mentioned. Catechin and its derivatives prevent fibril formation in various polypeptides through π-π interactions. This specific, non-covalent interaction effectively hinders amyloid fibril formation (Takai *et al.*, 2014a).

The thiophilic interaction of a sulfur-containing ligand is notably stronger with bicontinuous aromatic residues (such as Trp-Trp, Phe-Phe, or Tyr-Tyr) of $A\beta_{42}$ compared to a single aromatic residue (like Trp, Phe, or Tyr). This characteristic of

thiophilic interaction is anticipated to effectively prevent the formation of amyloid fibrils in an amyloid-β peptide, which contains the core sequence ^{16}KLVFF^{20}, where ^{19}FF^{20} might exhibit thiophilic interactions with a sulfur compound (Matejtschuk, 2004).

Takai *et al.* found that cysteine, an amino acid-rich in thiophilic properties, has been observed to reduce the number of fibrils formed during Aβ peptide fibrillization, thereby slowing down fibril formation (Takai *et al.*, 2014a).. This interaction is expected to effectively prevent the formation of amyloid fibrils, particularly those containing the KLVFF core sequence, where the phenylalanine residues (FF) can interact with sulfur compounds through these thiophilic interactions. Therefore, the study examined the impact of sulfur compounds on the inhibition of Aβ fibrillization and cytotoxicity (Figure 43).

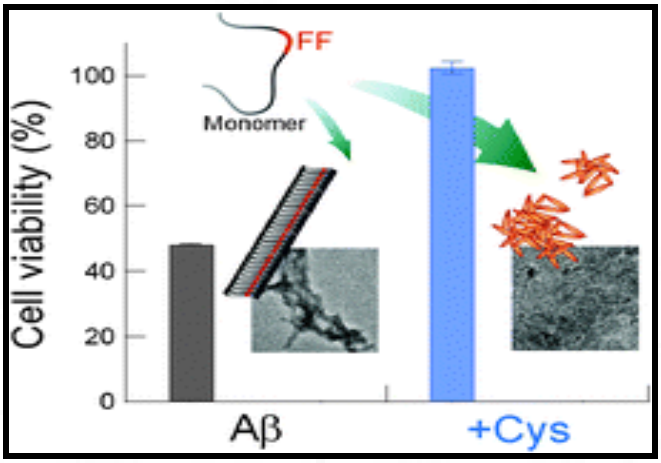

Figure 43. Cysteine inhibits the fibrillization of amyloid-beta $A\beta_{42}$ and $A\beta_{40}$ peptides through a thiophilic interaction. The figure reproduced from (Takai *et al.*, 2014a).

Kumar *et al.* have reported on D-amino acid-based peptide inhibitors, highlighting their non-toxic and stable properties, which are advantageous for targeting aggregation-prone sequences within the Aβ peptide (Kumar and Sim, 2014)

. Researchers have designed many peptide inhibitors utilizing the LVFFA domain of Aβ to hinder its self-assembly. While this approach can effectively prevent aggregation *in vitro,* other aggregation sites at the C-terminus might still promote aggregation independently. Additionally, the flexible N-terminus could be a promising target for promoting the clearance of aggregates. Therefore, a combination of these targets may ultimately offer the most effective therapeutic strategy.

2.3.4 Alternative Therapeutic Approaches in AD

The Tau hypothesis suggests that hyperphosphorylated Tau protein forms paired helical filaments (PHFs) in a β-folded conformation, which aggregate to form neurofibrillary tangles (NFTs). This hyperphosphorylation leads to a reduced affinity for microtubules and contributes to the disorderly aggregation into NFTs. Treatments focus on removing pathological Tau and modulating its phosphorylation(Busche and Hyman, 2020). Nanotechnology-mediated Tau inhibition has emerged as an advanced strategy to enhance treatment efficacy for AD (Ma *et al.*, 2024) .

According to the mitochondrial cascade hypothesis, mitochondrial dysfunction, characterized by mitochondrial DNA mutations, membrane damage, oxidative stress, and disrupted metabolism, is linked to AD pathogenesis. This dysfunction can both contribute to and be influenced by the abnormal accumulation of Aβ and Tau proteins, creating a vicious cycle that accelerates AD progression (Ashleigh, Swerdlow and Beal, 2023). Nanozymes, which are nanomaterials with enzyme-like properties, have gained attention for their role in mitochondrial recovery (Wei *et al.*, 2013).

Stem cell therapy represents a novel approach in regenerative medicine, aiming to repair or replace damaged tissue cells. Research indicates that

mesenchymal stem cells (MSCs) can inhibit Aβ plaque deposition, prevent Tau protein phosphorylation, regulate the inflammatory response, and promote nerve cell function recovery(Yuan *et al.*, 2019; Farahzadi, Fathi and Vietor, 2020). However, a significant limitation of MSC therapy for AD is the inability of MSCs to cross the BBB when administered intravenously. Nanotechnology-mediated MSC therapy for AD offers low immunogenicity and effective immunomodulatory capabilities, enhancing neuronal activity (Asil *et al.*, 2020).

Additionally, immunotherapy has been identified as a promising and safe therapeutic option to eliminate Aβ from the brain. However, its effectiveness is limited by side effects such as meningoencephalitis and brain microhemorrhage. Given the failure of single-target immune therapy to regulate cognitive decline despite reducing Aβ deposits, a multitarget approach combining Aβ-targeting strategies with nanotechnology would likely be more effective (Song *et al.*, 2022).

2.3.5 Photodynamic Therapy in AD

Current treatment strategies for AD primarily rely on chemotherapy, and only a few AD drugs have received FDA approval (Akushevich *et al.*, 2021). As an alternative, significant efforts have recently been dedicated to using photodynamic therapy (PDT) to target AD-related protein aggregations, such as Aβ through photon-triggered reactive oxygen species (ROS) generation (Li, Wang and Liu, 2020). Although PDT for AD is still in its early stages and faces many challenges, it is considered a promising alternative for addressing the current limitations of AD. Through photodynamic reactions, hydrophilic “O” atoms from ROS can be covalently incorporated into amyloid peptides/proteins via amino acid residue oxidation, thereby significantly reducing amyloid aggregation. In amyloid fibrils,

residues such as Tyr, Met, and His are susceptible to oxidation by light-triggered oxidative stress, may promote amyloid breakdown and reduce cytotoxicity.In recent years, various transition metal complexes have also been developed to facilitate the photodegradation of amyloid aggregates PDT (Xu *et al.*, 2022). Advancements in nanotechnology have significantly enhanced. Nanoparticles can be engineered to more effectively deliver photosensitizers to the brain, equipped with targeting ligands that specifically recognize and bind to AD biomarkers. Additionally, nanoparticles can improve the solubility, stability, and photophysical characteristics of photosensitizers. Various nanomaterials, including liposomes, polymeric nanoparticles like PLGA (poly(lactic-co-glycolic acid)), and metal nanoparticles such as gold and silver, are used in PDT (Menon *et al.*, 2013). These materials can amplify the effectiveness of PDT, offering a multi-modal strategy for AD therapy.

2.4 Blood-Brain Barrier (BBB)and Nanotechnology

Crossing the BBB remains one of the most difficult obstacles for delivering drugs to the brain. Various physiological mechanisms, such as receptor-mediated transcytosis (RMT) and adsorptive-mediated transcytosis (AMT), can be utilized to traverse the BBB. To achieve this, numerous nanocarrier systems including polymeric, lipid-based, and inorganic nanoparticles have been designed with tailored surface properties to facilitate BBB crossing. Studies have demonstrated that physically coating nanoparticles with surfactants and chemically functionalizing them with specific ligands can enhance their ability to cross the BBB via RMT or AMT(Lombardo *et al.*, 2020). The size and charge of nanoparticles also play crucial roles in their brain penetration (Figure 44). Smaller nanoparticles tend to cross the BBB and diffuse through the brain more efficiently, whereas larger nanoparticles, if

properly functionalized, can still cross the BBB but to a lesser extent. The optimal particle size is critical for maximizing drug delivery to the brain; larger particles can carry more drug but reach the brain in lower concentrations, while smaller particles carry less drug but reach the brain in higher concentrations (Asimakidou *et al.*, 2024).

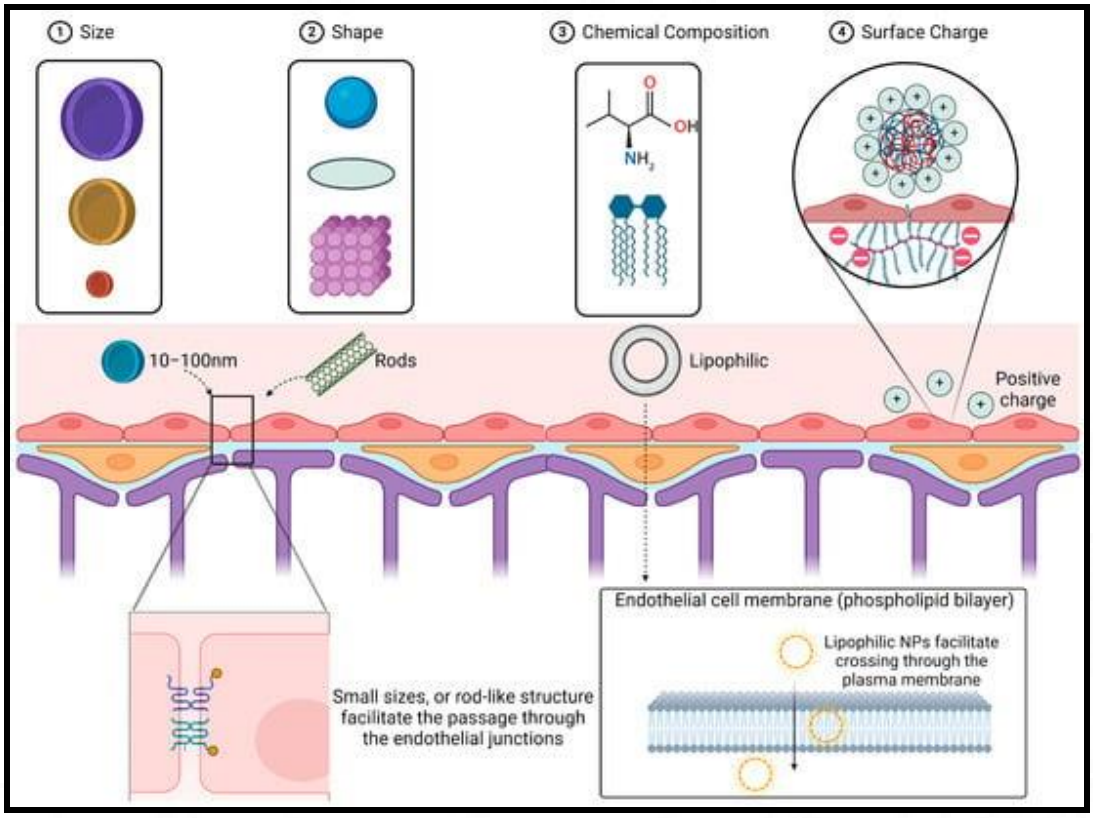

Figure 44. Factors enabling NPs' BBB penetration. Factors influencing NPs' ability to penetrate the BBB. The size, shape, chemical composition, and surface charge are four major factors that affect NPs' BBB penetration capability. The figure reproduced from (Asimakidou *et al.*, 2024).

One of the most promising carriers in this field is AuNCs. Recently, AuNCs have emerged as a promising tool for biomedical imaging due to their distinctive molecular-like characteristics and favorable biocompatibility. Due to quantum confinement effects, these clusters exhibit significant quantization of the conduction

band, allowing them to be energetically regarded as molecules. This results in unique optical properties, such as fluorescence, which arises from electron transitions between different energy levels when exposed to light. AuNCs absorb light in the near-infrared (NIR) range of 650 to 900 nm, making them especially useful for imaging in biological systems. NIR light penetrates tissue better than visible light and is less harmful than X-rays, which is advantageous for medical diagnostics. Furthermore, fluorescent probes emitting in the NIR range experience minimal interference from background fluorescence and light scattering, which enhances their utility in biological imaging (Dan *et al.*, 2022). In addition to their fluorescence, AuNCs are generally more biocompatible, photostable compared to many organic dyes, and feature a large Stokes shift and extended luminescence lifetime. The use of surface-protecting ligands helps stabilize AuNCs, preventing aggregation. These ligands also allow for the tuning of photoluminescent wavelengths by altering the size or surface chemistry of the metal core. Beyond imaging, AuNCs have potential therapeutic applications. By attaching drugs to either the capping ligands or the AuNCs themselves, these systems can assist in therapeutic interventions (S. Liu *et al.*, 2022). These characteristics, combined with their wide therapeutic applications, make AuNCs excellent candidates for BBB penetration. However, there have been limited studies on AuNCs crossing the BBB. For instance, Nair *et al.* reported that glutathione-coated gold clusters with high fluorescence yield could penetrate the BBB for imaging and drug delivery applications (Nair *et al.*, 2017a). These gold clusters were further modified with Levodopa (L-dopa) to exploit the large amino acid transporter 1 (LAT1) pathways to enhance brain entry. The uptake and

permeability of these nanoprobes were demonstrated using an established BBB model (Figure 45).

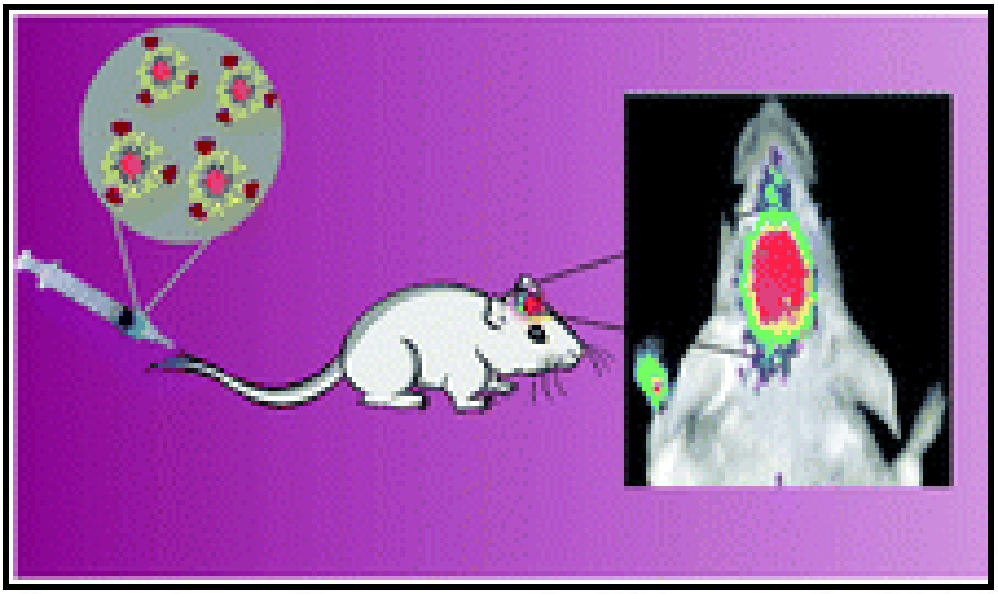

Figure 45. Brain imaging efficacy of glutathione-coated gold clusters *in vivo*. The figure reproduced from (Nair *et al.*, 2017a).

This chapter highlighted that nanoparticle-based biosensors for AD have shown higher detection sensitivity and real-time monitoring capabilities, required less time and reduced costs, thereby alleviating the economic burden on AD patients. Additionally, machine learning holds significant promise for AD prediction. In imaging, nanoparticles with NIR emission can address targeting issues and improve imaging outcomes. For treatment, gold-mediated nanoparticles show great potential in inhibiting Aβ fibrillization and have been reported to cross the BBB, effectively targeting specific areas or acting as nanocarriers to deliver substances to the brain. Therefore, nanotechnologies hold significant promise, and future developments of innovative nanoparticles with high effectiveness and biocompatibility are expected to enhance the early detection and intervention of AD.

CHAPTER 3

MATERIALS AND METHODS

To meet the objectives of this study, we have developed optical and electronic biosensors designed to detect biomarkers associated with mild cognitive impairment, facilitating the early diagnosis of AD. As therapeutics, we synthesized cysteine gold nanoclusters to manage AD. The therapeutic efficacy of these nanoclusters was tested using an AD mice model induced by streptozotocin. This chapter offers an in-depth explanation on the materials and methods adopted for the synthesis of nanostructures, their characterizations, design and development of sensor platforms, and *in vitro* and *in vivo* experiments performed.

3.1 Design and Development of Optical Biosensor

3.1.1 Materials

Gold (III) chloride trihydrate ($HAuCl_4.3H_2O$), Silver nitrate ($AgNO_3$), Chitosan, phosphate-buffered saline (PBS), (3-aminopropyl) triethoxysilane (APTES) (99%) and Bovine serum albumin (BSA) were purchased from Sigma-Aldrich, $A\beta_{40}$ protein, $A\beta_{40}$ antibody, $A\beta_{42}$ protein, $A\beta_{42}$ antibody, phospho T181 (p-Tau) protein, phospho T181(p-Tau) antibody, Total Tau (t-Tau) protein and Total Tau (t-Tau) antibody were purchased from Abcam. Acetic acid, glutaraldehyde (GA), and aluminum substrate (Al) were bought from Merk. All the glassware was cleaned using aqua regia. The water used in all experiments was Millipore Milli Q grade.

3.1.2 Synthesis of chitosan-coated Gold Nanoparticles (Cs-AuNPs)

To synthesize anisotropic- star-shaped gold nanoparticles, a gold/silver solution was prepared by mixing 20 mL of 10 mM aqueous $HAuCl_4$ with 2 mL of 10 mM aqueous

$AgNO_3$ in 1 mL of Milli-Q water. After thorough mixing, 4 mL of 100 mM aqueous ascorbic acid was quickly added, followed by pipetting and shaken for 20 s. The solution's color change from colorless to light blue indicated the successful formation of anisotropic-star-shaped gold nanoparticles. Following that, a 1% (v/v) aqueous chitosan solution was added to the gold nanoparticle solution (Cs-AuNPs). The mixture was then centrifuged and re-dispersed in deionized water for further use.

3.1.3 Fabrication of SERS-based Immunoassay Platform

Aluminium (Al) was used as the base material to prepare the SERS Immunoassay platform. It was first thoroughly rinsed with deionized water and then dried at 120 °C for 1 h under a nitrogen flow. Following the drying process, the samples underwent a chemical treatment with a 1% solution of APTES in toluene, which was evenly applied to the substrate using a spray coating method. The coated samples were then heated in a convection oven at 110 °C for 1 h. This step facilitated surface modification and promoted the formation of strong chemical bonds between the APTES and the aluminum substrate through silanization. Finally, the modified samples were stored in a vacuum for future use.

The silanized Al substrate was immersed in a 5% (w/w) aqueous GA solution at 40 °C for 30 min to introduce terminal aldehyde groups on the surface. Following this, the samples were rinsed with water and then placed in a Cs-AuNPs solution for 24 h, enabling covalent bonding of the nanoparticles to the Al surface. To eliminate unattached nanoparticles, the Cs-AuNPs immobilized Al surface (Cs-AuNPs-Al) was thoroughly washed multiple times using a 1 wt% acetic acid solution. For antibody conjugation, the substrates were treated with a 5% GA solution in deionized water at 40 °C for 3 h and then rinsed several times with PBS. This procedure allowed for the

covalent attachment of the antibodies. The substrates were subsequently immersed in an antibody solution ($A\beta_{42}$ and p-Tau) with varying concentrations ranging from micromolar to attomolar levels for 6 h at 4 °C. Finally, the fabricated substrates were washed multiple times with PBS at pH levels 5, 7.4, and 9 to remove any non-conjugated antibodies. The substrate's ability to detect these concentrations was evaluated by measuring changes in SERS intensity.

3.1.4 Material characterization

The absorbance spectra of the synthesized nanomaterials were recorded using a UV−Vis absorption spectrophotometer (Shimadzu UV-1800) across the wavelength range of 200–800 nm. The water contact angle (WCA) was determined at room temperature by placing a 3 ml drop of deionized water on a glass slide with a micro syringe, and the images were captured using the OCA15 Plus Optical Contact Angle System (Data Physics, Germany). FTIR spectra of each sample were obtained with an Agilent Cary 660 FTIR spectrometer in the range of 4000-400 cm^{-1}. Transmission electron microscopy (TEM) images were taken using a JEOL-JEM0310 microscope at an accelerating voltage of 80 kV to analyze the size and distribution of the particles. A diluted solution was applied to a carbon-coated copper grid (300 mesh) and allowed to dry at room temperature. The morphology of gold nanoparticles on Al surfaces was examined using scanning electron microscopy (SEM) with a KYKY Instruments SEM 70 EM3200 from China. To quantify the trace amount of gold and silver, Inductively Coupled Plasma Mass Spectrometry (ICP-MS) (iCAP Q, Thermo Fisher) were used. The Raman spectra were collected in a standard laboratory environment using an alpha 300RA Confocal Raman spectrometer (WITec, Germany) equipped with a 532 nm laser. A 20X objective lens focused the laser onto

the sample, producing a 1 µm spot size and delivering approximately 10 mW power. Each Raman spectrum was acquired with an integration time of 1 s to prevent potential sample damage.

3.1.5 Blood plasma collection and processing

We collected plasma samples from 75 participants recruited from the Neurology Department of Sree Chitra Tirunal Institute for Medical Science and Technology (SCTIMST), Thiruvananthapuram. This study was approved by the Institutional Ethics Committee of SCTIMST (Order no: SCT/IEC/IEC-1669/DECEMBER-2020). Participants were divided into three groups: AD patients (n = 25), MCI patients (n = 25), and healthy controls (C) (n = 25). Clinical diagnoses for AD and MCI patients were established by a trained neurologist after a careful review of their medical histories. Healthy controls were age-matched volunteers, typically spouses of the patients, who were in good health without any active major diseases, neurological disorders, or psychiatric conditions. They shared similar ethnic, socioeconomic, and environmental backgrounds, including age, diet, and lifestyle factors. Participants with pre-existing comorbidities such as diabetes, cardiovascular diseases, or infections were excluded to minimize potential confounding factors. Blood samples were collected using EDTA tubes and centrifuged at 4000 rpm at 24°C for 15 min within approximately 2 h of collection. Plasma was then aliquoted and stored at -80°C until further analysis.

A general summary of the demographic information for the study subjects is presented in Table 1.

Table 1. Demographic details of subjects involved in the SERS-AI platform

	AD (n=25)	MCI (n=25)	C (n=25)
Age in year ± STD	**69 ± 7**	**69 ± 8**	**63 ± 6**
Male	**12**	**17**	**12**
Female	**13**	**8**	**13**

3.1.6 AD biomarkers detection in clinical samples

To detect AD biomarkers in patient blood plasma samples using SERS analysis, antibodies-conjugated ($A\beta_{42}$, $A\beta_{40}$, p-Tau, and t-Tau) Al-SERS platform were utilized. Blood plasma samples from AD, MCI, and control groups were incubated with these platforms to measure the levels of composite biomarkers ($A\beta_{42}$, $A\beta_{40}$, p-Tau, and t-Tau). Initially, the blood samples were incubated for 30 min in a controlled vapor atmosphere with 10% ethanol to prevent the coffee ring effect. Subsequently, further incubation at room temperature continued for another 30 min. Following this incubation period, the platforms were used for SERS analysis to identify AD biomarkers.

3.1.7 Data Pre-processing and Analysis

The Raman spectra were subjected to baseline correction using WITec Project Plus 5 software, focusing on the 500 to 2000 cm^{-1} range. Subsequently, normalization was performed based on the intensity measured at 1000 cm^{-1}. These pre-processed datasets served as input variables for various multivariate analyses. Additionally,

intensity values corresponding to spectra were extracted for ratiometric and machine-learning analyses. The statistical significance of normalized spectral intensity values was assessed using T-tests conducted in SPSS-17 (SPSS Inc., Chicago, Illinois).

3.1.8 Artificial Neural Network (ANN) for Classification of SERS Data

We have used ANN-based algorithms, an important branch of Artificial Intelligence, for the study. These algorithms can identify patterns indicative of specific diseases or predict the likelihood of disease progression, helping clinicians make informed decisions about patient care. To conduct an effective study, we have used Multi-Layer Perceptron (MLP), Support Vector Machine (SVM), and Radial Basis Function (RBF) algorithms.

3.1.8.1 Multi-Layer Perceptron (MLP)

MLP is an important class of ANN. It consists of multiple layers of nodes called neurons, arranged in a feedforward manner. The last node of each layer connects with the subsequent layer, forming a fully connected network. For the present study, we used an MLP with a backpropagation algorithm to conduct the training and testing of the data. Classification is done as a two-class problem, where intensity values representing four biomarkers for AD vs. MCI, AD vs. Control, and Control vs. MCI were employed. During training, the network adjusts the weights and biases of the connections between neurons to minimize the difference between the actual and desired outputs. 70% of the data obtained from biomarkers is used for training, and the remaining 30% is used for testing and validation.

3.1.8.2 Support Vector Machine (SVM)

SVM is another vital class of machine learning models. It aims to find the optimal hyperplane that separates the two classes in the feature space. SVM uses the kernel

function to transform the input data into a higher-dimensional space where it can be linearly separated. The linear kernel function is used to transform the input data into high-dimensional spaces. The model is designed to train on 70% of the data, with 30% allocated for testing and validation purposes. The models are trained and evaluated for the present study and are used to predict the class labels of new, unseen data

3.1.8.3 Radial Basis Function Network (RBF)

An RBF Network is another important type of ANN that follows a three-layer network model: an input layer, a hidden layer, and an output layer. Each hidden node uses a Radial Basis Function (RBF). Each hidden unit calculates its output based on the distance between the input vector and its center using a radial basis function. The K-means clustering algorithm is used to cluster the input data, and thus, the center is chosen. The widths of the RBF units and the weights connecting the hidden layer to the output layer are adjusted during training using the gradient descent function. As mentioned in the previous session, 70% of the data is used for training and 30% of the data is used for testing and validation.

Dimensionality reduction was initially performed on high-dimensional spectral datasets (500 to 2000 cm^{-1}) using these machine learning algorithms. These algorithms were employed to classify AD, MCI, and control groups based on SERS spectra. Spectroscopically significant band intensities were used as input variables for these machine-learning models. Evaluation of the SERS-based detection model included assessing Accuracy, Sensitivity (true-positive rate), and Specificity (true-negative rate), which were calculated using equations derived from the confusion matrix.

$$\text{Sensitivity} = \frac{TP}{TP+FN}$$

$$\text{Accuracy} = \frac{TP+TN}{TP+TN+FP+FN}$$

$$\text{Specificity} = \frac{TN}{TN+FP}$$

Where TP=True Positive; TN=True Negative; FP=False Positive; FN=False Negative.

3.2 Design and Development of Electronic Biosensor

3.2.1 Materials

$HAuCl_4.3H_2O$, Chitosan, PBS, APTES (99%), sulphuric acid (H_2SO_4), 30% hydrogen peroxide (H_2O2), acetic acid, and GA and microscopic glass slides were purchased from Sigma-Aldrich. $A\beta_{40}$ protein, $A\beta_{40}$ antibody, $A\beta_{42}$ protein, $A\beta_{42}$ antibody, phospho T181(p-Tau) protein, phospho T181(p-Tau) antibody, Total Tau(t-Tau) protein, and Total Tau (t-Tau) antibody were acquired from Abcam. All glasswares were cleaned using aqua regia, and Millipore Milli Q grade water was used throughout all experiments.

3.2.2 Scanning Tunneling Microscopy (STM) Analysis of $A\beta_{42}$ and p-Tau Proteins

Lyophilized $A\beta_{42}$ and p-Tau proteins were reconstituted in 100 µL of PBS solution (pH 7.4) to achieve concentrations of 32 µM and 54 µM, respectively. A 10 µL aliquot of each protein solution was then deposited onto a freshly cleaved Highly Oriented Pyrolytic Graphite (HOPG) surface, which was mounted on the gold stub of the STM. After allowing the sample to incubate for 20 min to ensure thorough drying

and the elimination of water molecules. STM tips made from polycrystalline platinum-iridium wire were mechanically cut at an angle to the wire axis. Images were captured using constant current mode with a sample bias of -0.5 V and a tunneling current of 0.5 nA.

3.2.3 Scanning Tunneling Spectroscopy (STS) Analysis of $A\beta_{42}$ and p-Tau Proteins

In addition to the topographic images of $A\beta_{42}$ and p-Tau, STS offers insights into the local density of states (LDOS) of materials, allowing for localized study of electronic properties of $A\beta_{42}$ and p-Tau proteins. The measurements were conducted with an initial bias of -0.5 V and a tunnelling current of 0.5 nA. To examine the conduction and valence band states locally, dI/dV spectra were recorded using lock-in amplifier.

3.2.4 Synthesis of Gold nanoparticles (AuNPs)

For the synthesis of gold nanoparticles, a 10 mM aqueous solution of $HAuCl_4.3H_2O$ (1 mmol/L) was combined with 50 mg of chitosan in 5 ml of water. This mixture was stirred at 65 °C for 2 h until it turned purple, indicating the formation of gold nanoparticles. Afterward, the reaction was allowed to cool to 25 °C while being continuously stirred overnight. The resulting AuNPs were then purified via centrifugation and diluted with deionized water.

3.2.5 Fabrication of the Interdigitated Electrode (IDE) platform

To fabricate the IDE, microscopic glass slides were used as substrates. These glass slides were cut into 5cm x 5cm pieces and thoroughly cleaned with acetone, ethanol,

and deionized water. After cleaning, they were dried at 120 °C under a nitrogen flow for 1 h. The cleaned glass was then immersed in a piranha solution (a mixture of 7 parts H_2SO_4 and 3 parts 30% H_2O_2) at 80 °C for 30 min. Following this, the glass was rinsed four times with deionized water under sonication and immediately dried at 120 °C under nitrogen flow for 2 h. Next, the dried slides were immersed in a 1% APTES solution in toluene for 30 min at room temperature (25 °C). Gold film deposition was carried out using a thermal evaporator system at a pressure of approximately 10^{-6} Torr. The resulting interdigitated gold finger electrodes had a standardized width of 300 μm with a 300 μm gap between the fingers in the active area. Then, silanized IDE slides were treated with a 5% GA solution for 30 min at 40°C. The slides were then rinsed with water and dried. The overall dimensions of the IDE platform were 5 mm x 15 mm.

3.5.6 Surface Functionalization on IDE platform

To prepare the active layer, the slides were treated with AuNPs solution for 3 h. Subsequently, the AuNPs-immobilized IDE slides were washed with acetic acid (1 wt%) to remove non-absorbed nanoparticles. Then slides were treated with a 5% GA solution in deionized water at 40°C for 2 h, creating an aldehyde-activated surface. PBS was used to thoroughly wash away any unbound molecules. Next, 10μL of antibody solutions ($A\beta_{42}$ and p-Tau) were drop-cast onto the devices and incubated at 4°C for 3 h. After incubation, the samples were washed multiple times with PBS at pH levels 5, 7.4, and 9 to remove unbound antibodies and prevent the aggregation of antibodies on the sensor surface.

3.5.7 IDE-Based Immunoassay Platform for $A\beta_{42}$ and p-Tau Detection

IDEs were functionalized with $A\beta_{42}$ and p-Tau antibodies, targeting specific AD biomarkers, $A\beta_{42}$ and p-Tau antigens. These modified electrodes were tested using protein solutions with biomarker concentrations varying from micromolar to femtomolar levels. The effectiveness of the substrate in detecting these concentrations was assessed by observing changes in current. To detect the concentrations of antigens ($A\beta_{42}$ and p-Tau), a voltage of 1 V was applied across the two electrodes of the IDE. The resulting current flowing through the devices was recorded. The electrical current at various stages of device fabrication was measured using an Agilent B2900A source measurement unit.

3.5.8 Development of Portable Sensor Readout Circuit

A basic readout circuit was constructed utilizing electronic biosensor was assembled using a microcontroller circuit, LCD, and a potentiometer. To measure the current, a voltage drop induce across the biosensor (V), measuring the resistance (R), and finding the current, I as V/R. Our biosensors required a potential of 1 V across them to operate. To achieve this, a voltage divider circuit was used to ensure a 1 V drop across the biosensors.

3.5.9 Material Characterization

The Fourier-transform infrared (FTIR) spectra of the functionalized samples were obtained using an Agilent Cary 660 FTIR spectrometer, covering the wavelength range of 4000 to 400 cm^{-1}. The surface topography and electronic states of $A\beta_{42}$ and p-Tau on HOPG were analyzed using STM and STS with a nanoREV STM by

Quazar Technology, operating in constant current mode. The isoelectric point of $A\beta_{42}$ and p-Tau antigens were measured by Malvern Nano ZS instrument. Electrical measurements were conducted using an Agilent B2900A source measurement unit.

3.5.10 Blood Plasma Collection and Processing

Plasma samples were collected from 24 participants from the Neurology Department at SCTIMST in Thiruvananthapuram. This research was approved by the Institutional Ethics Committee of SCTIMST (Order no: SCT/IEC/IEC-1669/DECEMBER-2020). The participants were categorized into three groups: patients with Alzheimer's disease (AD) (n = 8), patients with Mild Cognitive Impairment (MCI) (n = 8), and healthy controls (C) (n = 8). Clinical diagnoses for AD and MCI were made by a neurologist after thoroughly reviewing the patients' medical histories. Healthy controls were age-matched volunteers, usually the patients' spouses, who were in good general health without major diseases, neurological disorders, or psychiatric conditions. They shared similar ethnic, socioeconomic, and environmental backgrounds, including age, diet, and lifestyle. To avoid confounding factors, participants with comorbidities such as diabetes, cardiovascular diseases, or infections were excluded.

Blood samples were collected in EDTA tubes, centrifuged at 4000 rpm for 15 min at 24°C within approximately 2 h of collection. The plasma was then aliquoted and stored at -80°C until further analysis.

A general summary of the demographic information for the study subjects is presented in Table 2.

Table 2. Demographic details of subjects involved in the IDE platform

	AD (n=8)	MCI (n=8)	C (n=8)
Age in year ± STD	**67 ± 5**	**68 ± 7**	**62 ± 7**
Male	**3**	**4**	**4**
Female	**5**	**4**	**4**

3.5.11 IDE Sensing of AD biomarkers in blood plasma samples

To detect biomarkers of AD in blood plasma samples, the $A\beta_{42}$, $A\beta_{40}$, p-Tau, and t-Tau antibodies-conjugated IDE platforms were utilized to assess levels of composite biomarkers including $A\beta_{42}$, $A\beta_{40}$, p-Tau, and t-Tau in plasma samples from AD, MCI and control groups. Initially, the plasma samples underwent a 30-min incubation in a controlled vapour atmosphere containing 10% ethanol to prevent the coffee ring effect. Subsequent incubation at room temperature continued for an additional 30 min. Following these incubation periods, the substrates were utilized for electrical measurements to identify AD biomarkers.

3.3 Development of cysteine gold nanocluster for blood brain barrier (BBB) imaging

3.3.1 Materials

$HAuCl_4.3H_2O$, Levodopa, MTT, Hoechst, 1-Ethyl-3-(3-dimethylaminopropyl) carbodiimide (EDC), N-Hydroxysuccinimide (NHS), 1,3-Diphenylisobenzofuran

(DPBF), Streptozotocin (STZ), ketamine and xylazine were purchased from Sigma and L-Cysteine hydrochloride (98%) was obtained from Alfa Aesar. bEnd.3 (brain endothelial cells) cells and astrocytes were purchased from ATCC. DMEM, Fetal Bovine Serum (FBS), and streptomycin were obtained from Himedia. $A\beta_{42}$ peptide was purchased from Abcam. All the glassware was cleaned using aqua regia. The water used in all experiments was Millipore Milli Q grade.

3.3.2 Synthesis of Cysteine Gold Nanoclusters (Cy-AuNCs)

In this study, we present a single-step method to synthesize fluorescent gold nanoclusters from $HAuCl_4$ using L-Cysteine as a reducing agent in an aqueous solution. The process begins by dissolving cysteine in de-ionized water to achieve a final concentration of 10 mg/mL. Subsequently, 0.5 mL of $HAuCl_4$ solution (0.5 mM) is added. The mixture is thoroughly shaken and then exposed to low microwave (MW) radiation (0.099 W/cm^2) for 60 s. Afterward, the Cy-AuNCs solution is allowed to cool, followed by purification through centrifugation at 10,000 rpm for 15 min, after which the pellet is collected.

3.3.3 Determination of singlet oxygen efficiency of Cy-AuNCs

1,3-Diphenylisobenzofuran (DPBF) served as the test dye to investigate the production of ROS by Cy-AuNCs. A volume of 50 µL of AuC (1 mg/mL) was introduced into a 3 mL solution of DPBF, followed by irradiation for 60 s using a 532 nm laser at a power density of 0.3 W/cm^2. The decrease in DPBF absorbance at 407 nm was monitored at specified time points.

3.3.4 Conjugation of Levodopa to Cy-AuNCs (AuCs-LD)

5 mg synthesized Cy-AuNCs were dissolved in 5 mL of deionized water. Then, 0.05 M EDC was added, the pH was adjusted to 4, and the solution was stirred for 2 h.

Subsequently, 0.05 M NHS was introduced, followed by the addition of 5 mL of 2 mM L-dopa in a basic pH solution. The final pH was adjusted to 9, and the reaction mixture was allowed to proceed for an additional 12 h. The AuCs-LD was then centrifuged at 15,000 rpm for 15 min in a 1:1 methanol-isopropanol mixture and washed twice with deionized water to eliminate any excess unreacted ligands.

3.3.5 Development of *in vitro* BBB Model

In this study, we established an *in vitro* BBB model using a co-culture of bEnd.3 cells and astrocytes. To create the BBB models, transwell inserts were positioned in a 12-well culture plate, and DMEM growth medium was added to the basolateral side of each well until the membranes in the inserts were fully moistened. bEnd.3 cells were then seeded onto the luminal surface of the membrane at a density of 2×10^5 cells per well, while astrocytes were seeded on the abluminal side at a density of 1×10^4 cells per well. Both cell types were cultured in DMEM growth medium supplemented with 10% FBS and maintained at 37°C in a humidified incubator with 5% CO_2.

3.3.6 *In vitro* cytotoxicity study

The MTT assay is utilized to measure both the quantity and viability of live cells and their mitochondrial activity. This assay depends on the capability of metabolically active fibroblast cells to transform the yellow, water-soluble tetrazolium salt (MTT) into purple formazan crystals through the action of the mitochondrial enzyme succinate dehydrogenase. The intensity of the purple color produced is directly proportional to the number of viable cells.

For the experiment, L929 mouse fibroblast cells were seeded in a 96-well tissue culture plate at a density of 5×10^3 cells per well in 100 µL of DMEM

containing 10% FBS to assess cell viability. Upon reaching 40-50% confluency, the cells were exposed to varying concentrations of Cy-AuNCs and AuCs-LD (10, 20, 40, 80, 160 µg/mL). After 24 h, the medium was removed and the wells were washed with phosphate-buffered saline. Subsequently, 100 µL of MTT (5 mg/mL) was added to each well. Following a 3-h incubation at 37°C, 100 µL of DMSO was added to each well. The plates were then incubated at room temperature for 30 min to ensure cell lysis. The absorbance of the resulting solution was immediately measured at 570 nm using an automated microplate reader. Cells treated with MTT solution without any materials served as controls. The percentage of viability was calculated as follows.

$$\% \text{ Cell Viability} = ([\text{Abs}] \text{ sample} / [\text{Abs}] \text{ Control}) \times 100.$$

3.3.7 Material Characterizations

UV-Vis absorption spectra were obtained using a Shimadzu UV-1800 spectrophotometer. Fluorescence measurements were conducted with a Fluoro Max spectrofluorometer from Horiba Instruments. FT-IR spectroscopy was performed using an Agilent Cary 660 FTIR spectrometer with a KBr pellet. High-resolution transmission electron microscopy (HRTEM) images were captured on a JEOL-JEM0310 microscope at an accelerating voltage of 80 kV to analyze particle size and distribution. Energy-dispersive X-ray spectroscopy (EDAX) analyses were done with the same microscope. For sample preparation, a diluted solution was placed on a carbon-coated copper grid (300 mesh) and allowed to dry at room temperature. Zeta potential measurements were performed with a Malvern Nano ZS instrument. Matrix Assisted Laser Deposition Mass Spectroscopy (MALDI) was recorded using the Bruker Daltonics flexAnalysis (ATS-00720-autoflexTOF/TOF) instrument. The X-ray

photoelectron spectroscopic data are recorded on an Omicron Nanotechnology X-ray photoelectron spectrometer (XPS) with an Al Kα = 280.00 eV excitation source. The binding energies of the core levels were calibrated with C 1s binding energy (BE) set at 284.0 eV. The quantum yield (QY) of fluorescent AuC was measured using Rhodamine 6G as a standard reference (QY: 95% in ethanol). Fluorescence lifetime measurements were performed using a Fluoro Max-4C Spectrofluorometer (Horiba Instruments, USA) and the time-correlated single-photon counting (TCSPC) technique with an excitation wavelength of 344 nm. *In vitro* fluorescence experiments were performed using an inverted fluorescence microscope (IX83; Olympus Corp., Tokyo,Japan) with a cooled CCD camera (XM10, monochrome, Olympus). Cyclic voltammetry (CV) was measured in a three-electrode system such as glassy carbon and platinum wire used as a working electrode, counter electrode and Ag/AgCl as a reference electrode and 0.1 M KCl solution as the supporting electrolyte. The CD spectra were obtained using a Jasco J-1500 spectropolarimeter (Jasco Co. Ltd., Tokyo, Japan). To quantify the trace amount of gold in the brain tissue, ICP-OES (5110 ICPOES,Agilent,USA) were used. In-vitro fluorescence experiments were executed using an Olympus IX83 inverted fluorescence microscope equipped with a cooled XM10 monochrome CCD camera. *In-vivo* and *ex-vivo* animal imaging was conducted with the Xenogen IVIS Spectrum live animal optical imaging system.

3.3.8 Barrier potential measurement in bEnd.3 cell

To evaluate membrane integrity, Trans epithelial/trans endothelial electrical resistance (TEER) was measured, a widely recognized quantitative method for assessing the integrity of tight junction dynamics in cell culture models of

endothelial and epithelial monolayers. Endothelial cells and astrocytes were cultured on a transwell membrane with a 0.4-micron pore size (Millipore) placed in a 12-well cell culture plate. The integrity of the formed endothelial barrier and tight junctions was assessed by measuring the TEER of the cells using an EVOM2-Epithelial Voltammeter. The TEER value was calculated using the formula

TEER (Ω x cm^2) = [(relative resistance of experimental wells - relative resistance of blank wells) x Membrane Surface Area (cm^2)](Srinivasan *et al.*, 2015)

Barrier potential measurement of each material was done in triplicate. A cell without material served as a control.

3.3.9 BBB permeability assay

To evaluate the BBB permeability of the material, 100 µL of 40 µg/mL Cy-AuNCs and AuCs-LD were added to the media in 12-well plates. Samples were then collected at various intervals, specifically at 1 , 2, 3, 6, and 24 h. The quantity of nanoparticles in the collected media was determined spectrometrically using a calibration curve. Millicell inserts without bEnd.3 cells were used as controls.

3.3.10 *In vitro* cellular uptake

To assess the cellular uptake efficiency of Cy-AuNCs and AuCs-LD, which exhibit inherent fluorescence, we used fluorescence microscopy on bEnd.3 cells. The cells were cultured on a coverslip with a seeding density of 1 x 10^5 cells per well. Once a complete monolayer was established, 40 µg/mL of Cy-AuNCs and AuCs-LD were added to separate wells. After an incubation period of 3 h, the cells were rinsed with PBS. For the fluorescence microscopy analysis, the cell nuclei were stained with Hoechst33342 according to the manufacturer's instructions, followed by another PBS

wash. The samples were then observed under a fluorescence microscope. Cells without added materials were considered as control.

3.3.11 Molecular docking study

To investigate the molecular interactions between Aβ and Cy-AuNCs, molecular docking studies were performed using the Patch Dock server. Following this, the interactions between Aβ and Cy-AuNCs were examined. The structure of $A\beta_{42}$ monomers was sourced from PubChem. After docking, the results were filtered based on their energy values, and the chosen pose cluster was analyzed using the BIOVIA Discovery Studio Visualizer.

3.3.12 Preparation of Aβ fibrils

To prepare Aβ fibrils, 1 mg of lyophilized amyloid $A\beta_{42}$ peptide powder was dissolved in 100 µL of 10 mM NaOH. The mixture was then vortexed at room temperature for 1 min at a moderate speed. Subsequently, the solution was diluted with PBS to achieve a concentration of 1 mg/mL. The diluted peptides were incubated in PBS (pH 7.4) at 37°C overnight to form Aβ fibrils.

3.3.13 Aβ Fibrillization kinetics

The kinetics of Aβ fibrillization was analyzed using the Thioflavin T (ThT) assay, a standard method for assessing $A\beta_{42}$ peptide activity. ThT fluorescence increases upon binding to Aβ fibrils, allowing for real-time kinetics assessment. $A\beta_{42}$ solution (100 µL) was mixed with a 1µM ThT solution to initiate the experiment. Fluorescence emissions were measured at an excitation wavelength of 440 nm, corresponding to ThT's peak absorption. The growth of $A\beta_{42}$ fibrils followed three distinct phases: lag, growth, and steady phases.

3.3.14 Inhibition of Aβ Fibrillization by Cy-AuNCs

To check the Cy-AuNCs' potential inhibition of Aβ fibrils, samples were prepared both with and without incubation of the Cy-AuNCs (20,40 and 60 µg/mL) with Aβ. These samples were then stained with ThT and examined using fluorescence microscopy for detailed analysis and imaging.

3.3.15 Circular dichroism (CD) studies

Circular dichroism (CD) studies were conducted to examine the inhibitory effect of Cy-AuNCs on $A\beta_{42}$ fibril formation. For the measurements, a 300-µL sample was placed in a quartz cuvette with a 1 mm path length. The experimental conditions were as follows: scan range from 190 to 260 nm, scan speed of 500 nm/min, and a bandwidth of 1 nm.

3.3.16 Inhibition of Aβ Fibrillization *in vitro*

To investigate how Cy-AuNCs affect the prevention of Aβ fibrillization *in vitro,* using Neuro-2a (N2A) mouse neuroblastoma cells treated with streptozotocin (STZ). Both treated and untreated cells were evaluated using a live/dead assay (using live/dead assay kit) to measure cell viability, with images taken 24 h after treatment.

3.3.17 *In-vivo* imaging

The Cy-AuNCs' ability to penetrate the BBB was assessed *in vivo* using a mouse model. All experimental procedures were approved by the Institute Animal Ethics Committee (IAEC approval No- SCT/IAEC-399/MARCH/2021/109). Swiss albino mice weighing between 25-40g were divided into three groups: control, Cy-AuNCs injected, and AuCs-LD injected. Prior to the experiment, mice were anesthetized with ketamine-xylazine (100mg/kg Ketamine and 16mg/kg Xylazine) and their fur was removed. On the day of the experiment, Cy-AuNCs (20mg/kg) and AuCs-LD

(20mg/kg) were intravenously administered to respective groups without further anesthesia. Control mice received no treatment. Immediately before imaging, all animals were anesthetized again. Imaging was performed at 1h and 4h post-injection using an *in vivo* Imaging Spectrum (IVIS Spectrum) to assess nanocluster distribution within the body. Post-imaging, mice were euthanized, and their organs were collected and imaged to evaluate nanocluster accumulation and distribution.

3.4 The therapeutic potential of gold nanocluster in Streptozotocin (STZ) induced AD animal model

3.4.1 Materials

$HAuCl_4.3H_2O$, Levodopa, EDC, NHS, STZ, ketamine, xylazine, hematoxylin, eosin and Thioflavin-S were purchased from Sigma. L-Cysteine hydrochloride (98%) was obtained from Alfa Aesar. The anti-beta amyloid 1-42 antibody, and anti-68kDa Neurofilament/NF-L antibody were procured from Abcam. DPX mounting medium was purchased from Leica CV Ultra. All the glassware was cleaned using aqua The water used in all experiments was Millipore Milli Q grade.

3.4.2 Development of STZ-induced AD Animal model

To develop an AD animal model induced by streptozotocin (STZ), Swiss albino mice weighing 25-40 grams were allocated into four groups (n=3 per group) following established protocols (Paxinos and Franklin, 2001). The mice underwent intracerebroventricular (ICV) injection into the lateral ventricle under ketamine (50 mg/kg) and xylazine (10 mg/kg) anesthesia in a sterile environment. Each mouse was positioned on a Kopf stereotaxic apparatus, and a midline scalp incision was made. A burr hole was drilled unilaterally on the right side at coordinates AP: -0.8, L: 0.5 mm

from bregma using a 0.1 mm tip micromotor drill. A custom microinjector cannula was inserted to a depth of 3 mm, and STZ was slowly injected at a rate of 3 µL/min via a Hamilton syringe connected by a microtube. After injection, the burr hole was sealed with bone wax, and the incision was sutured. Post-operative care included antibiotic and analgesic administration.

3.4.3 Behavioural Assessments

3.4.3.1 Spontaneous Alternation Test (Y-maze assay)

The evaluation of working memory was conducted using the Y-maze spontaneous alternation test. The Y-maze consists of three horizontal arms (each 40 cm long, 3 cm wide, and with walls 12 cm high). Each mouse was initially placed in one arm (A), and their sequence of arm entries (e.g., ABCACB, where letters denote arm codes) and the total number of arm entries were recorded over 5 min. To assess alternation, a sequence was defined as entries into all three arms consecutively (e.g., ABC, BAC, or CBA) without repetition. The percentage of alternation was determined using the following formula:

% Alternation = (Number of alternations) / (Total number of arm entries – 2) x 100 (Kraeuter, Guest and Sarnyai, 2019).

3.4.3.2 Novel Arm Test (Y-maze assay)

Spatial memory evaluation utilized the Y-maze Novel Arm Test. In this test, one arm of the maze (referred to as arm C) was temporarily closed by a removable door. Mice were then released into the remaining arms (A and B) to explore freely, while their movements were recorded using a digital camera over 15 min. 1 h later, the door was removed, and the procedure was repeated, recording their movements for 5 min. The

frequency of entries into the novel arm (C) was compared against entries into the other arms to assess spatial memory retention.

3.4.3.3 Open Field Test (OFT)

The Open Field Test (OFT) evaluates both locomotor activity and anxiety-related behaviors in rodents. The test took place inside a wooden container measuring 30×30×15cm, segmented into nine identical squares. Animals were individually placed in a grid-lined box and their movements were tracked. Locomotor activity was measured by counting the grid squares crossed with all four paws, while exploratory behaviors were assessed based on entries into the center of the box.

3.4.3.4 Novel Object Recognition Test (NOR)

The NOB was conducted using an open-field apparatus. Plastic objects of various shapes, made solely from primary colors, were positioned at the center of the apparatus. A day before the introduction of these objects, each animal underwent a 5-min habituation session without any objects present. After 24 h, the animals were placed in the center of the apparatus, now containing two identical objects, for a 5-min training phase. Following another 24 h, one of the objects was replaced with another of a different shape and color, and the animals' exploration of both objects was recorded for 5 min to assess short-term memory through the calculation of exploration time with novel object. The discrimination index was calculated using the formula

Discrimination index = Exploration time with novel object / (Exploration time with object 1 + novel object ×100) (Hashmi, Yaqinuddin and Ahmed, 2015)

3.4.4 Histomorphological evaluation

Coronal sections of the mouse brain at the middle of the protrusion of pons were taken according to the RENI guidelines (Ruehl-Fehlert *et al.*, 2003). The anterior part was preserved in Carnoy's fixative and used for immunohistochemistry (IHC) and immunofluorescence staining. The posterior part was preserved in 10% neutral buffered formalin and used for hematoxylin and eosin staining (H&E), and thioflavin S staining. The samples were processed with isopropanol and xylene in a tissue processor (Leica TP1020). The processed tissues were sectioned at a thickness of 4μm using a semi-automated microtome (Leica RM 2255). Images were captured at 10x and 40x magnifications to evaluate the morphological changes associated with the induction of AD by streptozotocin.

3.4.4.1 Hematoxylin and eosin staining

The tissue sections in the slides were deparaffinized in xylene and hydrated using ascending grades of isopropanol and water. It was stained with hematoxylin solution for 20 min, washed in running water for 5 min, differentiated in 1% acid alcohol with a dip, and washed in running tap water. The slides were then treated with ammonia water for bluing. After rinsing with water, sections were stained with eosin solution for 2.5 min. The slides were then dehydrated in isopropanol, cleared in xylene, and mounted using DPX mounting medium.

3.4.4.2 Thioflavin-S (ThS) staining

The tissue sections in the slides were deparaffinized in xylene and hydrated using ascending grades of isopropanol and water. The slides were then stained with 1%

ThS for 30–60 min. The slides were then dehydrated in isopropanol, cleared in xylene, and mounted using DPX mounting medium. The slides were then examined under a fluorescence microscope (IX83, Olympus Corp.). The student t-test is used to differentiate between the groups.

3.4.4.3 Immunohistochemistry (IHC) for Neurofilament Light Chain (NFL)

The NFL was detected by immunohistochemistry using Super Sensitive^{TM} Polymer-HRP IHC Detection System (BioGenex, USA cat no: QD430-XAKE) and counterstained with Harris's hematoxylin. The antibody dilution of 1:400 against NFL was performed. Briefly, the slides were deparaffinized in xylene and hydrated using ascending grades of isopropanol and water. The slides were then heated for 1 h in citrate buffer for antigen retrieval and allowed to cool. Then incubated for five min with 10% hydrogen peroxide and incubated for 30 min with 1% bovine serum albumin. The slides were then washed with 1X PBS and the primary antibody was added and incubated for 1 h. After the incubation, super enhancer from the kit was added and allowed to incubate for 30 min. The slides were then stained with Wiegert's hematoxylin, and chromogen 3,3'-diaminobenzidine was added and incubated for 5 min. The sections were then dehydrated, cleared, and mounted using a mounting media (Leica CV Ultra). The slides were allowed to dry and observed under a bright field microscope (Olympus BX51) and images were captured using a camera (DP71) attached to the microscope at 10x and 40x magnifications. The student t-test is used to differentiate between the groups.

3.4.4.4 Immunofluorescence of $A\beta_{42}$

The $A\beta_{42}$ was detected by immunofluorescence with antibody dilution 1:400. Briefly, the slides were deparaffinized in xylene and hydrated using ascending grades of isopropanol and water. The slides were then heated for 1 h in citrate buffer for antigen retrieval and allowed to cool. Then, the slides were incubated for 30 min with 1% bovine serum albumin. The primary antibody was added and incubated for 2 h, and the slides were then incubated for 2 h with the secondary antibody. The slides were then washed with 1X PBS and mounted using fluorescent mounting media.

Chapter 4

Results and Discussion

Accurate and early disease detection is crucial for improving patient care, but traditional diagnostic methods often fail to identify diseases in their early stages, leading to poor treatment outcomes. Recent advancements in nanoscience and nanotechnology have led to the development of advanced systems, characterized by their complex nanostructures and unique chemical compositions that provide distinct physical properties. Nanotechnology shows great promise in neurodegenerative diseases like AD, where early detection and effective treatment are crucial. This chapter covers the synthesis, detailed characterization, and evaluation of the nanoprobes, which include their physico-chemical properties, bio-sensing, bio-imaging and therapeutic potential. The first section describes the design of an optical biosensor for precise and ultrasensitive detection of AD biomarkers from human blood samples. The second section discusses the development of an electronic biosensor for the same purpose. The third section focuses on developing atomically precise gold nanoclusters (AuNCs) that possess real-time optical imaging capabilities and can cross BBB. Additionally, these clusters have the ability to inhibit/disintegrate Aβ fibrillization, presenting a therapeutic approach to enhance Alzheimer's disease (AD) treatment and management. The fourth section explores the therapeutic potential of the AuNCs *in vivo*, in a streptozotocin (STZ)-induced AD animal model.

4.1 Design and Development of Optical Biosensor

At present, the clinical diagnosis of AD heavily relies on neuropsychological assessments and neuroimaging techniques. However, the precision of cognitive evaluations is limited, and the expense associated with brain imaging is substantial, leading to delayed/improper diagnoses for numerous AD patients. Given the absence of therapeutic options capable of arresting or reversing AD advancement, early identification of AD biomarkers is pivotal for optimizing available drug treatments.

In recent years, nanoscience and spectroscopy for disease detection and diagnosis have rapidly advanced and expanded. This is attributed to the distinct optical properties of nanoparticles with specific shapes and structures, along with the strong analytical capabilities of spectroscopic detection methods (Jibin *et al.*, 2021; Chauhan *et al.*, 2023). SERS has gathered significant attention in biological and medical research as an exceptionally sensitive spectroscopic detection technique. This is because it offers ultra-high sensitivity, enables non-invasive biomolecule detection, provides unique fingerprint information about biomolecules, resists photobleaching and photodegradation, and exhibits low interference in water(Liu *et al.*, 2020; H. Liu *et al.*, 2022; Elsheikh *et al.*, 2024). We introduce an immunoassay-based SERS platform for the quantitative analysis of AD biomarkers ($A\beta_{40}$, $A\beta_{42}$, p-Tau, and t-Tau). This platform is built using spiky star-shaped chitosan-coated gold nanoparticles. Anisotropic gold nanoparticle-based SERS probes generate reproducible and strong local electric fields. This facilitates the plasmon coupling effect, thereby amplifying the Raman signal (Kohout, Santi and Polito, 2018; Tim, Błaszkiewicz and Kotkowiak, 2021). We have also evaluated the potential of SERS to identify MCI, a potential pre-AD condition from AD patients through clinical

analysis. We have achieved this objective by employing a range of machine-learning algorithms on SERS data. These algorithms can identify patterns indicative of specific diseases or predict the likelihood of disease progression, aiding clinicians in making informed decisions about patient care. Our SERS−machine learning integrated method analyzes blood plasma samples from three different groups: AD patients, individuals with MCI, and healthy controls. This approach suggests a novel avenue for developing a rapid, reliable, and cost-effective blood plasma test, which could serve as a valuable tool for early AD detection.

4.1.1 Synthesis of spiky star-shaped chitosan-coated gold nanoparticles

Spiky star-shaped chitosan-coated gold nanoparticles (Cs-AuNPs) were prepared by mixing aqueous $HAuCl_4$ with $AgNO_3$, followed by the addition of the appropriate amount of ascorbic acid (A.A) as the reducing agent. This method generates spiky star-shaped nanoparticles within a minute. Subsequently, chitosan is utilized as the stabilizing agent (Figure 46). The amount of Au and Ag measured by ICP-MS was found to be 24ppm and 0.63ppm respectively.

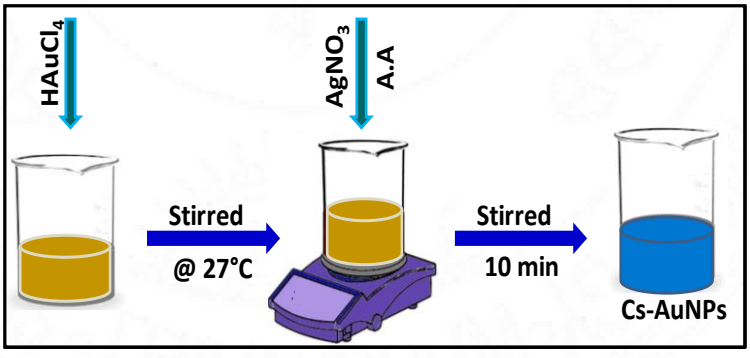

Figure 46. Schematic representation of synthesis of Cs-AuNPs.

The optical properties of branched nanoparticles, including star-shaped ones, are primarily determined by dipole extinction at their tips. Elongation of the

nanoparticles or their tips causes the longitudinal plasmon peak to shift to longer wavelengths. Figure 47a illustrates the UV-Vis absorption spectra of the nanoparticles showing a strong absorption at 685 nm. An additional peak is observed at 270 nm which is attributed to the transverse dipole polarization modes. This is in accordance with the modified Mie Theory, which says that non-spherical nanoparticles possess two distinct peaks, one in the longitudinal, and the other in the transverse dipole polarization modes (Toma *et al.*, 2010). Figure 47b &c provides a visual representation of this concept using transmission electron microscopy (TEM). It shows that these gold nanoparticles have spiky star-shaped morphology with an average size of 67.41±9 nm.

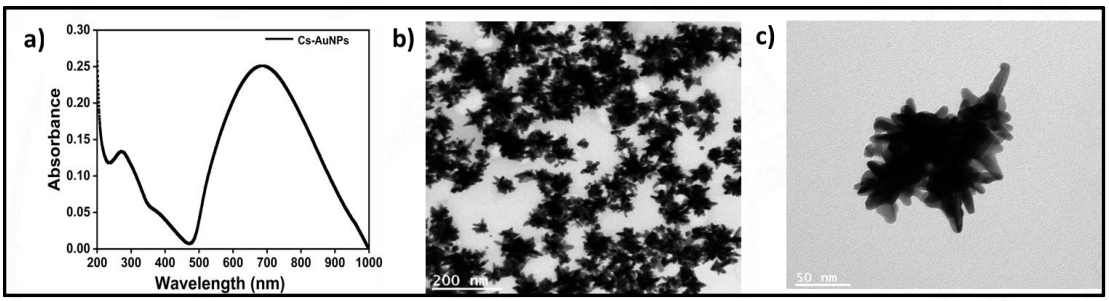

Figure 47. a) UV-Vis absorption spectra of the spiky star-shaped Cs-AuNPs b &c) TEM image of Cs-AuNPs.

4.1.2 Fabrication of SERS-based Immunoassay platform and characterization

Our design incorporates an aluminium (Al) substrate as the base platform to fabricate the SERS immunoassay platform. Al is chosen for its low fluorescence, ready availability and cost-effectiveness. The surface properties of the Al platform were enhanced through a chemical modification using a strong adhesive, 3-aminopropyltriethoxysilane (APTES) through a spray-coating method. Afterward, the APTES-coated platform (Al-APTES) underwent heat treatment at 110 °C for 1 h.

The thermal treatment was performed to alter the surface of the Al platform, facilitating the silanization process and forming strong chemical bonds between APTES and the Al platform. After surface modification, Cs-AuNPs were directly immobilized onto the surface using glutaraldehyde (GA) as a linker. This facilitated the coupling of amine groups on the APTES-Al surface to those on the Cs-AuNPs surface.

Water Contact Angle (WCA) measurements were performed to evaluate the wettability of the Al surfaces during each stage of the fabrication process (Figure 48a). In biosensor applications, regulating the surface wettability of materials is essential for ensuring effective interactions with target molecules or analytes. The unaltered Al surface displayed a WCA of 108°, while following the formation of a silane layer (APTES) on the Al surface, the WCA reduced to 95°. This decrease can be attributed to the exposure of silane hydrocarbon groups and amine groups on the Al surface, favorably to suit the wettability properties of the platform (Sypabekova *et al.*, 2023). After the Cs-AuNPs were conjugated onto the Al surface, WCA decreased even further to 64°. This reduction in WCA also indicates a surface functionalization of Cs-AuNPs of the Al surface imparting enhanced hydrophilicity (Majdi *et al.*, 2019). A hydrophilic surface promotes more effective interactions with aqueous solutions and target biomolecules. In optical detection-based sensors, this increased hydrophilicity can enhance analyte transport and boost signal generation efficiency (Fan and Guo, 2020; Ji *et al.*, 2022). Figure 48b illustrates a scanning electron microscopy (SEM) image of the Cs-AuNPs-Al surface, which confirms the successful immobilization of Cs-AuNPs on the Al surface.

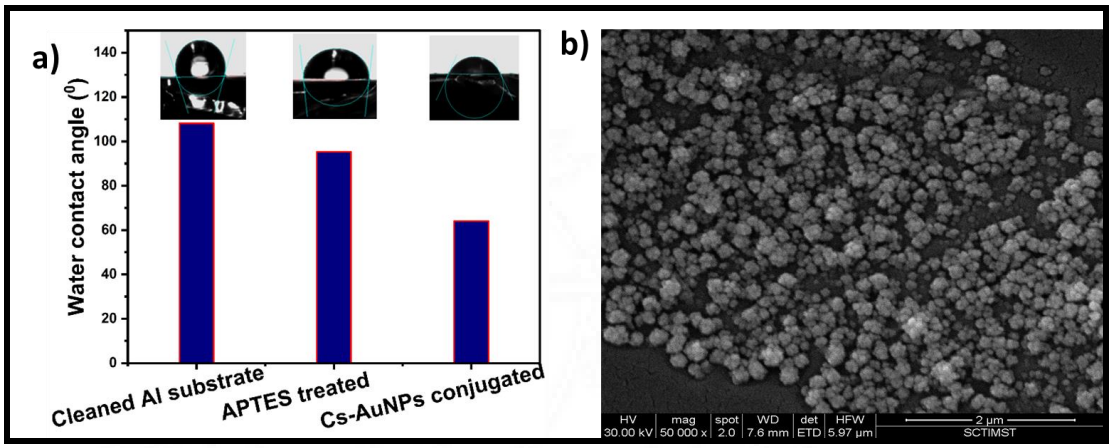

Figure 48. a) Water contact angle images of different samples, b) SEM image of Cs-AuNPs-Al surface.

To investigate the potential use of the developed platform for SERS application, a Raman-active dye, Crystal Violet (CV) was applied onto both the uncoated Al platform and the SERS-Al platform. Figure 49 shows the normal Raman spectra and SERS spectra of CV. Both spectra were compared and the analytical enhancement factor (AEF), was calculated according to the following equation (Rekha, Nayar and Gopchandran, 2018; Liyanage *et al.*, 2020).

$$AEF = I_{SERS}/I_{Raman} \times C_{Raman}/C_{SERS}$$

where I represent the intensity, C denotes the concentrations of analyte molecules deposited on both the Al-SERS platform and bare Al platform, which is directly correlated with the concentration of CV deposited in each case. An enhancement factor of 16.85×10^6 was observed with the plasmonic Cs-AuNPs SERS-Al platform compared to the bare Al platform.

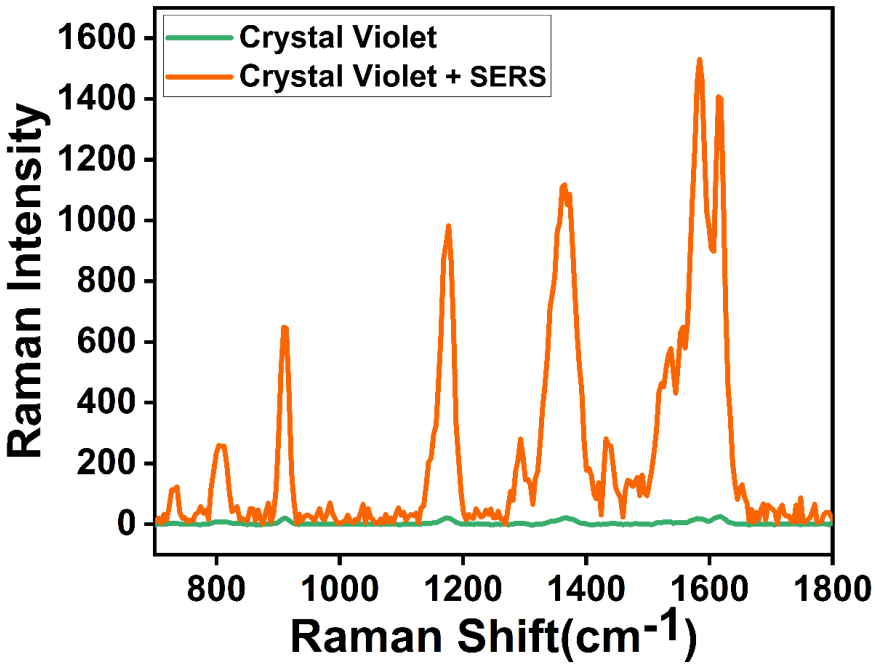

Figure 49. Raman spectra of CV solution with and without SERS enhancement.

For using the developed platform for human blood sample testing, antibodies were conjugated to the Cs-AuNPs-Al surface by placing them in a GA solution which allowed for the covalent bonding of the antibodies (figure 50).

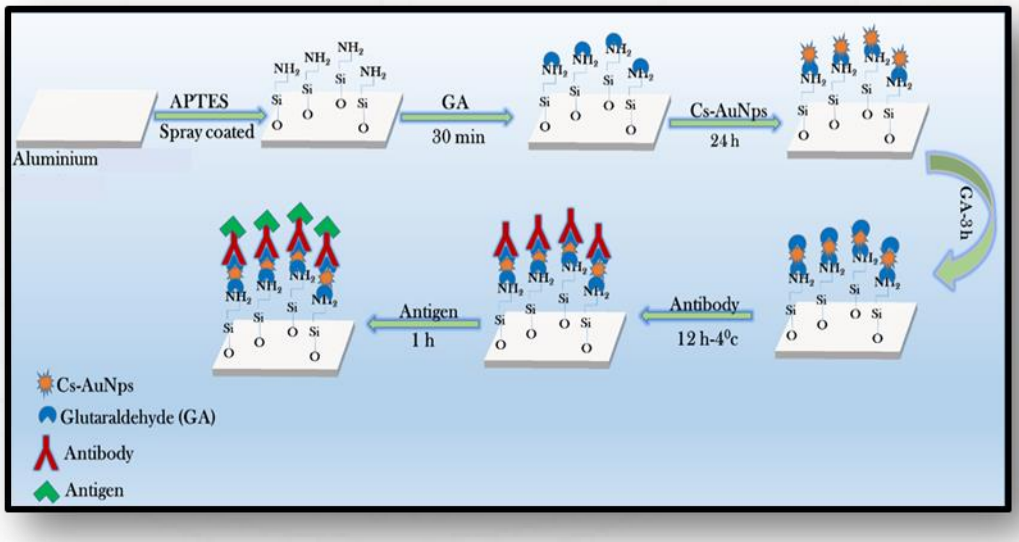

Figure 50. Schematic representation SERS-based Immunoassay platform

The formation of each functionalization was carefully analyzed and characterized. Figure 51 shows FTIR spectra illustrating the sequential functionalization process, starting from APTES onto the Al surface, followed by conjugation of Cs-AuNPs onto the APTES-modified Al surface, and finally, the attachment of antibodies onto the Cs-APTES-Al surface. The spectrum of bare Al platform exhibits no observable peaks (Figure 51(i)). In contrast, the spectrum of the Al platform treated with APTES reveals distinctive -NH peaks at 3300 cm^{-1}. This peak is indicative of the presence of primary amine groups derived from APTES. Furthermore, peaks associated with Si-O stretching were identified at 1200 cm^{-1}, while the peak at 1000 cm^{-1} can be attributed to the formation of the Si-O-Si network, resulting from the silanization process involving APTES (Figure 51(ii)) (Kunst *et al.*, 2015; Lee *et al.*, 2019). After the covalent attachment of Cs-AuNPs to the APTES-modified Al platform, a broad peak in the range of 3200-3600 cm^{-1} emerges, corresponding to OH and NH groups inherent to chitosan (Figure 51(iii). In the final step, following the introduction of the antibody, notable strengthening of peaks is observed at 3200–3600 cm^{-1} and 1864–2922 cm^{-1}, attributed to the presence of amine and acid groups, along with aliphatic C-H bonds within the antibody. Additionally, peaks at 1642, 1690, and 1729 cm^{-1} signify the existence of amide, esteric, and acidic carbonyl groups within both the antibody and chitosan (Figure 51(iv)) (Majdi *et al.*, 2019).

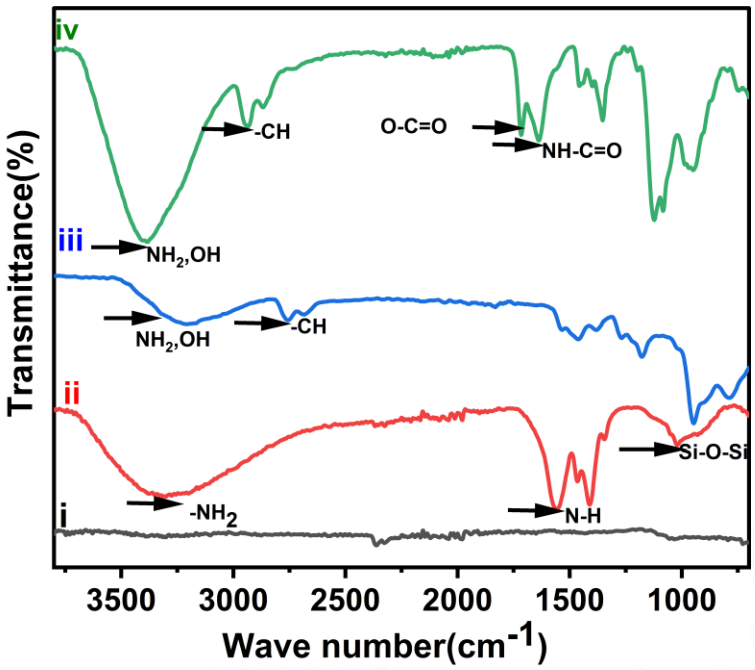

Figure 51. FTIR spectra of i) bare Al platform ii) APTES treated iii) Cs-AuNPs treated iv) Antibody treated Al substrates.

4.1.3 SERS-based Immunoassay Platform (SERS-AI) for Aβ42 and p-Tau detection

Proteins exhibit weak Raman scattering signals due to their low Raman cross-sections (Cai *et al.*, 2022). This poses a challenge when they are studied directly using Raman spectroscopy. The SERS technique addresses the sensitivity challenge by amplifying the Raman signal millions of times through the proximity of protein molecules to metallic nanostructures. This enables a thorough analysis of proteins, including those in low concentration. In Raman spectra, the amide band region (1580−1700 cm^{-1}-amide I, 1520−1570 cm^{-1}-amide II, 1200−1500 cm^{-1}-amide III) offers insights into the secondary structural alterations of proteins. Furthermore, the concentration of the target analytes can be assessed by analyzing the intensity of a

specific band (Abalde-Cela *et al.*, 2010; H. J. Park *et al.*, 2020; Jeon, Lee and Jang, 2022).

The amide I band is sensitive to the changes in the protein's secondary structure, including processes like aggregation and fibril formation (Miller, Bourassa and Smith, 2013). The performance of the developed SERS-Al platform was assessed using commercially acquired $A\beta_{42}$ and p-Tau proteins, recognized as significant contributors to the cause of AD (Kim *et al.*, 2020). To selectively detect $A\beta_{42}$, and p-Tau proteins, SERS spectra were acquired after introducing varying concentrations (ranging from micromolar to attomolar) of these proteins onto SERS-Al platform treated with their respective antibodies (Figure 52a &b). The response of the $A\beta_{42}$ SERS-Immunoassay platform, the intensity values for $A\beta_{42}$ decrease as the concentration decreases from 2.5 μM to 7.8 aM. This is expected, as lower concentrations would lead to fewer molecules interacting with the SERS substrate, resulting in a weaker signal. Similar to $A\beta_{42}$, the intensity values for p-Tau decrease with decreasing concentration from5.4 μM to 37.3 aM. These results demonstrated that the SERS-Al platform is capable of detecting and quantifying both $A\beta_{42}$ and p-Tau at low concentrations. Figures 52 b & d display the SERS spectra of the $A\beta_{42}$ and p-Tau at aM concentration. Remarkably, even at these low concentrations, the SERS-AI platform exhibits prominent Raman bands.

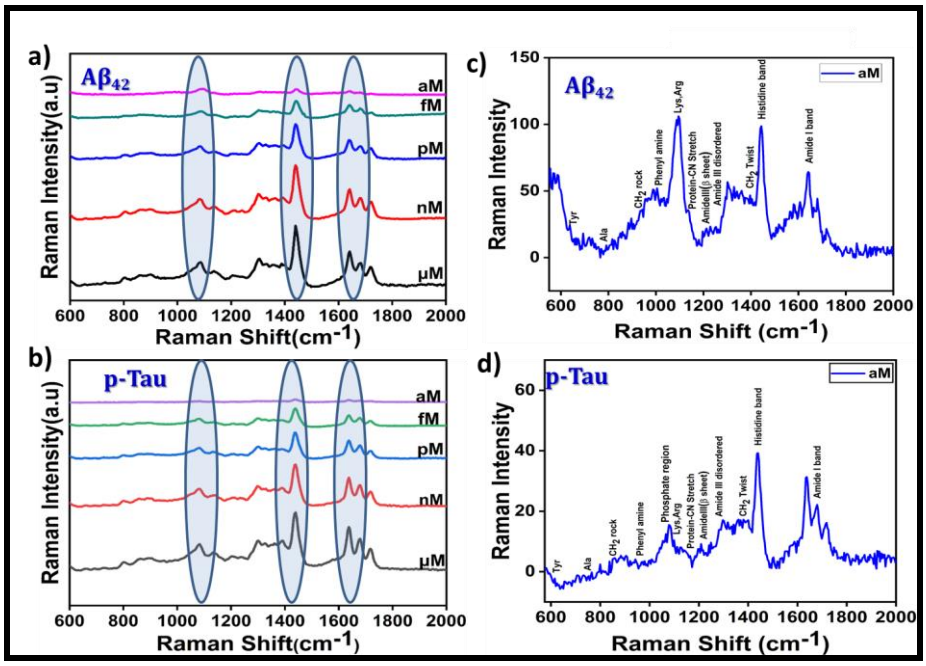

Figure 52. SERS spectra of a) Aβ$_{42}$ & b) p-Tau at different concentrations, b) & d) Aβ$_{42}$ and p-Tau acquired with the SERS-AI platform at attomolar concentration respectively.

The correlation coefficients (R^2) obtained were 0.964 for Aβ$_{42}$ antigens and 0.976 for p-Tau, respectively (Figure 53a & b). The high correlation coefficients indicate a strong and reliable association, demonstrating the effectiveness of the assay in accurately detecting these biomarkers.

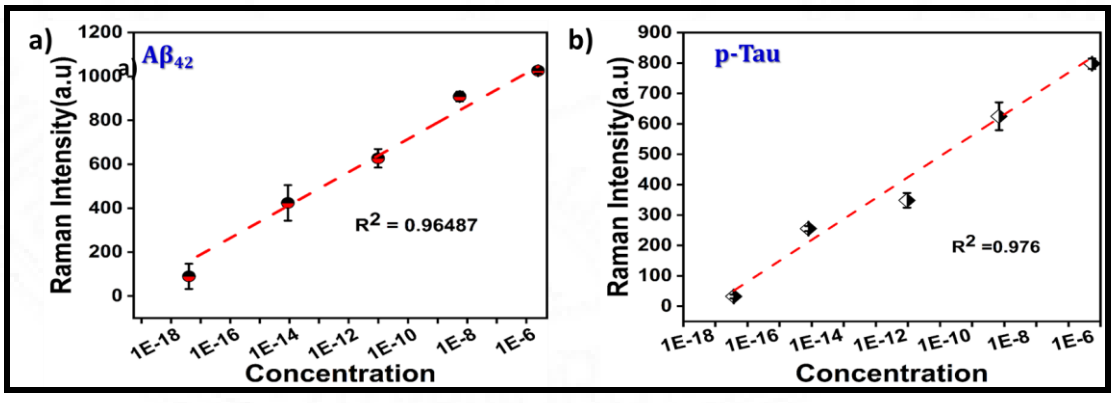

Figure 53. The calibration curves of the peak intensity at 1445 cm^{-1} changed with protein concentration: (**a**) Aβ$_{42}$ and (**b**) p-Tau.

The main amide bands relevant to SERS analysis are Amide I and Amide III. The amide I band typically appears in the range of 1580 to 1700 cm^{-1} in SERS spectra and primarily arises from the C=O stretching vibrations coupled with some contributions from C-N stretching and N-H bending vibrations. In addition, in figure 52 a&b (represented within circles), amino acid residues like phenylalanine, tryptophan, tyrosine, and cysteine can also influence the Raman signal of proteins within the range of approximately 635-1090 cm^{-1}. It is highly sensitive to the secondary structure of proteins, such as α-helices, β-sheets, and random coils. The band at around 1640 cm^{-1} within the amide I band of the $A\beta_{42}$ Raman spectrum is assigned to intermolecular β-sheet structures, whereas the band at about 1675 cm^{-1} has been associated to the intra-molecular β-sheet within the protein. The Amide I band in the tau protein spectrum manifests within a similar range and elucidates the secondary structure of tau. The distinct wavenumber ranging from 1650 to 1660 cm^{-1} signifies the prevalence of random coil and α-helical secondary structures. The histidine band around 1455 cm^{-1} also holds substantial importance in interpreting the functionality and misfolding of Aβ and Tau proteins (Dong *et al.*, 2003; Juszczak, 2004; Chou *et al.*, 2008; Demeritte *et al.*, 2015; Ryzhikova *et al.*, 2015). Observed frequencies of the Raman bands of Aβ and Tau proteins are assigned in Table 3.

Table 3. Raman Modes of Aβ and Tau Protein

Vibration mode	Raman band position (cm^{-1})
amide I	~1640
amide II	~1550
histidine band	~1455
CH_2 twist	~1385
amide III bands due to α-helical structure	~ 1270
amide III bands due to β-sheet conformation	~1224

protein −CN band	~1090
phenylamine band	~1004
tyrosine	~1170 , ~ 910, ~ 635

The limit of detection (LOD) of biosensors is a crucial parameter determined statistically as described in equation (1), where σ is the standard deviation of the blank and m is the slope of the calibration curve.

$$LOD=3\sigma/m \quad \ldots\ldots\ldots\ldots (1)$$

The σ was found to be 5.446. The slope for $A\beta_{42}$ was 1.197×10^{18} and for p-tau, it was 5.712×10^{17} Therefore, the LOD of the sensors was calculated to be 13.64 aM for $A\beta_{42}$ and 28.6 aM for p-Tau.

4.1.4 Specificity of the SERS-AI platform

The specificity of the prepared immunoassay was verified by adding different antigens to the SERS-Al platform. Initially, nanomolar (nM) concentrations of $A\beta_{42}$ protein, p-Tau protein, and BSA protein were individually added to the $A\beta_{42}$ antibody-conjugated platform for detection. Similarly, nM concentrations of $A\beta_{42}$ protein, p-Tau protein and BSA protein were added to the p-Tau antibody-conjugated platform. It is clear from figure 54a that, the $A\beta_{42}$ antibody-conjugated detection system exhibited a strong Raman signal for $A\beta_{42}$ protein detection, whereas the Raman intensity for other proteins (p-Tau and BSA protein) was very weak. Similarly, the p-Tau antibody-conjugated detection system had a strong Raman signal on the detection of the p-Tau protein, while the Raman intensity of other proteins ($A\beta_{42}$ and BSA protein) was very weak (Figure 54b). The findings demonstrate that the suggested immunoassay can accurately and efficiently detect the

specific protein. The intensity of the Raman signal was significantly enhanced due to the antigen-antibody binding.

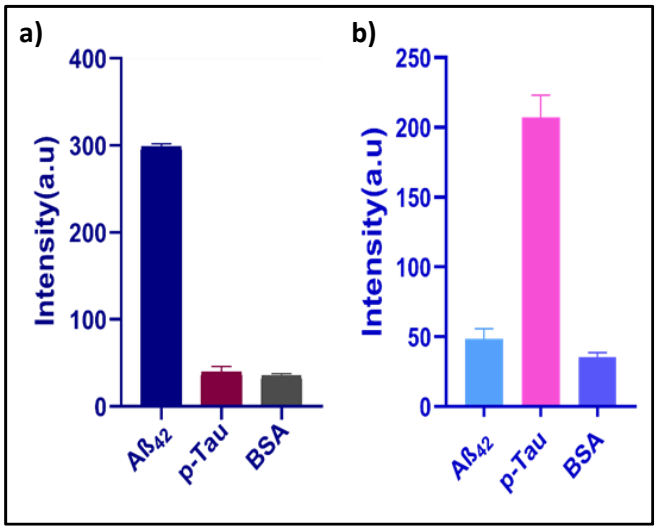

Figure 54. Specificity verification of proposed immunoassay platform. (**a**) $A\beta_{42}$ antibody-conjugated immunoassay. (**b**) p-Tau antibody-conjugated immunoassay.

4.1.5 SERS Immunoassay platform for AD biomarkers detection from clinical samples

After confirming that the Al-SERS platform could detect $A\beta_{42}$ and p-tau proteins with high sensitivity and selectivity, the same approach was applied to evaluate several AD biomarkers ($A\beta_{42}$, $A\beta_{40}$, p-Tau, and t-Tau) from blood plasma samples. Direct detection techniques have been utilized in antibody-linked nanoplatforms, enabling the detection of AD biomarkers even at very low concentrations. The levels of composite biomarkers ($A\beta_{42}$, $A\beta_{40}$, p-Tau, and t-Tau) in plasma were measured by exposing blood plasma samples from patients with AD and mild cognitive impairment (MCI) to an antibody-conjugated SERS-AI platform. Healthy individuals served as controls. The age range was similar across all groups. During subject recruitment, various confounding factors were taken into account, including abnormal cardiovascular or hepatic functions, infections, alcoholism, dietary habits,

age, and gender (Samieri, 2018). The figure 55 (a,b.c, and d) displays the normalized average SERS spectra (550-2000cm^{-1}) for $A\beta_{40}$, $A\beta_{42}$, p-Tau, and t-Tau biomarkers across the AD, MCI, and healthy control plasma samples, with each group comprising 25 samples. Table 4 shows the spectroscopically significant bands in the SERS spectrum of blood plasma and their assignments.

Table 4. Assignment of the spectroscopically significant bands in the SERS spectrum of blood plasma.

Peak position (Raman Shift cm-1)	Assignment
624	Phenylalanine
704-710	methionine sulfoxide
752	Alanine
816	Tyrosine
858	Tyrosine
954	CH_2 symmetric rock + C-Cα
1004	Phenylalanine
1008	S=O, methionine sulfoxide
1038	C−O stretching mode in oligomeric Aβ and fibril Aβ proteins.
1078	[C-C and C-N stretch], Lysine, Arginine, Glutamine, Asparagine
1136	Valine, Isoleucine + [C-Cα and C-N stretch]
1156	[C-N] + Isoleucine
1176	Tyrosine, Phenylalanine
1205	Tyrosine, Phenylalanine
1241	amide III in â-sheet
1257	amide III disordered
1283	CH_2 bending mode in oligomeric tau protein
1317	amide III and CH_2 twist/wag
1361	[Cα-H bend + Cα-C stretch] + CH2 twist/wag
1396	COO- symmetric stretch in Asp, Glu
1458	C−C stretching mode and CH_2 bending mode in oligomeric Aβ and oligomeric tau proteins.
1583	Phenylalanine
1603	histidine, Phenylalanine, Tyrosine
1637	C=O
1641	Amide I α-helix

1645	Amide I β-sheet
1649-1680	Amide I disordered

To explore the differences in protein bands across the groups, we initially compared the normalized intensities at around 1078 cm^{-1}, 1458 cm^{-1} and 1678 cm^{-1}. It is important to note that amino acid residues (~635-1090 cm^{-1}) are highly sensitive to the secondary structures of proteins, such as α-helices, β-sheets, and random coils. The histidine band near 1455 cm^{-1} is particularly significant for understanding the functionality and misfolding of Aβ and Tau proteins. Additionally, the band around 1675 cm^{-1} is associated with the intra-molecular β-sheet structure within the protein (Amide I disordered).

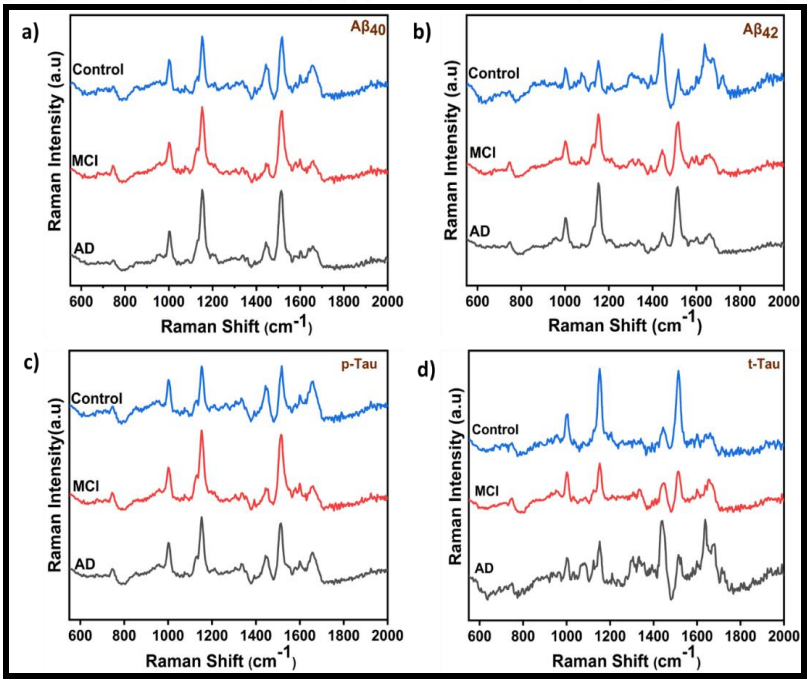

Figure 55. Normalized SERS spectra of a) $Aβ_{40}$, b) $Aβ_{42}$, c) p-Tau, and d) t-Tau biomarkers of AD, MCI and healthy control group's blood plasma samples.

Figure 56 shows boxplots that define these protein bands among the groups, offering clear visual validation of the distinctions among the three groups viz, AD, MCI and control. The box plot was used to identify and evaluate the differences between the selected spectroscopically significant band intensities. As illustrated in the box plot, no significant differences in the intensity of the selected bands were observed for any of the three wavenumbers for $A\beta_{40}$ (Figure 56 a, b &c). For $A\beta_{42}$, significant difference is observed in the intensity of 1078 and 1678cm^{-1} peaks between AD and control, as well as between MCI and control (Figure 56 d & f). At 1458 cm^{-1}, a noteworthy difference is evident between AD and control, as well as between AD and MCI (Figure 56 e). In the case of p-Tau, a significant difference is evident between AD and control, as well as between AD and MCI, at 1078 cm^{-1} (Figure 56 g). Significant differences were observed between AD and MCI, as well as between AD and control, at both the 1457 cm^{-1} and 1676 cm^{-1} positions (Figure 56 h & i). For t-Tau, significant differences were observed between AD and control, as well as between MCI and control, at both the 1078 cm^{-1} and 1457 cm^{-1} band positions (Figure 56 j & k). At 1676 cm^{-1}, significant differences were evident between AD and control, as well as between AD and MCI (Figure 56). Therefore, using the selected spectroscopically significant band intensities, we can classify control, AD, and MCI groups.

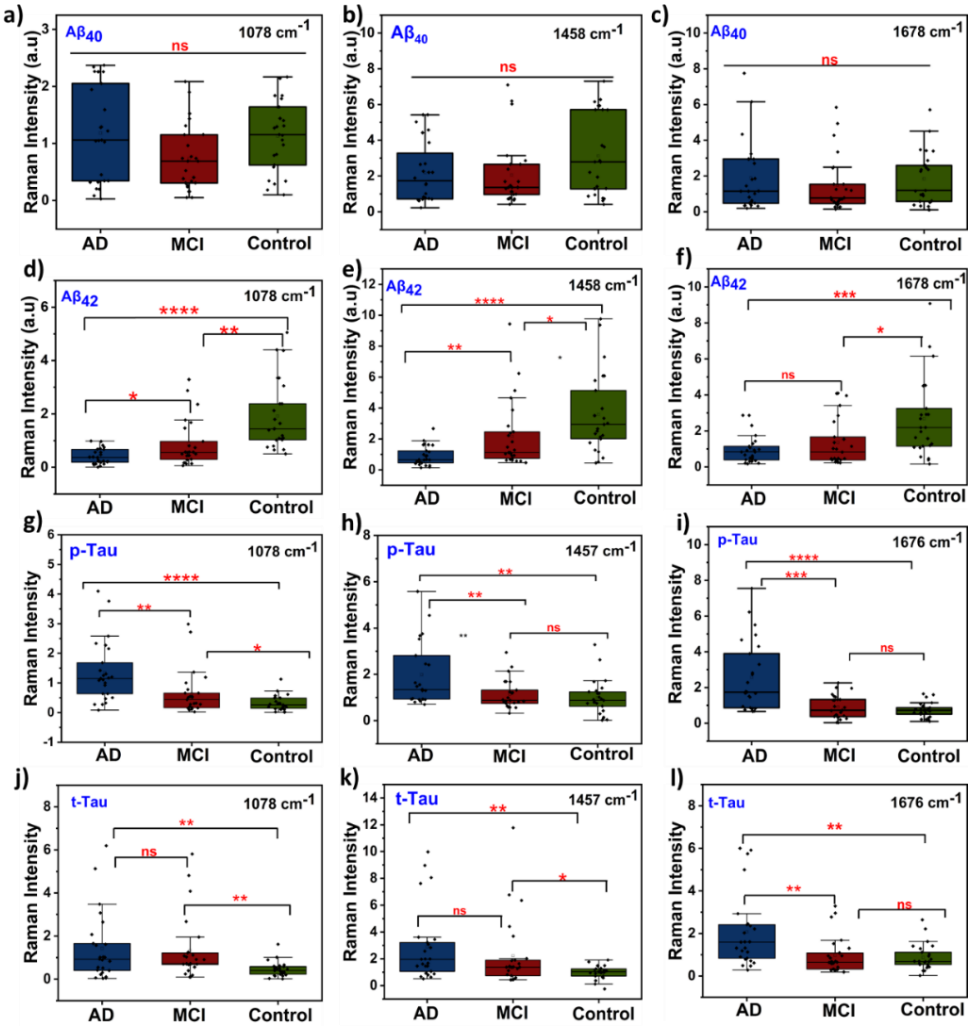

Figure 56. Box plot of Aβ$_{40}$ (a-c), Aβ$_{42}$ (d-f),p-Tau(g-i) and t-Tau(j-l) proteins comparison between groups.

4.1.6 Receiver Operating Characteristic (ROC) Analysis of SERS data

The results were validated using ROC curve analysis, which provided Area Under the Curve (AUC) values. An AUC greater than 0.7 is generally considered to indicate effective classification (Yu *et al.*, 2021). However, the AUC values for Aβ$_{40}$ ranged between 0.5112 and 0.6872 for all the 3 peaks across the three comparisons, AD vs. MCI, MCI vs. Control, and AD vs. Control, suggesting that this biomarker is not suitable for classification among these groups (Figure 57).

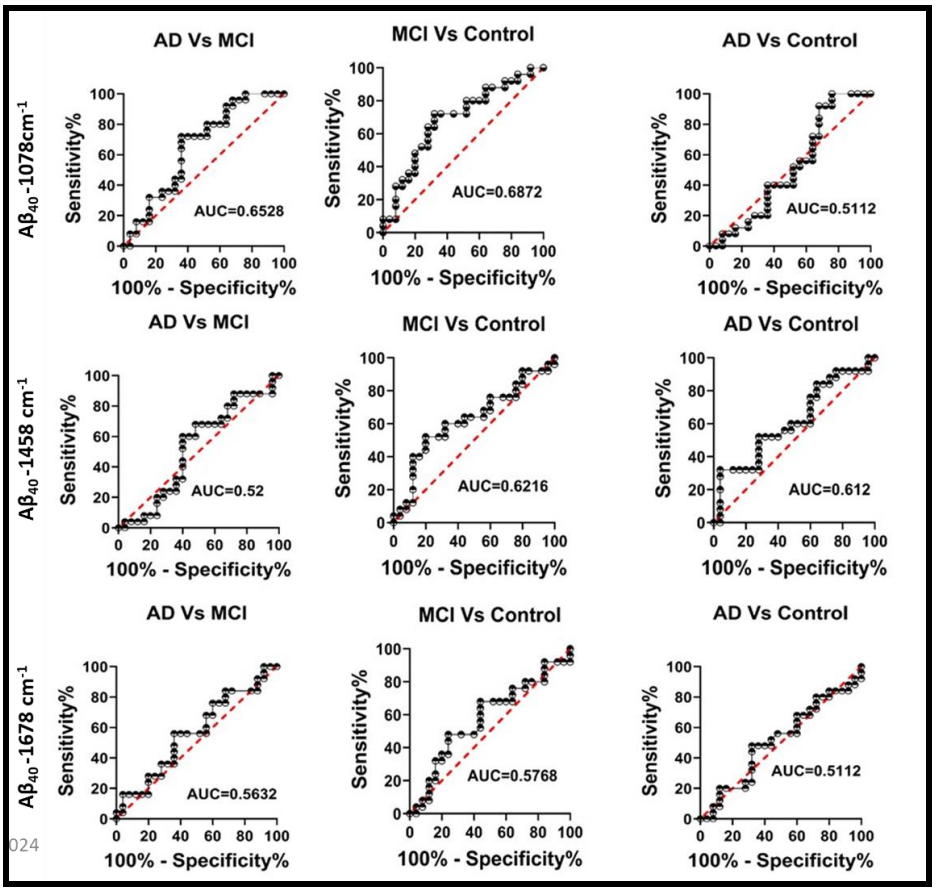

Figure 57. ROC curves of Aβ$_{40}$ proteins to discriminate between AD, MCI and healthy controls.

For Aβ$_{42}$, the AUC value at the 1078 cm^{-1} band is notably significant, with values of 0.81 for MCI vs. Control and 0.95 for AD vs. Control. At the 1458 cm^{-1} band, the AUC values are significant across all groups, with values of 0.72, 0.70, and 0.88 for AD vs. MCI, MCI vs. Control, and AD vs. Control, respectively. In the 1678 cm^{-1} band, the AUC values are also significant for MCI vs. Control and AD vs. Control, with values of 0.80 and 0.91, respectively (Figure 58).

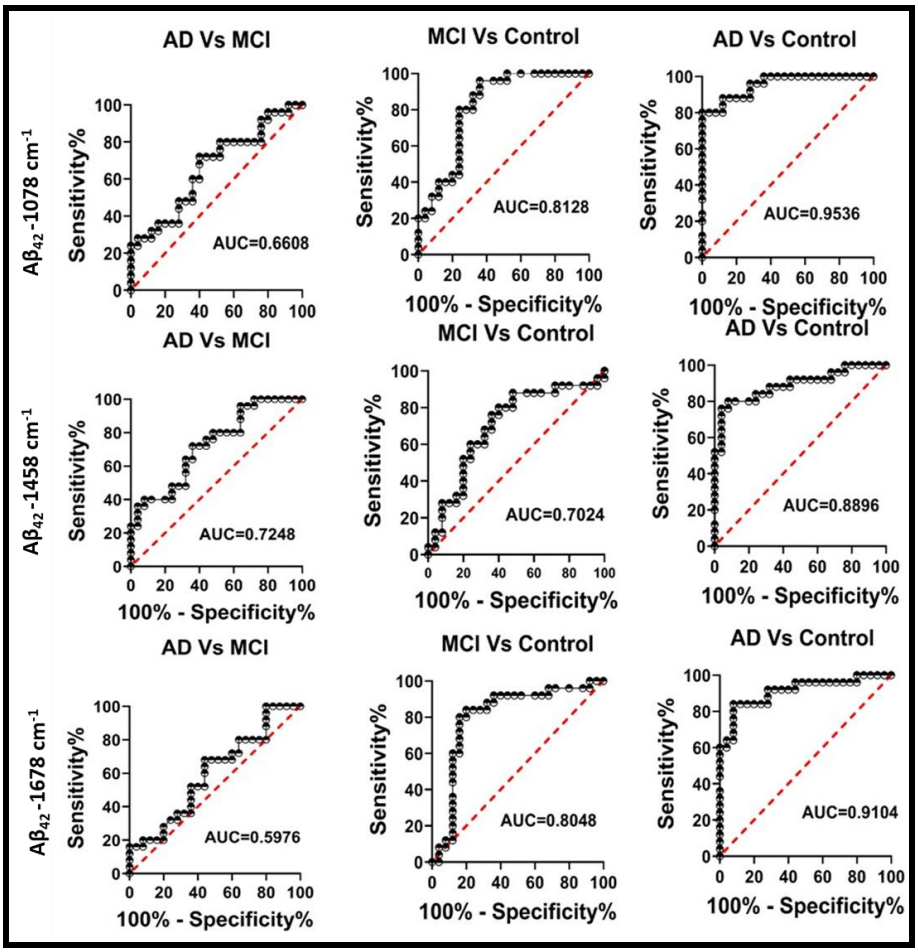

Figure 58. ROC curves of Aβ42 proteins to discriminate between AD, MCI and healthy controls.

In p-Tau, the AUC value at the 1078 cm^{-1} band is significant, with values of 0.74 for AD vs. MCI and 0.88 for AD vs. Control. At the 1457 cm^{-1} band, the AUC value is also significant, with values of 0.75 for AD vs. MCI and 0.77 for AD vs. Control. Similarly, at the 1676 cm^{-1} band, the AUC values are 0.80 for AD vs. MCI and 0.86 for AD vs. Control, indicating a strong distinction (Figure 59).

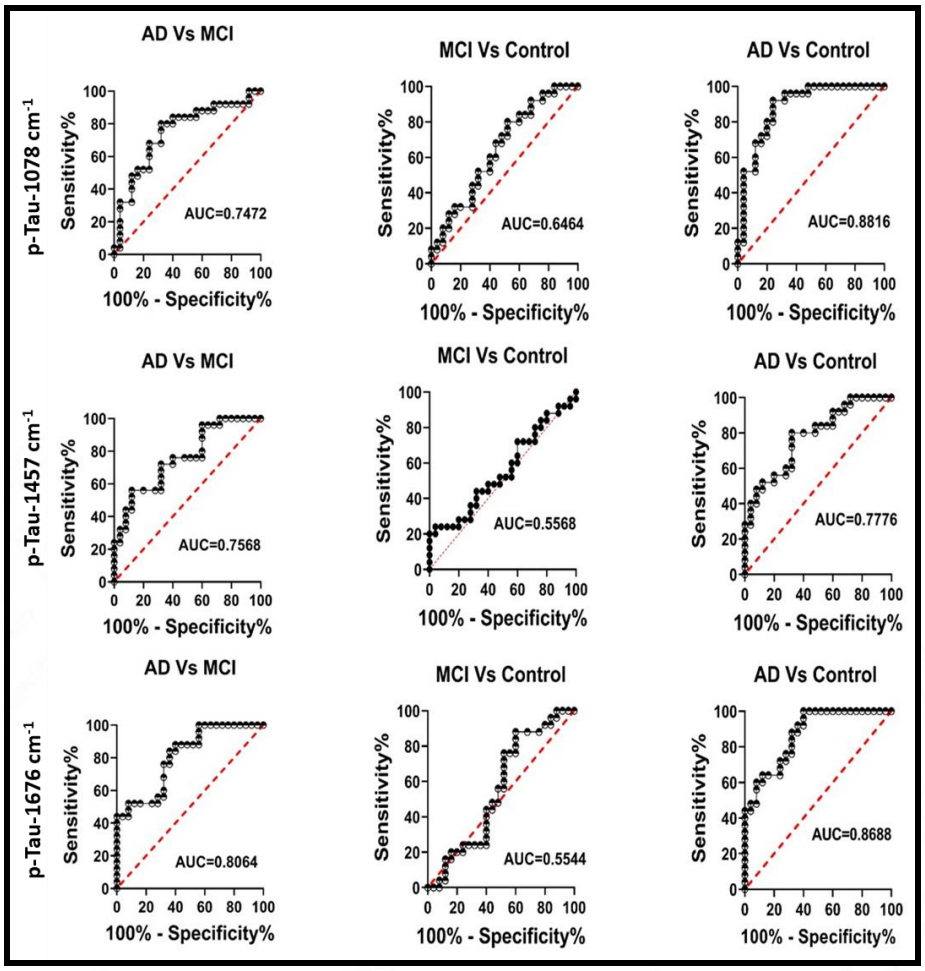

Figure 59. ROC curves of p-Tau proteins to discriminate between AD, MCI and healthy controls.

For the t-Tau biomarker, the band at 1078 cm^{-1} shows a significant AUC value of 0.78 for differentiating MCI from Control and 0.70 for AD from Control. The band at 1457 cm^{-1} is significant only for AD Vs Control, with an AUC value of 0.76. At 1676 cm^{-1}, the AUC values are significant for AD Vs MCI and AD Vs Control, with values of 0.74 and 0.75, respectively (Figure 60).

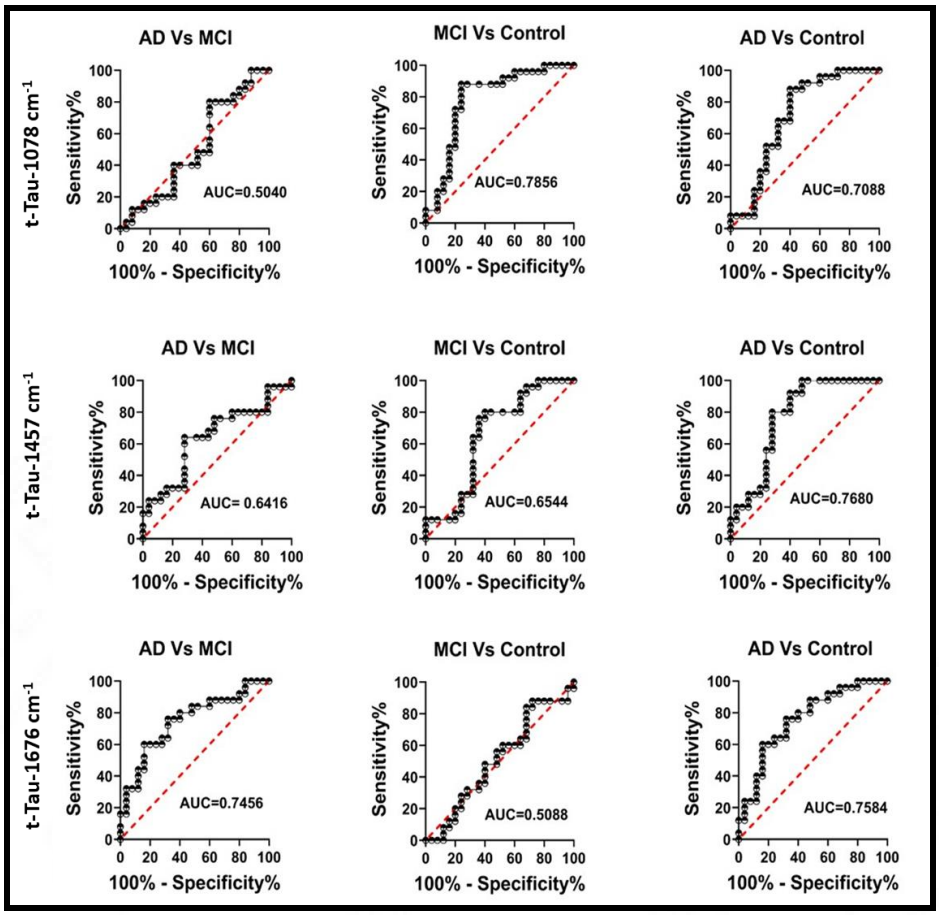

Figure 60. ROC curves of t-Tau proteins to discriminate between AD, MCI and healthy controls.

These findings suggest that while $A\beta_{40}$ may not be suitable, $A\beta_{42}$, p-Tau, and T-tau hold promise as biomarkers for AD classification using SERS technique. Hence, the detection of these biomarkers using the developed SERS platform confirms its suitability to function as initial indicators for the early detection of AD. To further enhance the classification, a range of machine learning algorithms has been subsequently applied to the complete spectral dataset.

4.1.7 Artificial Neural Network (ANN) for the classification of SERS data

Artificial Intelligence plays a significant role in the medical field across various aspects, revolutionizing healthcare delivery, diagnosis, treatment, and patient care. Here we have used Artificial Neural Network (ANN), an important branch of

artificial Intelligence-based algorithms for the easy implementation of SERS based diagnostics in the clinical decisions. Additionally, various machine learning algorithms have been employed on the full spectral data to improve classification accuracy, sensitivity and specificity. Intensity values corresponding to Table 2 were also extracted and subjected to ratiometric and machine learning analysis.

The interpretability of machine learning was demonstrated by applying three ANN models to the SERS data, for early detection of AD. Multi-layer perceptron (MLP), Radial Basis Function (RBF), and Support Vector Machine (SVM) enabled the identification of biomarkers present in minute quantities in diseased samples, potentially aiding in the early detection and comprehension of disease pathology. These algorithms used the normalized spectra, as well as spectroscopically significant band intensities, to obtain accuracy, sensitivity, and specificity results (Table 5 and Figure 61).

According to previous studies, the ratios of $A\beta_{42}/A\beta_{40}$ serve as more precise diagnostic biomarkers for predicting the progression of AD and distinguishing AD patients from normal controls compared to the single biomarker $A\beta_{42}$. In this study, we focus on the $A\beta_{42}/A\beta_{40}$ ratio, along with p-Tau and t-Tau biomarkers, for the classification of SERS data. When using an MLP model, the accuracy ranged from 80-93% for distinguishing between Control and MCI, 66-93% for Control vs. AD, and 46-53% for MCI vs. AD. Sensitivity was 70-80% for Control vs. MCI, 54-87% for Control vs. AD, and 40-57% for MCI vs. AD. Specificity was 60-100% for Control vs. MCI, 71-85% for Control vs. AD, and 37-42% for MCI vs. AD. Using an RBF model, the accuracy was 66-93% for Control vs. MCI, 86% for Control vs. AD, and 46-70% for MCI vs. AD. Sensitivity was 81-100% for Control vs. MCI, 83-

100% for Control vs. AD, and 61-70% for MCI vs. AD. Specificity ranged from 75-100% for Control vs. MCI, 55-75% for Control vs. AD, and 40-71% for MCI vs. AD. With an SVM model, accuracy ranged from 66-86% for Control vs. MCI, 66-80% for Control vs. AD, and 40-53% for MCI vs. AD. Sensitivity was 80-100% for Control vs. MCI, 75-100% for Control vs. AD, and 58-100% for MCI vs. AD, while specificity was 54-80% for Control vs. MCI, 45-62% for Control vs. AD, and 40-54% for MCI vs. AD.

Table 5. Classification of Control, MCI and AD using various machine learning tools

		C vs MCI			C vs AD			MCI vs AD		
		Accuracy	Sensitivity	Specificity	Accuracy	Sensitivity	Specificity	Accuracy	Sensitivity	Specificity
Bands MLP	**$A\beta_{40}$**	80	75	57	66	80	80	53	66	44
	$A\beta_{42}$	53	60	40	53	62	42	52	60	50
	$A\beta_{42/40}$	93	75	100	93	54	85	53	40	40
	p-Tau	80	80	80	80	87	71	47	50	42
	t-Tau	80	70	60	66	87	71	46	57	37
Bands RBF	**$A\beta_{40}$**	53	66	44	53	62	42	46	66	41
	$A\beta_{42}$	60	85	62	73	80	50	52	54	50
	$A\beta_{42/40}$	93	100	85	86	100	75	60	61	50
	p-Tau	86	81	100	86	100	75	70	70	71
	t-Tau	66	100	75	86	83	55	46	60	40
Bands SVM	**$A\beta_{40}$**	60	71	50	60	71	50	40	50	36
	$A\beta_{42}$	66	83	55	66	83	55	41	40	41
	$A\beta_{42/40}$	86	100	75	66	100	54	40	58	40
	p-Tau	73	80	80	80	85	62	40	54	50
	t-Tau	66	100	54	66	75	45	53	100	54

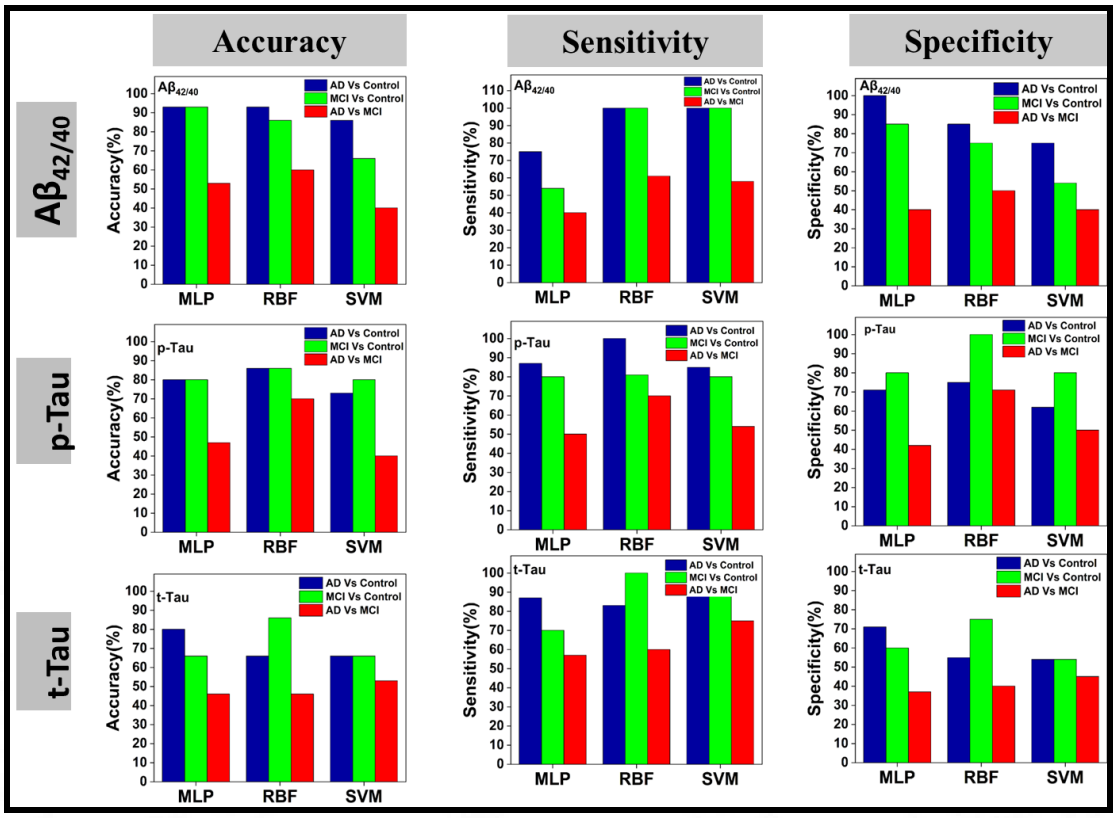

Figure 61. Classification of Control, MCI and AD groups using various machine learning tools.

Classification between Control and MCI is crucial for early detection and effective patient management. Currently, there are no studies that have focused on differentiating between MCI, which is considered as possible early stage of AD and controls using SERS signals derived from blood samples. Existing research has primarily focused on distinguishing between Controls and AD patients. In our study, we could successfully differentiate between control and MCI by analyzing variations in key spectroscopic peak intensities and applying a range of advanced machine learning techniques, such as MLP, RBF, and SVM. The comparison of normalized intensities at specific Raman peaks revealed statistically significant differences between the Control and MCI groups. Among these machine learning techniques, RBF proved to be the most effective in distinguishing between control vs. MCI,

control vs. AD, and AD vs. MCI. Therefore, combining significant Raman peak intensities with RBF presents itself as the most promising method for early AD detection using SERS data. Our integrated SERS-machine learning approach not only advances AD research but also highlights the effectiveness of a cost-effective, easily-prepared Al-SERS platform for clinical diagnosis.

4.2 Design and Development of Electronic Biosensor

Encouraged by the positive results of optical (SERS based) sensor to detect biomarkers associated with AD, we aimed at developing an electronic biosensor to function as a point-of-care device for the same purpose. For this, we had a more serious approach with an initial attempt made to understand the complex folding and assembly properties of proteins using Scanning tunnelling microscopy (STM). STM allows the visualization of Aβ and tau molecules at an atomic level, revealing the core regions of Aβ hairpins and various unfolded peptide assembly structures. The information on the misfolding and aggregation of Aβ and tau are crucial for both developing treatments and understanding the disease mechanisms of AD. Scanning tunnelling spectroscopy (STS) is an extension of STM that provides information not just about the surface structure but also about the electronic properties of the sample (Lee et al., 2009; Rodríguez-Galván and Contreras-Torres, 2022). The interaction between antigens and antibodies alters the overall charge density, and changes in the device's current can easily record this interaction. The charge transport layer must be highly mobile and conductive to ensure accurate transmission of charge changes to measuring devices.

Considering the sensing platform, though numerous methods and devices have been suggested in the literature, the most effective ones are biosensors based on

interdigitated electrodes (IDE), particularly those with chemically modified surfaces. The development of chemically functionalized IDE biosensors marks a significant milestone in biosensing technology. These biosensors offer several advantages, including eliminating the need for a reference electrode, operating at low-amplitude alternating voltage (avoiding Faraday processes on electrodes), being insensitive to light, and enabling easy miniaturization and integration using cost-effective thin-film technology (Yoo *et al.*, 2021). They detect changes in electrical resistance or conductance caused by analyte binding. The IDE patterns on the biosensor surface provide a large area for biomolecule binding, significantly enhancing detection sensitivity. Moreover, the specific chemical coatings on the electrode surface enable the selective binding of target molecules, reducing interference from other substances in the biological sample.

The unique combination of STM, STS and IDE sensor platform makes them ideal for the accurate and reliable detection of AD biomarkers. This capability has the potential to transform personalized healthcare by facilitating proactive and targeted treatments. Consequently, to meet the demand for effective, rapid, specific, and cost-efficient solutions, we present a highly sensitive IDE sensor platform designed for the multiplexed detection of $A\beta_{42}$ and p-Tau, which exhibit distinct electrical properties in physiological fluids. The isoelectric points (pI) of these biomarkers determine their surface charges under physiological conditions, which our IDE platform exploits to generate distinct output signals for each biomarker. To enhance the selectivity and sensitivity of the IDE sensor system, we integrated gold nanoparticle (AuNP) with the Aβ and tau sensing system. This enhancement allows the IDE sensor platform to discriminate AD patients from normal controls by

estimating the levels of composite AD biomarkers ($A\beta_{42}/A\beta_{40}$), p-tau/$A\beta_{42}$ and t-tau/$A\beta_{42}$) in human plasma.

4.2.1 Characterization of $A\beta_{42}$ and p-Tau Proteins Using STM and STS

STM has emerged as a powerful technique for studying organic and biological molecules, offering high structural resolution and adaptability to various environments, including liquid–solid interfaces and ultrahigh vacuum conditions. This technique has been successfully applied to probe the structures of various molecular monolayers with submolecular resolution (Mao *et al.*, 2009; Yang and Wang, 2013). $A\beta_{42}$ is a small peptide with a rigid structure prone to forming specific folds like beta hairpins, while tau is a much larger protein with inherent flexibility, which typically doesn't form such well-defined structures. Instead, STM reveals the overall morphology of tau aggregates rather than individual hairpin structures within them. A typical STM image of $A\beta_{42}$ assemblies, shown in Figure 62a, was recorded after $A\beta_{42}$ antigen was deposited from the solution onto the surface of highly oriented pyrolytic graphite (HOPG). The image shows $A\beta_{42}$ molecules, represented by bright features, aligned parallel to each other, forming hairpin structures (Figure 62b). Two discernible regions within the lamellae are visible: one side (marked by a white arrow) is slightly brighter than the other (marked by a green arrow). These structural characteristics revealed through STM provide insights into the core regions of $A\beta_{42}$ assemblies at the molecular level.

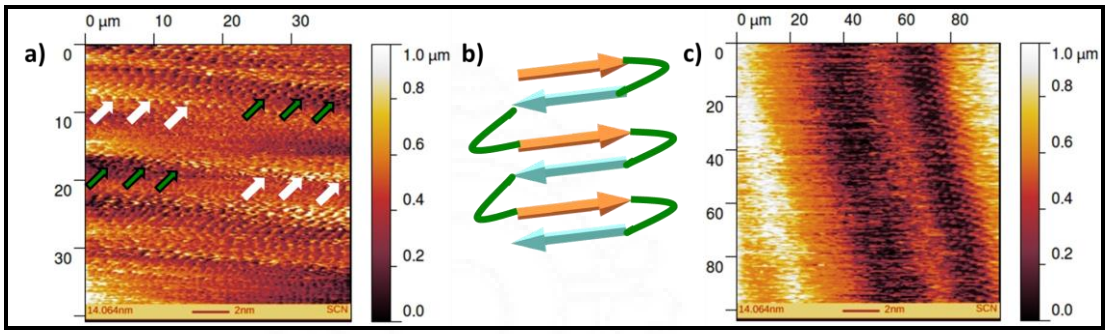

Figure 62. a) STM of Aβ$_{42}$ antigen on HOPG surface b) Aβ$_{42}$ hairpin structure c) STM of p-Tau antigen on HOPG surface

Figure 62c presents an STM image of phosphorylated tau (p-Tau) antigen, which does not display a hairpin structure but rather an overall tangled or extended conformation of the protein on the HOPG surface. These images offer atomic-level resolution structural information for both Aβ$_{42}$ and p-tau, enhancing our understanding of their assembly and morphology.

STS is a powerful technique for investigating the electronic properties of materials at the atomic and molecular levels. By measuring the tunneling current between the tip and the sample at varying voltages, STS provides information about the electronic density of states of the sample. Figure 63a shows the current-voltage (I-V) curve of the Aβ$_{42}$ antigen, which exhibits negative current (pA) at zero voltage. This negative current indicates the negative surface charge effect of the Aβ$_{42}$ antigen. The amino acid sequence and folding structure of Aβ$_{42}$ contribute to its slight electron-accepting tendency. Additionally, the net charge of an amino acid in Aβ$_{42}$ depends on its specific side chain and the surrounding environment, particularly the pH. Aβ$_{42}$ is composed of various amino acids with side chains that can be positively charged (basic), negatively charged (acidic), or neutral. At physiological pH (around 7.4), Aβ$_{42}$ typically has a net negative charge due to its higher content of acidic

residues (Aspartic acid - D, Glutamic acid - E) compared to basic residues (Lysine - K, Arginine - R). The isoelectric point (pI) of $A\beta_{42}$ is approximately 3.92. This value also indicates that $A\beta_{42}$ is negatively charged in PBS solution (pH = 7.4) (Figure 64a).

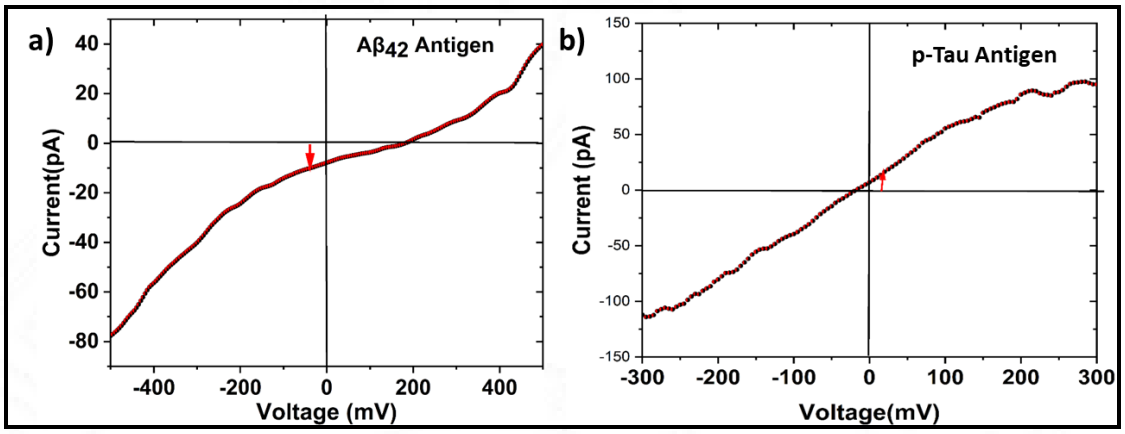

Figure 63. I-V spectra of a) $A\beta_{42}$ antigen and b)p-Tau antigen using STS measurement.

In the case of the p-Tau antigen, the positive current at zero voltage in the I-V curve indicates the positive surface charge effect of the p-Tau antigen (Figure 63b). This phenomenon is influenced by the intrinsic electronic properties of the protein, including its amino acid sequence and folding structure, which may impart a slight electron-donating tendency. Phosphorylation can modify the electronic characteristics of proteins, and depending on the specific phosphorylation site on p-Tau, it might enhance this electron-donating nature. The charge of individual amino acids in p-Tau (phosphorylated tau protein) varies based on the specific amino acid and its position in the sequence. Overall, p-Tau protein has a net positive charge due to its higher content of positively charged amino acids (lysine and arginine) compared to negatively charged ones (aspartic acid and glutamic acid). The isoelectric point (pI) of p-Tau antigen is approximately 8.43, indicating that p-Tau is

positively charged in a PBS solution (pH = 7.4) (Figure 64b). Understanding these charge distributions in $A\beta_{42}$ antigen and p-Tau antigen provides insights into their interactions with other molecules and their potential role in AD.

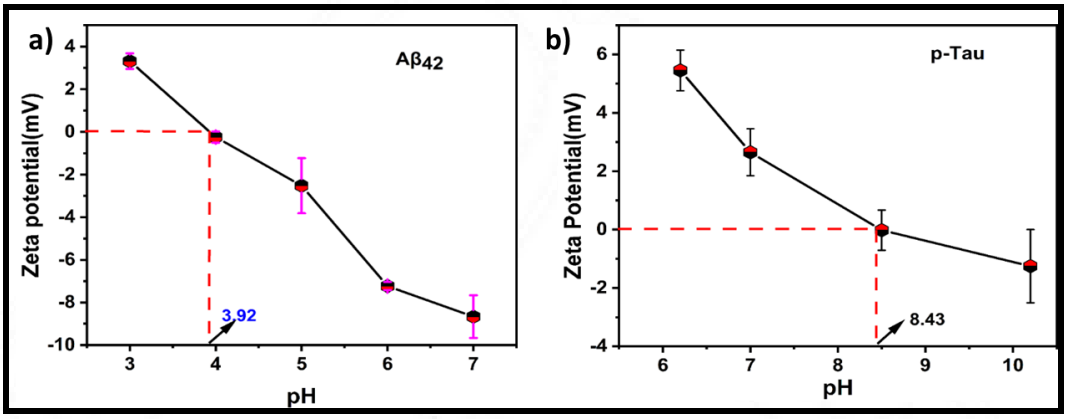

Figure 64. a) Isoelectric point value of $A\beta_{42}$ and b) p-Tau antigen

The local density of states (LDOS), is determined by the dI/dV curve at a modulation frequency of 2.5 kHz which depends on the relative positions of the Fermi levels (E_f). In the case of $A\beta_{42}$ antigen, the Fermi level is located close to the conduction (LUMO) edge indicating the n-type nature of the $A\beta_{42}$ antigen (Figure 65a). Conversely, in the case of p-Tau antigen, the fermi level is located close to the valance (HOMO) edge indicating the p-type nature of the p-Tau antigen (Figure 65b).

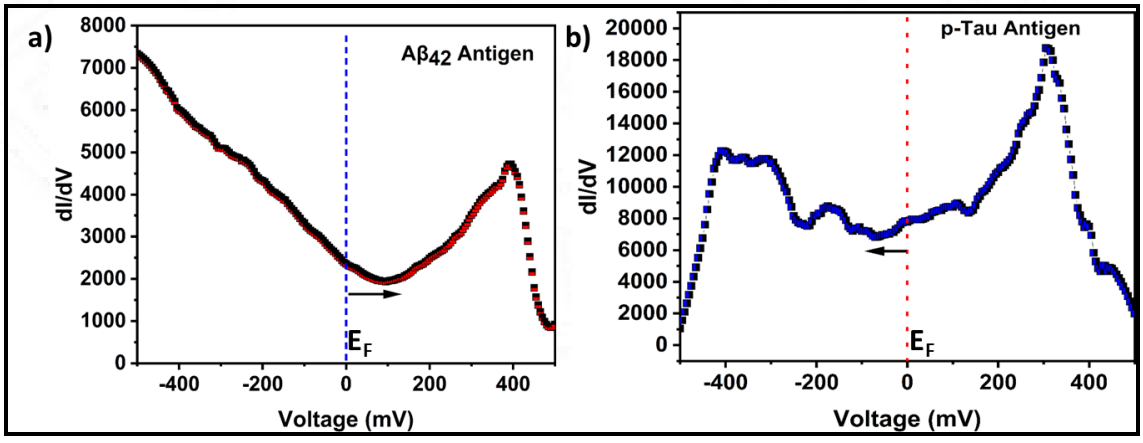

Figure 65. dI/dV spectra of a) $A\beta_{42}$ antigen and b) p-Tau antigen using STS measurement.

4.2.2 Antibody-antigen interaction in STM and STS

The surface charge of $A\beta_{42}$ and p-Tau antibodies is generally negative. This negative charge arises from the acidic amino acids, like aspartic acid and glutamic acid, present in the antibody. The interaction between the $A\beta_{42}$ antibody and antigen was observed through STM ((Figure 66 a & b) and STS ((Figure 66c). It reveals a negative current at zero voltage for the antibody, indicating its negative surface charge. Upon the addition of the $A\beta_{42}$ antigen, this negative current increases, likely due to a change in the electronic states near the Fermi level (Figure 66c). STM images display brighter edges after antigen addition, potentially reflecting a change in protein conformation or increased density at the edges upon binding (Figure 66b).

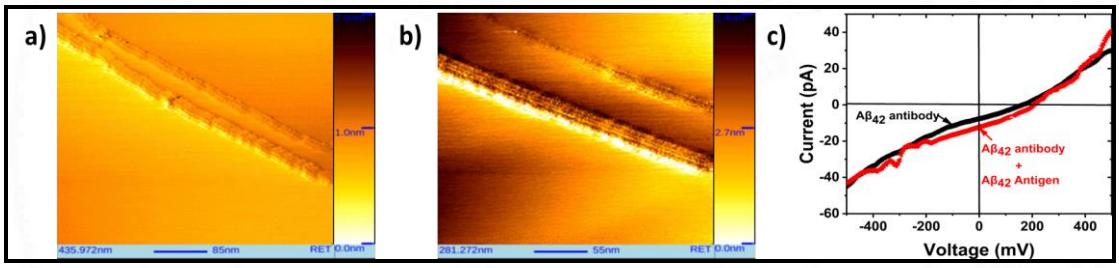

Figure 66. a) STM image of $A\beta_{42}$ antibody (scale bar: 85nm) b) $A\beta_{42}$ antibody and $A\beta_{42}$ antigen (scale bar: 55nm) on HOPG surface c) I-V spectra of $A\beta_{42}$ antibody and $A\beta_{42}$ antigen using STS.

The p-Tau antibody exhibits a negative current at zero voltage. However, introducing the p-Tau antigen, decreases this negative current likely due to the positive surface charge of p-Tau antigen (Figure 67c). Corresponding STM images for p-Tau showed darker spots after antigen addition, possibly due to changes in the electronic properties of the protein complex (Figure 67b).

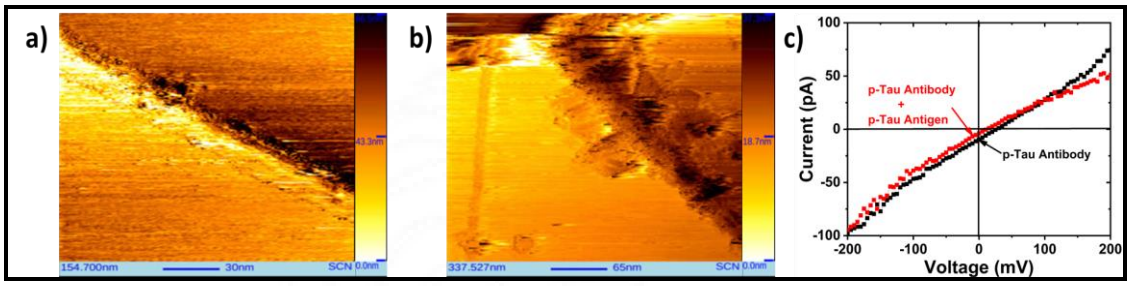

Figure 67. a) STM image of p-Tau antibody (scale bar 30nm) b) p-Tau antibody and p-Tau antigen (scale bar:65nm) on HOPG surface c) I-V spectra of p-Tau antibody and p-Tau antigen using STS.

4.2.3 Fabrication of the Interdigitated Electrode (IDE) sensor

The STM and STS measurements revealed that Aβ and tau proteins exhibit distinct conductivity properties. These differences in conductivity are attributed to their unique structural features. Based on these findings, we designed an Interdigitated Electrode **(**IDE) sensor with a modified electrode surface that selectively interacts with Aβ and tau, enabling their differentiation based on their surface charges. The preparation process involved functionalizing a cleaned glass slide with APTES, depositing a gold film with IDE pattern, treating the silanized slides with glutaraldehyde, immobilizing AuNPs and conjugating them with antibodies that serves as a biorecognition layer that can selectively bind to the target analyte. Figure 68 illustrates the fabrication steps of the IDE sensor platform, while Figure 69 shown a schematic representation of the IDE sensor platform.

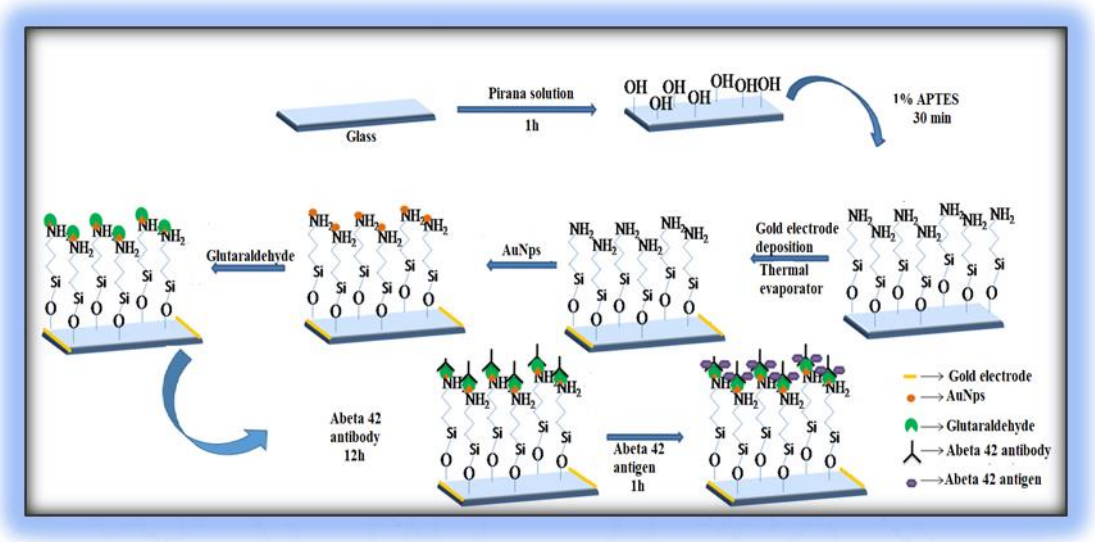

Figure 68. Schematic illustration of the fabrication steps of the IDE sensor platform

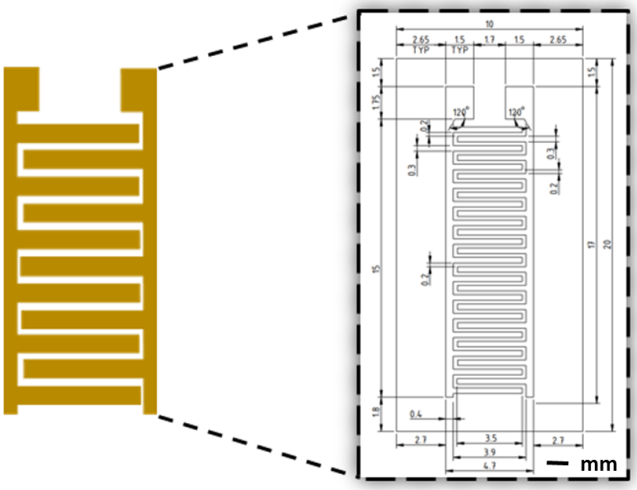

Figure 69. Schematic representation of IDE platform

Figure 70 shows the FTIR spectra of the glass slide chip functionalized step by step. Initially, the FTIR spectra of the bare glass slides showed a strong peak in the 1000–1100 cm^{-1} range, corresponding to the characteristic Si-O-Si peak. Following the addition of APTES, new peaks appeared at 3650, 2830–2950, 1730, and 1590 cm^{-1}, indicating the stretching vibrations of amine, aliphatic –CH, steric

carbonyl groups, and bending vibrations of amine groups, respectively. When AuNPs were covalently added to the APTES-modified glass slides, a new peak at 1647 cm^{-1} emerged, attributed to the formation of amide groups from the reaction between glutaraldehyde and the amine groups of chitosan and APTES. Additionally, a broad peak at 3200-3600 cm^{-1} was observed, associated with the OH and NH groups of chitosan. In the final step, after the addition of antibodies, the intensification of peaks at 3200–3600 and 1864–2922 cm^{-1} was due to the presence of amine, acid groups, and aliphatic C-H of the antibody. Peaks at 1642, 1690, and 1729 cm^{-1} were related to the amide, esteric, and acidic carbonyl groups of the antibody and chitosan. Thus, the step-by-step covalent addition of APTES to the glass slide, AuNPs to the APTES-modified glass slide, and finally, antibodies to the AuNPs-APTES glass slide were confirmed by the FTIR spectra (Majdi *et al.*, 2019).

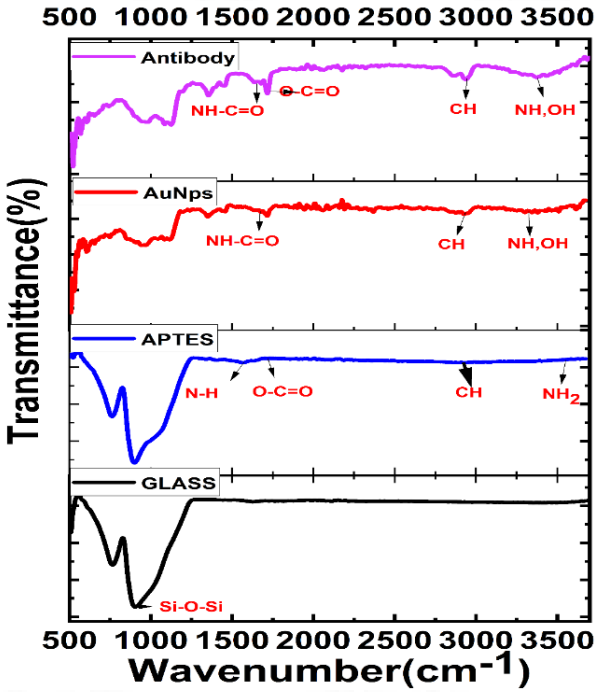

Figure 70. FTIR spectra of stepwise functionalization of IDE sensor platform

4.2.4 IDE sensor platform for $A\beta_{42}$ and p-Tau detection

Before detecting AD biomarkers in blood plasma, we evaluated the fabricated devices for their ability to detect AD biomarkers specifically in PBS solution. From the STS study, it was clear that $A\beta_{42}$ and p-Tau carry negative and positive surface charges at physiological pH, respectively, while both antibodies for $A\beta_{42}$ and p-Tau possess negative surface charges at the same pH. The IDE sensor's capability to detect $A\beta_{42}$ and p-Tau was validated using conductometric sensing with AuNPs. As illustrated in the figure 71a, an increase in $A\beta_{42}$ concentration from fM to μM led to a rise in net carrier density and current. Conversely, the presence of p-Tau caused a decrease in net carrier density due to the binding interaction between p-Tau and its antibody, attributable to their opposite charges (Figure 71b).

To calculate the sensitivity of $A\beta_{42}$ at varying concentrations (from μM to fM), the current changes on an $A\beta_{42}$ antibody-functionalized IDE surface were monitored. To nullify the baseline variations in the devices, the sensor response was calculated using the formula:

$$I_{Response} = I_{target} - I_0/I_0 \quad \ldots\ldots\ldots\ldots (1)$$

where I_{target} is the current measured in the presence of the antigen, and I_0 is the baseline current with the antibody-conjugated IDE surface.

The response of the $A\beta_{42}$ IDE sensor current ranged from 1.76 ± 0.244 for 2 μM to 0.33 μA ± 0.302 for 8.7 fM. For p-Tau, the response of the IDE sensor current was -0.7 ± 0.05 for 3.35 μM and -0.98 ± 0.025 for 8.3. The correlation coefficients (R^2) obtained were 0.951 for $A\beta_{42}$ antigens and 0.953 for p-Tau, respectively (Figure 71c & d).

The limit of detection (LOD) of biosensors is a crucial parameter determined statistically as described in Equation (2), where σ is the standard deviation of the blank and m is the slope of the calibration curve. The σ was found to be 0.0251. The slope for $A\beta_{42}$ was 8.41×10^{12} and for p-tau, it was 5.915×10^{12}. Therefore, the LOD of the sensors was calculated to be 8.95 fM for $A\beta_{42}$ and 12.76 fM for p-Tau.

$$LOD = 3\sigma/m \quad \ldots\ldots\ldots\ldots (2)$$

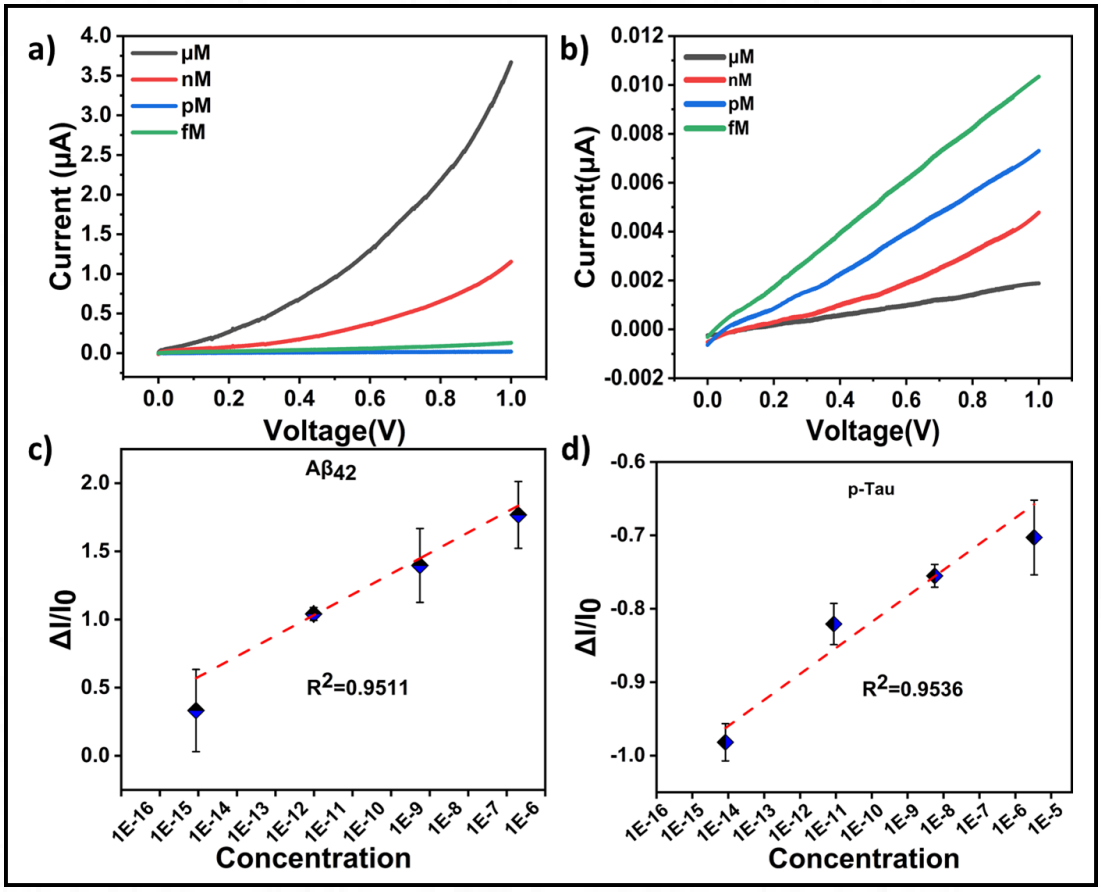

Figure 71. a) I-V spectra of $A\beta_{42}$ antigen b) p-Tau antigen at different concentrations c) linear regression graph of $A\beta_{42}$ and d) p-tau antigen

In addition to sensitivity, selectivity is another crucial parameter of a biosensor. To assess the selectivity of the developed sensor, it was tested with total-Tau (t-Tau) and Neurofilament light chain (NFL), other two biomarkers of AD. The

pI value of t-Tau is approximately 8.24, making it positively charged at a pH of 7.4, while the pI value of NFL is 4.62, rendering it negatively charged at the same pH (Bocquet *et al.*, 2009; D. Park *et al.*, 2020). When the $A\beta_{42}$ antibody-immobilized sensor was incubated with t-Tau, a non-specific protein with opposite electrical charges to the specific target, the current decreases. Additionally, because NFL carries a negative charge and is a non-specific protein, it is expected to introduce significant noise, complicating accurate detection when NFL interacts with the $A\beta_{42}$ antibody-immobilized sensor. So, the final response of the sensor was found to be negligible for t-tau and NFL antigen as compared to the response demonstrated for $A\beta_{42}$ antigen (Figure 72a).

The current response over time was also evaluated with varying concentrations of $A\beta_{42}$ antigen, ranging from µM to fM. It was found that the current remained almost constant for up to 800 s (Figure 72b). This constant current response suggests a strong, high-affinity interaction between the $A\beta_{42}$ antigen and the target molecule or surface. If the binding were weak, the molecules would likely dissociate over time, resulting in a decrease in current. This implies that all available $A\beta_{42}$ antigen molecules are bound, and additional amounts would not significantly change the current. By performing these tests, we can gain a clearer picture of the antigen-antibody interaction of the IDE sensor.

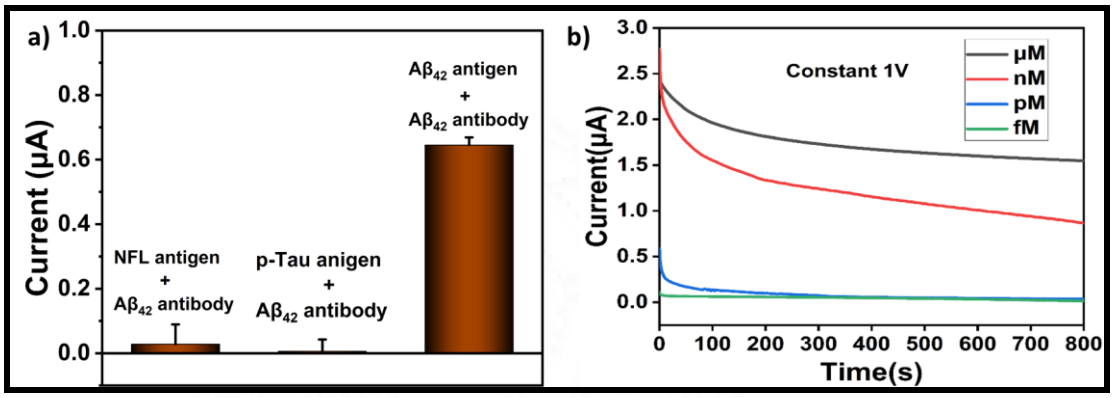

Figure 72. a) Selectivity of $A\beta_{42}$ antigen b) $A\beta_{42}$ antigen response at a constant voltage.

In biosensors, the antigen-antibody interaction is driven by various forces such as hydrogen bonds, van der Waals forces, hydrophobic interactions, and electrostatic forces between the epitope of the antigens and the paratope of the antibodies (Reverberi and Reverberi, 2007). Among these, electrostatic forces play a particularly important role. Antigens and antibodies, based on their surface charges, can either attract or repel each other, leading to the formation of complexes and changes in the overall charge of these complexes. Through STS analysis, it was observed that $A\beta_{42}$ and p-Tau shift the Fermi level in opposite directions due to their differences in pI and surface charge density. This change in surface charge affects the current density when the antigen is added to the IDE platform.

4.2.5 IDE sensor platform for AD biomarkers detection from clinical samples

We explored the clinical potential of our IDE platform by analyzing samples from individuals diagnosed with AD, those with mild cognitive impairment (MCI), and healthy controls. The IDE device was modified with antibodies specifically targeting $A\beta_{40}$, $A\beta_{42}$, p-tau181 and t-tau to demonstrate the sensor array's capabilities. As illustrated in Figure 73(a, b, c & d), the sensor arrays effectively distinguished between the different AD biomarkers. Previous research reported that the ratios of

$A\beta_{42}/A\beta_{40}$ and p-tau181/$A\beta_{42}$ serve as more precise diagnostic markers for predicting the progression of AD and differentiating AD patients from healthy individuals, due to the inverse relationship between tau protein levels and $A\beta_{42}$. Additionally, longitudinal studies have shown that the ratios of $A\beta_{42}/A\beta_{40}$ and p-tau181/$A\beta_{42}$ significantly increase approximately 15 years before the clinical symptoms of AD appear, whereas the level of $A\beta_{42}$ starts to decline around 10 years before symptom onset (Kim *et al.*, 2020).

In figure 73 e, f &g, we compared the blood plasma levels of composite biomarkers ($A\beta_{42}/A\beta_{40}$ and p-tau181/$A\beta_{42}$) among AD patients, MCI patients, and healthy control groups. The results revealed highly significant differences in the levels of composite biomarkers between the AD group and normal controls, as well as between the MCI group and normal controls. In contrast, when comparing the levels of single biomarkers, there were no significant differences in the levels of the $A\beta_{40}$ biomarker between the groups, whereas in the case of $A\beta_{42}$, p-Tau and t-Tau, differences were observed (Figure 73 a, b,c &d).

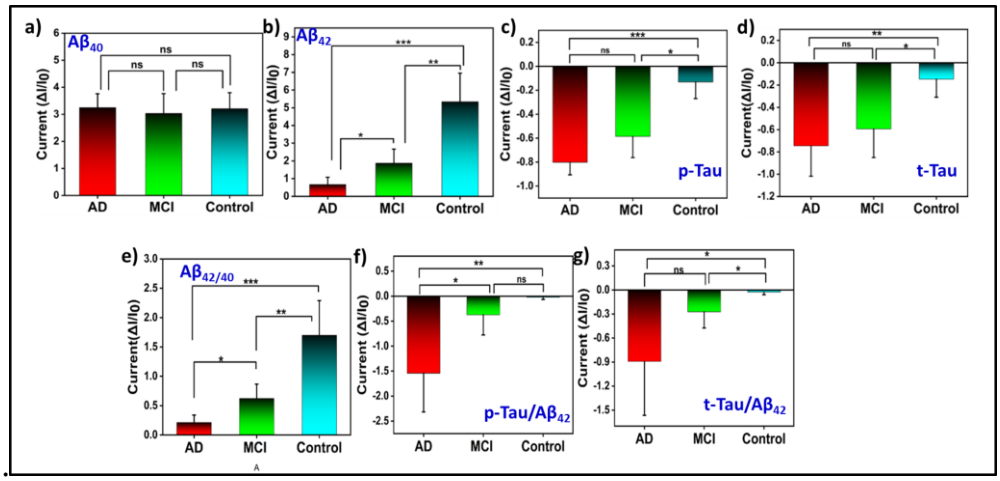

Figure 73. Clinical evaluation of AD biomarkers in blood plasma samples a) $A\beta_{40}$ b) $A\beta_{42}$.c) p-Tau, d) t-Tau, e) $A\beta_{42/40}$, f) p-Tau/ $A\beta_{42}$ and g) t-Tau/$A\beta_{42}$ of AD, MCI and healthy control.

4.2.6 Development of a Readout Circuit for a Portable Biosensor

As a final step toward developing a portable biosensor for detecting and quantifying AD markers in clinical settings, a simple readout circuit was assembled using a microcontroller, an LCD display, and a potentiometer (Figure 74). The system measured current by inducing a voltage drop (V) across the biosensor and calculating the resistance (R), with the current (I) determined using Ohm's law (I = V/R). The current values before and after introducing the antigen were recorded as I_o and I_{target}, respectively.

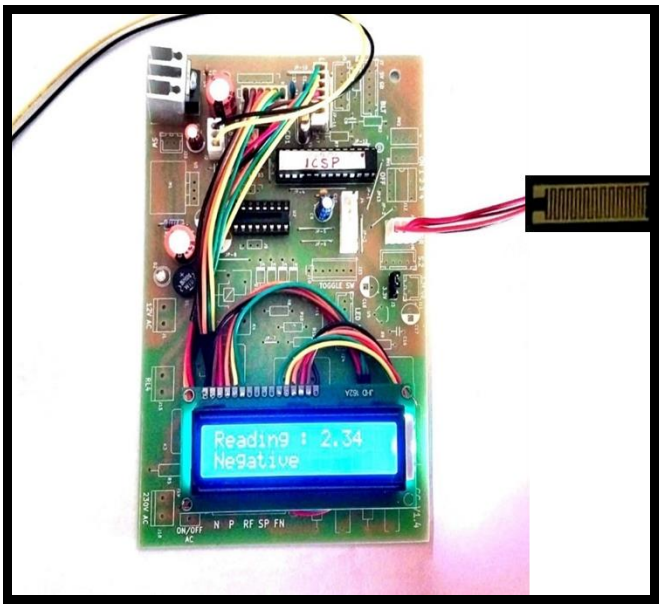

Figure 74. Diagram showing the assembled read-out circuit

The algorithm then calculated the sensor's response, $I_{response}$, using the formula $(I_{target} - I_o)/I_o$, after performing a conditional check. This allowed the estimation of AD biomarker concentration. The biosensor operated at a potential of 1 V, achieved through a voltage divider circuit designed to maintain this voltage across the biosensors.

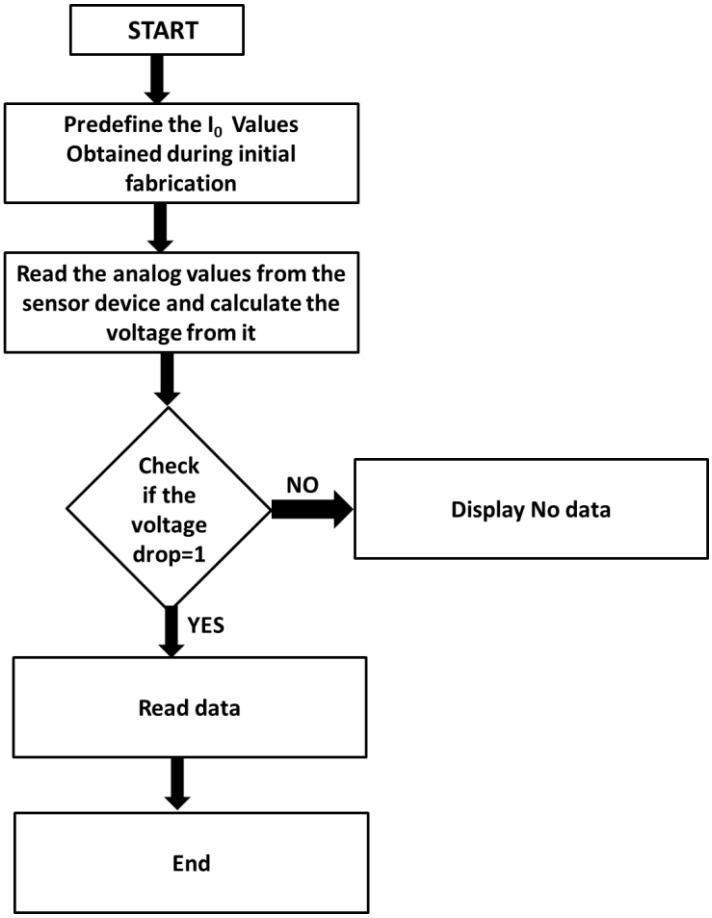

Figure 75. Flowchart of the algorithm developed for the detection of AD biomarker concentrations

Due to slight variations in the baseline resistance of each biosensor, the potential divider circuit needed adjustment to ensure accurate current measurement. A potentiometer was used to match the resistance of the biosensor to the circuit, ensuring accurate calculation of I_{target}. The readout circuit captured the $I_{response}$, which was then processed by the algorithm loaded onto the microcontroller to calculate the AD biomarker concentration.

The logic of the algorithm is illustrated in the flowchart (Figure 75), which outlines the condition checks for each subroutine, determining the AD biomarker concentration detected by the sensor. This proof-of-concept device offers a promising

alternative to bulky benchtop equipment, with a miniaturized and compact interface capable of quantitative analysis.

Finally, this research introduces a novel, high-performance platform for early AD biomarker detection by leveraging the unique surface charge properties of Aβ and tau proteins. By combining STM, STS and electronic immunoassay, we developed a sensitive and selective sensor capable of accurately distinguishing AD patients from healthy individuals. A technology lead based on the concept of electronic sensor has been arrived. This innovative technology holds immense promise for improving early diagnosis and treatment strategies for AD.

In conclusion, we have successfully developed two innovative biosensors specifically designed for the diagnosis of AD. These biosensors hold significant potential for early detection which is a critical factor in ensuring effective disease management.

4.3 Development of Blood-Brain Barrier permeable nanocarriers for Imaging and Inhibition of Amyloid Beta Fibrillization

Further to the development of biosensors, we have also implemented a nanomaterial-based strategy aimed at the management of AD. In particular, we have utilized gold nanoclusters in this attempt, whose unique properties could offer an enhanced therapeutic approach for AD management.

One of the significant factors identified as the cause of AD is the conversion of amyloid beta (Aβ) peptide from physiological monomeric forms to amyloid fibrils which are abnormal structures observed in patient's brain during the progress of the disease. Therefore, therapeutic strategies focusing on the inhibition/disintegration of Aβ fibrils are promising approaches for the prevention and treatment of AD. Nanotechnology offers advancement in the field of drug delivery and imaging moieties. In this regard, a novel approach for the management of AD was developed with the introduction of metallic nanoclusters. The multi-function nanoprobes were prepared using a suitable ligand which is proven to interact with the Aβ peptide through thiophilic interactions, so that the ligand molecule chosen acts as a drug to inhibit Aβ fibrillization. The biocompatible nature and ultra-small size of metallic nanoclusters facilitate their facile penetration through the BBB. Moreover, the intrinsic fluorescence of these nanoclusters renders them suitable for biomedical imaging applications. In this context, this study investigates the effectiveness of Cysteine gold nanoclusters (Cy-AuNCs) in

preventing Aβ fibrillization. These nanoclusters are engineered for targeted delivery across the BBB and leverage the inherent fluorescence of the gold clusters for bio-imaging. The present study offers significant insights into the potential of Cy-AuNCs as a promising therapeutic agent for AD.

4.3.1 Design of self-assembled Cysteine gold nanocluster (Cy-AuNCs) and its characterization

The development of facile Cy-AuNCs was carried out using a simple one-pot microwave synthesis (Figure 76). Microwave-assisted synthesis has emerged as a highly efficient technique for the production of nanomaterials. By significantly reducing reaction time and enhancing both yield and consistency, this method enables the fabrication of uniform nanostructures with precise control over size and composition. Highly fluorescent Cy-AuNCs was prepared using L-cysteine, which acts as both ligand and reducing agent. Due to the strong affinity of L-Cysteine (L-Cys) for gold ions and its role as an energy-harvesting antenna for emissive centers, this ligand and technique enabled the creation of highly fluorescent Cy-AuNCs.

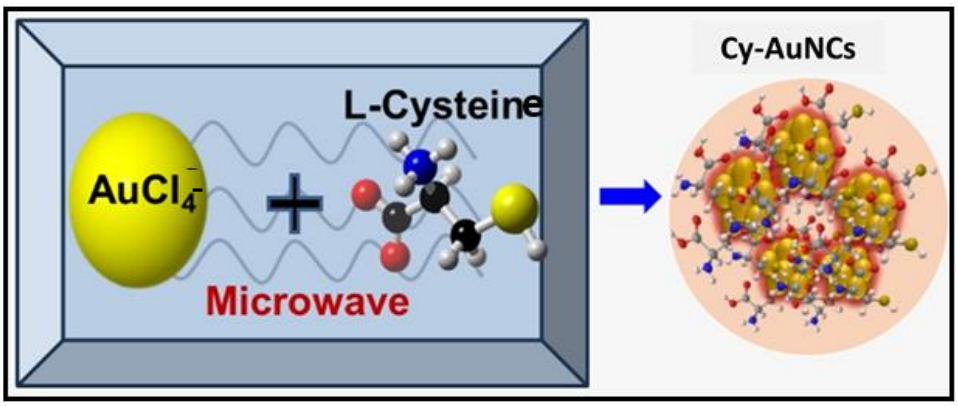

Figure 76. Schematic representation of the microwave-assisted synthesis of Cy-AuNCs.

The HR-TEM image of the synthesized Cy-AuNCs exhibited self-assembled structures composed of monodispersed clusters (Figures 77a & b). The proximity and arrangement of these nanoclusters within the self-assembled structures can result in inter-cluster coupling, influencing the optical and electrical properties of the synthesized Cy-AuNCs. A schematic representation of the self-assembled architecture of Cy-AuNCs is shown in Figure 77c. The average particle size of the prepared Cy-AuNCs was determined to be 3 nm. In the UV-visible spectrum, Cy-AuNCs displayed a prominent absorption peak at 385 nm (Figure 77d). When compared to gold nanoparticles, a blue shift in the absorption of the Cy-AuNCs was observed which arises from the quantum confinement of the gold nanoclusters at the atomic size range, along with the contribution from the capping material, L-Cys. Elemental mapping analysis showed a homogeneous distribution of Au, S, O, N, and C (Figure 77e). The FTIR spectrum of L-cysteine exhibited characteristic peaks at 2549, 1580, and 1530 cm^{-1}, corresponding to the stretching band of -SH, asymmetric stretching band of COO-, and bending vibrations of -NH, respectively (Krisnawati *et al.*,

2021) (Figure 77f). In the Cy-AuNCs, FTIR peaks of cysteine showed minor shifts due to changes in the dipole moment of cysteine conjugated to metallic nanoclusters. The diminished intensity of the characteristic thiol (-SH) peak of L-cysteine (2549 cm^{-1}) in the FTIR spectrum of Cy-AuNCs confirmed the binding of L-cysteine with gold (Au−S bond).

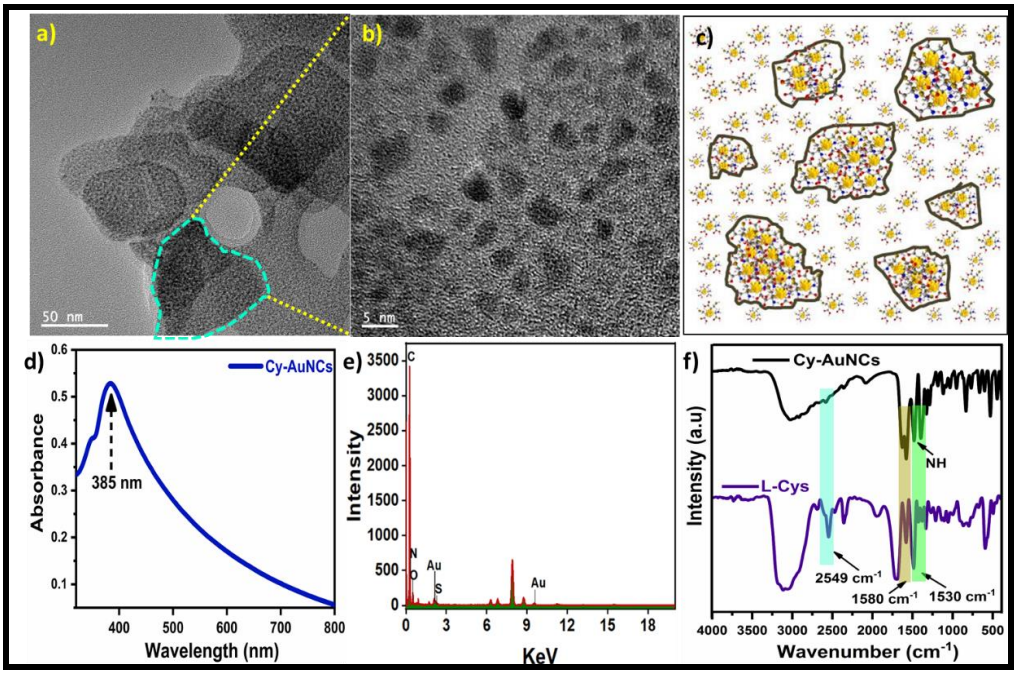

Figure 77. Physico-chemical characterization of Cy-AuNCs. a) HR-TEM image of the self-assembled Cy-AuNCs, b) Higher magnification image of the Cy-AuNCs. c) Scheme representing the nanoarchitectonics of Cy-AuNCs in the self-assembled structures. d) UV-visible absorption spectrum of Cy-AuNCs. e) EDX spectra of Cy-AuNCs and f) FTIR spectra of L-Cysteine and Cy-AuNCs

MALDI-MS analysis provided insights into the ionization of the cluster and the quantification of atoms and ligands present within the nanocluster. The number of core atoms and ligands influences the optical characteristics of the cluster. Based on prior observations of emission and absorption, the Cy-AuNCs in this study is assigned to have 13 core gold atoms (Negishi and

Tsukuda, 2003; Chang *et al.*, 2017). Corresponding to the assigned core atoms, the number of ligands was calculated as four from the MALDI spectra (Figure 78a). The cluster composition was estimated to be $[Au_{13}(L\text{-}Cys)_4]$. Further investigation of the oxidation states and chemical interactions between L-cysteine and metallic gold was carried out using X-ray photoelectron spectroscopy (XPS) as illustrated in figure 78b. The Au 4f peak was resolved into spin-orbit components. The binding energies (BE) of the Au $4f_{7/2}$ and $4f_{5/2}$ peaks at 84.5 and 88.2 eV, respectively, fall between the BE of Au (0) in metallic gold (84 eV) and Au(I) in gold thiolate (85 eV), indicating the coexistence of Au (0) and Au(I) in Cy-AuNCs. The 3.7 eV binding energy gap between these peaks suggests that Cy-AuNCs is trapped within the L-cysteine framework. A detailed analysis of Au $4f_{7/2}$ revealed that the photoemission phenomenon depends on core and surface atoms. Negishi et al. observed that the peak position representing the inner Au shifted monotonically from 84.0 to 84.3 eV with a reduction in core size, thereby decreasing the kinetic energy of the outgoing photoelectron (known as the 'final-state effect') (Negishi, Nobusada and Tsukuda, 2005; Russier-Antoine *et al.*, 2016). Conversely, the peak position of the surface Au atoms shifted to higher energy, ranging from 84.3 to 84.7 eV, attributed to an 'initial state effect,' where electron donation occurs from the surface Au atoms to the thiolates. For the Cy-AuNCs in the current study, the peak position of Au $4f_{7/2}$ was at 84.5 eV, within the range of 84.3-84.7 eV. Therefore, it is plausible to attribute the observed chemical changes primarily to the initial-state effect.

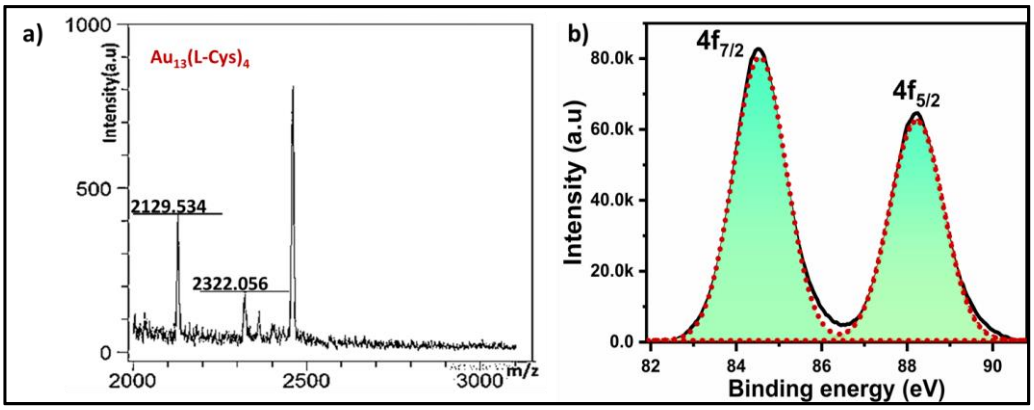

Figure 78. a) MALDI-MS spectral data of Cy-AuNCs b) XPS spectral data of Au 4f of Cy-AuNCs.

4.3.2 Fluorescence property of Cy-AuNCs

The Cy-AuNCs showed a strong fluorescence emission at 610 nm and a shoulder peak at 665 nm (Figure 79a) resulting from the quantum confinement and molecular-like features of the nanocluster. CIE plot (Chromaticity Diagram) was used to study the optical emission characteristics of the Cy-AuNCs. The sensitivity of the fluorescence emission was inferred from the chromaticity diagram, which allowed for the analysis of the colour transparency of the emission. Accordingly, the colour sensitivity expressed in CIE coordinates (0.435, 0.388) shows the emission from the cluster for the excitations at 385 nm (Figure 79a inset). The distribution of optical energy over the fluorescence spectrum is analyzed using the corresponding power spectrum (Figure 79b). The fluorescence intensity of Cy-AuNCs was evaluated for 6 months (Figure 79c) for any signs of aggregation. No significant loss in the fluorescence intensity was observed proving the long-term stability of the material. The interference from the excitation light was minimal due to the large Stokes shift of 225 nm exhibited by the Cy-AuNCs (Figure 79d) which is very advantageous for optical imaging applications. Additionally, Cy-AuNCs

is an excellent candidate for biomedical imaging due to their inherent red emission in a variety of media (water, cell culture media (DMEM), and saline) increasing its scope for multiple applications (Figure 79e). The time-resolved decay time of Cy-AuNCs was measured at excitation and emission wavelengths of 344 and 610 nm respectively. The photoluminescence lifetime was measured to be 0.16 μs (Figure 79f, Table 6).

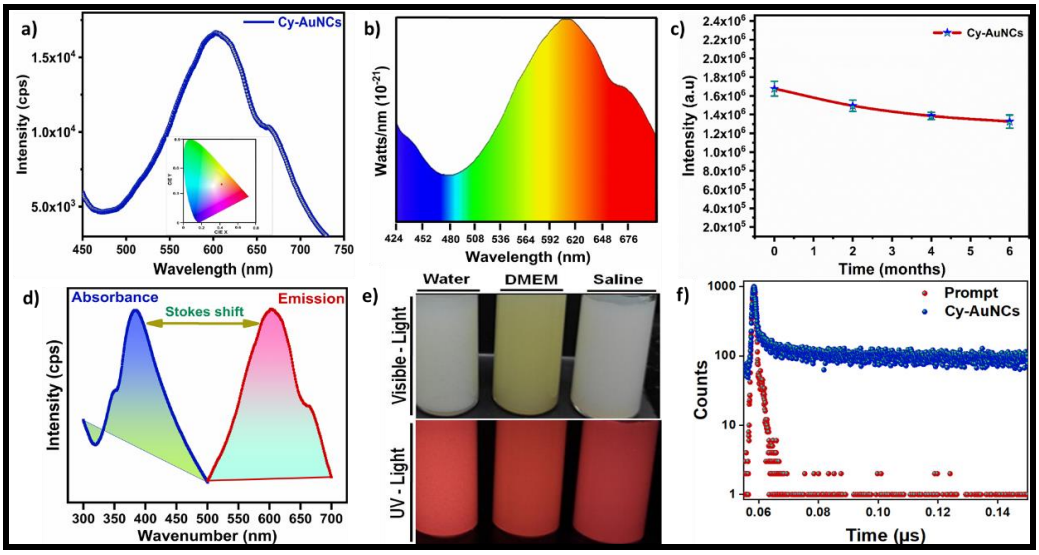

Figure 79. Optical property of Cy-AuNCs. a) Fluorescence spectrum of Cy-AuNCs and inset shows chromaticity diagram, and b) the corresponding power spectrum c) Photostability of Cy-AuNCs over 6 months, d) Stokes shift between the emission and excitation peak of Cy-AuNCs and e) Orange-red fluorescence emission of Cy-AuNCs in various media under visible and UV light, and f) Fluorescence lifetime measurements of Cy-AuNCs

Table 6. Lifetime measurement

$$\tau = A_1 \tau_1^2 + A_2 \tau_2^2 + A_3 \tau_3^2 / A_1 \tau_1 + A_2 \tau_2 + A_3 \tau_3$$

Sample	**λ_{em}**	**τ_1 (ns)**	**A_1(%)**	**τ_2 (ns)**	**A_2(%)**	**τ_3(ns)**	**A_3(%)**	**χ^2**
Cy-AuNCs	610	6.35	2.9	161	49.64	0.019	47.45	1.18

Additionally, the Quantum yield (QY) of Cy-AuNCs was determined to be 7.2% when compared to Rhodamine 6G (QY: 95%) (Table 7). The prepared Cy-AuNCs exhibited better QY compared to many of the previously reported metal clusters (Wen *et al.*, 2012; Zhang *et al.*, 2015; Han *et al.*, 2020).

Table 7. Quantum yield measurement of Cy-AuNCs

Sample	**Refractive index(η)**	**Quantum yield (Q) (%)**
Rhodame 6G	1.36 (ethanol)	95
Cy-AuNCs	1.33 (Water)	7.2

The quantum yield was calculated based on the following equation:

$$Q_x = Q_R \times I_x/I_R \times A_R/A_x \times \eta^2{}_x/\eta^2{}_R$$

Where, Q is quantum yield, I is the integrated PL intensity of the sample, A is the absorbance intensity, η is the refractive index for the solvent, x means as-prepared Cy-AuNCs, and R refers to Rhodamine 6G as reference fluorophore.

4.3.3 Aggregation Induced Emission property of Cy-AuNCs

Based on the HR-TEM image, the distinctive structures created by the gold clusters suggest the possibility of self-assembly (Figure 77a). The formation of such aggregates can be due to intermolecular interactions, which occur when molecules or particles come into proximity and interact through intermolecular forces that lead to unique nanoarchitectonics of individual units into larger structures or aggregates. It can also be due to the solvent effect in which the properties of solvent such as polarity, hydrogen bonding and viscosity affect

the intermolecular interactions that lead to the formation of self-assembled nanoarchitectonics (Luo *et al.*, 2012; Goswami *et al.*, 2016; Jin *et al.*, 2022). The exact mechanism behind aggregation-induced emission (AIE) in Cy-AuNCs is not yet fully understood, but it is believed to be related to the restriction of intramolecular motions or the suppression of non-radiative energy relaxation pathways upon aggregation. The close packing of the clusters is expected to limit the rotation or vibration of certain molecular segments, leading to enhanced radiative decay and higher emission intensity. To confirm the contribution of AIE, and the reason behind it, we performed a solvent effect study. Initially, the emission spectrum of Cy-AuNCs was investigated in different water: ethanol fractions (f_w). Intense emission was observed with increased f_w without any peak shift (Figure 80a). However, the emission behaviour was not observed in 100% ethanol. In high f_w, the Cy-AuNCs is expected to come closer due to intermolecular interactions resulting in larger assemblies, which can exhibit enhanced fluorescence due to AIE. To validate the observed aggregation behaviour, the absorbance of two different water: ethanol fractions (80 & 99%) with Cy-AuNCs was analyzed (Figure 80b). In the visible region, a level-off tail was observed in water dominant solution, which was not the case with ethanol dominant solution. This clearly indicates the formation of solvent effect -induced aggregation, and these results are in accordance with the previous report.

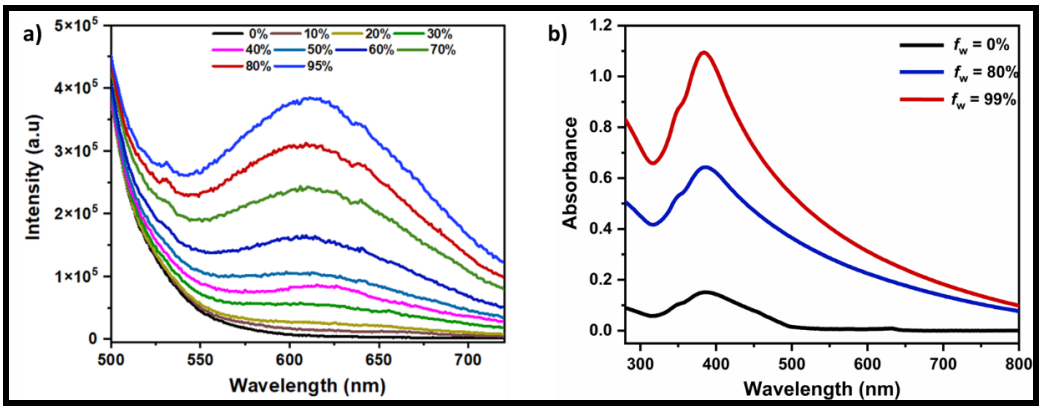

Figure 80. a) Fluorescence spectra of Cy-AuNCs in water:ethanol mixtures with different f_w values b) Absorption spectra of Cy-AuNCs in water:ethanol mixtures with different f_w values. Level-off tail observed in f_w -80 and 99% whereas it is not observed in f_w -0%

4.3.4 Photosensitizing property of Cy-AuNCs

Photodynamic therapy is a minimally invasive therapeutic approach for cancer treatment, utilizing light-activated photosensitizers (PSs) to generate cytotoxic free radicals or reactive oxygen species (ROS). Despite its promising potential, the therapeutic efficacy of PDT is limited by the inherent challenges associated with conventional PSs thereby hindering its widespread applications. Conventional PSs were expected to have the following critical requirements: (i) The ability to absorb light within the therapeutic range (600-800 nm), ii) The high probability of intersystem spin-crossing, facilitating the efficient population of the triplet excited state, iii) Larger energy gap between the T1 and S0 states (>0.98 eV), corresponding to the energy needed to activate molecular oxygen. Even though, the porphyrin-based PSs satisfies the critical requirements, their insoluble nature hinders their clinical translation in biological media, no selectivity to the tumor site and their PS effectiveness relies on oxygen atmosphere which restricts its application in the hypoxic

tumor(Drzewiecka-Matuszek and Rutkowska-Zbik, 2021). The nanocluster has emerged as an efficient PSs to overcome the limitations of conventional PSs. Hence, the photosensitizing property of Cy-AuNCs was investigated by evaluating its optical and electrochemical bandgap. The optical band gap of Cy-AuNCs from *tau* plot was calculated to be 1.15 eV (Figure 81a). Similarly, the electrochemical bandgap was 1.56 eV and the redox potential of the conduction band (E_{CB}) and valence band (E_{VB}) are determined to be -0.81 and 1.68 eV respectively (Figure 81b). Notably, E_{CB} lies below the reduction potential (E^o) of $O_2/^{\bullet}O_2^-$ (-0.16 eV), suggesting efficient energy transfer to adjacent O_2 molecules to generate reactive oxygen species (He *et al.*, 2014).

The potential of Cy-AuNCs for generating radicals was demonstrated using a model dye DPBF. DPBF is a molecular probe used to determine the PDT efficacy and it reacts with singlet oxygen radical and result in reduction of DPBF intensity at 407 nm. The interaction of Cy-AuNCs with DPBF for 5 min exhibited no significant decrease in the absorbance, which showed the negligible role of adsorption (Figure 81c). Similarly, laser irradiation alone showed no obvious change in the DPBF absorbance (Figure 81d), whereas, in the presence of both Cy-AuNCs and laser irradiation (180 s), an obvious decrease in absorbance upto 60% was observed (Figure 81 e and f). This result suggests the photosensitizing property of Cy-AuNCs.

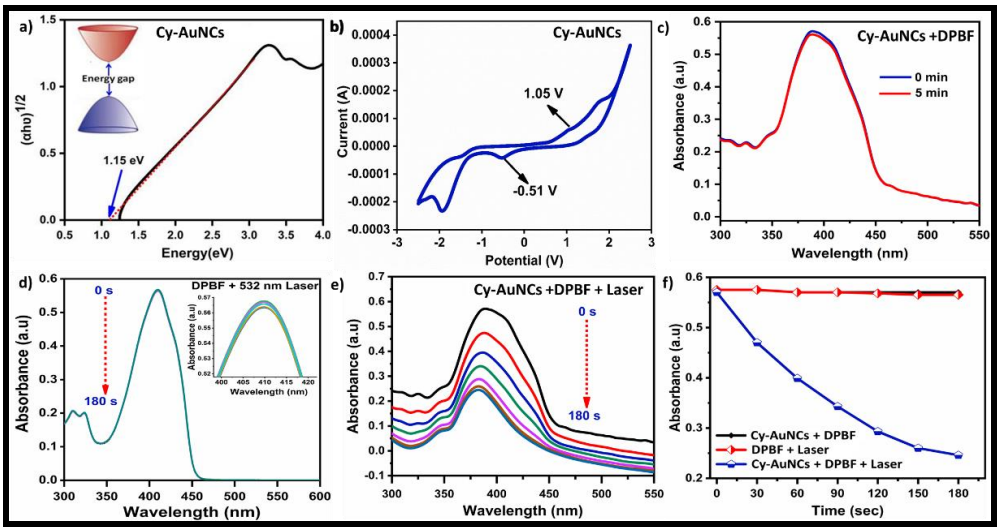

Figure 81. Evaluation of Photosensitizing property of Cy-AuNCs. a) Plots of $(\alpha h\upsilon)^{1/2}$ and photon energy ($h\upsilon$) for the band gap energy, b) CV curve of Cy-AuNCs, c and d) represent absorption spectra of Cy-AuNCs and DPBF under 532 nm laser irradiation (0.3 W/cm$^{2)}$ for 180 s. e) decrease in absorption of Cy-AuNCs under 532 nm laser irradiation f) normalized decay curves of the absorption density at 407 nm.

4.3.5 Development of Aβ fibrils

In this study, the $A\beta_{42}$ peptide, a precursor to amyloid fibrils, was used to generate initial Aβ fibril samples. Fibrillization was monitored over time using the Thioflavin T (ThT) dye assay, which is a fibril specific dye that is a standard method used to confirm the activity of Aβ peptide. ThT emission gets enhanced when it is bound to Aβ fibrils. ThT has a single C-C bond connecting its benzothiazole and aniline rings. Around this C-C bond, the two aromatic rings can freely rotate. ThT may relax from its radiative locally energized (LE) state to a non-radiative charge transfer (CT) state upon excitation because of this rotation. The molecular rotor behaviour of ThT is caused by a phenomenon, known as twisted-internal-CT (TICT), which also causes quenching of ThT fluorescence. When ThT attaches to an amyloid fibril, the rotation around the C-C bond is blocked and the TICT process is consequently

hindered. As a result, the relaxation from the radiatively excited state to the ground state produces ThT fluorescence (Qin *et al.,* 2017; Xue *et al.,* 2017). This feature is used for the detection of various fibrillization stages of Aβ. Emission studies were performed at an excitation wavelength of 440 nm which corresponds to the absorption peak of ThT. As shown in figure 82, fibrillization progressively increases over a period of 0 to 72 h.

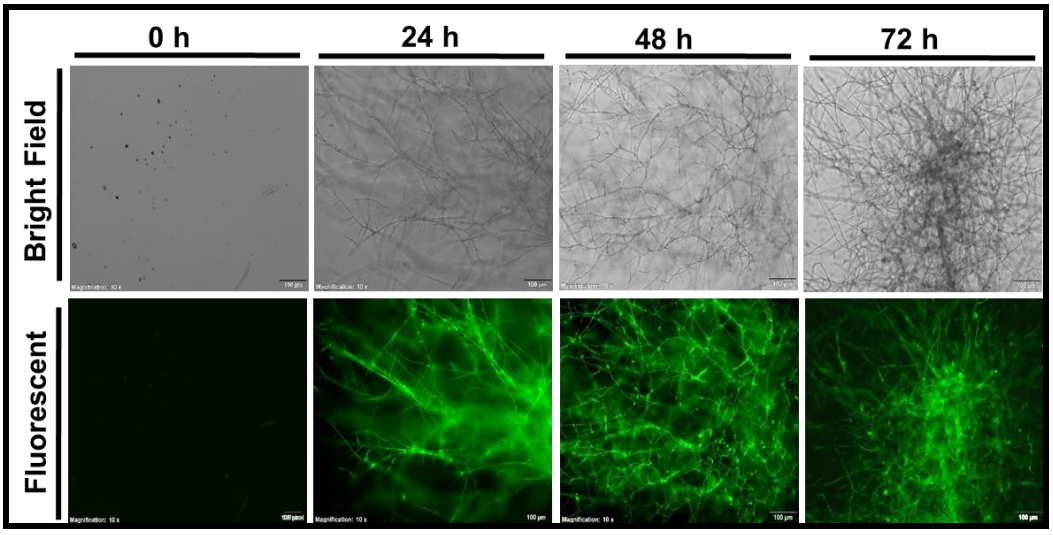

Figure 82. Thioflavin T-stained fluorescence images of $A\beta_{42}$ samples at different periods. Scale bar of all the images are 100 µm.

4.3.6 Interaction of Cy-AuNC with Aβ fibrils and Aβ defibrillization kinetics

Although numerous studies have explored the use of nanoparticles for targeted drug delivery in AD, the interactions between nanomaterials and AD-associated Aβ plaques or fibrils remain under investigation. Previous research has indicated that cysteine, a compound containing sulfhydryl groups, can inhibit amyloid fibril formation through thiophilic interactions (Takai *et al.*, 2014b). These interactions are non-covalent and occur between a sulfur-containing compound and the aromatic amino acids of a protein in solution.

The strength of thiophilic interactions is notably greater with bi-continuous aromatic residues (such as Trp-Trp, Phe-Phe, or Tyr-Tyr) than with single aromatic residues (like Trp, Phe, or Tyr) (Takai *et al.*, 2014b).

Defibrillization kinetics study was performed by incubating Cy-AuNCs at different concentrations (20, 40 and 60 µg/mL) to evaluate their efficacy in inhibition of fibrils. During the experiments, the $A\beta_{42}$ peptide was dissolved in 10 mM NaOH solution and was incubated at 37 °C without any addition of nanocluster, the ThT fluorescence exhibited a sigmoidal pattern over time (black curve in Figure 83a), consistent with the standard nucleation-growth process. Notably, the presence of Cy-AuNCs in the $A\beta_{42}$ solution resulted in significant inhibition of Aβ fibrillization, as indicated by a 14% and 11% ((40 and 60 µg/mL concentration) reduction in the maximum ThT fluorescence intensity compared to the control (green and blue curves in Figure 83a). This indicates that Cy-AuNCs hinder Aβ fibrillization by prolonging the lag phase and decreasing the aggregation rate. It is important to highlight that the unbound sulfhydryl groups in Cy-AuNCs inhibit Aβ fibrillization due to their thiophilic interactions with Aβ in solution. In addition to the conformational transition, the influence of Cy-AuNCs on the morphological changes of Aβ fibrillization is examined using fluorescence microscopy. The fibril formation was significantly decreased in the Cy-AuNCs incubated wells (40 and 60 µg/mL) compared to the control. Lower concentration of 20 µg/mL of Cy-AuNCs did not show a significant reduction in fibril formation (Figure 83 a and b). This demonstrates the excellent efficacy of Cy-AuNCs in inhibiting Aβ fibrillization.

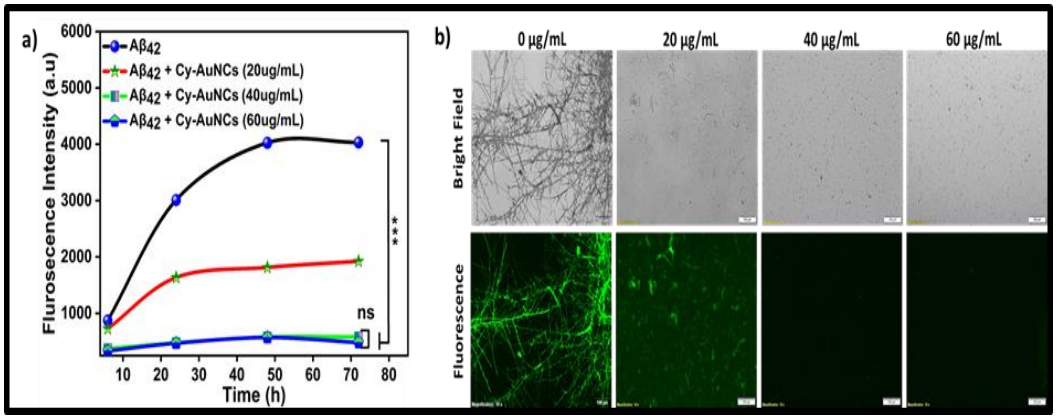

Figure 83. Aβ Fibrillization inhibition assessment of Cy-AuNCs. a) Quantification of respective ThT fluorescence intensity and b) The fluorescence micrograph of Aβ fibrillization with Cy-AuNCs at different concentrations. The scale bar is 100 µm in all cases

The effect of Cy-AuNCs on the inhibition of Aβ fibril formation was further confirmed through circular dichroism (CD) spectroscopy. In control, Aβ fibrils typically exhibit a β-sheet-rich structure, characterized by a positive CD peak at 197 nm and a negative minimum at 216 nm (black curve in Figure 84) (Hou *et al.*, 2020). The addition of Cy-AuNCs (20, 40, 60 µg/mL), the structural transition of Aβ from its native random coil to β-sheet conformation in solution was potentially hindered. This observation further supports the inhibitory action of Cy-AuNCs.

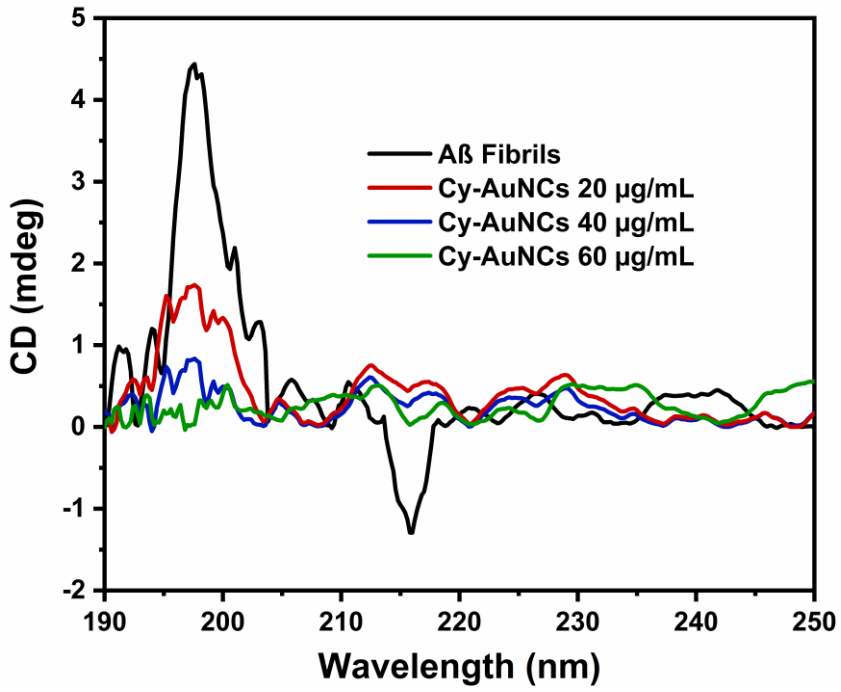

Figure 84. CD spectra of Aβ in the absence and presence of Cy-AuNCs.

The presence of unbound sulfhydryl group in Cy-AuNCs was confirmed by XPS analysis. The deconvoluted S2p peaks revealed two distinct peaks at 162.8 eV and 164.1 eV, which correspond to bound and unbound thiol groups, respectively (Castner, Hinds and Grainger, 1996) (Figure 85a). The $S2p_{3/2}$ peak at 162.8 eV indicates sulfur atoms bonded to the gold surface as thiolate species, while the peak at 164.1 eV represents unbound sulfur, suggesting the presence of free or unbound thiol on the surface of Cy-AuNCs.

To further explore the interaction of sulfhydryl groups in Cy-AuNCs with Aβ, a docking study was performed using Patch Dock and analyzed with the BIOVIA Discovery Studio visualizer (Figure 85b). The results demonstrated a strong interaction between Cy-AuNCs and Aβ, forming four contacts mediated by hydrogen bonding (Phe19, bond length 2.29 Å), S-type

hydrogen bonding (GLN15, bond length 1.75 Å), and two Van der Waals interactions (LYS16, VAL12). The thiophilic interaction is expected to efficiently inhibit amyloid fibril formation, particularly involving the core sequence of Aβ peptide (KLVFF, 16-20), where phenylalanine ('FF') may interact with sulfur compounds, as supported by molecular docking data. The strong interactions between cysteine and 'FF' in Aβ peptides during nucleus formation may be crucial for the inhibitory effect. This is verified by results showing that, the presence of cysteine increases the lag time of fibril formation, indicating a significant impact on nucleus formation. Thus, cysteine derivatives or peptides containing cysteine residues could be effective in inhibiting fibril formation.

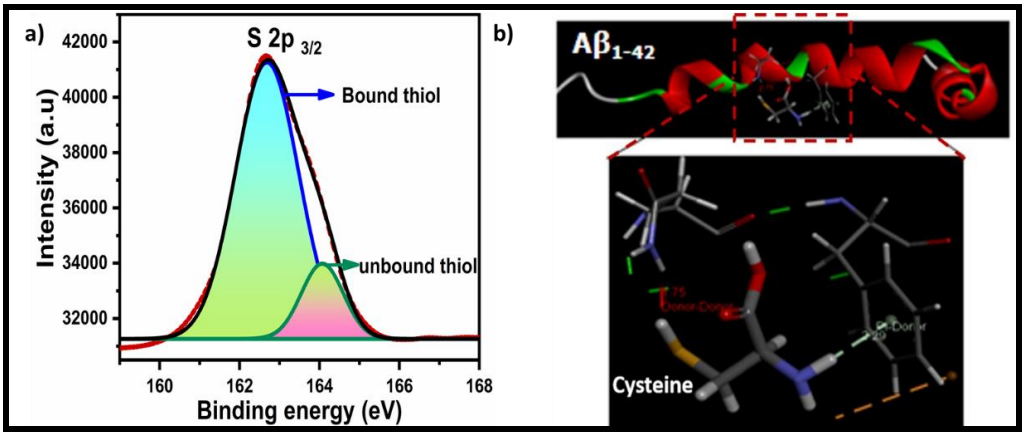

Figure 85. a) XPS deconvoluted S 2p spectra of Cy-AuNCs b) Molecular interaction of Cy-AuNCs with Aβ

4.3.7 In vitro Aβ fibrillization studies

4.3.7.1 Inhibition of Aβ fibrillization

To examine the therapeutic effect of Cy-AuNCs, an *in vitro* Streptozotocin (STZ) induced AD model was developed in Neuro2A cells. The mouse neuronal Neuro2A cells were treated with 1000 μM STZ for 48 h. This

treatment induces AD like conditions like decrease in choline levels, increased acetylcholinesterase (AChE) activity, tau phosphorylation, and amyloid aggregation which significantly reduces the cell viability (Biswas *et al.*, 2016). The formation of extracellular Aβ fibrils were observed using the ThT assay (Figure 86). STZ treatment significantly increased the accumulation of Aβ fibrils. In contrast, cells co-incubated with Cy-AuNCs effectively mitigated STZ-induced Aβ fibrillization. Additionally, laser irradiation-induced ROS generation *via* the photodynamic effect further enhanced the inhibitory effects of Cy-AuNCs on Aβ fibrillization. These results collectively demonstrate the efficacy of Cy-AuNCs in inhibiting the formation of Aβ fibrils and enhancing the cell viability.

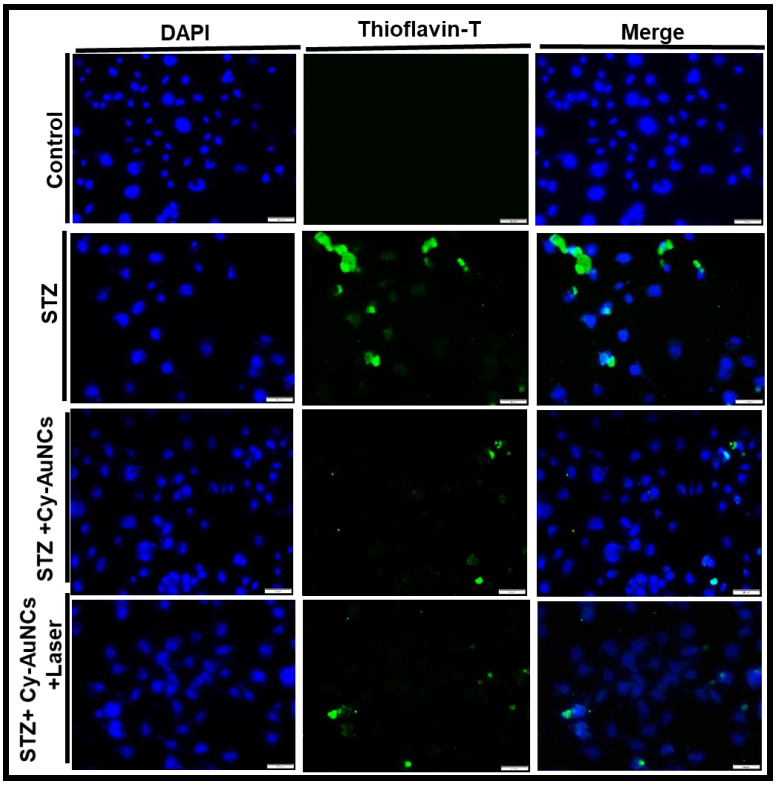

Figure 86. An *in vitro* STZ-induced AD model in Neuro-2A cells. Images illustrating ThT staining in STZ, Cy-AuNCs and laser-treated cells. Scale bar is 100 µm in all cases.

4.3.7.2 Inhibition of Aβ-Induced Cellular Toxicity

Additionally, a live/dead assay was performed with and without Cy-AuNCs treatment (40 μg/mL) (Figure 87). When compared to control group, the STZ treated group showed increased dead cells. In the Cy-AuNCs treated groups the number of live cells is significantly enhanced, suggesting the therapeutic role of Cy-AuNCs. In the presence of laser irradiation, the cell viability was further improved. The produced cytotoxic radicals during laser irradiation does not affect the healthy cells because they are formed in proximity to the fibrils brought on by the binding of cysteine to the fibrils. These findings underscore the therapeutic potential of Cy-AuNCs in targeting and treating amyloid-related conditions.

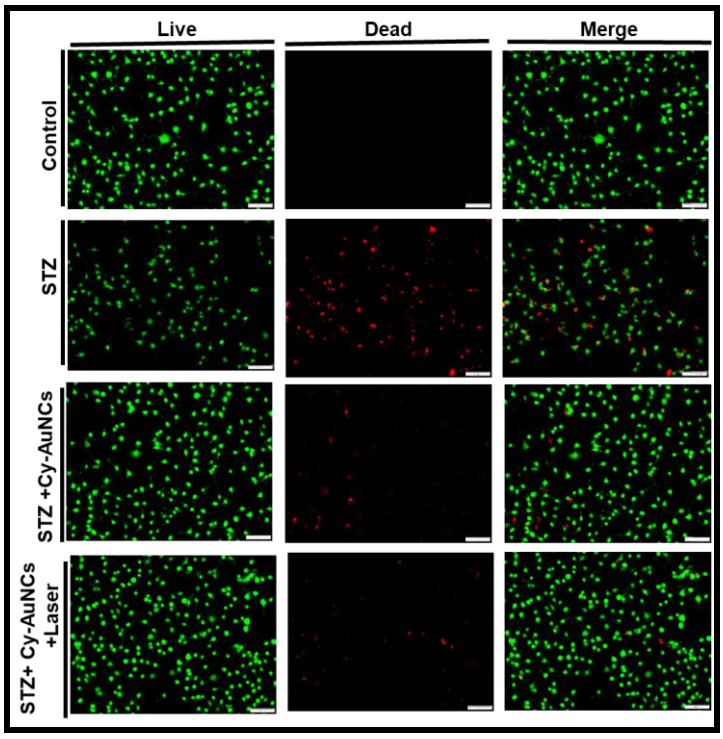

Figure 87. Live/dead assay on Neuro-2A cells where the viability of the cells was evaluated when treated with STZ in the presence and absence of the Cy-AuNCs. Scale bar is 100 µm in all cases

4.3.8 Blood-Brain Barrier Permeation Study

In the real situation, to effectively target Aβ fibrillization, the material must cross the BBB. To achieve this, we conjugated a brain-targeting agent, L-dopa, to Cy-AuNCs using EDC-NHS coupling chemistry, resulting in AuCs-LD. The large neutral amino acid transporter (LAT1) receptors, which are specialized membrane proteins, are expected to facilitate the penetration of L-dopa across the BBB (Nair *et al.*, 2017b). The successful conjugation of L-dopa to Cy-AuNCs was confirmed by FTIR spectroscopy (Figure 88a). In the FTIR spectrum of Cy-AuNCs, peaks at 1580 and 1616 cm^{-1} correspond to the C=O stretching vibration of the amide I band and N-H bending vibration of the amide II band, respectively. In AuCs-LD, these amides I and II bands disappeared, and a new peak appeared at 1640 cm^{-1}, confirming the functionalization of L-dopa on Cy-AuNCs. Additionally, a decrease in the negative zeta potential of Cy-AuNCs from -32 mV to -25 mV in AuCs-LD further confirmed the functionalization (Figure 88b). The cell viability assay using mouse fibroblast L929 cells showed that more than 80% of cells remained viable at a relatively high concentration of 160 µg/mL (Figure 88c). In the cellular uptake study, the red fluorescence observed from the brain endothelial (bEnd.3) cells showed higher internalization of AuCs-LD than Cy-AuNCs (Figure 88d).

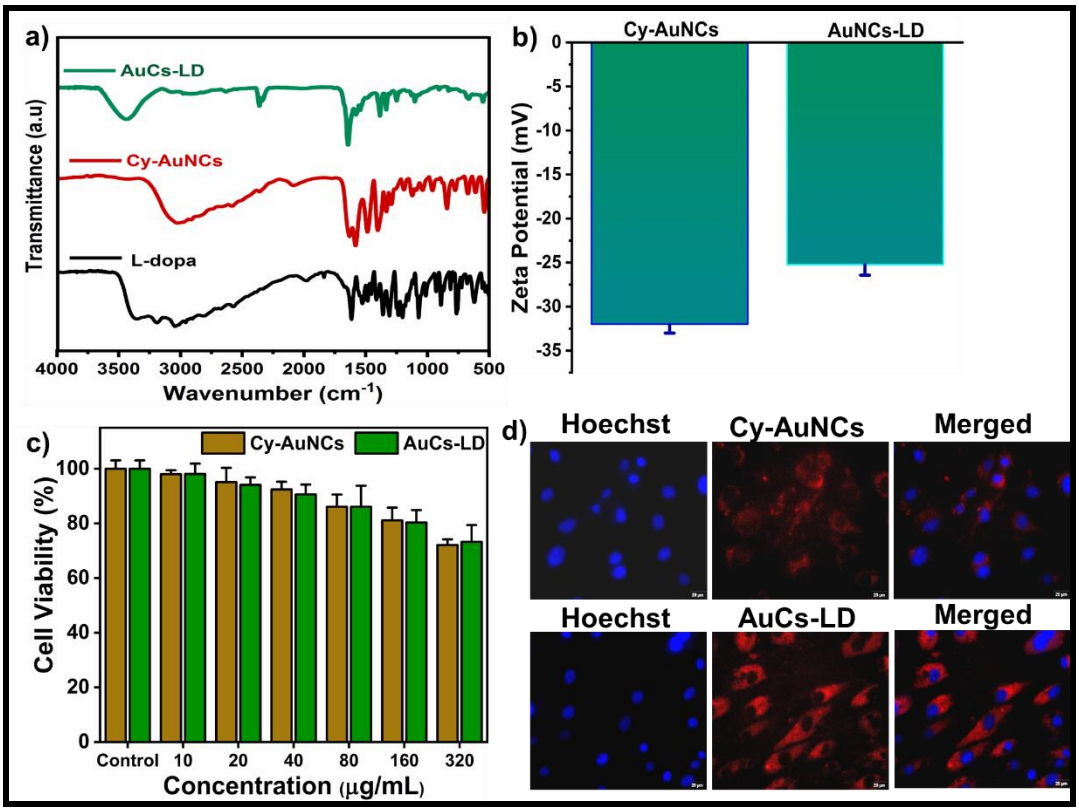

Figure 88. Functionalization and biocompatibility of AuCs-LD a) FTIR spectra b) Zeta potential analysis c) Biocompatibility evaluation and d) Cellular uptake of Cy-AuNCs and AuCs-LD. Scale bar is 20 µm in all cases. The error bar represents the SD of three independent experiments.

4.3.9 BBB Potential and Permeability

An *in vitro* BBB model was established using a co-culture of bEnd.3 and astrocytes (C8-D30) to evaluate the capability of nanoclusters to cross the BBB. The C8-D30 cells were cultured on the basolateral side, while the bEnd.3 cells were on the apical side of the insert. The tight junction formation, crucial for BBB integrity, was confirmed by an increase in transendothelial electrical resistance (TEER), reflecting resistance to ion flow(Srinivasan *et al.*, 2015). Over five days, the TEER values steadily increased, peaking at around 179 ± 11.93 Ωcm², indicating successful tight junction formation (Figure 89a). Upon introducing varying concentrations of Cy-AuNCs and AuCs-LD to the BBB

model, a temporary reduction in barrier potential was observed, which normalized after 6 h (Figure 89b). This fluctuation in TEER values during nanocluster treatment can be due to local changes in the extracellular environment of the cells. The negatively charged nanoclusters might have influenced extracellular calcium levels, crucial for maintaining tight junctions. Disruptions in extracellular calcium can temporarily affect BBB integrity by impacting the adherens junctions between endothelial cells, leading to changes in BBB permeability and loosening of tight junctions (Brown and Davis, 2002).

Following established protocols, we investigated the permeability of nanoclusters (Cy-AuNCs and AuCs-LD) through an *in vitro* BBB model at various time intervals (Nair *et al.*, 2017b). BBB model comprising brain endothelial cells and astrocytes were treated with 100 µL of Cy-AuNCs and AuCs-LD (40 µg/mL). The concentration of nanoparticles in the media collected from the lower chamber of the insert was quantified using UV/Visible spectroscopy. After 3 h, 74% of AuCs-LD and 66% of Cy-AuNCs had crossed the barrier, which increased to over 90% for AuCs-LD and 70% for Cy-AuNCs after 24 h (Figure 89c). These findings suggest that AuCs-LD permeates the BBB more rapidly, potentially facilitated by L-dopa targeting *via* the LAT1 transporter.

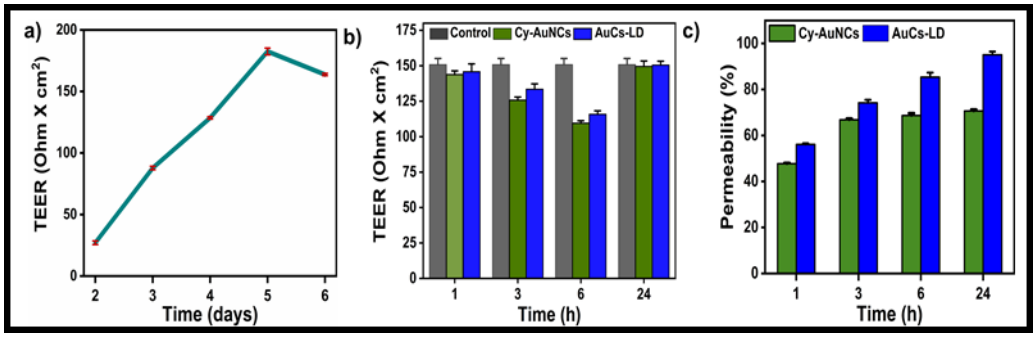

Figure 89. Effect of Cy-AuNCs and AuCs-LD on *in vitro* BBB model a) TEER values of the co-culture layer in control cells to ascertain the formation of BBB and tight junction, b) TEER value variation on addition of the nanoclusters and c) barrier permeability of Cy-AuNCs and AuCs-LD. Error bar indicates the SD of three independent experiments.

4.3.10 *In vivo* imaging of Cy-AuNCs and AuCs-LD

The ability of the nanoclusters to cross the BBB was assessed in Swiss albino mice by using the intrinsic fluorescent property of Cy-AuNCs and AuCS-LD. Swiss albino mice weighing between 25-40 gram were divided into three groups: control, Cy-AuNCs injected, and AuCs-LD injected. On the day of the experiment, Cy-AuNCs (20mg/kg) and AuCs-LD (20mg/kg) were intravenously administered to respective groups. Control mice received no treatment. Imaging was performed at 1h and 4h post-injection using an *in vivo* Imaging Spectrum (IVIS Spectrum) to assess nanocluster distribution within the body (Figures 90a &b). The image clearly depicted the fluorescent signals from AuCs-LD in the brain, indicating significant accumulation by crossing the BBB. In contrast, no such signal was observed in Cy-AuNCs treated animals, it may be due to the lack of targeting moiety. However, the fluorescent signals of Cy-AuNCs were observed in other parts of the body.

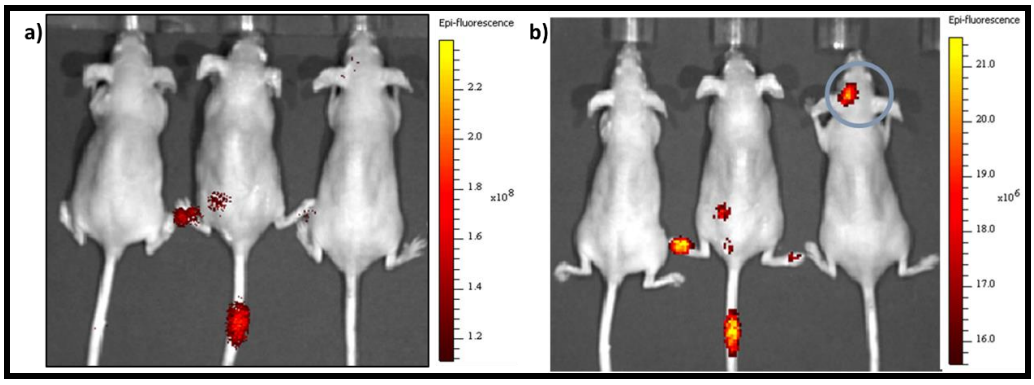

Figure 90. Brain imaging of live animals after the injection of Cy-AuNCs and AuCs-LD at a)1 h and b) 4 h

After 5 h, the animals were sacrificed, and their organs were collected and imaged to evaluate the biodistribution of the materials in different organs. Figure 91a illustrates the *in vivo* imaging results, with the highest signal observed in the brains of animals injected with AuCs-LD. The higher internalization of AuCs-LD in the brain is attributed to the targeting *via* the LAT1 transporter pathway. No such signals were observed in the brain of Cy-AuNcs. Figure 91b shows the organ-wise distribution of the nanoclusters. In the Cy-AuNCs-treated animal, a significant concentration of the nanocluster is observed in the liver, while no such accumulation was observed in the AuCs-LD-treated animal. because of no target moiety, the Cy-AuNCs would have directly taken up the clearance pathway after entering into the blood stream making its presence more in the liver. To further confirm the presence of Au in brain, the brain tissue was examined using ICP-OES (Table 8). The AuCs-LD mice showed 2.07 ppm of Au in the brain tissue of treated animal, this indicates successful delivery of AuCs-LD in the brain and its retention there till 4 h.

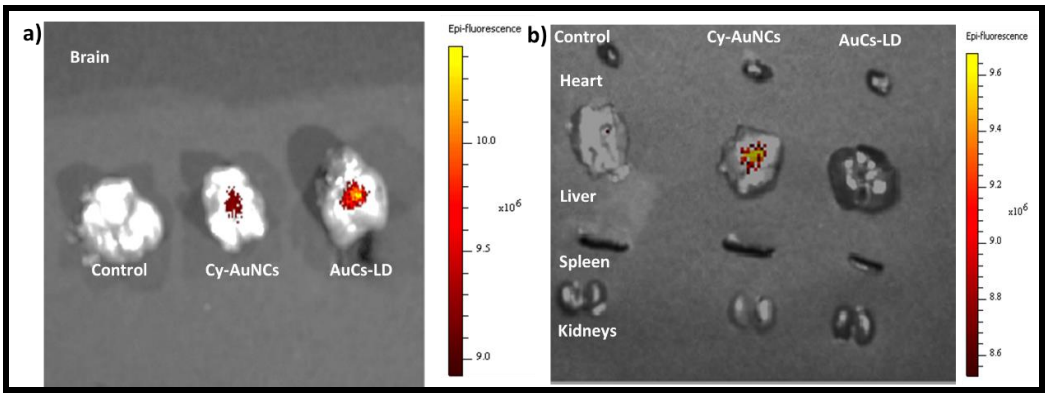

Figure 91. Ex-vivo fluorescence imaging of a) brains and b) different organs of mice treated with Cy-AuNCs and AuCs-LD

Table 8: ICP-OES analysis

Label	Solution concentration	Unit	SD	% RSD	Intensity	Calculated concentration
Au	0.02	ppm	0.02	0.92	187.05	2.07 (ppm)

In conclusion, this work successfully synthesized Cy-AuNCs using a one-pot approach, demonstrating their potential as multifunctional nanomaterials. Cy-AuNCs exhibited excellent bioimaging capabilities, effectively crossed the BB, and inhibited Aβ fibrillization through thiophilic interactions. These findings highlight the promising therapeutic potential of Cy-AuNCs for AD. By targeting Aβ fibrillization, Cy-AuNCs offer a safe and effective approach for the management of AD. Furthermore, the incorporation of L-dopa into Cy-AuNCs enhanced their brain-targeting and BBB-crossing properties, as demonstrated in both *in vitro* and *in vivo* experiments.

4.4 Therapeutic potential of gold nanocluster in Streptozotocin (STZ) induced AD mice model

Developing effective therapeutic agents that can cross the BBB is crucial for advancing AD treatment. Our preliminary findings demonstrated that Cy-AuNCs inhibit the Aβ fibrillization (Section 4.3.7**)**. Functionalization of a brain-targeting moiety L-dopa with Cy-AuNCs (AuCs-LD) confirmed its brain-targeting ability by crossing the BBB after intravenous administration without causing significant toxicity (Section 4.3.10). Therefore, we further explored the therapeutic potential of AuCs-LD using streptozotocin (STZ)-induced AD model in mice.

4.4.1 Development of STZ-induced AD animal model

The strong inhibitory impact of AuCs-LD on Aβ fibrillization, along with their excellent BBB permeability and biocompatibility, motivated us to explore their therapeutic efficacy in an *in vivo* STZ-induced AD model. To develop an AD animal model , Swiss albino mice underwent ICV injection of STZ into the lateral ventricle in a sterile environment (Figure 92). A burr hole was drilled unilaterally on the right side and STZ was slowly injected at a rate of 3 µL/min. ICV injection of STZ are known to induce central insulin resistance and glucose hypometabolism, frequently used to model AD-like pathology. These metabolic disturbances lead to inflammation, oxidative stress, Aβ production, and hyperphosphorylation of tau proteins, which are associated with synaptic loss and neurodegeneration, ultimately resulting in cognitive and

memory deficits. Due to these STZ-induced changes, this mouse model is valuable for testing new therapeutic strategies against AD (Grieb, 2016).

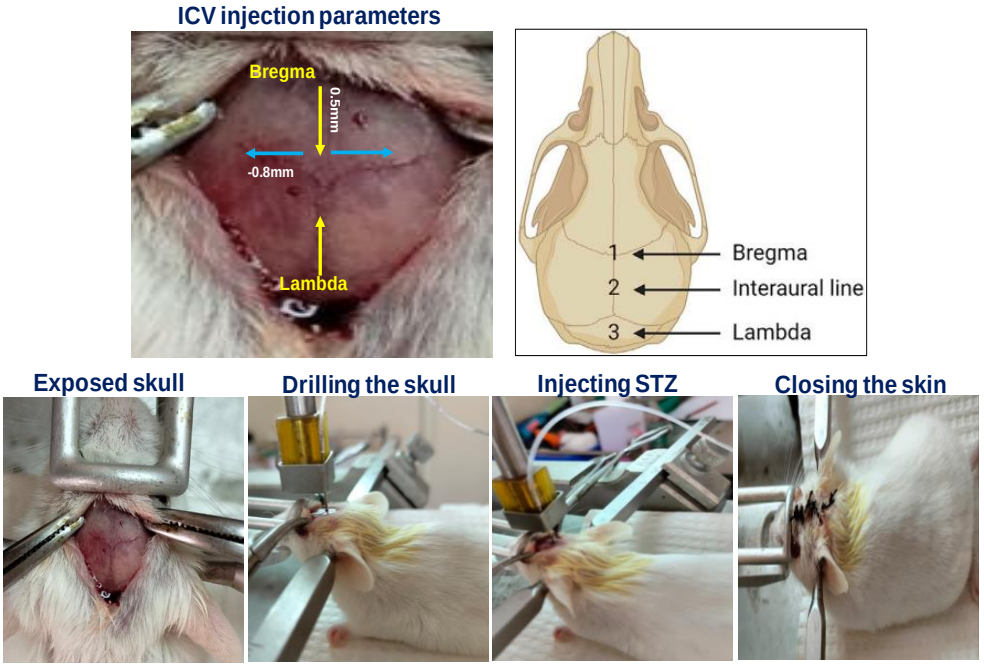

Figure 92. Outline of ICV injection procedure

The animals were divided into four groups for this study. Group 1 received a single ICV injection of saline, then, after 10 days, four IV saline injections every 72 h. Group 2 received a single ICV injection of STZ, then, after 10 days, four IV saline injections every 72 h. Group 3 was given a single ICV injection of STZ, and 10 days later, four IV injections of AuCs-LD every 72 h (Inhibition model). Group 4 received a single ICV injection of STZ, 21 days later followed by four IV injections of AuCs-LD every 72 h (Disintegration model). After these treatments, the animals underwent behavioural assessment to evaluate the therapeutic potential of the AuCs-LD. On day 38, the mice were sacrificed, and their brains were dissected for further

detailed analysis (Figure 93).

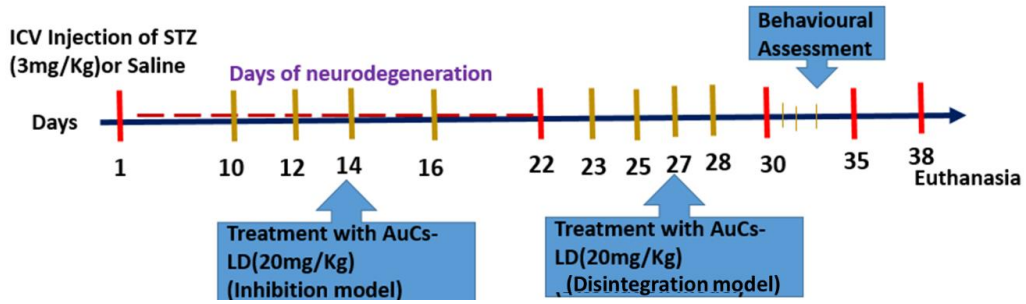

Figure 93. Experimental design for the development of STZ-induced AD model and its treatment.

4.4.2 *In-vivo* effect of the AuCs-LD in STZ-induced AD mice model

4.4.2.1 Behavioural Assessment

To evaluate the impact of AuCs-LD on inhibiting/disintegrating Aβ fibrillization and its potential for treatment, behavioural studies such as spontaneous alternation, novel arm tests, open field tests and novel object recognition tests were conducted on the experimental animals. These tests were used to assess the behaviour of the animals and to analyse any deviation from the natural behaviour in response to treatment.

4.4.2.1.1 Spontaneous alternation test

Spontaneous alternation is a measure of spatial working memory, assessed by allowing mice to explore all three arms of a maze freely (Kraeuter, Guest and Sarnyai, 2019). This behavior is driven by the innate curiosity of rodents to explore new areas. Mice with intact working memory will remember the arms they have already visited, and tend to enter a less recently visited arm. This task requires interaction across various brain regions, including the hippocampus and prefrontal cortex. Mice are introduced to a specific position

in the maze and allowed to explore the arms for a short period. An entry is recorded when all four limbs of the mouse are within an arm, and an alternation is defined as consecutive entries into all three arms. The number of arm entries and alternations are recorded to calculate the percentage of alternation behavior (Figure 94a). A high percentage of alternation indicates a high proportion of entries into the arms, indicating a good and intact working memory while a low percentage of alternation indicates poor working memory, with more repeated entries into the same arm (Figure 94b). In this study, the STZ-AD-induced group did not explore all the arms and showed a significant decrease in the percentage of alternation, in comparison to the control However, both the inhibition and disintegration groups in the AuCs-LD/STZ treatment, showed a significant increase in their percentage of alternation (Figure 94c)., denoting that the treatment with the clusters was able to partially restore the working memory of the mice.

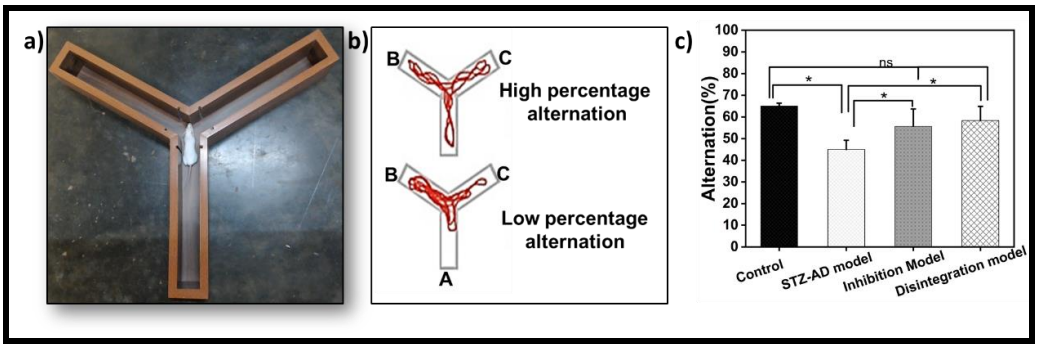

Figure 94. Y-maze performance and alternation behavior. a) Schematic representation of a Y-maze apparatus. (b) Representation of high and low percentage alternation behavior in a Y-maze. (c) Percentage of alternation in the Y-maze for different experimental groups, n= 3, * represents p-value ≤0.05.

4.4.2.1.2 Novel arm test

Spatial reference memory can also be evaluated using a Y-maze test where the mouse is initially placed in the maze with one arm blocked (Training session) (Kraeuter, Guest and Sarnyai, 2019). This blocked arm is considered the novel arm (Figure 95a). After a specific time during which the mouse is removed from the maze, it is returned with all arms open. The mouse, guided by spatial cues, should recognize and explore the previously inaccessible novel arm more frequently than the other arms (Figure 95b). The frequency of entries into the novel arm compared to the other arms is used to measure spatial memory (Figure 95c). A mouse that shows no preference for any arm during the testing session indicates impaired spatial memory, potentially reflecting hippocampal dysfunction. In this experiment, the STZ-induced AD model mice showed fewer entries into the novel arm, whereas mice in the inhibition and disintegration models in the AuCs-LD/STZ treatment exhibited higher entries into the novel arm compared to the STZ-induced AD model. These results suggest that the nanoclusters were effective to improve hippocampal function and spatial reference memory (Figure 95d).

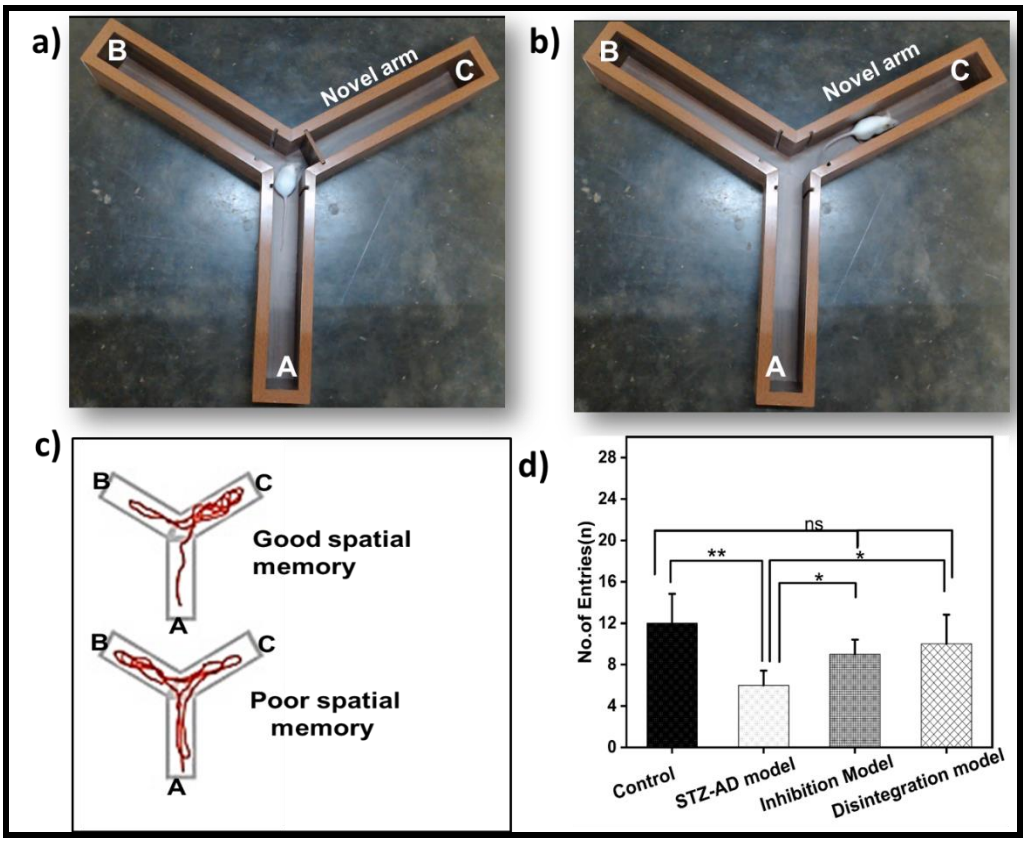

Figure 95. Y-maze performance and spatial memory assessment. (a, b) Representative images of a mouse exploring the Y-maze. Novel arms are indicated by C.(c) Schematic representation of high and low spatial memory performance in the Y-maze. (d) Percentage of alternation in the Y-maze for different experimental groups, n= 3, * represents p value ≤0.05.

4.4.2.1.3 Open Field Test (OFT)

The Open Field Maze (OFM) was developed to measure emotionality in rodents. The open field maze consists of a wall-enclosed area that is of sufficient height to prevent the subject from escaping (Figure 96a). Typical maze shapes are circular or square with an area large enough, based on the size of the subject tested, to elicit a feeling of openness in the center of the maze. Two measures of emotionality can be analyzed, locomotor activity and fecal boli deposits or defecation. Thigmotaxis is a sign of anxious behaviour in mice, with thigmotaxis levels increasing with increasing anxiety (Seibenhener and

Wooten, 2015). Thigmotaxis, in this test, is measured by the time spent by the mice close to the walls as opposed to exploring the center (Figure 96b). It can be observed that the control mouse has spent most of the time near the walls or has avoided the centre of the maze, showing natural anxiety. Whereas, a deviation in this behaviour is observed in STZ-treated mice. While the AuCs-LD/STZ treated animals show reduced entries to the centre, where the behaviour is similar to that of the control mouse (Figure 96c).

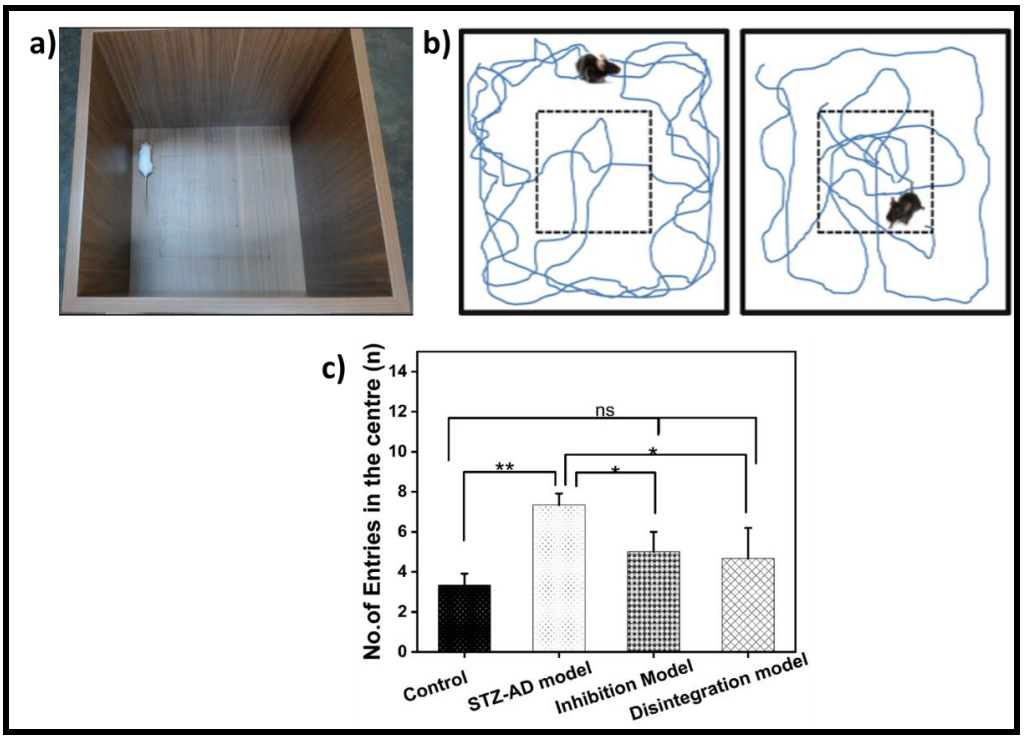

Figure 96. Open Field Test (OFT) analysis. a) Schematic representation of the open field apparatus. b) Representative tracks of mice in the open field. The central zone is indicated by the dashed square. c) Number of entries into the center zone during the OFT. n= 3, * represents p value ≤0.05.

4.4.2.1.4 Novel Object Recognition Test (NOR)

The object recognition test (ORT), also known as the novel object recognition test (NOR), is a relatively fast and efficient means for testing different phases

of learning and memory in mice (Hashmi, Yaqinuddin and Ahmed, 2015; Lueptow, 2017). The test relies on as few as three sessions: one habituation session, one training session, and one test session (Figure 97a). Training simply involves visual exploration of two identical objects, while the test session involves replacing one of the previously explored objects with a novel object. Because rodents have an innate preference for novelty, a rodent that remembers the familiar object will spend more time exploring the novel object. The mice from all groups were allowed to explore two objects (Object 1 and Object 2) and after which one object was replaced with the Novel Object. In all the groups, the amount of time taken to explore both the objects was almost similar, as observed in figure 97b. The time taken to explore the novel object is significantly higher in the control animal, which shows natural behaviour. The STZ treated group showed less exploration while significantly higher time was spent by the AuCs-LD/STZ treated groups and similar to the time spent by the control animal (Figure 97c). However, the total time taken to explore all the objects by all the animals is not significantly different (Figure 97d). STZ treated animals showed a lower percentage of discrimination, while the AuCs-LD/STZ treatment groups showed a significantly high discrimination. When compared to the control animal, the nanocluster groups, showed a similar percentage of discrimination (Figure 97e).

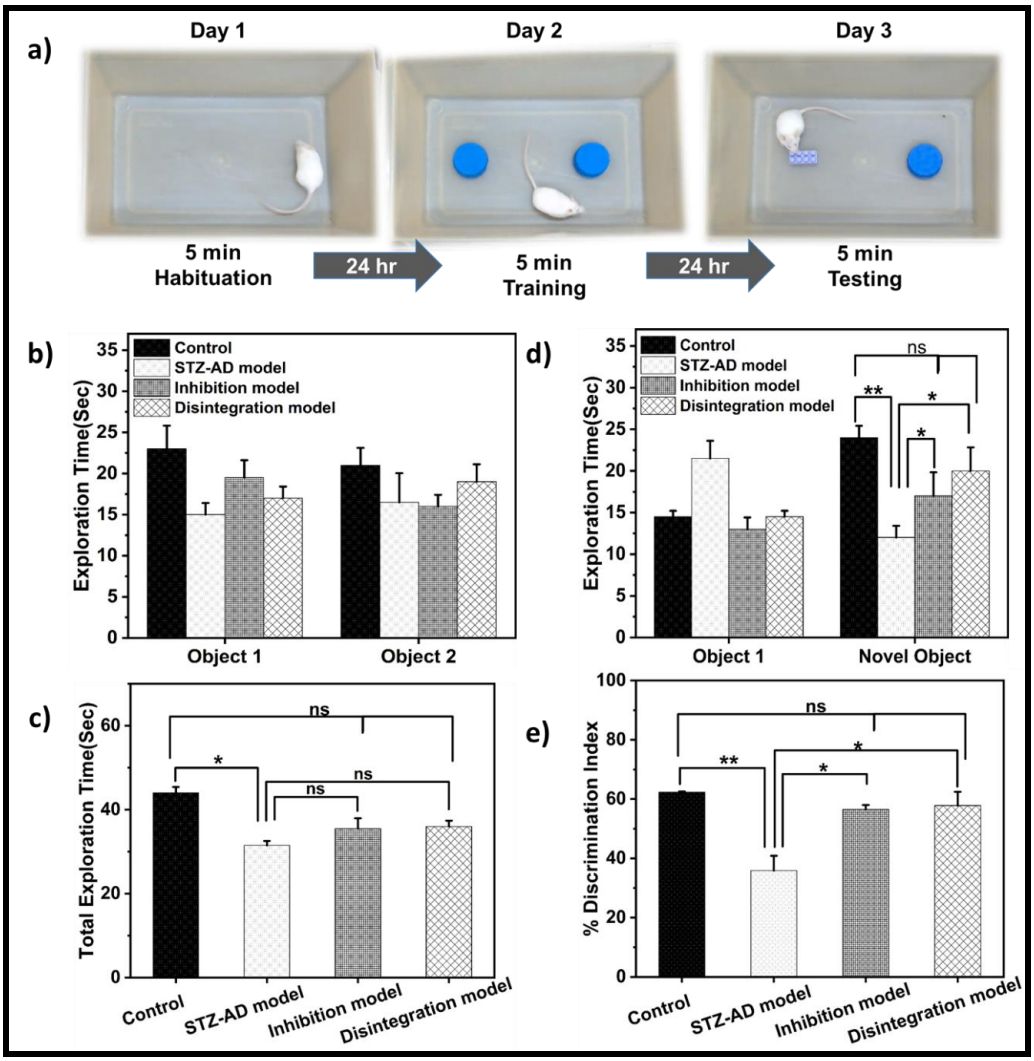

Figure 97. Behavioural assessment of object recognition in experimental models(a) Experimental model. Mice were subjected to a three-day object recognition task. (b) Exploration time of Object 1 and Object 2 on Day 2. (c) Total exploration time of both objects on Day 2. (d) Exploration time of Object 1 and novel object on Day 3. (e) Discrimination index, n= 3, * represents p value ≤0.05.

The various behavioural tests performed demonstrated that the administration of STZ affected the mice's brain which in turn significantly modified the natural behaviour of the mice, confirming the successful development of AD model using the STZ-ICV injection method. Subsequently, the group that were treated with gold nanoclusters, (Inhibition/Disintegration) showed partial restoration to the animal's natural behaviour confirming the

potential of AuCs-LD to reduce the symptoms of AD. This is due to the interference of the nanoclusters to inhibit/ disintegrate the amyloid fibrils and prevent plaque formation, allowing the animals to behave naturally at par with control animals, highlighting the therapeutic efficacy of the nanoclusters.

4.4.3 Neuropathology evaluation by H&E staining

After behavioural tests, histological tests were conducted to further analyze the formation of AD model and the therapeutic efficacy of the AuCs-LD. ICV injections of streptozotocin (STZ) cause metabolic disruptions that initiate inflammation, oxidative stress, elevated Aβ production, and tau hyperphosphorylation. These factors collectively contribute to synaptic loss, neurodegeneration, and subsequent cognitive and memory deficits. STZ-injected animals exhibited significant hippocampal lesions compared to the control group giving a pathological confirmation of the successful development of AD model. The STZ group displayed morphological alterations in hippocampal cells, including the appearance of elongated cells. However, these alterations were not observed in the AuCs-LD/STZ group compared to the STZ group (Figure 98) indicating the possibility of reducing the progression of AD resulted by the formation of excess amyloid fibrils. The mice treated with AuCs-LD/STZ showed fewer lesions in both inhibition and disintegration models (Figure 94). The result also validates the capability of disintegrating or inhibiting the amyloid fibrils in the *in vivo* models which likely would have led to the reduction in the lesions as observed in the treated groups.

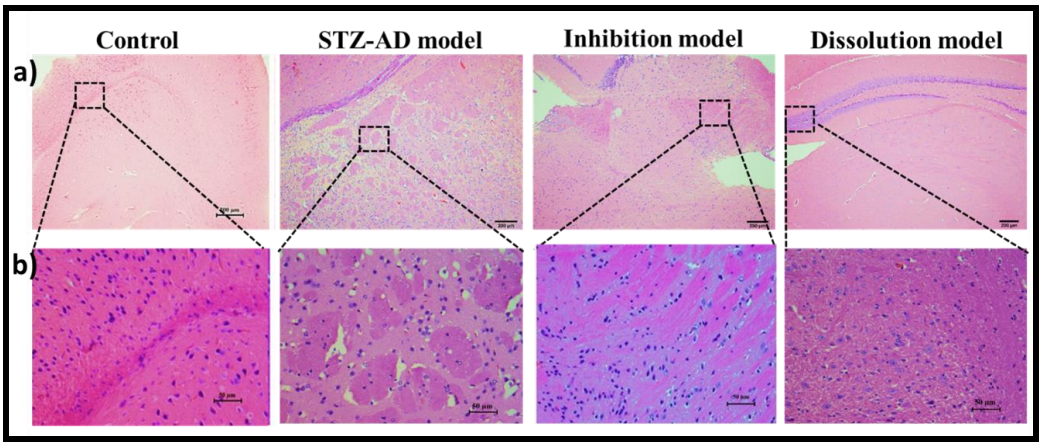

Figure 98. H&E staining of the hippocampal sections of the brain at 10x magnification (a) and 40x magnification (b). scale bars: 200 µm and 50 µm.

4.4.4 Evaluation of Aβ Aggregates

The fluorescent probe Thioflavin S (ThS) is commonly used for detecting Aβ aggregates (MacKeigan, Morgan and Stys, 2023). The figure 99a shows the images of brain tissue sections stained with thioflavin S, a dye that specifically binds to Aβ plaques, making them fluoresce green. The result illustrates the formation of Aβ plaques across various experimental models. These plaques are a key characteristic of AD. In the STZ-AD model, there is a notably higher number of Aβ plaques (47.5 ± 4.94) compared to the control group (1.5 ± 0.7), indicating successful induction of AD pathology. In the inhibition and disintegration group, the count was significantly reduced to 27 ± 2.82 and 20 ± 1.41 respectively (Figure 99b).

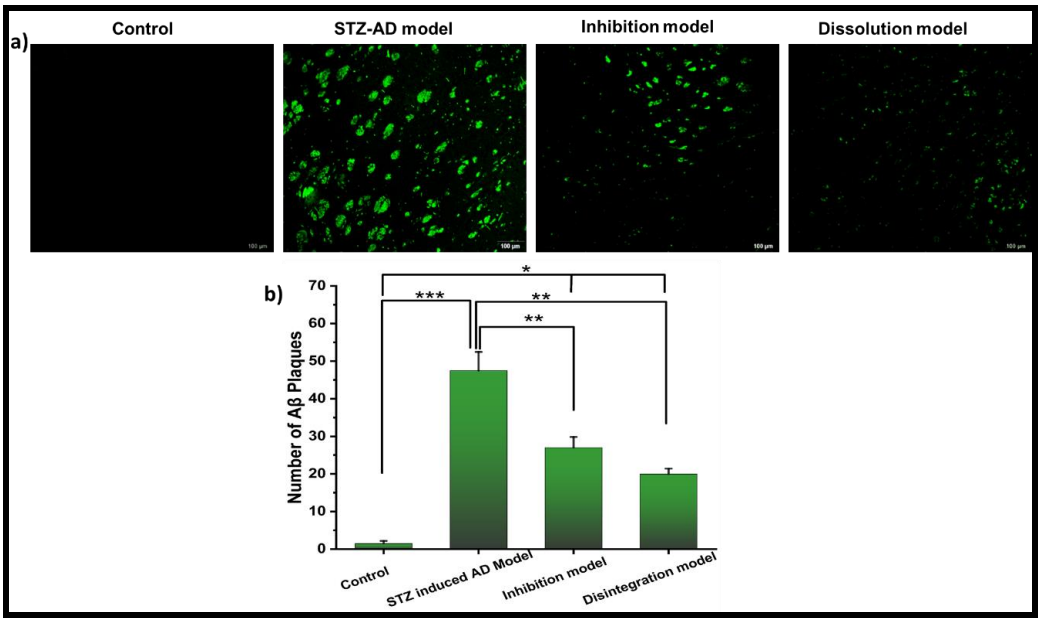

Figure 99. a) Thioflavin S staining and b) quantification of Aβ plaques. n= 3, * represents p value ≤0.05, scale bar: 100 µm.

4.4.5 Immunohistochemistry (IHC) of NFL

The neurofilament light chain (NFL) has become increasingly recognized as an important biomarker for neuronal damage in various neurodegenerative conditions (Gallingani *et al.*, 2024). In the *in vivo* experiment we have investigated the STZ induced neurodegeneration by assessing the independent marker NFL using anti-68kDa neurofilament/NF-L antibody. In STZ-AD model, NFL levels were observed to be higher (38.33 ± 5.85) compared to the control group (6.5 ± 3), which confirmed the neurodegeneration (Figure 100a). In inhibition and disintegration models the NFL levels were significantly reduced to 10.75 ± 2.36 and 11 ± 3.55 respectively (Figure 100b).

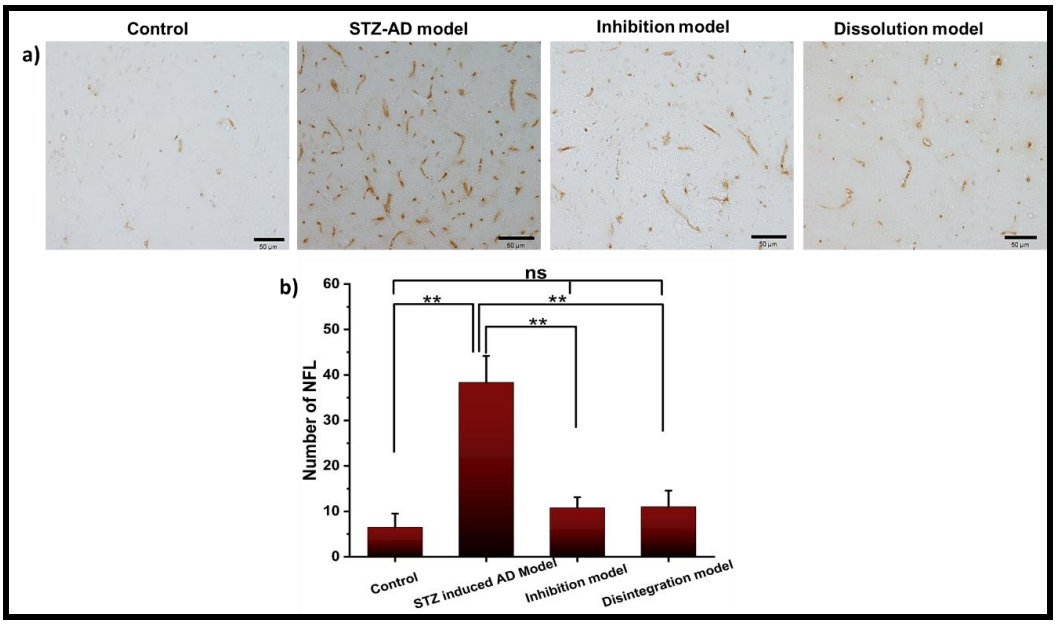

Figure 100. a) Immunohistochemistry of NFL in STZ-AD model, inhibition model, and disintegration model. b) quantification of Aβ plaques, n= 3, * represents p-value ≤0.05, scale bar: 50 µm.

4.4.6 Immunofluorescence (IF) of $A\beta_{42}$

Immunofluorescence study of the brain tissue showed a significant increase in $A\beta_{42}$ level in the STZ-AD model compared to the control group. At the same time, the inhibition and disintegration models showed a reduction in $A\beta_{42}$ levels relative to the STZ-AD model (Figure 101a). The results demonstrated that the inhibition and disintegration models had lower level of $A\beta_{42}$ when compared to the STZ-AD model. The quantitative analysis revealed that the mean fluorescence intensity of $A\beta_{42}$ in the STZ-AD model was 137.43 ± 41.99, compared to 25.90 ± 10.55 in the control group, 53.88 ± 20.16 in the inhibition group, and 48.92 ± 16.25 in the disintegration group (Figure 101b).

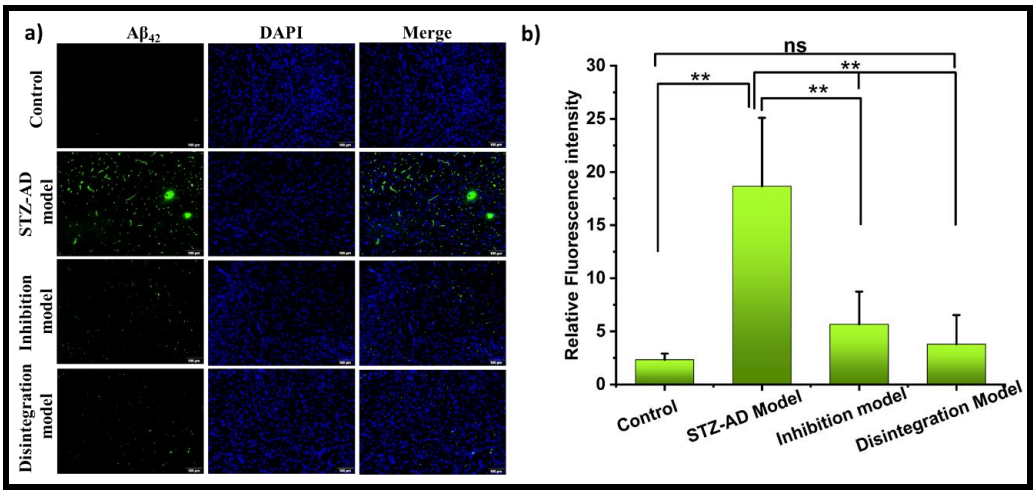

Figure 101. a) Immunofluorescence Staining for $A\beta_{42}$ b) quantification of mean fluorescence $A\beta_{42}$ intensity, n= 3, * represents p value ≤0.05, scale bar: 100 µm.

To summarize, histological evaluation revealed a significant increase in amyloid plaque formation and $A\beta_{42}$ levels in STZ-treated groups. However, administration of nanoclusters resulted in a marked reduction of these pathological markers, suggesting their therapeutic potential for Alzheimer's disease (AD). Moreover, STZ-induced behavioural alterations and neuropathological changes were significantly ameliorated following nanocluster treatment, further supporting their efficacy in mitigating the progression of AD.

.

.

Chapter 5

Summary and Conclusion

Alzheimer's disease is a severe neurodegenerative condition that impacts millions globally, presenting a major public health issue. Conventional treatments have faced difficulties in managing the disease effectively and additionally, the presence of BBB hinders proper drug delivery to the brain. However, the emergence of nanotechnology has offered new hope, providing innovative approaches to diagnosing and managing this challenging disorder. The success of nanotechnology-based methods in diagnosing and managing AD, as presented in this thesis, underscores the importance of interdisciplinary research in the early diagnosis and potential treatment of AD.

The first part of the study demonstrated the efficacy of the SERS-immunoassay technique as an effective, simple, and highly sensitive method for detecting AD biomarkers as an early and non-invasive method for detecting AD biomarkers from the blood sample. The platform exhibited remarkable sensitivity, with detection limits of 13.64 aM for $A\beta_{42}$ and 28.6 aM for p-Tau, covering a broad dynamic range from aM to μM concentrations. This SERS-immunoassay method offers significant advantages over traditional techniques, including its speed and cost-efficiency. To explore its potential, the sensor was employed to detect multiple AD biomarkers from human blood, namely $A\beta_{42}$, $A\beta_{40}$, t-Tau, and p-Tau to distinguish between AD patients, individuals with MCI, and healthy controls. For precise and sensitive AD

detection, the SERS immunoplatform has been integrated with advanced machine learning (ML) algorithms. Machine learning analysis of spectroscopically significant peak intensities shows superior classification performance compared to normalized spectral data from all datasets. Among the various ML methods evaluated, the radial basis function (RBF) method excelled in distinguishing between groups. Therefore, the combination of Raman peak intensities and RBF emerges as the most effective tool for early AD detection using the SERS dataset. This approach suggests a novel avenue for developing a rapid, reliable, and cost-effective blood plasma test, which could serve as a valuable tool for early AD detection.

In the second part of the study, we developed a conductometric platform for detecting Aβ and tau proteins based on their surface charge density. Here STM was used to examine the folding characteristics of Aβ and tau protein, identifying molecularly resolved core regions of Aβ hairpins and unfolded peptide assembly structures. Additionally, by exploiting the distinct surface charges of these core biomarkers under physiological conditions, as determined by their isoelectric points, STS based platform generates unique output signals for each biomarker, enhancing the accuracy and reliability of AD diagnosis. Based on this background, we developed a conductometric immunosensor incorporating the design of an inter digitated electrode to detect AD biomarkers. It demonstrated excellent performance, detecting AD biomarkers rapidly and over a broad detection range from fM to µM. Specifically, concentrations of $A\beta_{42}$ and p-Tau were detected within this range, with minimum detection limits of 8.95 fM and 12.76 fM respectively. Beyond its sensitivity, the multiplexed sensor array selectively recognized four different core AD biomarkers in blood plasma. By simultaneously detecting combinations of

biomarkers such as t-tau/$A\beta_{42}$, p-tau/$A\beta_{42}$, and $A\beta_{42/}A\beta_{40}$ in clinical plasma samples, the sensor array effectively distinguished AD patients from healthy controls. The ability to distinguish biomarkers based on their surface charge adds a new dimension to the analysis of AD, potentially facilitating more comprehensive disease characterization and personalized treatment strategies.

In the third part of this study, we focused on the therapeutic management of AD. As a first step, we developed a nanocarrier with the potential to cross BBB and provide real-time imaging, contributing to effective AD management. While various studies have explored nanosystems for AD treatment, none have combined both imaging and therapeutic capabilities.

We synthesized Cy-AuNCs using a one-pot method, where L-Cysteine acted as both a reducing and capping agent. These nanoclusters exhibited inherent fluorescence with a strong emission at 610 nm and a shoulder peak at 665 nm, making them suitable for imaging applications. The nanoclusters had a self-assembled structure with an average particle size of 3 nm, and their fluorescence, arising from quantum confinement, could be utilized for bio-imaging without interference from autofluorescence or the need for toxic fluorophores.

Beyond imaging, the Cy-AuNCs demonstrated photosensitizing properties, generating ROS that can be employed for therapeutic applications. Additionally, due to cysteine's ability to form thiophilic interactions with amyloid proteins, the Cy-AuNCs promoted the inhibition and disintegration of amyloid fibrils. Molecular docking studies confirmed the strong thiophilic interactions between the sulfur atom of Cy-AuNCs and the aromatic rings of Aβ fibrils.

The conjugation of L-Dopa to the nanoclusters (AuCs-LD) facilitated their passage across the BBB, leading to significant accumulation in the brain. The results indicated that these cysteine gold clusters could cross the BBB, be imaged in real time, and act as therapeutic agents by disintegrating Aβ fibrils.

Encouraged by these findings, the fourth part of this thesis focused on evaluating the therapeutic potential of AuCs-LD in an AD mouse model induced by STZ. To assess their effect on Aβ fibril inhibition/disintegration, the STZ-induced AD mice were treated with AuCs-LD via tail vein injection. They were then subjected to behavioural tests, including spontaneous alternation, novel arm, object recognition, and open field tests. Treated animals showed improved behaviour compared to untreated animals.

The therapeutic efficacy was further validated through histological analyses, such as H&E staining, Thioflavin S assay, immunohistochemistry for NFL and immunofluorescence for $A\beta_{42}$. Histological evaluations revealed a significant reduction in amyloid plaques and $A\beta_{42}$ levels in treated mice, whereas these markers remained elevated in the STZ-treated group.

The histopathology results, aligned with the behavioural findings, underscored the therapeutic potential of these nanoclusters in managing AD. This study represents a substantial step forward in developing innovative and effective treatments for AD, overcoming the limitations of conventional therapies, and improving outcomes for patients suffering from this neurodegenerative disease.

In summary, two distinct ultrasensitive nanosensor platforms have been developed and tested for their ability to detect AD biomarkers from blood samples across three groups. The results clearly demonstrate that the sensor can effectively

differentiate between AD, MCI, and healthy control groups, allowing for the early identification of AD patients and facilitating the planning of appropriate treatment strategies.

On the therapeutic front, we introduced a novel multifunctional metallic nanocluster for AD management. These multifunctional nanoprobes can inhibit Aβ-induced neurotoxicity without the need for additional drugs. They also exhibit high biocompatibility, permeability across the BBB, and potential for imaging applications. We investigated the therapeutic and imaging efficacy of these nanoclusters both *in vitro* and *in vivo*, successfully demonstrating their ability to inhibit the progression of AD.

Gold-based nanoparticles are making a significant impact on modern technology, particularly in biological applications. Their versatility enables the development of biosensors with enhanced sensitivity, improved selectivity, broad detection ranges, and ease of fabrication. Additionally, the biocompatibility of these nanomaterials makes them suitable for therapeutic purposes.

This research focuses on creating a gold-based nanomaterial for the diagnosis and management of Alzheimer's disease (AD). In this context, both SERS and electronic sensors have shown promising results, though further advancements are needed to develop a product suitable for clinical application. Given the current lack of effective drugs for AD, gold nanoclusters also hold substantial commercial potential. However, they must undergo rigorous evaluation before they can be applied in clinical settings.

CHAPTER 6

REFERENCES

Abalde-Cela, S. *et al.* (2010) 'Surface-enhanced Raman scattering biomedical applications of plasmonic colloidal particles', *Journal of the Royal Society Interface*, 7(Suppl 4), p. S435. doi: 10.1098/RSIF.2010.0125.FOCUS.

Ahmadi, S. *et al.* (2018) 'Thiol-Capped Gold Nanoparticle Biosensors for Rapid and Sensitive Visual Colorimetric Detection of Klebsiella pneumoniae', *Journal of fluorescence*, 28(4), pp. 987–998. doi: 10.1007/S10895-018-2262-Z.

Akushevich, I. *et al.* (2021) 'Chemotherapy and the Risk of Alzheimer's Disease in Colorectal Cancer Survivors: Evidence From the Medicare System', *JCO Oncology Practice*, 17(11), p. e1649. doi: 10.1200/OP.20.00729.

Arano-Martinez, J. A. *et al.* (2022) 'A Framework for Biosensors Assisted by Multiphoton Effects and Machine Learning', *Biosensors 2022, Vol. 12, Page 710*, 12(9), p. 710. doi: 10.3390/BIOS12090710.

Ashleigh, T., Swerdlow, R. H. and Beal, M. F. (2023) 'The role of mitochondrial dysfunction in Alzheimer's disease pathogenesis', *Alzheimer's & dementia : the journal of the Alzheimer's Association*, 19(1), pp. 333–342. doi: 10.1002/ALZ.12683.

Asil, S. M. *et al.* (2020) 'Application of Nanotechnology in Stem-Cell-Based Therapy of Neurodegenerative Diseases', *Applied Sciences 2020, Vol. 10, Page 4852*, 10(14), p. 4852. doi: 10.3390/APP10144852.

Asimakidou, E. *et al.* (2024) 'Blood–Brain Barrier-Targeting Nanoparticles: Biomaterial Properties and Biomedical Applications in Translational Neuroscience', *Pharmaceuticals 2024, Vol. 17, Page 612*, 17(5), p. 612. doi: 10.3390/PH17050612.

Baig, N. *et al.* (2021) 'Nanomaterials: a review of synthesis methods, properties, recent progress, and challenges', *Materials Advances*, 2(6), pp. 1821–1871. doi: 10.1039/D0MA00807A.

Baldeiras, I. *et al.* (2018) 'Addition of the Aβ42/40 ratio to the cerebrospinal fluid biomarker profile increases the predictive value for underlying Alzheimer's disease dementia in mild cognitive impairment', *Alzheimer's Research & Therapy*, 10(1). doi: 10.1186/S13195-018-0362-2.

Barthélemy, N. R. *et al.* (2024) 'Highly accurate blood test for Alzheimer's disease is similar or superior to clinical cerebrospinal fluid tests', *Nature Medicine 2024 30:4*, 30(4), pp. 1085–1095. doi: 10.1038/s41591-024-02869-z.

Bhalla, N. *et al.* (2016) 'Introduction to biosensors', *Essays in Biochemistry*, 60(1), pp. 1–8. doi: 10.1042/EBC20150001.

Biswas, J. *et al.* (2016) 'Streptozotocin Induced Neurotoxicity Involves

Alzheimer's Related Pathological Markers: a Study on N2A Cells', *Molecular neurobiology*, 53(5), pp. 2794–2806. doi: 10.1007/S12035-015-9144-Z.

Bocquet, A. *et al.* (2009) 'Neurofilaments Bind Tubulin and Modulate Its Polymerization', *Journal of Neuroscience*, 29(35), pp. 11043–11054. doi: 10.1523/JNEUROSCI.1924-09.2009.

Bouwman, F. H. *et al.* (2022) 'Clinical application of CSF biomarkers for Alzheimer's disease: From rationale to ratios', *Alzheimer's & Dementia : Diagnosis, Assessment & Disease Monitoring*, 14(1). doi: 10.1002/DAD2.12314.

Brown, R. C. and Davis, T. P. (2002) 'Calcium modulation of adherens and tight junction function: a potential mechanism for blood-brain barrier disruption after stroke', *Stroke*, 33(6), pp. 1706–1711. doi: 10.1161/01.STR.0000016405.06729.83.

Busche, M. A. and Hyman, B. T. (2020) 'Synergy between amyloid-β and tau in Alzheimer's disease', *Nature neuroscience*, 23(10), pp. 1183–1193. doi: 10.1038/S41593-020-0687-6.

Cai, L. *et al.* (2022) 'Label-Free Surface-Enhanced Raman Spectroscopic Analysis of Proteins: Advances and Applications', *International Journal of Molecular Sciences*, 23(22). doi: 10.3390/IJMS232213868.

Castner, D. G., Hinds, K. and Grainger, D. W. (1996) 'X-ray photoelectron spectroscopy sulfur 2p study of organic thiol and bisulfide binding interactions with gold surfaces', *Langmuir*, 12(21), pp. 5083–5086. doi: 10.1021/LA960465W/ASSET/IMAGES/LARGE/LA960465WF00003.JPEG .

Chakraborty, A. *et al.* (2023) 'Impact of nanoparticles on amyloid β-induced Alzheimer's disease, tuberculosis, leprosy and cancer: a systematic review', *Bioscience Reports*, 43(2). doi: 10.1042/BSR20220324.

Chang, C. C. *et al.* (2019) 'Gold Nanoparticle-Based Colorimetric Strategies for Chemical and Biological Sensing Applications', *Nanomaterials*, 9(6). doi: 10.3390/NANO9060861.

Chang, H.-Y. *et al.* (2017) 'The effect of ligand–ligand interactions on the formation of photoluminescent gold nanoclusters embedded in Au(<scp>i</scp>)–thiolate supramolecules', *Physical Chemistry Chemical Physics*, 19(19), pp. 12085–12093. doi: 10.1039/C7CP01915G.

Chauhan, N. *et al.* (2023) 'Advances in surface-enhanced Raman spectroscopy-based sensors for detection of various biomarkers', *Progress in Biophysics and Molecular Biology*, 184, pp. 32–41. doi: 10.1016/J.PBIOMOLBIO.2023.08.003.

Chehelgerdi, Mohammad *et al.* (2023) 'Progressing nanotechnology to improve targeted cancer treatment: overcoming hurdles in its clinical implementation', *Molecular Cancer*, 22(1). doi: 10.1186/S12943-023-01865-0.

Chen, L. *et al.* (2019) 'A tyrosinase-induced fluorescence immunoassay for

detection of tau protein using dopamine-functionalized CuInS2/ZnS quantum dots', *Analytical and Bioanalytical Chemistry*, 411(20), pp. 5277–5285. doi: 10.1007/S00216-019-01909-9.

Cho, I. H., Kim, D. H. and Park, S. (2020) 'Electrochemical biosensors: perspective on functional nanomaterials for on-site analysis', *Biomaterials Research*, 24(1). doi: 10.1186/S40824-019-0181-Y.

Chou, I. H. *et al.* (2008) 'Nanofluidic biosensing for β-amyloid detection using surface enhanced raman spectroscopy', *Nano Letters*, 8(6), pp. 1729–1735. doi: 10.1021/NL0808132/SUPPL_FILE/NL0808132-FILE002.PDF.

Correia, J. H. *et al.* (2021) 'Photodynamic Therapy Review: Principles, Photosensitizers, Applications, and Future Directions', *Pharmaceutics*, 13(9). doi: 10.3390/PHARMACEUTICS13091332.

Curulli, A. (2021) 'Electrochemical Biosensors in Food Safety: Challenges and Perspectives', *Molecules (Basel, Switzerland)*, 26(10). doi: 10.3390/MOLECULES26102940.

Dai, Y., Molazemhosseini, A. and Liu, C. C. (2017) 'A Single-Use, In Vitro Biosensor for the Detection of T-Tau Protein, A Biomarker of Neuro-Degenerative Disorders, in PBS and Human Serum Using Differential Pulse Voltammetry (DPV)', *Biosensors*, 7(1), pp. 1–11. doi: 10.3390/bios7010010.

Damborský, P., Švitel, J. and Katrlík, J. (2016) 'Optical biosensors', *Essays in Biochemistry*, 60(1), p. 91. doi: 10.1042/EBC20150010.

Dan, Q. *et al.* (2022) 'Gold Nanoclusters-Based NIR-II Photosensitizers with Catalase-like Activity for Boosted Photodynamic Therapy', *Pharmaceutics*, 14(8). doi: 10.3390/PHARMACEUTICS14081645.

Daniels, J. S. and Pourmand, N. (2007) 'Label-Free Impedance Biosensors: Opportunities and Challenges', *Electroanalysis*, 19(12), p. 1239. doi: 10.1002/ELAN.200603855.

Deepak, F. L. (2017) 'Metal nanoparticles and clusters: Advances in synthesis, properties and applications', *Metal Nanoparticles and Clusters: Advances in Synthesis, Properties and Applications*, pp. 1–426. doi: 10.1007/978-3-319-68053-8.

Dementia (no date). Available at: https://www.who.int/en/news-room/fact-sheets/detail/dementia (Accessed: 1 March 2022).

Demeritte, T. *et al.* (2015) 'Hybrid Graphene Oxide Based Plasmonic-Magnetic Multifunctional Nanoplatform for Selective Separation and Label-Free Identification of Alzheimer's Disease Biomarkers', *ACS Applied Materials and Interfaces*, 7(24), pp. 13693–13700. doi: 10.1021/ACSAMI.5B03619/SUPPL_FILE/AM5B03619_SI_001.PDF.

Dong, J. *et al.* (2003) 'Metal binding and oxidation of amyloid-beta within isolated senile plaque cores: Raman microscopic evidence', *Biochemistry*, 42(10), pp. 2768–2773. doi: 10.1021/BI0272151.

DR, T. *et al.* (2001) 'Electrochemical biosensors: recommended definitions and classification', *Biosensors & bioelectronics*, 16(1–2), pp. 121–131. doi:

10.1016/S0956-5663(01)00115-4.

Drzewiecka-Matuszek, A. and Rutkowska-Zbik, D. (2021) 'Application of TD-DFT Theory to Studying Porphyrinoid-Based Photosensitizers for Photodynamic Therapy: A Review', *Molecules*, 26(23), p. 7176. doi: 10.3390/molecules26237176.

Dzyadevych, S. and Jaffrezic-Renault, N. (2014) 'Conductometric biosensors', *Biological Identification: DNA Amplification and Sequencing, Optical Sensing, Lab-On-Chip and Portable Systems*, pp. 153–193. doi: 10.1533/9780857099167.2.153.

Elsheikh, S. *et al.* (2024) 'Advancing Brain Research through Surface-Enhanced Raman Spectroscopy (SERS): Current Applications and Future Prospects', *Biosensors 2024, Vol. 14, Page 33*, 14(1), p. 33. doi: 10.3390/BIOS14010033.

Fan, H. and Guo, Z. (2020) 'Bioinspired surfaces with wettability: Biomolecule adhesion behaviors', *Biomaterials Science*, 8(6), pp. 1502–1535. doi: 10.1039/C9BM01729A.

Farahzadi, R., Fathi, E. and Vietor, I. (2020) 'Mesenchymal Stem Cells Could Be Considered as a Candidate for Further Studies in Cell-Based Therapy of Alzheimer's Disease via Targeting the Signaling Pathways', *ACS chemical neuroscience*, 11(10), pp. 1424–1435. doi: 10.1021/ACSCHEMNEURO.0C00052.

Fu, L. *et al.* (2023) 'Plasmonic Nanoparticle-Enhanced Optical Techniques for Cancer Biomarker Sensing', *Biosensors*, 13(11). doi: 10.3390/BIOS13110977.

Gallingani, C. *et al.* (2024) 'Neurofilaments Light Chain in Neurodegenerative Dementias: A Review of Imaging Correlates', *Brain Sciences 2024, Vol. 14, Page 272*, 14(3), p. 272. doi: 10.3390/BRAINSCI14030272.

Gao, F. *et al.* (2023) 'SERS-Based Optical Nanobiosensors for the Detection of Alzheimer's Disease', *Biosensors*, 13(9). doi: 10.3390/BIOS13090880.

Gao, G. *et al.* (2017a) 'The size-effect of gold nanoparticles and nanoclusters in the inhibition of amyloid-β fibrillation', *Nanoscale*, 9(12), pp. 4107–4113. doi: 10.1039/C7NR00699C.

Gao, G. *et al.* (2017b) 'The size-effect of gold nanoparticles and nanoclusters in the inhibition of amyloid-β fibrillation', *Nanoscale*, 9(12), pp. 4107–4113. doi: 10.1039/C7NR00699C.

Gao, H. M. and Hong, J. S. (2008) 'Why neurodegenerative diseases are progressive: uncontrolled inflammation drives disease progression', *Trends in immunology*, 29(8), p. 357. doi: 10.1016/J.IT.2008.05.002.

Garcia, M. A. (2011) 'Surface plasmons in metallic nanoparticles: Fundamentals and applications', *Journal of Physics D: Applied Physics*, 44(28). doi: 10.1088/0022-3727/44/28/283001.

Goswami, N. *et al.* (2016) 'Luminescent Metal Nanoclusters with Aggregation-Induced Emission', *Journal of Physical Chemistry Letters*, 7(6), pp. 962–975.

doi: 10.1021/ACS.JPCLETT.5B02765/ASSET/IMAGES/LARGE/JZ-2015-02765H_0008.JPEG.

Granqvist, N. and Laurila, J. (2011) 'Rage against self-replicating machines: Framing science and fiction in the US nanotechnology field', *Organization Studies*, 32(2), pp. 253–280. doi: 10.1177/0170840610397476.

Grieb, P. (2016) 'Intracerebroventricular Streptozotocin Injections as a Model of Alzheimer's Disease: in Search of a Relevant Mechanism', *Molecular Neurobiology*, 53(3), pp. 1741–1752. doi: 10.1007/S12035-015-9132-3.

Grieshaber, D. *et al.* (2008) 'Electrochemical Biosensors - Sensor Principles and Architectures', *Sensors (Basel, Switzerland)*, 8(3), p. 1400. doi: 10.3390/S80314000.

Han, R. *et al.* (2020) 'Super-efficient in Vivo Two-Photon Photodynamic Therapy with a Gold Nanocluster as a Type i Photosensitizer', *ACS Nano*, 14(8), pp. 9532–9544. doi: 10.1021/ACSNANO.9B05169/SUPPL_FILE/NN9B05169_SI_001.PDF.

Hao, S. *et al.* (2019) 'CLVFFA-Functionalized Gold Nanoclusters Inhibit Aβ40 Fibrillation, Fibrils' Prolongation, and Mature Fibrils' Disaggregation', *ACS chemical neuroscience*, 10(11), pp. 4633–4642. doi: 10.1021/ACSCHEMNEURO.9B00469.

Hashmi, A. N., Yaqinuddin, A. and Ahmed, T. (2015) 'Pharmacological effects of Ibuprofen on learning and memory, muscarinic receptors gene expression and APP isoforms level in pre-frontal cortex of AlCl3-induced toxicity mouse model', *International Journal of Neuroscience*, 125(4), pp. 277–287. doi: 10.3109/00207454.2014.922972.

He, W. *et al.* (2014) 'Predicting and identifying reactive oxygen species and electrons for photocatalytic metal sulfide micro–nano structures', *Journal of Catalysis*, 320(1), pp. 97–105. doi: 10.1016/J.JCAT.2014.10.004.

Hersh, A. M., Alomari, S. and Tyler, B. M. (2022) 'Crossing the Blood-Brain Barrier: Advances in Nanoparticle Technology for Drug Delivery in Neuro-Oncology', *International Journal of Molecular Sciences*, 23(8), p. 4153. doi: 10.3390/IJMS23084153.

Hong, Y. *et al.* (2012) 'Nanobiosensors Based on Localized Surface Plasmon Resonance for Biomarker Detection', *Journal of Nanomaterials*, 2012(1), p. 759830. doi: 10.1155/2012/759830.

Hou, K. *et al.* (2020) 'Chiral gold nanoparticles enantioselectively rescue memory deficits in a mouse model of Alzheimer's disease', *Nature Communications*, 11(1). doi: 10.1038/S41467-020-18525-2.

How Is Alzheimer's Disease Treated? | National Institute on Aging (no date). Available at: https://www.nia.nih.gov/health/alzheimers-treatment/how-alzheimers-disease-treated (Accessed: 10 August 2024).

Huang, H. *et al.* (2023) 'Gold Nanoparticles: Construction for Drug Delivery and Application in Cancer Immunotherapy', *Pharmaceutics*, 15(7). doi: 10.3390/PHARMACEUTICS15071868.

Huang, Y., Fuksman, L. and Zheng, J. (2018) 'Luminescence mechanisms of ultrasmall gold nanoparticles', *Dalton transactions (Cambridge, England : 2003)*, 47(18), p. 6267. doi: 10.1039/C8DT00420J.

Iqbal, K. *et al.* (2010) 'Tau in Alzheimer Disease and Related Tauopathies', *Current Alzheimer research*, 7(8), p. 656. Available at: /pmc/articles/PMC3090074/ (Accessed: 5 November 2021).

Ishikawa-Ankerhold, H. C., Ankerhold, R. and Drummen, G. P. C. (2012) 'Advanced Fluorescence Microscopy Techniques—FRAP, FLIP, FLAP, FRET and FLIM', *Molecules 2012, Vol. 17, Pages 4047-4132*, 17(4), pp. 4047–4132. doi: 10.3390/MOLECULES17044047.

Janeiro, M. H. *et al.* (2021) 'Biomarkers in Alzheimer's disease', *Advances in Laboratory Medicine / Avances en Medicina de Laboratorio*, 2(1), pp. 27–37. doi: 10.1515/ALMED-2020-0090.

Javed, I. *et al.* (2019) 'Inhibition of amyloid beta toxicity in zebrafish with a chaperone-gold nanoparticle dual strategy', *Nature Communications 2019 10:1*, 10(1), pp. 1–14. doi: 10.1038/s41467-019-11762-0.

Jeon, G. W., Lee, S. H. and Jang, J. W. (2022) 'Opposite Raman Shift of Ring Stretching Dependent on the Coordinated Silver Volume in Surface-Enhanced Raman Spectroscopy of Polypyrrole', *The journal of physical chemistry letters*, 13(5), pp. 1300–1306. doi: 10.1021/ACS.JPCLETT.1C04069.

Ji, G. *et al.* (2022) 'Optical Biosensor Based on Graphene and Its Derivatives for Detecting Biomolecules', *International Journal of Molecular Sciences 2022, Vol. 23, Page 10838*, 23(18), p. 10838. doi: 10.3390/IJMS231810838.

Jibin, K. *et al.* (2021) 'Nanohybrids of Magnetically Intercalated Optical Metamaterials for Magnetic Resonance/Raman Imaging and in Situ Chemodynamic/Photothermal Therapy', *ACS Applied Bio Materials*, 4(7), pp. 5742–5752. doi: 10.1021/ACSABM.1C00510/SUPPL_FILE/MT1C00510_SI_001.PDF.

Jin, Y. *et al.* (2022) 'Aggregation-induced barrier to oxygen—a new AIE mechanism for metal clusters with phosphorescence', *National Science Review*, 9(8). doi: 10.1093/NSR/NWAB216.

Johnson, K. A. *et al.* (2012) 'Brain Imaging in Alzheimer Disease', *Cold Spring Harbor Perspectives in Medicine*, 2(4). doi: 10.1101/CSHPERSPECT.A006213.

Jones, R. R. *et al.* (2019) 'Raman Techniques: Fundamentals and Frontiers', *Nanoscale Research Letters 2019 14:1*, 14(1), pp. 1–34. doi: 10.1186/S11671-019-3039-2.

Joudeh, N. and Linke, D. (2022) 'Nanoparticle classification, physicochemical properties, characterization, and applications: a comprehensive review for biologists', *Journal of Nanobiotechnology 2022 20:1*, 20(1), pp. 1–29. doi: 10.1186/S12951-022-01477-8.

Juszczak, L. J. (2004) 'Comparative Vibrational Spectroscopy of Intracellular Tau

and Extracellular Collagen I Reveals Parallels of Gelation and Fibrillar Structure', *Journal of Biological Chemistry*, 279(9), pp. 7395–7404. doi: 10.1074/JBC.M309971200.

Khan, A. K. *et al.* (2014) 'Gold Nanoparticles: Synthesis and Applications in Drug Delivery', *Tropical Journal of Pharmaceutical Research*, 13(7), pp. 1169–1177. doi: 10.4314/TJPR.V13I7.23.

Khan, N. I. and Song, E. (2020) 'Lab-on-a-chip systems for aptamer-based biosensing', *Micromachines*, 11(2), pp. 1–30. doi: 10.3390/MI11020220.

Khan, Z. A. and Park, S. (2022) 'AuNPs- Aβ-Ni-HRP sandwich assay: A new sensitive colorimetric method for the detection of Aβ 1-40', *Talanta*, 237, p. 122946. doi: 10.1016/J.TALANTA.2021.122946.

Khanna, G. *et al.* (2024) 'Aducanumab', *Drugs of the Future*, 44(2), pp. 115–121. doi: 10.1358/dof.2019.44.2.2895649.

Kim, H. *et al.* (2019) 'A Nanoplasmonic Biosensor for Ultrasensitive Detection of Alzheimer's Disease Biomarker Using a Chaotropic Agent', *ACS Sensors*, 4(3), pp. 595–602. doi: 10.1021/acssensors.8b01242.

Kim, K. *et al.* (2020) 'Clinically accurate diagnosis of Alzheimer's disease via multiplexed sensing of core biomarkers in human plasma', *Nature Communications*, 11(1), pp. 1–9. doi: 10.1038/s41467-019-13901-z.

Kim, K., Lee, C. H. and Park, C. B. (2020) 'Chemical sensing platforms for detecting trace-level Alzheimer's core biomarkers', *Chemical Society Reviews*, 49(15), pp. 5446–5472. doi: 10.1039/D0CS00107D.

Kim, S., Wark, A. W. and Lee, H. J. (2016) 'Femtomolar Detection of Tau Proteins in Undiluted Plasma Using Surface Plasmon Resonance', *Analytical Chemistry*, 88(15), pp. 7793–7799. doi: 10.1021/acs.analchem.6b01825.

Kohout, C., Santi, C. and Polito, L. (2018) 'Anisotropic Gold Nanoparticles in Biomedical Applications', *International Journal of Molecular Sciences 2018, Vol. 19, Page 3385*, 19(11), p. 3385. doi: 10.3390/IJMS19113385.

Kong, F. Y. *et al.* (2017) 'Unique Roles of Gold Nanoparticles in Drug Delivery, Targeting and Imaging Applications', *Molecules : A Journal of Synthetic Chemistry and Natural Product Chemistry*, 22(9). doi: 10.3390/MOLECULES22091445.

Kraeuter, A. K., Guest, P. C. and Sarnyai, Z. (2019) 'The Y-Maze for Assessment of Spatial Working and Reference Memory in Mice', *Methods in molecular biology (Clifton, N.J.)*, 1916, pp. 105–111. doi: 10.1007/978-1-4939-8994-2_10.

Krishnan, K. M. (2010) 'Biomedical Nanomagnetics: A Spin Through Possibilities in Imaging, Diagnostics, and Therapy', *IEEE transactions on magnetics*, 46(7), p. 2523. doi: 10.1109/TMAG.2010.2046907.

Krisnawati, D. I. *et al.* (2021) 'The Use of the ROS Scavenger Cysteine as a Surface Ligand of Metal Nanoclusters and Its Bactericidal Elimination Effect', *Applied Sciences*, 11(9), p. 4095. doi: 10.3390/app11094095.

Kumar, J. and Sim, V. (2014) 'D-amino acid-based peptide inhibitors as early or preventative therapy in Alzheimer disease', *Prion*, 8(1), p. 119. doi: 10.4161/PRI.28220.

Kumar, S. *et al.* (2023) 'Optically Active Nanomaterials and Its Biosensing Applications—A Review', *Biosensors*, 13(1). doi: 10.3390/BIOS13010085.

Kunst, S. R. *et al.* (2015) 'Characterization of Siloxane-poly(methyl methacrylate) Hybrid Films Obtained on a Tinplate Substrate Modified by the Addition of Organic and Inorganic Acids', *Materials Research*, 18(1), pp. 151–163. doi: 10.1590/1516-1439.299514.

Lee, J. H. *et al.* (2009) 'Electrical detection of β-amyloid (1-40) using scanning tunneling microscopy', *Ultramicroscopy*, 109(8), pp. 923–928. doi: 10.1016/J.ULTRAMIC.2009.03.009.

Lee, S. H. *et al.* (2019) 'High-Performance Adhesives Based on Maleic Anhydride-g-EPDM Rubbers and Polybutene for Laminating Cast Polypropylene Film and Aluminum Foil', *Coatings 2019, Vol. 9, Page 61*, 9(1), p. 61. doi: 10.3390/COATINGS9010061.

Li, C., Wang, J. and Liu, L. (2020) 'Alzheimer's Therapeutic Strategy: Photoactive Platforms for Suppressing the Aggregation of Amyloid β Protein', *Frontiers in Chemistry*, 8. doi: 10.3389/FCHEM.2020.00509.

Li, M., Cushing, S. K. and Wu, N. (2015) 'Plasmon-enhanced optical sensors: a review', *The Analyst*, 140(2), pp. 386–406. doi: 10.1039/C4AN01079E.

Li, P. *et al.* (2021) 'From Diagnosis to Treatment: Recent Advances in Patient-Friendly Biosensors and Implantable Devices', *ACS Nano*, 15(2), pp. 1960–2004. doi: 10.1021/ACSNANO.0C06688.

Liao, Y. H. *et al.* (2012) 'Negatively charged gold nanoparticles inhibit Alzheimer's amyloid-β fibrillization, induce fibril dissociation, and mitigate neurotoxicity', *Small*, 8(23), pp. 3631–3639. doi: 10.1002/SMLL.201201068.

Lighting up! Fluorescence, Chemiluminescence and Bioluminescence- what's the difference? | *Blog* | *Biosynth* (no date). Available at: https://www.biosynth.com/blog/lighting-up-fluorescence-chemiluminescence-and-bioluminescence-whats-the-difference (Accessed: 9 August 2024).

Lin, J. C. *et al.* (2009) 'Synthesis of Fluorescent Metallic Nanoclusters toward Biomedical Application: Recent Progress and Present Challenges'.

Liu, B. *et al.* (2018) 'Lanthanide Functionalized Metal-Organic Coordination Polymer: Toward Novel Turn-On Fluorescent Sensing of Amyloid β-Peptide', *Analytical Chemistry*, 90(21), pp. 12449–12455. doi: 10.1021/ACS.ANALCHEM.8B01546/ASSET/IMAGES/LARGE/AC-2018-01546V_0005.JPEG.

Liu, H. *et al.* (2022) 'SERS Tags for Biomedical Detection and Bioimaging', *Theranostics*, 12(4), p. 1870. doi: 10.7150/THNO.66859.

Liu, J. *et al.* (2018) 'Recent Advances of Plasmonic Nanoparticles and their Applications', *Materials*, 11(10). doi: 10.3390/MA11101833.

Liu, S. *et al.* (2020) 'Recent advances in surface-enhanced Raman spectroscopy for the detection of tumor markers', *Kexue Tongbao/Chinese Science Bulletin*, 65(15), pp. 1448–1462. doi: 10.1360/TB-2019-0640.

Liu, S. *et al.* (2022) 'The Recent Development of Multifunctional Gold Nanoclusters in Tumor Theranostic and Combination Therapy', *Pharmaceutics*, 14(11). doi: 10.3390/PHARMACEUTICS14112451.

Liyanage, T. *et al.* (2020) 'Optimization of electromagnetic hot spots in surface-enhanced Raman scattering substrates for an ultrasensitive drug assay of emergency department patients' plasma', *Analyst*, 145(23), pp. 7662–7672. doi: 10.1039/D0AN01372B.

Lombardo, S. M. *et al.* (2020) 'Key for crossing the BBB with nanoparticles: the rational design', *Beilstein Journal of Nanotechnology*, 11, p. 866. doi: 10.3762/BJNANO.11.72.

Lueptow, L. M. (2017) 'Novel Object Recognition Test for the Investigation of Learning and Memory in Mice', *Journal of Visualized Experiments : JoVE*, 2017(126), p. 55718. doi: 10.3791/55718.

Luo, Z. *et al.* (2012) 'From aggregation-induced emission of Au(I)-thiolate complexes to ultrabright Au(0)@Au(I)-thiolate core-shell nanoclusters', *Journal of the American Chemical Society*, 134(40), pp. 16662–16670. doi: 10.1021/JA306199P.

M, N. and H, H. (2019) 'An ultrasensitive electrochemical aptasensor for early diagnosis of Alzheimer's disease, using a fern leaves-like gold nanostructure', *Talanta*, 198, pp. 510–517. doi: 10.1016/J.TALANTA.2019.01.109.

Ma, R. *et al.* (2024) 'Nanotechnology for tau pathology in Alzheimer's disease', *Materials Today Bio*, 27, p. 101145. doi: 10.1016/J.MTBIO.2024.101145.

MacKeigan, T. P., Morgan, M. L. and Stys, P. K. (2023) 'Quantitation of Tissue Amyloid via Fluorescence Spectroscopy Using Controlled Concentrations of Thioflavin-S', *Molecules 2023, Vol. 28, Page 4483*, 28(11), p. 4483. doi: 10.3390/MOLECULES28114483.

Mahato, K. *et al.* (2019) 'Gold nanoparticle surface engineering strategies and their applications in biomedicine and diagnostics', *3 Biotech*, 9(2), p. 57. doi: 10.1007/S13205-019-1577-Z.

Majdi, H. *et al.* (2019) 'Antibody conjugated green synthesized chitosan-gold nanoparticles for optical biosensing', *Colloids and Interface Science Communications*, 33. doi: 10.1016/J.COLCOM.2019.100207.

Maji, S. K. *et al.* (2010) 'CSF biomarkers for Alzheimer's disease diagnosis', *International Journal of Alzheimer's Disease*. doi: 10.4061/2010/606802.

Malik, S., Muhammad, K. and Waheed, Y. (2023) 'Emerging Applications of Nanotechnology in Healthcare and Medicine', *Molecules*, 28(18). doi: 10.3390/MOLECULES28186624.

Mao, X. *et al.* (2009) 'Structural characteristics of the beta-sheet-like human and rat islet amyloid polypeptides as determined by scanning tunneling

microscopy', *Journal of Structural Biology*, 167(3), pp. 209–215. doi: 10.1016/J.JSB.2009.05.009.

Martin Prince, A. *et al.* (2015) 'World Alzheimer Report 2015: The global impact of dementia: An analysis of prevalence, incidence, cost and trends'. Available at: https://www.alzint.org/resource/world-alzheimer-report-2015/ (Accessed: 9 August 2024).

Martinelli, C. *et al.* (2020) 'Antioxidants and Nanotechnology: Promises and Limits of Potentially Disruptive Approaches in the Treatment of Central Nervous System Diseases', *Advanced Healthcare Materials*, 9(3). doi: 10.1002/ADHM.201901589.

Matejtschuk, P. (2004) 'Thiophilic affinity chromatography and related methods.', *Methods in molecular biology (Clifton, N.J.)*, 244, pp. 195–204. doi: 10.1385/1-59259-655-X:195.

Meesaragandla, B. *et al.* (2020) 'Biopolymer-coated gold nanoparticles inhibit human insulin amyloid fibrillation', *Scientific Reports*, 10(1). doi: 10.1038/S41598-020-64010-7.

Meng, X. *et al.* (2020) 'Greater SERS Activity of Ligand-Stabilized Gold Nanostars with Sharp Branches', *Langmuir*, 36(13), pp. 3558–3564. doi: 10.1021/ACS.LANGMUIR.0C00079.

Menon, J. U. *et al.* (2013) 'Nanomaterials for Photo-Based Diagnostic and Therapeutic Applications', *Theranostics*, 3(3), pp. 152–166. doi: 10.7150/THNO.5327.

Mild Cognitive Impairment (MCI) | Symptoms & Treatments | alz.org (no date). Available at: https://www.alz.org/alzheimers-dementia/what-is-dementia/related_conditions/mild-cognitive-impairment (Accessed: 19 July 2024).

Miller, L. M., Bourassa, M. W. and Smith, R. J. (2013) 'FTIR spectroscopic imaging of protein aggregation in living cells', *Biochimica et biophysica acta*, 1828(10), pp. 2339–2346. doi: 10.1016/J.BBAMEM.2013.01.014.

Mir Najib Ullah, S. N. *et al.* (2023) 'Nanomedicine in the Management of Alzheimer's Disease: State-of-the-Art', *Biomedicines 2023, Vol. 11, Page 1752*, 11(6), p. 1752. doi: 10.3390/BIOMEDICINES11061752.

Montesinos, J. *et al.* (2020) 'The Alzheimer's disease-associated C99 fragment of APP regulates cellular cholesterol trafficking', *The EMBO journal*, 39(20). doi: 10.15252/EMBJ.2019103791.

MP, M. and H, L. (2010) 'Alzheimer's disease and the amyloid-beta peptide', *Journal of Alzheimer's disease : JAD*, 19(1), pp. 311–323. doi: 10.3233/JAD-2010-1221.

Muhammad-Tahir, Z. and Alocilja, E. C. (2003) 'A conductometric biosensor for biosecurity', *Biosensors and Bioelectronics*, 18(5–6), pp. 813–819. doi: 10.1016/S0956-5663(03)00020-4.

Mussa Farkhani, S. *et al.* (2024) 'Tailoring gold nanocluster properties for biomedical applications: From sensing to bioimaging and theranostics',

Progress in Materials Science, 142, p. 101229. doi: 10.1016/J.PMATSCI.2023.101229.

Nair, L. V. *et al.* (2017a) 'Blood brain barrier permeable gold nanocluster for targeted brain imaging and therapy: an in vitro and in vivo study.', *Journal of Materials Chemistry B*, 5(42), pp. 8314–8321. doi: 10.1039/C7TB02247F.

Nair, L. V. *et al.* (2017b) 'Blood brain barrier permeable gold nanocluster for targeted brain imaging and therapy: an in vitro and in vivo study', *Journal of materials chemistry. B*, 5(42), pp. 8314–8321. doi: 10.1039/C7TB02247F.

Negishi, Y., Nobusada, K. and Tsukuda, T. (2005) 'Glutathione-protected gold clusters revisited: Bridging the gap between gold(I)-thiolate complexes and thiolate-protected gold nanocrystals', *Journal of the American Chemical Society*, 127(14), pp. 5261–5270. doi: 10.1021/ja042218h.

Negishi, Y. and Tsukuda, T. (2003) 'One-Pot Preparation of Subnanometer-Sized Gold Clusters via Reduction and Stabilization by meso -2,3-Dimercaptosuccinic Acid', *Journal of the American Chemical Society*, 125(14), pp. 4046–4047. doi: 10.1021/ja0297483.

Oh, J. *et al.* (2013) 'A carbon nanotube metal semiconductor field effect transistor-based biosensor for detection of amyloid-beta in human serum', *Biosensors and Bioelectronics*, 50, pp. 345–350. doi: 10.1016/j.bios.2013.07.004.

van Oostveen, W. M. and de Lange, E. C. M. (2021) 'Imaging Techniques in Alzheimer's Disease: A Review of Applications in Early Diagnosis and Longitudinal Monitoring', *International Journal of Molecular Sciences 2021, Vol. 22, Page 2110*, 22(4), p. 2110. doi: 10.3390/IJMS22042110.

Overchuk, M. *et al.* (2023) 'Photodynamic andPhotothermal Therapies: Synergy Opportunitiesfor Nanomedicine', *ACS Nano*, 17(9), p. 7979. doi: 10.1021/ACSNANO.3C00891.

Palmal, S. *et al.* (2014) 'Inhibition of amyloid fibril growth and dissolution of amyloid fibrils by curcumin-gold nanoparticles', *Chemistry (Weinheim an der Bergstrasse, Germany)*, 20(20), pp. 6184–6191. doi: 10.1002/CHEM.201400079.

Panza, F. *et al.* (2016) 'Tau-based therapeutics for Alzheimer's disease: Active and passive immunotherapy', *Immunotherapy*, 8(9), pp. 1119–1134. doi: 10.2217/imt-2016-0019.

Panza, F. *et al.* (2019) 'A critical appraisal of amyloid-β-targeting therapies for Alzheimer disease', *Nature reviews. Neurology*, 15(2), pp. 73–88. doi: 10.1038/S41582-018-0116-6.

Park, D. *et al.* (2020) 'Multiplexed femtomolar detection of Alzheimer's disease biomarkers in biofluids using a reduced graphene oxide field-effect transistor', *Biosensors and Bioelectronics*, 167, p. 112505. doi: 10.1016/J.BIOS.2020.112505.

Park, H. J. *et al.* (2020) 'Carboxylic Acid-Functionalized, Graphitic Layer-Coated Three-Dimensional SERS Substrate for Label-Free Analysis of Alzheimer's

Disease Biomarkers', *Nano Letters*, 20(4), pp. 2576–2584. doi: 10.1021/ACS.NANOLETT.0C00048/SUPPL_FILE/NL0C00048_SI_001.PDF.

Paxinos, G. and Franklin, K. B. J. (2001) 'The mouse brain in stereotaxic coordinates: hard cover edition.', *Academic Press*, 2nd Editio, p. 360. Available at: https://www.elsevier.com/books/paxinos-and-franklins-the-mouse-brain-in-stereotaxic-coordinates-compact/franklin/978-0-12-816159-3 (Accessed: 25 December 2022).

Phan, L. M. T. *et al.* (2021) 'Nanomaterial-based Optical and Electrochemical Biosensors for Amyloid beta and Tau: Potential for early diagnosis of Alzheimer's Disease', *Expert Review of Molecular Diagnostics*, 21(2), pp. 175–193. doi: 10.1080/14737159.2021.1887732.

Pilot, R. *et al.* (2019) 'A Review on Surface-Enhanced Raman Scattering', *Biosensors*, 9(2). doi: 10.3390/BIOS9020057.

Poderys, V. *et al.* (2020) 'Protein-stabilized gold nanoclusters for PDT: ROS and singlet oxygen generation', *Journal of Photochemistry and Photobiology B: Biology*, 204, p. 111802. doi: 10.1016/J.JPHOTOBIOL.2020.111802.

Purohit, R. and Singh, S. (2018) 'Fluorescent gold nanoclusters for efficient cancer cell targeting', *International Journal of Nanomedicine*, 13(T-NANO 2014 Abstracts), pp. 15–17. doi: 10.2147/IJN.S125003.

Qi, Y. *et al.* (2023) 'Recent Progresses in Machine Learning Assisted Raman Spectroscopy', *Advanced Optical Materials*, 11(14), p. 2203104. doi: 10.1002/ADOM.202203104.

Qin, Z. *et al.* (2017) 'Kinetic Mechanism of Thioflavin T Binding onto the Amyloid Fibril of Hen Egg White Lysozyme', *Langmuir*, 33(22), pp. 5398–5405. doi: 10.1021/ACS.LANGMUIR.7B00221/SUPPL_FILE/LA7B00221_SI_001.PDF.

Ragavan, K. V., Rastogi, N. K. and Thakur, M. S. (2013) 'Sensors and biosensors for analysis of bisphenol-A', *TrAC Trends in Analytical Chemistry*, 52, pp. 248–260. doi: 10.1016/J.TRAC.2013.09.006.

Rekha, C. R., Nayar, V. U. and Gopchandran, K. G. (2018) 'Synthesis of highly stable silver nanorods and their application as SERS substrates', *Journal of Science: Advanced Materials and Devices*, 3(2), pp. 196–205. doi: 10.1016/J.JSAMD.2018.03.003.

Reverberi, R. and Reverberi, L. (2007) 'Factors affecting the antigen-antibody reaction', *Blood Transfusion*, 5(4), p. 227. doi: 10.2450/2007.0047-07.

Riley, R. S. and Day, E. S. (2017) 'Gold nanoparticle-mediated photothermal therapy: applications and opportunities for multimodal cancer treatment', *Wiley interdisciplinary reviews. Nanomedicine and nanobiotechnology*, 9(4). doi: 10.1002/WNAN.1449.

Rodríguez-Galván, A. and Contreras-Torres, F. F. (2022) 'Scanning Tunneling Microscopy of Biological Structures: An Elusive Goal for Many Years',

Nanomaterials 2022, Vol. 12, Page 3013, 12(17), p. 3013. doi: 10.3390/NANO12173013.

Ruehl-Fehlert, C. *et al.* (2003) 'Revised guides for organ sampling and trimming in rats and mice – Part 1: A joint publication of the RITA and NACAD groups', *Experimental and Toxicologic Pathology*, 55(2–3), pp. 91–106. doi: 10.1078/0940-2993-00311.

Russier-Antoine, I. *et al.* (2016) 'Chiral supramolecular gold-cysteine nanoparticles: Chiroptical and nonlinear optical properties', *Progress in Natural Science: Materials International*, 26(5), pp. 455–460. doi: 10.1016/j.pnsc.2016.08.008.

Ryzhikova, E. *et al.* (2015) 'Raman spectroscopy of blood serum for Alzheimer's disease diagnostics: specificity relative to other types of dementia', *Journal of biophotonics*, 8(7), p. 584. doi: 10.1002/JBIO.201400060.

Ryzhikova, E. *et al.* (2019) 'Multivariate Statistical Analysis of Surface Enhanced Raman Spectra of Human Serum for Alzheimer's Disease Diagnosis', *Applied Sciences 2019, Vol. 9, Page 3256*, 9(16), p. 3256. doi: 10.3390/APP9163256.

Sadigh-Eteghad, S. *et al.* (2015) 'Amyloid-beta: A crucial factor in Alzheimer's disease', *Medical Principles and Practice*, 24(1), pp. 1–10. doi: 10.1159/000369101.

Saido, T. C. and Iwata, N. (2006) 'Metabolism of amyloid β peptide and pathogenesis of Alzheimer's disease', *Neuroscience Research*, 54(4), pp. 235–253. doi: 10.1016/j.neures.2005.12.015.

Samieri, C. (2018) 'Epidemiology and risk factors of Alzheimer's disease: A focus on diet', *Neuromethods*, 137, pp. 15–42. doi: 10.1007/978-1-4939-7674-4_2.

Sanati, M. *et al.* (2019) 'Impact of Gold Nanoparticles on Amyloid β-Induced Alzheimer's Disease in a Rat Animal Model: Involvement of STIM Proteins', *ACS chemical neuroscience*, 10(5), pp. 2299–2309. doi: 10.1021/ACSCHEMNEURO.8B00622.

Schackart, K. E. and Yoon, J. Y. (2021) 'Machine learning enhances the performance of bioreceptor-free biosensors', *Sensors*, 21(16). doi: 10.3390/S21165519.

Seibenhener, M. L. and Wooten, M. C. (2015) 'Use of the Open Field Maze to Measure Locomotor and Anxiety-like Behavior in Mice', *Journal of Visualized Experiments : JoVE*, (96), p. 52434. doi: 10.3791/52434.

Sethi, J. *et al.* (2020) 'A label-free biosensor based on graphene and reduced graphene oxide dual-layer for electrochemical determination of beta-amyloid biomarkers', *Microchimica Acta*, 187(5), pp. 1–10. doi: 10.1007/S00604-020-04267-X/FIGURES/8.

Sevigny, J. *et al.* (2016) 'The antibody aducanumab reduces Aβ plaques in Alzheimer's disease', *Nature 2016 537:7618*, 537(7618), pp. 50–56. doi: 10.1038/nature19323.

Shekhar, S. *et al.* (2016) 'Estimation of Tau and phosphorylated Tau181 in serum of Alzheimer's disease and mild cognitive impairment patients', *PLoS ONE*, 11(7), pp. 1–10. doi: 10.1371/journal.pone.0159099.

Shukla, R. K. *et al.* (2021) 'Genotoxic Potential of Nanoparticles: Structural and Functional Modifications in DNA', *Frontiers in Genetics*, 12. doi: 10.3389/FGENE.2021.728250.

Si, P. *et al.* (2021) 'Gold nanomaterials for optical biosensing and bioimaging', *Nanoscale Advances*, 3(10), pp. 2679–2698. doi: 10.1039/D0NA00961J.

Skaria, A. P. (2022) 'The Economic and Societal Burden of AlzheimerDisease: Managed Care Considerations', *American Journal of Managed Care*, 28, pp. S188–S196. doi: 10.37765/AJMC.2022.89236.

Song, C. *et al.* (2022) 'Immunotherapy for Alzheimer's disease: targeting β-amyloid and beyond', *Translational Neurodegeneration*, 11(1). doi: 10.1186/S40035-022-00292-3.

Sonia *et al.* (2021) 'Gold nanoclusters: An ultrasmall platform for multifaceted applications', *Talanta*, 234. doi: 10.1016/j.talanta.2021.122623.

Sood, K. and Shanavas, A. (2022) 'Gold Nanoclusters as Emerging Theranostic Interventions for Biomedical Applications', *BioSensing, Theranostics, and Medical Devices: from Laboratory to Point-of-Care Testing*, pp. 1–31. doi: 10.1007/978-981-16-2782-8_1.

Sousa, A. A., Schuck, P. and Hassan, S. A. (2021) 'Biomolecular interactions of ultrasmall metallic nanoparticles and nanoclusters', *Nanoscale Advances*, 3(11), pp. 2995–3027. doi: 10.1039/D1NA00086A.

Srinivasan, B. *et al.* (2015) 'TEER measurement techniques for in vitro barrier model systems', *Journal of laboratory automation*, 20(2), p. 107. doi: 10.1177/2211068214561025.

Strianese, M. *et al.* (2012) 'Fluorescence-based biosensors', *Methods in Molecular Biology*, 875, pp. 193–216. doi: 10.1007/978-1-61779-806-1_9.

Sypabekova, M. *et al.* (2023) 'Review: 3-Aminopropyltriethoxysilane (APTES) Deposition Methods on Oxide Surfaces in Solution and Vapor Phases for Biosensing Applications', *Biosensors*, 13(1). doi: 10.3390/BIOS13010036.

Ta, N. *et al.* (2024) 'Applications of optical control materials based on localized surface plasmon resonance effect in smart windows', *Tungsten 2024*, pp. 1–21. doi: 10.1007/S42864-024-00273-1.

Takai, E. *et al.* (2014a) 'Cysteine inhibits the fibrillisation and cytotoxicity of amyloid-β 40 and 42: implications for the contribution of the thiophilic interaction', *Physical chemistry chemical physics : PCCP*, 16(8), pp. 3566–3572. doi: 10.1039/C3CP54245A.

Takai, E. *et al.* (2014b) 'Cysteine inhibits the fibrillisation and cytotoxicity of amyloid-β 40 and 42: implications for the contribution of the thiophilic interaction', *Physical Chemistry Chemical Physics*, 16(8), pp. 3566–3572. doi: 10.1039/C3CP54245A.

Teixeira, M. I. *et al.* (2023) 'Surface-modified lipid nanocarriers for crossing the blood-brain barrier (BBB): A current overview of active targeting in brain diseases', *Colloids and Surfaces B: Biointerfaces*, 221, p. 112999. doi: 10.1016/J.COLSURFB.2022.112999.

Teleanu, D. M. *et al.* (2018) 'Blood-Brain Delivery Methods Using Nanotechnology', *Pharmaceutics*, 10(4). doi: 10.3390/PHARMACEUTICS10040269.

Terse-Thakoor, T., Badhulika, S. and Mulchandani, A. (2017) 'Graphene based biosensors for healthcare', *Journal of Materials Research 2017 32:15*, 32(15), pp. 2905–2929. doi: 10.1557/JMR.2017.175.

Tim, B., Błaszkiewicz, P. and Kotkowiak, M. (2021) 'Recent Advances in Metallic Nanoparticle Assemblies for Surface-Enhanced Spectroscopy', *International Journal of Molecular Sciences 2022, Vol. 23, Page 291*, 23(1), p. 291. doi: 10.3390/IJMS23010291.

Tiwari, P. M. *et al.* (2011) 'Functionalized Gold Nanoparticles and Their Biomedical Applications', *Nanomaterials*, 1(1), p. 31. doi: 10.3390/NANO1010031.

Tolar, M., Abushakra, S. and Sabbagh, M. (2020) 'The path forward in Alzheimer's disease therapeutics: Reevaluating the amyloid cascade hypothesis', *Alzheimer's & Dementia*, 16(11), pp. 1553–1560. doi: 10.1016/J.JALZ.2019.09.075.

Toma, H. E. *et al.* (2010) 'The coordination chemistry at gold nanoparticles', *Journal of the Brazilian Chemical Society*, 21(7), pp. 1158–1176. doi: 10.1590/S0103-50532010000700003.

Vigneshvar, S. *et al.* (2016) 'Recent advances in biosensor technology for potential applications - an overview', *Frontiers in Bioengineering and Biotechnology*, 4(FEB), pp. 1–9. doi: 10.3389/fbioe.2016.00011.

Vu Nu, T. T. *et al.* (2018) 'Blood-based immunoassay of tau proteins for early diagnosis of Alzheimer's disease using surface plasmon resonance fiber sensors', *RSC Advances*, 8(14), pp. 7855–7862. doi: 10.1039/C7RA11637C.

Wang, H. *et al.* (2021) 'Regulation of beta-amyloid production in neurons by astrocyte-derived cholesterol', *Proceedings of the National Academy of Sciences of the United States of America*, 118(33), p. e2102191118. doi: 10.1073/PNAS.2102191118/SUPPL_FILE/PNAS.2102191118.SAPP.PDF.

Wang, S. X. *et al.* (2017) 'Detection of the tau protein in human serum by a sensitive four-electrode electrochemical biosensor', *Biosensors and Bioelectronics*, 92, pp. 482–488. doi: 10.1016/j.bios.2016.10.077.

Wang, W. *et al.* (2019) 'Effects of Gold Nanospheres and Nanocubes on Amyloid-β Peptide Fibrillation', *Langmuir*, 35(6), pp. 2334–2342. doi: 10.1021/ACS.LANGMUIR.8B04006.

Wang, Z. *et al.* (2022) 'Rapid Biomarker Screening of Alzheimer's Disease by Interpretable Machine Learning and Graphene-Assisted Raman Spectroscopy', *ACS nano*, 16(4), pp. 6426–6436. doi:

10.1021/ACSNANO.2C00538.

Wasilewski, T., Kamysz, W. and Gębicki, J. (2024) 'AI-Assisted Detection of Biomarkers by Sensors and Biosensors for Early Diagnosis and Monitoring', *Biosensors*, 14(7), p. 356. doi: 10.3390/BIOS14070356.

Wei, H. *et al.* (no date) 'Chem Soc Rev Chemical Society Reviews Nanomaterials with enzyme-like characteristics (nanozymes): next-generation artificial enzymes (II) †', *Chem. Soc. Rev*, 48, p. 1004. doi: 10.1039/c8cs00457a.

Wei, H., Hossein Abtahi, S. M. and Vikesland, P. J. (2015) 'Plasmonic colorimetric and SERS sensors for environmental analysis', *Environmental Science: Nano*, 2(2), pp. 120–135. doi: 10.1039/C4EN00211C.

Wen, X. *et al.* (2012) 'Fluorescence dynamics in BSA-protected Au 25 nanoclusters', *Journal of Physical Chemistry C*, 116(35), pp. 19032–19038. doi: 10.1021/JP305902W/ASSET/IMAGES/MEDIUM/JP-2012-05902W_0009.GIF.

Willets, K. A. and Van Duyne, R. P. (2007a) 'Localized surface plasmon resonance spectroscopy and sensing', *Annual review of physical chemistry*, 58, pp. 267–297. doi: 10.1146/ANNUREV.PHYSCHEM.58.032806.104607.

Willets, K. A. and Van Duyne, R. P. (2007b) 'Localized Surface Plasmon Resonance Spectroscopy and Sensing', *http://dx.doi.org/10.1146/annurev.physchem.58.032806.104607*, 58, pp. 267–297. doi: 10.1146/ANNUREV.PHYSCHEM.58.032806.104607.

Xu, Y. *et al.* (2022) 'Photodynamic Alzheimer's disease therapy: From molecular catalysis to photo-nanomedicine', *Coordination Chemistry Reviews*, 470, p. 214726. doi: 10.1016/J.CCR.2022.214726.

Xue, C. *et al.* (2017) 'Thioflavin T as an amyloid dye: fibril quantification, optimal concentration and effect on aggregation', *Royal Society Open Science*, 4(1). doi: 10.1098/RSOS.160696.

Yadav, P. and Mandal, C. C. (2023) 'Bioimaging: Usefulness in Modern Day Research', *Practical Approach to Mammalian Cell and Organ Culture: With 261 Figures and 89 Tables*, pp. 1205–1230. doi: 10.1007/978-981-19-1731-8_23-1.

Yang, C. C. *et al.* (2018) 'Assay of Plasma Phosphorylated Tau Protein (Threonine 181) and Total Tau Protein in Early-Stage Alzheimer's Disease', *Journal of Alzheimer's disease : JAD*, 61(4), pp. 1323–1332. doi: 10.3233/JAD-170810.

Yang, J. K. *et al.* (2019) 'Reaction Kinetics-Mediated Control over Silver Nanogap Shells as Surface-Enhanced Raman Scattering Nanoprobes for Detection of Alzheimer's Disease Biomarkers', *Small*, 15(19), p. 1900613. doi: 10.1002/SMLL.201900613.

Yang, Y. and Wang, C. (2013) 'Single-molecule studies on individual peptides and peptide assemblies on surfaces', *Philosophical Transactions of the Royal Society A: Mathematical, Physical and Engineering Sciences*, 371(2000). doi: 10.1098/RSTA.2012.0311.

Yoo, J. *et al.* (2021) 'Interdigitated Electrode Biosensor Based on Plasma-Deposited TiO2 Nanoparticles for Detecting DNA', *Biosensors 2021, Vol. 11, Page 212*, 11(7), p. 212. doi: 10.3390/BIOS11070212.

Yu, D. *et al.* (2021) 'SERS-Based Immunoassay Enhanced with Silver Probe for Selective Separation and Detection of Alzheimer's Disease Biomarkers', *International Journal of Nanomedicine*, 16, p. 1901. doi: 10.2147/IJN.S293042.

Yuan, O. *et al.* (2019) 'Exosomes Derived from Human Primed Mesenchymal Stem Cells Induce Mitosis and Potentiate Growth Factor Secretion', *Stem cells and development*, 28(6), pp. 398–409. doi: 10.1089/SCD.2018.0200.

ZEISS Microscopy Online Campus | Microscopy Basics | Fluorescence Microscopy (no date). Available at: https://zeiss-campus.magnet.fsu.edu/articles/basics/fluorescence.html (Accessed: 9 August 2024).

Zhan, Y. *et al.* (2022) 'Ultrasensitive detection of multiple Alzheimer's disease biomarkers by SERS-LFA', *Analyst*, 147(18), pp. 4124–4131. doi: 10.1039/D2AN00717G.

Zhang, C. *et al.* (2015) 'Gold Nanoclusters-Based Nanoprobes for Simultaneous Fluorescence Imaging and Targeted Photodynamic Therapy with Superior Penetration and Retention Behavior in Tumors', *Advanced Functional Materials*, 25(8), pp. 1314–1325. doi: 10.1002/ADFM.201403095.

Zhang, C. *et al.* (2022) 'Advances of gold nanoclusters for bioimaging', *iScience*, 25(10). doi: 10.1016/J.ISCI.2022.105022.

Zhang, L. *et al.* (2023) 'Electrochemical biosensors represent promising detection tools in medical field', *Advanced Sensor and Energy Materials*, 2(4), p. 100081. doi: 10.1016/J.ASEMS.2023.100081.

Zu, L. *et al.* (2024) 'Ultrasensitive and Multiple Biomarker Discrimination for Alzheimer's Disease via Plasmonic & Microfluidic Sensing Technologies', *Advanced Science*, 11(24). doi: 10.1002/ADVS.202308783.

ANNEXURES

List of publications from Thesis

1) **Resmi A.N,** S. Sivaselvam, Rekha.C.R, Emilia Papasoulib, Kunnumpurathu Jibin, C.S. Praveen,Emmanuel N. Koukaras, Michel Rerat, Panaghiotis Karamanis,Ramapurath.S.Jayasree. (2024). Nanoarchitectonics of Fluorescent Gold Nanoclusters: A Platform for Image Guided Photodynamic Therapy of Hypoxic Tumor, *Applied Materials Today,*39,102273.

2) **Resmi A. N.,** Rekha, C. R., Dhushyandhun, M. E., Elangovan, S., Shenoy, S. J., Gulia, K. K., & Jayasree, R. S. (2023). Bifunctional cysteine gold nanoclusters for β-amyloid fibril inhibition and fluorescence imaging: a distinctive approach to manage Alzheimer's disease, *Journal of Materials Chemistry B, 11*(21), 4715-4724.

3) **Resmi A.N**., Shaiju S Nazeer, M. E. Dhushyandhun, Willi Paul, Binu P Chacko, Ramshekhar N. Menon, Ramapurath.S.Jayasree.(2024). Ultra-Sensitive Detection of Blood-Based Alzheimer's Biomarkers: AComprehensive SERS-Immunoassay Platform Enhanced by MachineLearning. (Communicated to *Analytical chemistry*)

4) **Resmi A.N.,** Rekha, C. R, M. E. Dhushyandhun, Jayasree, R. S "Nanomaterial-Enhanced Blood-based Biosensors: A New Era in Alzheimer's Disease Diagnostics". (Under revision)

5) **Resmi A**.N., M. E. Dhushyandhun, Pratheesh K V,Siva selvam, Jayasree, R. S. "The effect of Cysteine gold cluster on streptozotocin-induced Alzheimer's disease model: emphasis on inhibition and disintegration of amyloid beta growth." (Under Preparation)

6) **Resmi A.N.,** Archana Thomas, Abijith, M. E. Dhushyandhun, Jijo P T Jayasree, R. S. "A Multifaceted Approach to Early Alzheimer's Disease Diagnosis: Unveiling Protein Folding and Utilizing Surface Charge for Sensitive Biomarker Detection". (Under Preparation)

Book Chapter

Resmi A. N., Resmi, V. N., Rekha, C. R., Lakshmi, V. N., Nazeer, S. S., & Jayasree, R. S. (2022). Phototherapy Using Nanomaterials, *Bionanotechnology in Cancer: Diagnosis and Therapy*, 373. (Publisher: Jenny Stanford Publishing, Singapore).

Patent

Indian Patent 'Bifunctional Cysteine Gold Nanocluster for Imaging and Inhibition of Amyloid beta fibrils" was applied in the name of Sree Chitra

Tirunal Institute for Medical Sciences and Technology and Department of Biotechnology. (**Patent Application No. 202341037775 dated 01.06.2023**)

Conference Presentations & Awards

1) Presented a poster in 35 th Kerala Science Congress during 12 th -14 th February, 2023, for the paper entitled, "Bifunctional Gold Nanocluster as a Theranostic Probe for the Management of Alzheimer's disease" (**Best poster presentation award**)

2) Presented a poster on 'Dual-functional Gold Nanoclusters: A promising therapeutic agent for the management of Alzheimer's Disease, with real-time fluorescence monitoring' in Indo-France Seminar organized by CEFIPRA on October 2-5th, 2023 at the Institute of Nano Science and Technology (INST), Mohali, Punjab, India

3) Presented a poster in Bengaluru INDIA NANO 2022 entitled "Subatomic sized gold cluster for simultaneous imaging and photodynamic therapy" from 7th – 8th March 2022

4) Presented a paper on 'Gold nanocluster based nanoprobe for the simultaneous Fluorescence Imaging and Targeted Photodynamic Therapy 'in International Conference on Material Science and Technology (ICMT-2021), Organized by Mahatma Gandhi University, Kottayam on November 12, 13, and 14th, 2021

5) Presented a paper on 'Gold nanocluster as an efficient theranostic probe for the management of Alzheimer's Disease in 'Nanomedicine: Biomolecules for human health (NBHH- 2021)', International Conference Organized by Nanobiotech Lab, Kirori Mal College, the University of Delhi on September 27-28th, 2021

6) Presented a paper on 'Fluorescent Nanoparticle-mediated theranostic approaches for neurodegenerative diseases' in 'NANOSCIENCE 2021', International Webinar Organized by the Department of Physics, and Christian College Kattakkadaduring 28-30 July 2021

Student Outreach program

- Presented a talk on "Fostering a Scientific Temper in Young Minds" at Victory Vocational Higher Secondary School,Trivandrum, on February 13, 2024, as part of an outreach program aimed at popularizing science among school students.

CURRICULUM VITAE

ACADEMIC QUALIFICATION

Examination	Institution	University / Board	Year	Aggregate
B.Ed Physical Science	St:Thomas Training College, Trivandrum	Kerala University	2009-2010	73%
MSc Physics	Mahatma Gandhi College, Trivandrum	Kerala University	2007-2009	79%
BSc Physics	Mar Ivanios College, Trivandrum	Kerala University	2004-2007	85%
+2	St.John's Model HSS, Trivandrum	Board of Higher Secondery Education, Kerala	2002-2004	73.5%
SSLC	St.Goretti's HSS , Trivandrum	Board of Higher Secondary Education, Kerala	2001-2002	86.6%

RESEARCH EXPERIENCE

1. Division of Biophotonics and Imaging, Sree Chitra Tirunal Institute for Medical Sciences and Technology, Trivandrum.

   Currently doing PhD

2. Division of Biophotonics and Imaging, Sree Chitra Tirunal Institute for Medical Sciences and Technology, Trivandrum

   Junior Research Fellow-DBT project-17/01/2019 to 02/04/2023 (Blood Brain Barrier Permeable nanocarriers for diagnosis and therapy of neurodegenerative diseases)

3. Department of Physics, Indian Institute of Space Science and Technology, Valiyamla

   Junior Project Fellow - ISRO –IISU project-08/03/2018 to 16/01/2019(Surface Engineering Techniques for

   Improving the Life Performance of Ball Bearings in ISRO Spacecraft Mechanisms)

4. Department of Physics, Indian Institute of Space Science and Technology,

Valiyamla

Junior Project Fellow- IIST Project- 27/05/2014 to 26/05/2017(Electronic Manipulation of Surface Plasmon Polaritons in Graphene Using Scanning Tunneling Microscope (STM)).

5. Department of Physics, St:Xavier's college, Thumba

   Guest Lecturer in Physic – 08/06/2011 to 30/03/2013(UG and PG)

RESEARCH SKILL

- Functional Nanomaterial Synthesis, Spectroscopic and Microscopic analysis of various functional materials. Graphitic meta-material synthesis, *in vitro* and *in vivo* experimental expertise. *In vivo* and *ex vivo* imaging analysis.
- Device development for biomedical applications.
- Operating Skill of Nd-YAG Laser, Spectroscopic, Microscopic Instruments- UV-spectrophotometer, Fluorimeter, FTIR, STM and STS, *In vivo* animal imager, Optical microscope.

ACHIEVEMENTS

- **Best poster presentation award** in 35 th Kerala Science Congress
- **Thirteen international Journal papers** have been published with good impact factor
- Received certificate from the **Honourable President of India** (Rashtrapathi Award) for Bharat Scouts and Guides association activities.
- Received certificate from the **Honourable Governor of Kerala state** for Bharat Scouts and Guides association activities.
- Achieved **Best Volunteer Award** in National Service Scheme.
- Achieved **District Level First Prize** in Screen Printing.

Appendices

APPENDIX A – ETHICS COMMITTEE APPROVAL

i. Blood Plasma samples were collected from the Neurology Department at Sree Chitra Tirunal Institute for Medical Science and Technology (SCTIMST) in Thiruvananthapuram,approved by the Institutional Ethics Committee of SCTIMST (Order no: SCT/IEC/IEC-1669/DECEMBER-2020).

ii. Animal procedures were approved by the Institute Animal Ethics Committee of Sree Chitra Tirunal Institute for Medical Sciences and Technology, Trivandrum (IAEC approval No-SCT/IAEC399/MARCH/2021/109).

APPENDIX B - PUBLICATIONS

1. Anjusha, A. J., Thirunavukkarasu, S., **Resmi A. N.,** Jayasree, R. S., Dhanapandian, S., & Krishnakumar, N. (2023). Multifunctional amino functionalized graphene quantum dots wrapped upconversion nanoparticles for photodynamic therapy and X-ray CT imaging. *Inorganic Chemistry Communications*, *149*, 110428.

2. Nazeer, S. S., Saraswathy, A., Nimi, N., Sarathkumar, E., **Resmi A. N**., Shenoy, S. J., & Jayasree, R. S. (2023). Fluorescent carbon dots tailored iron oxide nano hybrid system for *in vivo* optical imaging of liver fibrosis. *Methods and Applications in Fluorescence*, *11*(2), 024002.

3. Ram Prasad; Sudheendran Leena, Sruthi; Deepthi, Ani;Jayasree, Ramapurath; **Resmi A.N** ; Athipettah , Jayakrishna,(2024). Sustained Delivery of Doxorubicin for the Treatment of Glioblastoma Using Doxorubicin-Polysorbate-80. *RSC Pharmaceutics.*

4. Muthu, C., **Resmi A. N**., Ajayakumar, A., Ravindran, N. A., Dayal, G., Jinesh, K. B., ... & Vijayakumar, C. (2024). Self-Assembly of Delta-Formamidinium Lead Iodide Nanoparticles to Nanorods: Study of Memristor Properties and Resistive Switching Mechanism. *Small*, 2304787.

5. Muthu, C., **Resmi A. N**., Pious, J. K., Dayal, G., Krishna, N., Jinesh, K. B., & Vijayakumar, C. (2021). Resistive switching in formamidinium lead iodide perovskite nanocrystals: a contradiction to the bulk form. *Journal of Materials Chemistry C*, *9*(1), 288-293.

6. Sundararajan, M., Rejith, R. G., Renjith, R. A., Mohamed, A. P., Gayathri, G. S., **Resmi A.N**.,Loveson, V. J. (2021). Raman-XPS spectroscopic investigation of heavy mineral sands along Indian coast. *Geo-Marine Letters*, *41*(2), 22.

7. Thomas, A., **Resmi A. N**., Ganguly, A., & Jinesh, K. B. (2020). Programmable electronic synapse and nonvolatile resistive switches using MoS2 quantum dots. *Scientific Reports*, *10*(1), 12450.

8. Sukumaran, S. S., Tripathi, S., **Resmi A. N**., Gopchandran, K. G., & Jinesh, K. B. (2019). Influence of surfactants on the electronic properties of liquid-phase exfoliated graphene. *Materials Science and Engineering: B*, *240*, 62-68.

9. Sukumaran, S. S., Rekha, C. R., **Resmi A. N**., Jinesh, K. B., & Gopchandran, K. G. (2018). Raman and scanning tunneling spectroscopic investigations on graphene-silver nanocomposites. *Journal of Science: Advanced Materials and Devices*, *3*(3), 353-358.,

10. Hazra, P., **Resmi A. N**., & Jinesh, K. B. (2016). Gate controllable resistive random access memory devices using reduced graphene oxide. *Applied Physics Letters*, *108*(15).

11. Mangalam, J., Agarwal, S., **Resmi A. N**., Sundararajan, M., & Jinesh, K. B. (2016). Resistive switching in polymethyl methacrylate thin films. *Organic Electronics*, *29*, 33-38.

12. Enhancing Lateral Flow Assay performance for clinical diagnosis: Integration of Nanozyme and Paraphenylenediamine as a Transformative Biomedical Sensor. (Communicated to Biomaterials)

APPENDIX D – PLAGIARISM CHECK REPORT

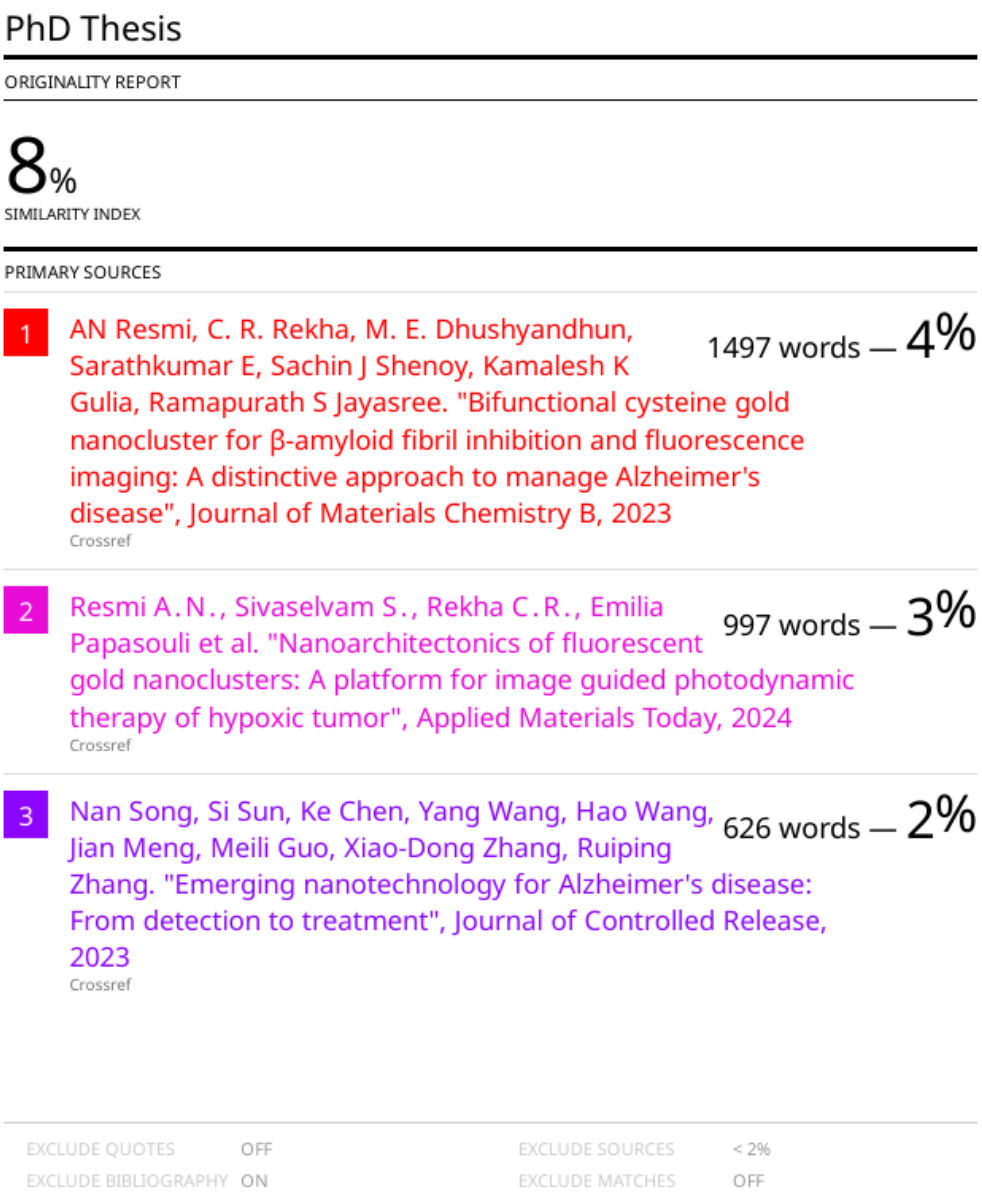

PhD Thesis

ORIGINALITY REPORT

8%
SIMILARITY INDEX

PRIMARY SOURCES

1 AN Resmi, C. R. Rekha, M. E. Dhushyandhun, Sarathkumar E, Sachin J Shenoy, Kamalesh K Gulia, Ramapurath S Jayasree. "Bifunctional cysteine gold nanocluster for β-amyloid fibril inhibition and fluorescence imaging: A distinctive approach to manage Alzheimer's disease", Journal of Materials Chemistry B, 2023
Crossref
1497 words — 4%

2 Resmi A.N., Sivaselvam S., Rekha C.R., Emilia Papasouli et al. "Nanoarchitectonics of fluorescent gold nanoclusters: A platform for image guided photodynamic therapy of hypoxic tumor", Applied Materials Today, 2024
Crossref
997 words — 3%

3 Nan Song, Si Sun, Ke Chen, Yang Wang, Hao Wang, Jian Meng, Meili Guo, Xiao-Dong Zhang, Ruiping Zhang. "Emerging nanotechnology for Alzheimer's disease: From detection to treatment", Journal of Controlled Release, 2023
Crossref
626 words — 2%

EXCLUDE QUOTES OFF
EXCLUDE BIBLIOGRAPHY ON
EXCLUDE SOURCES < 2%
EXCLUDE MATCHES OFF